Guide to Wave Analysis and Forecasting

DRAFT VERSION FOR APPROVAL

2018 edition

WEATHER CLIMATE WATER

WORLD METEOROLOGICAL ORGANIZATION

WMO-No. 702

Guide to Wave Analysis and Forecasting

2018 edition

WORLD
METEOROLOGICAL
ORGANIZATION

WMO-No. 702

EDITORIAL NOTE

METEOTERM, the WMO terminology database, may be consulted at http://public.wmo.int/en/resources/meteoterm.

Readers who copy hyperlinks by selecting them in the text should be aware that additional spaces may appear immediately following http://, https://, ftp://, mailto:, and after slashes (/), dashes (-), periods (.) and unbroken sequences of characters (letters and numbers). These spaces should be removed from the pasted URL. The correct URL is displayed when hovering over the link or when clicking on the link and then copying it from the browser.

WMO-No. 702

Chair, Publications Board
World Meteorological Organization (WMO)
7 bis, avenue de la Paix
P.O. Box 2300
CH-1211 Geneva 2, Switzerland

Tel.: +41 (0) 22 730 84 03
Fax: +41 (0) 22 730 81 17
Email: publications@wmo.int

ISBN 978-92-63-10702-2

PUBLICATION REVISION TRACK RECORD

Date	*Part/ chapter/ section*	*Purpose of amendment*	*Proposed by*	*Approved by*

CONTENTS

Page

FOREWORD ... **ix**

ACKNOWLEDGEMENTS ... **x**

INTRODUCTION ... **xi**
Overview ... xi
Terminology ... xii
Climatological issues ... xiii
Structure of this guide ... xiii

CHAPTER 1. OCEAN-SURFACE WAVES ... **1**

1.1 INTRODUCTION ... **1**

1.2 SIMPLE LINEAR WAVES ... **2**
1.2.1 Basic definitions ... 2
1.2.2 Basic relationships ... 3
1.2.3 Orbital motion of water particles ... 4
1.2.4 Energy in waves ... 5
1.2.5 Influence of water depth ... 5
1.2.6 Refraction and diffraction ... 7
1.2.7 Breaking waves ... 9

1.3 WAVE FIELDS ON THE OCEAN ... **10**
1.3.1 Decomposition of simple waves ... 10
1.3.2 Wave groups and group velocity ... 11
1.3.3 Statistical description of wave records ... 12
1.3.4 Duration of wave records ... 13
1.3.5 Use of statistical parameters ... 14
1.3.6 Distribution of wave heights ... 14
1.3.7 Wave spectra ... 15
1.3.8 Wave parameters derived from a spectrum ... 18
1.3.9 Model forms of wave spectra ... 20
1.3.10 Remarks on the directional wave spectrum ... 22

CHAPTER 2. OCEAN-SURFACE WINDS ... **24**

2.1 INTRODUCTION ... **24**

2.2 SOURCES OF MARINE DATA ... **25**
2.2.1 Ship weather reports ... 25
2.2.1.1 Estimated winds ... 26
2.2.1.2 Measured winds ... 27
2.2.2 Moored and drifting buoy reports ... 27
2.2.3 Land (coastal) stations ... 28
2.2.4 Common height adjustment of in situ data ... 28
2.2.5 Satellite data ... 29

2.3 MARINE BOUNDARY LAYERS ... **30**
2.3.1 Constant flux layer ... 32
2.3.2 Surface roughness ... 33
2.3.3 Stability effects ... 34

2.4 LARGE-SCALE METEOROLOGICAL FACTORS AFFECTING OCEAN-SURFACE WINDS **36**
2.4.1 Wind and pressure analyses ... 37
2.4.2 Geostrophic wind ... 39
2.4.3 Gradient wind ... 42
2.4.4 Surface friction effects ... 44

Page

2.4.5 Thermal wind 46
2.4.6 Isallobaric wind 47
2.4.7 Diffluence of wind fields 47
2.4.8 Wind shear in frontal zones 49
2.4.9 Streamline analyses in the tropics 49
2.4.10 Tropical cyclone analysis 50

2.5 NUMERICAL WEATHER PREDICTION. 52
2.5.1 Grid-point models 53
2.5.2 Spectral models 54
2.5.3 Limited-area models 54
2.5.4 Boundary-layer parameterization 54
2.5.5 Coupled models. 55
2.5.6 Data assimilation 56
2.5.7 Reanalyses. 56
2.5.8 Ensemble prediction 56

CHAPTER 3. WAVE GENERATION AND DECAY 60

3.1 INTRODUCTION. 60

3.2 WIND-WAVE GROWTH. 60
Empirical formulae and wind-wave growth curves. 62

3.3 WAVE PROPAGATION 65
3.3.1 Angular spreading 65
3.3.2 Dispersion. 66

3.4 WAVE DISSIPATION 68
3.4.1 Deep-water-wave dissipation. 68
3.4.2 Shallow-water-wave dissipation. 68
3.4.3 Swell dissipation. 70

3.5 NON-LINEAR WAVE–WAVE INTERACTIONS. 70

3.6 GENERAL NOTES ON SOURCE TERMS 73

CHAPTER 4. MANUAL WAVE FORECASTING 75

4.1 INTRODUCTION. 75

4.2 EMPIRICAL WORKING PROCEDURES. 77
4.2.1 Variable winds 78
4.2.2 Estimating fetch 78
4.2.3 Wave growth 78
4.2.4 Swell decay 79
4.2.5 Speed and motion of wave groups 80
4.2.6 Miscellaneous. 80

4.3 COMPUTATION OF WIND WAVES 81
4.3.1 Determination of sea-state characteristics for given wind speed and fetch. 81
4.3.2 Determination of sea state for increasing wind speed 81
4.3.3 Extrapolation of an existing wave field with further development from a constant wind. 83
4.3.4 Extrapolation of an existing wave field with further development from an increasing wind. 83
4.3.5 Determination of the effects of a dynamic or trapped fetch for a tropical cyclone moving at different speeds. 84

Page

4.4 COMPUTATION OF SWELL 86
4.4.1 Distant storms 86
4.4.2 Distant storms with long fetch 88
4.4.3 Swell arriving at point of observation from a nearby storm 89
4.4.4 Further examples 92

4.5 COMPUTATION OF SHALLOW-WATER EFFECTS 94
4.5.1 Shoaling and refraction of swell in a coastal zone 95
4.5.1.1 Variation in wave height due to shoaling 95
4.5.1.2 Variation of wave height due to refraction 97
4.5.1.3 Dorrestein's method for determining refraction factor. 98
4.5.2 Wind waves in shallow water 99

4.6 MODIFICATION OF NUMERICAL GUIDANCE 100
4.6.1 Possible model issues. 100
4.6.2 Model operational verification 101
4.6.2.1 Wind 101
4.6.2.2 Waves 102
4.6.2.3 Other effects 102
4.6.3 Forecast cycle: analysis, diagnosis and prognosis 103

4.7 RIP CURRENT FORECASTING 104
4.7.1 Basic forecasting method 104
4.7.2 Forecasting considerations 104
4.7.3 Tips for creating a forecasting scheme 106

CHAPTER 5. NUMERICAL WAVE MODELLING 109

5.1 INTRODUCTION 109

5.2 BASIC CONCEPTS 109

5.3 WAVE-ENERGY-BALANCE EQUATION 111

5.4 ELEMENTS OF WAVE MODELLING 111
5.4.1 Initial conditions. 111
5.4.2 Winds. 113
5.4.3 Input and dissipation. 114
5.4.4 Non-linear interactions 115
5.4.5 Propagation 115
5.4.5.1 Discrete-grid methods 116
5.4.5.2 Ray-tracing methods 117
5.4.6 Directional relaxation and wind-sea–swell interaction. 118
5.4.7 Depth. 118
5.4.8 Effects of boundaries, coast-lines and islands. 118

5.5 MODEL CLASSES. 119
5.5.1 Decoupled propagation models 120
5.5.2 Coupled hybrid models 120
5.5.3 Coupled discrete models 122
5.5.4 Third-generation models 123

5.6 NEW DEVELOPMENTS. 124

CHAPTER 6. OPERATIONAL WAVE MODELS 126

6.1 INTRODUCTION. 126

6.2 TWO-DIMENSIONAL SPECTRAL WAVE MODELS 126

Page

6.2 TWO-DIMENSIONAL SPECTRAL WAVE MODELS ... 127

6.3 WAVE CHARTS ... 129

6.4 CODED WAVE-MODEL PRODUCTS ... 133
6.4.1 GRIB ... 133
6.4.2 NetCDF ... 134

6.5 VERIFICATION OF WAVE MODELS ... 134

6.6 ENSEMBLE PREDICTION SYSTEMS ... 137

CHAPTER 7. WAVE DATA: OBSERVED, MEASURED AND MODELLED ... 142

7.1 INTRODUCTION ... 142

7.2 IN SITU WAVE DATA ... 142
7.2.1 Differences between visual and instrumental data ... 142
7.2.1.1 Estimating significant wave height from visual sea and swell ... 143
7.2.1.2 Partitioning spectral wave data into wind sea and swell ... 143
7.2.2 Visual observations ... 143
7.2.2.1 Visual observations from ships ... 144
7.2.2.2 Sources of visual wave data from ships ... 145
7.2.2.3 Visual observations from coastal stations ... 146
7.2.3 Measured wave data ... 146
7.2.3.1 Wave measurements from below the surface ... 147
7.2.3.2 Wave measurements from buoys ... 147
7.2.3.3 Other wave measurements at the sea surface ... 152
7.2.3.4 Measurements from above, but near the surface ... 153

7.3 REMOTE-SENSING DATA ... 154
7.3.1 Active sensing of the ocean surface with electromagnetic waves ... 154
7.3.2 Space-based remote sensing ... 156
7.3.2.1 Radar altimeters ... 156
7.3.2.2 Synthetic aperture radars ... 158
7.3.2.3 Scatterometers ... 161
7.3.2.4 Microwave radiometers ... 161
7.3.2.5 Emerging technologies ... 161
7.3.3 Surface-based remote sensing ... 162
7.3.3.1 Oblique platform-mounted sensors ... 162
7.3.3.2 Ground-wave and sky-wave high-frequency radars ... 162

7.4 MODELLED DATA ... 163
7.4.1 Hindcasting ... 163
7.4.2 Reanalysis ... 164
7.4.2.1 European Centre for Medium-Range Weather Forecast ERA5 reanalysis ... 164
7.4.2.2 National Oceanic and Atmospheric Administration/National Centers for Environmental Prediction Climate Forecast System Reanalysis ... 165
7.4.3 Operational modelling ... 165

ANNEX 1. WAVE NOMOGRAMS ... 166

ANNEX 2. WAVE FORECASTING: BASICS AND TIPS ... 174

REFERENCES ... 176

FOREWORD

National Meteorological and Hydrological Services (NMHSs) of numerous maritime countries have been engaged in the provision of ocean wave forecast and hindcast services in support of user requirements across the whole range of maritime activities (shipping, fisheries, offshore mining, commerce, coastal engineering, construction, recreation and so on) for many years. In recognition of this, and of the relative lack of easily accessible guidance material on wave forecasting methodology suitable for use by NMHSs in developing countries, the *Guide to Wave Analysis and Forecasting* was originally prepared by a group of experts and published in 1988 as WMO-No. 702. This formal Guide updated and replaced the earlier and very popular *Handbook on Wave Analysis and Forecasting* (WMO-No. 446), published in 1976. The 1988 edition of the Guide was subsequently updated in 1998 (second edition). This 2018 version (third edition) represents the latest updates, taking into account the dramatic improvements in wave modelling and observational capability over the last two decades.

In further recognition of the requirements of NMHSs for the provision of ocean-wave-related services and also of the rapid developments that were occurring in wave measurement, analysis and forecast techniques, the WMO Commission for Marine Meteorology (CMM) established a WMO Wave Programme in 1984. The various elements of this programme have been implemented, reviewed and updated, initially by the CMM Subgroup on Wave Modelling and Forecasting, and since the creation of the WMO–International Oceanographic Commission Joint Technical Commission on Oceanography and Marine Meteorology, by an expert team dedicated to waves and storm surge. One of these elements involves the continuous review and revision, as necessary, of the *Guide to Wave Analysis and Forecasting*. Therefore, the expert team established an ad hoc group of experts in 2011, under the chairmanship of Mr Thomas Bruns (Germany), to undertake complete revision and updating of the Guide, in the light of new developments and especially of feedback from users of the 1998 edition.

The international experts, directed by Mr Bruns, have prepared substantially revised versions of the chapters of the Guide. These individual contributions were subsequently coordinated, assembled and edited by Mr Bruns into a draft, which was then submitted to a wide network of wave experts for review and comment. Reviewers' comments were incorporated, to the extent possible, and a final edit of the third edition of this Guide was made by Mr Bruns.

No publication such as this can ever be perfect, particularly in a continuously developing field of science and technology; further additions and modifications will undoubtedly be required in the future. Nevertheless, this third edition of the *Guide to Wave Analysis and Forecasting* will be a very valuable publication in support of the marine services provided by maritime WMO Members. It is also believed that the Guide continues to meet its twofold objectives: to provide introductory but self-sufficient guidance material for use in the provision of basic wave forecast services, while at the same time acting as a source text and a guide to further reading on the subject.

Each chapter gives acknowledgements to authors as appropriate, but I would like here, on behalf of WMO, to express my sincere appreciation to all the experts (authors, reviewers and particularly Mr Bruns) who have contributed so much to this important and valuable publication.

(Petteri Taalas)
Secretary-General

ACKNOWLEDGEMENTS

The revision of this *Guide to Wave Analysis and Forecasting* has been a team effort, involving experts from several countries in various aspects of ocean waves. Mr Thomas Bruns (Germany) has undertaken overall direction of the project. The chapter editors/authors have had overall responsibility for the revision of chapters; in cases where substantial assistance has been given, co-authors are also acknowledged.

Much of the material is derived from the first and second editions of the Guide. The present editor would like to acknowledge the efforts put into the previous publications by the editors E. Bouws and A.K. Laing, and the chapter editors J.A. Battjes, E. Bouws, L. Burroughs, D.J.T. Carter, L. Draper, L. Eide, J.A. Ewing, W. Gemmill, L. Holthuijsen, M. Khandekar, A.K. Laing, A.K. Magnusson, M. Reistad and V. Swail.

This edition has been produced with the following specific contributions:

- Overall direction and introduction:
  T. Bruns, Deutscher Wetterdienst, Branch Office Hamburg, Germany;
- Chapter 1:
  F. Ocampo-Torres, Oceanografía Física, Centre for Scientific Research and Higher Education at Ensenada, Mexico;
- Chapter 2:
  T. Bruns, Deutscher Wetterdienst, Branch Office Hamburg, Germany;
- Chapter 3:
  A. Chawla, National Center for Weather & Climate Prediction, National Oceanic Atmospheric Administration, College Park, Maryland, United States of America;
- Chapter 4:
  D. Mercer, **J. Mclean** and **S. Desjardins**, Environment and Climate Change Canada, Halifax, Canada;
- Chapter 5:
  J.-R. Bidlot, European Centre for Medium-Range Weather Forecasts, Reading, United Kingdom of Great Britain and Northern Ireland;
- Chapter 6:
  A. Saulter, Met Office, Exeter, United Kingdom of Great Britain and Northern Ireland;
- Chapter 7:
  V. Swail, Environment and Climate Change Canada, Toronto, Canada;
  F. Ocampo-Torres, Oceanografía Física, Centre for Scientific Research and Higher Education at Ensenada, Mexico.

Contact with contributors can be made through the Marine Meteorology and Ocean Affairs Division of the WMO Secretariat, mmo@wmo.int.

The editor would like to thank the Secretariat staff who assisted in the preparation of this publication.

INTRODUCTION

Overview

The subject of this *Guide to Wave Analysis and Forecasting* is ocean waves, specifically those generated by the wind. Such waves affect coasts and activities near the coast and out to sea. At any given time, the waves are a result of the recent history of winds over broad expanses of ocean. Knowledge of the winds allows diagnosis of the wave conditions. The progress in numerical weather prediction over many years has resulted in as good predictability for the waves as for the wind. The objective of this Guide is to provide basic information and techniques on the analysis and forecasting of ocean waves. It is not intended to give a comprehensive theoretical treatment of waves, nor does it contain details of present research activity. Rather, it focuses on providing a general overview, with details on aspects considered useful for wave analysis and forecasting.

Readers interested in fundamental research issues of wave processes and modelling are referred to the benchmark publication *Dynamics and Modelling of Ocean Waves* (Komen et al., 1994). An extensive treatment of problems related to wave data and their use is provided in *Waves in Ocean Engineering: Measurement, Analysis, Interpretation* (Tucker, 1991). A comprehensive reference for problems specifically related to coastal engineering is the *Shore Protection Manual* by the Coastal Engineering Research Center (CERC, 1973, 1984).

The primary users of this publication are seen as being professionals and technicians involved in operations affected by ocean waves, that is, a wide community of marine operators and those providing specialized services to them. Marine weather forecasters form a key group, but the Guide is equally intended for the potential users of wave data analyses, forecasts and climatological products.

This third edition of the *Guide to Wave Analysis and Forecasting* replaces the 1988 and 1998 editions of the same name (WMO, 1988, 1998), which in turn replaced the *Handbook on Wave Analysis and Forecasting* (WMO, 1976). All editions recognize that the interpretation of wave data and products requires a good understanding of the processes by which these products are derived. An overview of the elementary theory is therefore necessary in this Guide. Sufficient background information is included to make this publication as self-contained as possible wherever a technique or source of data are introduced.

While many of the basics have remained consistent throughout the editions, there are developments creating new opportunities in wave information services. In recent decades, an increasing number of wave products have incorporated data from satellites or data synthesized from simulations using numerical wave models run operationally by many forecasting centres. Effective use of these products is possible only if the forecasters and other users have sufficient knowledge about the physical background of wave modelling and satellite observations.

Wave modelling was firstly given prominence in the 1988 edition of the Guide. This emphasis has been retained in the 1998 edition and the present edition. The concerted international effort of the 1980s to develop physically realistic wave models has culminated in a generation of wave models that have been thoroughly researched, tested and utilized operationally.

However, there are still problems to solve. For example, dissipation, which plays a critical role in the energy balance, is still the subject of research, including on wave breaking and swell damping.

Furthermore, for computational reasons, operational models still use parameterizations of the wave–wave interactions that control the distribution of energy within the wave spectrum. In recent years, with increasingly available computer power, comparisons between parameterizations and exact solutions have become possible. This will eventually result in more-realistic parameterizations, particularly in extreme situations such as tropical storms. The problems of wave evolution in shallow water and interaction with surface currents also require

continuing efforts. None of these new developments will be discussed in the present edition of the Guide, because progress is manifold and will most probably not influence forecasters' daily business.

Some years after the publication of the 1998 edition of the Guide, it was recognized that national and international agencies had carried out a significant amount of research which contributed valuable information on wave forecasting and climatology. In view of ongoing developments of practices in numerical wind wave forecasting, a need arose for continuous updating of the Guide. The idea of a dynamic part of a Guide has already been utilized for the *Guide to the Applications of Marine Climatology* (WMO, 1994) and will now also be adopted for the present edition of this Guide.

The 1998 edition of this Guide included a catalogue describing operational wave models. For the present edition, it was considered useful to outsource these descriptions to a web-based dynamic part, owing to the frequent changes in operational model configurations (operational wave model information is also available from the WMO Lead Centre for Wave Forecast Verification, as well as ongoing results from the WMO–International Oceanographic Commission Joint Technical Commission on Oceanography and Marine Meteorology Wave Forecast Verification Project). Some text in this Guide is linked directly to the dynamic part, where the desired information can be found in a list of web links. The dynamic part will be expanded with other contributions (for example, recent publications related to the topics covered in this Guide and advances in ocean wave forecasting) in the future, to keep abreast of new developments.

Wave modelling is used extensively in synthesizing wave data for climatological purposes. Its use is briefly described in section 7.4. The *Guide to the Applications of Marine Climatology* (WMO, 1994) gives a detailed description of wave hindcasting procedures and their use in wave climatology, so the chapter on wave climate statistics in the previous edition of this Guide was considered redundant. However, wave climatologies based on reanalysed wind fields are available from some national forecast centres.

The previous edition discussed the increase in wave and wind data available from satellites. This third edition includes new material on this source of data, particularly in the chapters on wind fields (Chapter 2) and wave data (Chapter 7). These data have become indispensable for improved numerical model initializations and for validation of hindcast data. Some of the work being carried out in this regard is discussed.

Notwithstanding such advances, it is recognized that many wave products are based on visual observations, and that manual analyses and forecasts are still widely used. Hence, material on manual methods has been retained in the present edition. A new section on rip current forecasting has been added in view of the many lives lost on beaches worldwide. The manual methods are linked with the numerical methods by demonstrating their joint physical basis.

Terminology

This Guide uses "analysis of waves" to refer to a broad range of procedures. The conventional meteorological context of analysis involves data assimilation, but this has had limited application in deriving wave products because wave data have been too scarce. Today, satellites provide a large volume of wind and wave data assimilated into numerical models.

"Wave analysis" incorporates the procedures for estimating, calculating or diagnosing wave conditions. There is a direct relationship between wind and waves, which, in principle, is a matter of calculation by manual or automatic means. Sometimes, this relationship is simple and can be represented by a table showing the wave height for a given wind speed (and possibly wind direction). However, in many cases, a more complicated approach is required, depending on: (a) the amount of detail needed (information on wave periods, wave steepness and so forth); (b) the environmental conditions of the forecasting area, including the geometry of coast-lines, bathymetry and currents; and (c) the nature of the wind, which can sometimes be variable (with changes taking place before a stationary wave condition has been reached).

"Forecasting" has a meaning in this Guide which is slightly different from that common in meteorology. When issuing a wave forecast, the propagation of wave energy can be forecast, but the evolution (growth) of the wave energy is dependent on the wind; therefore, a major part of the procedure is referring to the forecast of the winds that cause the waves. The wave growth is, in fact, diagnosed from the forecast wind.

"Hindcasting" refers to the diagnosis of wave information based on historical wind data. A computation based on present wind data is commonly referred to as "wave analysis". The term "nowcast" is increasingly used in meteorology in a similar context.

Some notational conventions are adopted in the formulations used in this Guide. In particular, vector quantities are written in bold italic type (for example, $\boldsymbol{a}$) to distinguish them from scalar quantities (for example, a).

Climatological issues

An appreciation of wave climatology is essential, whatever the main objective of the wave analysis or forecast. However, with all computations, sensible results are more likely if the local wave climate is known, particularly the ranges and likelihood of various wave parameters (for example, height and period) in the sea or ocean area of interest. Furthermore, experience should give a feeling for the probable values that might occur under the given wind conditions. Therefore, it is of great importance that any investigation, including training for wave forecasting, starts with a detailed study of the geography and climatology of the area of interest, to appreciate the limitations of wind fetch for certain wind directions, the existence of strong ocean currents, the typical configuration of wind fields in the weather patterns prevailing over the area and the climatological probability of wind speeds and directions.

It is useful to know the general range of wave heights and periods that may occur at sea. Individual waves higher than 20 m are rare, which implies that characteristic or significant wave heights will not often exceed 10 m. Characteristic wave periods usually vary between 4 and 15 s and are seldom greater than 20 s. Furthermore, waves can travel long distances and still retain appreciable height and energy. For instance, waves generated in mid-latitude storms in the North Atlantic Ocean have been observed as swell in the South Atlantic, and certain atolls in the equatorial Pacific have been damaged by swell waves that must have travelled several thousands of kilometres.

If regular wave forecasting is required for a fixed position or area (for example, in support of coastal or offshore engineering or other marine operations such as ship loading), it is preferable to arrange for regular wave measurement at suitable points. This provides data for verification of wave forecasts or validation of models for hindcasting. In a few instances, it may even be possible to develop a sufficiently homogeneous set of measured data for determining the wave climate from statistical analysis. In many applications, the only way to obtain a satisfactory dataset is to hindcast the waves for a sufficiently long time period, using wind fields derived from historical weather charts or archived air-pressure data from atmospheric models. However, the current availability of more than 10 years of satellite altimeter data globally allows wave-height climatology to be accurately described, at least in areas of the world's oceans not affected by tropical storms, down to the spatial resolution of the satellite data.

Structure of this guide

The Guide is organized into seven chapters and two annexes. Early chapters comprise general background material, leading to a chapter on traditional manual wave forecasting techniques. Later chapters focus on wave modelling and complications arising from waves either entering or being generated in finite-depth or shallow waters.

Chapter 1 gives an overview of the theory of free water waves. Simple linear waves are introduced and their behaviour described. These are the building blocks for more complex descriptions of wave fields, especially the frequency–direction spectrum. Other topics introduced

include: concepts of wave energy and group velocity (which are particularly important in discussions of the propagation of surface-wave energy), the effects of depth on simple waves and elementary statistical descriptions of wave records.

Chapter 2 is devoted to specification of the winds that drive wave generation. Due to the high sensitivity of wave growth to wind speed, reliable wave forecasts are possible only if the wind input is of sufficient accuracy. An overview of sources of surface wind data and winds derived from meteorological analyses is given. The complication of marine boundary layers is also discussed.

Chapter 3 introduces the physical background of processes that control the evolution of wave conditions. These are primarily wave generation by the wind, propagation across the ocean surface, dissipation and the reshuffling of energy within the wave spectrum caused by weakly non-linear wave–wave interactions. The formulation of these processes is given for application in manual forecasting procedures and in numerical modelling.

While numerical wave modelling has become the norm in many centres, there is still widespread use of manual methods. These methods have been in operational use for more than 40 years and are well proven. Hence, Chapter 4 has survived largely intact from the original Handbook. Manual procedures are described for determining wind waves, and examples illustrate how the procedures are applied in progressively more complicated situations. Simple manual methods illustrate estimation of the bottom influence on wave height. The chapter ends with a section on manual rip current forecasting. Nomograms and tips for manual wave forecasting are compiled in the annexes.

Chapter 5 describes the general structure of numerical wave models based on an equation describing the energy balance of a surface-wave field. Each of the identified elements is formulated and its use in wave models discussed. Full calculation of all the processes is not computationally viable in an operational environment, and so wave models do not necessarily treat all of the components explicitly. Certain trade-offs are employed to improve operability. Some of these trade-offs are historical, arising from an era when computational power was limited and the dominant mechanisms were not as well attributed. The classes of wave models arising from this evolution are described.

The generation of new waves in shallow water and the formulation of dissipation due to bottom friction for inclusion in numerical wave models are considered. The chapter also addresses some of the problems encountered in the near-shore zone, such as breaking waves and wave-induced set-up and currents.

The operation of numerical wave models is given further attention in Chapter 6. Important operational considerations are the model outputs, including a range of charts and coded formats, and the verification of the model products.

Finally, Chapter 7 encompasses a wide range of sources of visually observed, measured and modelled wave data. Organized by method of observation, the chapter deals with wave buoys, ships and remotely sensed observations, including space-based observations from altimeter and synthetic aperture radar, as well as surface-based observations, including high-frequency band radar, X-band radar and others. Another important source of data used especially for climate analysis is wave hindcast databases, including reanalyses, derived from numerical models forced by regional to global wind fields.

It is acknowledged that this Guide includes material that is dated and “perishable”. It is inevitable that information on the status of data acquisition, models being used, products being delivered, studies in progress and other activities, which was correct at the time of writing, is going to change. However, inclusion of these items is necessary in a publication of this type.

This Guide is intended to provide guidance in solving day-to-day problems in wave analysis and forecasting. However, in some cases, the problems concerned go beyond the scope of this publication. If the reader wishes to pursue particular topics, then sufficient references are included to provide a gateway to the open literature. The editor of the relevant chapter may

also be contacted; names and affiliations are listed in the acknowledgements. The Guide is not intended to be a self-contained training course. Specialist training courses are recommended for marine forecasters required to make wave forecasts. For example, interpretation of the guidance that the output from a particular wave model provides for a particular national forecast service goes well beyond the scope of this Guide.

CHAPTER 1. OCEAN-SURFACE WAVES

Editor: A.K. Laing, updated by F. Ocampo-Torres

1.1 INTRODUCTION

Ocean waves are the result of forces acting on the ocean. The predominant natural forces are pressure or stress from the atmosphere (especially through the winds), earthquakes, gravity of the Earth and celestial bodies (Moon and Sun), the Coriolis force (due to the Earth's rotation) and surface tension. Characteristics of the waves depend on the controlling forces. Tidal waves are generated by the response to gravity of the Moon and Sun and are large-scale waves. At the other end of the scale, capillary waves are dominated by surface tension in the water. There are gravity waves where the Earth's gravity and the buoyancy of the water are the major determining factors.

Waves may be characterized by their period. This is the time taken by successive wave crests to pass a fixed point. The type and scale of forces acting to create the wave are usually reflected in the period. Figure 1.1 illustrates such a classification of waves.

On large scales, ordinary tides are ever present but predictable. Less predictable are tsunamis (generated by earthquakes or land movements), which can be catastrophic, and storm surges. The latter are associated with the movement of synoptic or mesoscale atmospheric features and may cause coastal flooding.

Wind-generated gravity waves are almost always present at sea. These waves are generated by winds somewhere on the ocean, be it locally or thousands of kilometres away. They affect a wide range of activities such as shipping, fishing, recreation, coastal and offshore industry, coastal management (defences) and pollution control. They are also important in the climate processes as they play a large role in exchanges of heat, energy, gases and particles between the oceans and atmosphere. These waves are the subject in this Guide.

A model is needed to analyse and predict such waves. That is, there needs to be a theory for how they behave in response to the relevant forcing. If the ocean surface is observed, it can be seen that the waves often form a complex pattern. A simple starting model will be sought to begin with. This will be consistent with the known dynamics of the ocean surface. Then, a more complete picture of the wind waves observed will be derived.

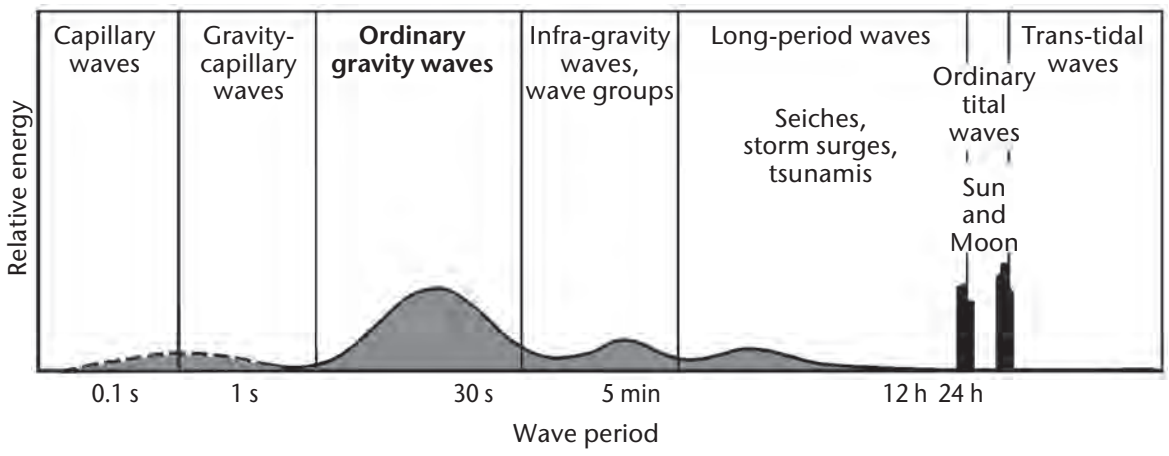

Figure 1.1. Classification of ocean waves by wave period

Source: Derived from Munk (1951)

The model of the ocean used to develop this picture is based on a few simple assumptions:

- Incompressibility of water: the density is constant and hence a continuity equation for the fluid can be derived, expressing the conservation of fluid within a small cell of water (called a water particle).
- Inviscid nature of water: the only forces acting on a water particle are gravity and pressure (which acts perpendicular to the surface of the water particle); friction is ignored.
- Fluid flow is irrotational: the individual particles do not rotate. They may move around each other, but there is no twisting action. This allows the motions of neighbouring particles to be related by defining a scalar quantity, called the velocity potential, for the fluid. The fluid velocity is determined from spatial variations of this quantity.

Using these assumptions, equations may be written to describe the motion of the fluid. This Guide will not present the derivation, which is given in most textbooks on waves or fluids (for example, Kinsman, 1965; Neumann and Pierson, 1966; Crapper, 1984; Massel, 2013).

1.2 SIMPLE LINEAR WAVES

The simplest wave motion may be represented by a sinusoidal, long-crested, progressive wave. The sinusoidal descriptor means that the wave repeats itself and has the smooth form of the sine curve as shown in Figure 1.2. The long-crested descriptor says that the wave is a series of long and parallel wave crests, which are all equal in height and equidistant from each other. The progressive nature is seen in their moving at a constant speed in a direction perpendicular to the crests and without change of form.

1.2.1 Basic definitions

- Wavelength, λ, is the horizontal distance (in metres, for example) between two successive crests.
- Period, T, is the time interval (in seconds) between the passage of successive crests past a fixed point.
- Frequency, f, is the number of crests that pass a fixed point in 1 s. It is usually measured in numbers per second (Hertz) and is the same as $1/T$.
- Amplitude, a, is the magnitude of the maximum displacement from mean sea level. It is usually indicated in metres (or feet).
- Wave height, H, is the difference in surface elevation between the wave crest and the previous wave trough. For a simple sinusoidal wave, $H = 2a$.
- Rate of propagation, c, is the speed at which the wave profile travels, that is, the speed at which the crest and trough of the wave advance. It is commonly referred to as wave speed or phase speed.
- Steepness of a wave is the ratio of the wave's height to its length (H/λ).

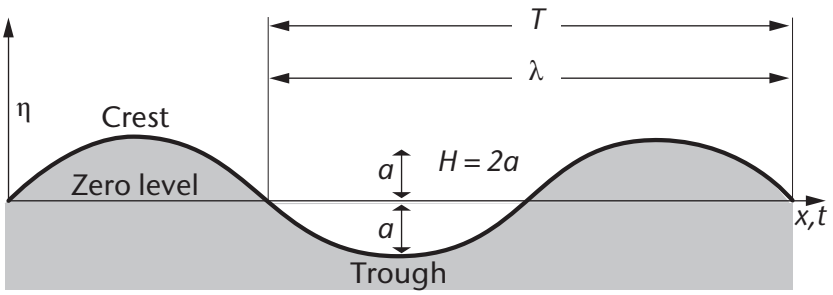

Figure 1.2. A simple sinusoidal wave

1.2.2 **Basic relationships**

For all types of truly periodic progressive waves,

$$\lambda = cT. \tag{1.1}$$

That is, the wavelength of a periodic wave is equal to the product of the wave speed (or phase speed) and the period of the wave. This formula is easy to understand. Let, at a given moment, the first of two successive crests arrive at a fixed observational point. Then, one period (T seconds) later, the second crest will arrive at the same point. In the meantime, the first crest has covered a distance c times T.

The simple linear wave profile has the form of a sinusoidal wave:

$$\eta(x,t) = a\sin(kx - \omega t). \tag{1.2}$$

In Equation 1.2, $k = 2\pi/\lambda$ is the wave number and $\omega = 2\pi/T$ is the angular frequency. The wave number is a cyclic measure of the number of crests per unit distance, and the angular frequency is the number of radians per second. One wave cycle is a complete revolution, which is 2π radians. Equation 1.2 contains both time (t) and space (x) coordinates. It represents the view as may be seen from an aircraft, describing both the change in time and the variations from one point to another. It is the simplest solution to the equations of motion for gravity wave motion on a fluid – linear surface waves.

The wave speed c in Equation 1.1 can be written as λ/T, or, now that k has been defined, as ω/k. The variation of wave speed with wavelength is called dispersion, and the functional relationship is called the dispersion relation. The relation follows from the equations of motion. For deep water, it can be expressed in terms of frequency and wavelength or, as usually written, between ω and k:

$$\omega^2 = gk, \tag{1.3}$$

where g is the acceleration due to gravity, so that the wave speed is

$$c = \frac{\lambda}{T} = \frac{\omega}{k} = \sqrt{\frac{g}{k}}. \tag{1.4}$$

If a snapshot at time $t = 0$ is considered, the horizontal axis is then x and the wave profile is "frozen" as

$$\eta(x) = a\sin(kx). \tag{1.5}$$

However, the same profile is obtained when the wave motion is measured using a wave recorder placed at the position $x = 0$. The profile then recorded is

$$\eta(t) = a\sin(-\omega t). \tag{1.6}$$

Equation 1.6 describes the motion of, for instance, a moored float bobbing up and down as a wave passes by.

The important parameters when wave forecasting or carrying out measurements for stationary objects, such as offshore installations, are therefore wave height, wave period (or wave frequency) and wave direction. An observer required to give a visual estimate will not be able to fix any zero level as in Figure 1.2 and cannot therefore measure the amplitude of the wave. Instead, the vertical distance between the crest and the preceding trough (the wave height) is reported.

In reality, the simple sinusoidal waves described above are never found at sea; only swell, passing through an area with no wind, may come close. The reason for starting with a description of simple waves is that they represent the basic solutions of the physical equations that govern waves on the sea surface. They are the "building blocks" of the real wave fields occurring at sea, as shall be seen later. In fact, the concept of simple sinusoidal waves is frequently used as an aid to understanding and describing waves on the sea surface. In spite of this simplified description, the definitions and formulae derived from it are extensively used and have proved their worth.

1.2.3 Orbital motion of water particles

It is evident that water particles move up and down as waves travel through water. By carefully watching small floating objects, it can be seen that the water also moves backwards and forwards. It moves forwards on the crest of a wave and backwards in the trough. If the water is not too shallow relative to the wavelength, the displacements are approximately as large in the horizontal plane as in the vertical plane. In fact, during one cycle of a simple wave (a wave period), the particles describe a circle in a vertical plane. The vertical plane is the cross-section drawn in Figure 1.2. In shallow water, the motion is an ellipse. Figure 1.3 illustrates this particle motion for a simple sinusoidal wave in deep water.

Consider the speed at which a water particle completes its path. The circumference of the circle is equal to πH. This circumference is covered by a particle within a time equal to one period T. The speed of the water is therefore $\pi H/T$. This is also the greatest forward speed reached in the crests. The speed of individual water particles should not be confused with the speed at which the wave profile propagates (wave speed). The propagation rate of the wave profile is usually far greater, as it is given by λ/T, and the wavelength λ is generally much greater than πH.

Figure 1.3 has been slightly simplified to show the progression of wave crests and troughs as the result of water particle motion. In reality, depending on the wave steepness, a water particle does not return exactly to the starting point of its path; it ends up at a slightly advanced position in the direction in which the waves are travelling (Figure 1.4). In other words, the return movement in the wave trough is slightly less than the forward movement in the wave crest, so that a small net forward shift remains. The effect is commonly termed "Stokes drift" and is increased in steep waves (see section 1.2.7).

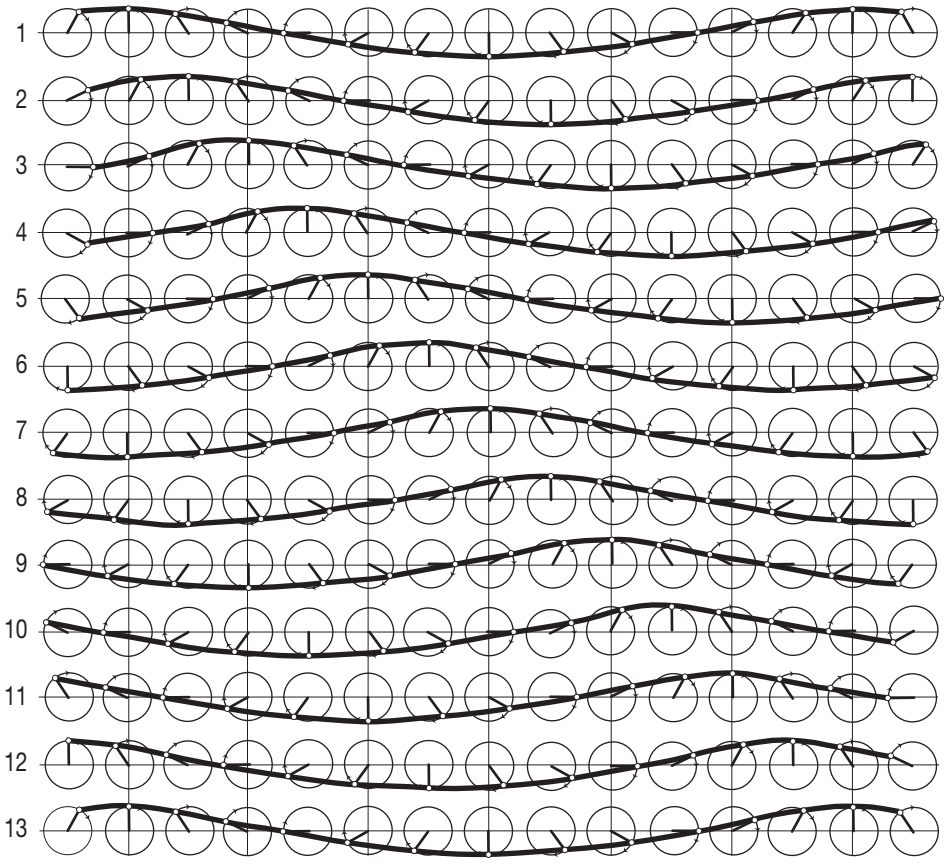

Figure 1.3. Progression of a wave motion: 13 snap shots, each with an interval of one twelfth of a period

Source: Derived from Gröen and Dorrestein (1976)

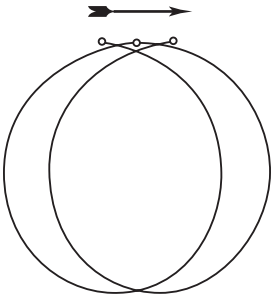

Figure 1.4. Path shift of a water particle during two wave periods

1.2.4 Energy in waves

Waves are associated with motion in the water. Therefore, as a wave disturbs the water, there is kinetic energy associated with the wave, which moves along with the wave. Waves also displace particles in the vertical and so affect the potential energy of the water column. This energy also moves along with the wave. It is an interesting feature of the waves that the total energy is equally divided between kinetic energy and potential energy. This is called the equipartition of energy.

The energy does not move at the same speed as the wave, the phase speed. It moves with the speed of groups of waves rather than individual waves. The concept of a group velocity will be discussed in section 1.3.2, but it is worth noting here that, in deep water, the group velocity is half the phase speed. The total energy of a simple linear wave can be shown to be $\rho_w g a^2/2$, which is the same as $\rho_w g H^2/8$, where ρ_w is the density of water. This is the total of the potential and kinetic energies of all particles in the water column for one wavelength.

1.2.5 Influence of water depth

As a wave propagates, the water is disturbed so that both the surface and the deeper water under a wave are in motion. If the water column is deep enough, particles also describe vertical circles, which become progressively smaller with increasing depth (Figure 1.5). In fact, the decrease is exponential.

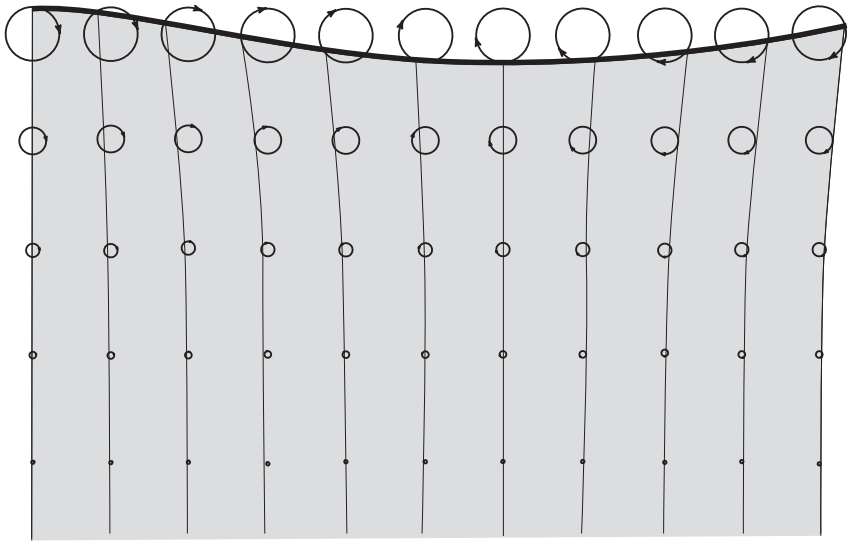

Figure 1.5. Paths of water particles at various depths in a wave on deep water. Each circle is one ninth of a wavelength below the one immediately above it. The wave profile advances from left to right.

Below a depth corresponding to half a wavelength, the displacements of the water particles in deep water are less than 4% of those at the surface. The result is that, as long as the depth of the water is greater than the value corresponding to $\lambda/2$, the influence of the bottom on the movement of water particles can be considered negligible. Thus, the water is called deep with respect to a given surface wave when its depth is at least half the wavelength. In practice, it is common to take the transition from deep to transitional depth water at $h = \lambda/4$. In deep water, the displacements at this depth are about 20% of those at the surface. However, as long as the water is deeper than $\lambda/4$, the surface wave is not appreciably deformed, and its speed is close to the speed on deep water. The following terms are used to characterize the ratio between depth (h) and wavelength (λ):

- Deep water, $h > \lambda/4$;
- Transitional depth, $\lambda/25 < h < \lambda/4$;
- Shallow water, $h < \lambda/25$.

Wave dissipation due to interactions with the bottom (friction, percolation or sediment motion) has not yet been taken into account here.

When waves propagate into shallow water, for example when approaching a coast, nearly all the characteristics of the waves change as they begin to "feel" the bottom. Only the period remains constant. The wave speed decreases with decreasing depth. The relation $\lambda = cT$ shows that the wavelength also decreases.

From the linearized theory of wave motion, an expression relating wave speed c to wave number $k = 2\pi/\lambda$ and water depth h can be derived as

$$c^2 = \frac{g}{k} \tanh kh, \tag{1.7}$$

where g is the acceleration due to gravity and tanh x denotes the hyperbolic tangent:

$$\tanh x = \frac{e^x - e^{-x}}{e^x + e^{-x}}. \tag{1.8}$$

The dispersion relation for finite-depth water is much like Equation 1.7. In terms of the angular frequency and wave number, the generalized form for Equation 1.3 is

$$\omega^2 = gk \tanh kh. \tag{1.9}$$

In deep water ($h > \lambda/4$), tanh kh approaches unity and c is greatest. Equation 1.7 then reduces to

$$c^2 = \frac{g}{k} = \frac{g\lambda}{2\pi}, \tag{1.10}$$

or when using $\lambda = cT$ (Equation 1.1),

$$T = \sqrt{\frac{2\pi\lambda}{g}}, \tag{1.11}$$

$$\lambda = \frac{gT^2}{2\pi} \tag{1.12}$$

and

$$c = \frac{gT}{2\pi} = \frac{g}{2\pi f} = \frac{g}{\omega}. \tag{1.13}$$

Expressed in units of metres and seconds, the term $g/2\pi = 1.56$ m s^{-2}. In this case, $\lambda = 1.56T^2$ m and $c = 1.56T$ m s^{-1}. If λ is given in feet and c in knots, these become $\lambda = 5.12T^2$ feet and $c = 3.03T$ knots.

When the relative water depth becomes shallow ($h < \lambda/25$), Equation 1.10 can be simplified to

$$c = \sqrt{gh}. \tag{1.14}$$

This relation is of importance when dealing with long-period, long-wavelength waves, often referred to as "long waves". When such waves travel in shallow water, the wave speed depends only on water depth. This relation can be used, for example, for tsunamis for which the entire ocean can be considered as shallow.

If a wave is travelling in water with transitional depths ($\lambda/25 < h < \lambda/4$), approximate formulae can be used for the wave speed and wavelength in shallow water:

$$c = c_0\sqrt{\tanh k_0 h} \tag{1.15}$$

and

$$\lambda = \lambda_0\sqrt{\tanh k_0 h}, \tag{1.16}$$

where c_0 and λ_0 are the deep-water wave speed and wavelength according to Equations 1.10 and 1.12, respectively, and k_0 is the deep-water wave number $2\pi/\lambda_0$.

A further feature of changing depth is changing wave height. As a wave approaches the shore, its height increases. This is a result of changes in the group velocity. The energy propagating towards the coast must be conserved, at least until friction becomes appreciable, so that if the group velocity decreases and wavelength decreases, the energy in each wavelength must increase. From the expression for energy in section 1.2.4, this means that the height of the wave must increase.

1.2.6 Refraction and diffraction

As waves begin to feel the bottom, a phenomenon called refraction may occur. When waves enter water of transitional depth, if they are not travelling perpendicular to the depth contours, the part of the wave in deeper water moves more rapidly than the part in shallower water, according to Equation 1.15, causing the crest to turn parallel to the bottom contours. Figures 1.6, 1.7 and 1.8 show some examples of refraction patterns.

Generally, any change in the wave speed, for instance due to gradients of surface currents, may lead to refraction, irrespective of the water depth. Section 4.5.1 gives a few examples illustrating refraction under simplified conditions. The second edition of the *Guide to Wave Analysis and Forecasting* (WMO, 1998), Chapter 7, and the *Shore Protection Manual* (CERC, 1984) give more complete descriptions of methods for the analysis of refraction and diffraction.

The phenomenon of wave diffraction should also be mentioned. It most commonly occurs in the lee of obstructions such as breakwaters. The obstruction causes energy to be transferred

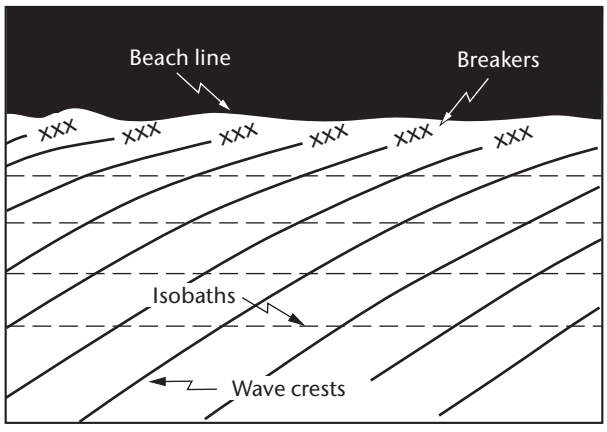

Figure 1.6. Refraction along a straight beach with parallel bottom contours

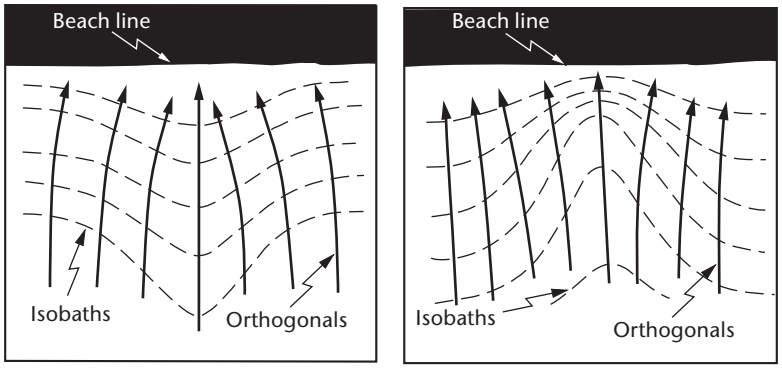

Figure 1.7. Refraction by: (a) a submarine ridge and (b) a submarine canyon

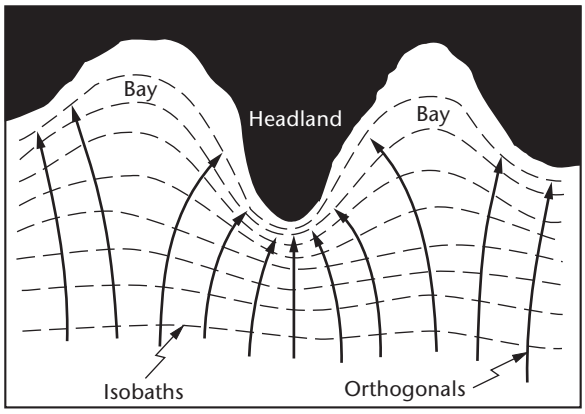

Figure 1.8. Refraction along an irregular shoreline

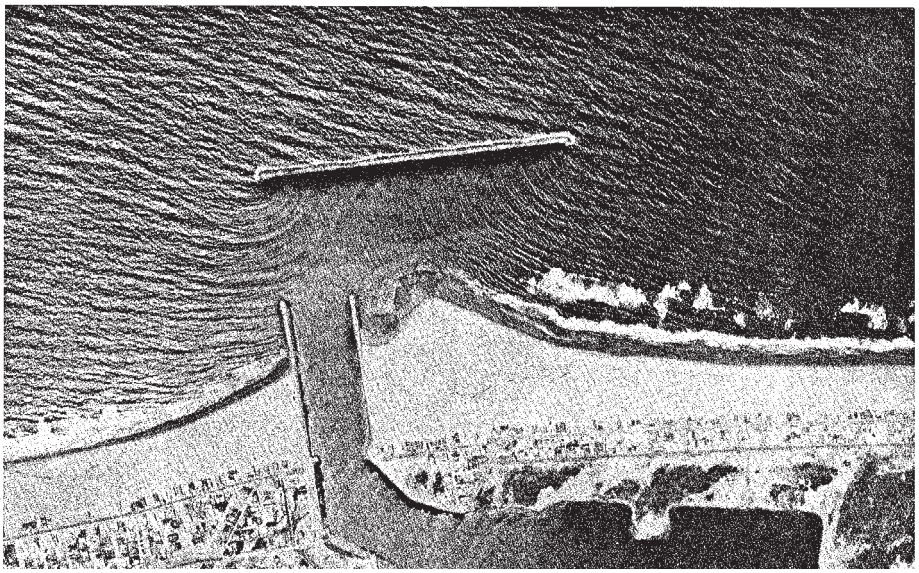

Figure 1.9. Wave diffraction at Channel Islands harbour breakwater (California)

Source: CERC (1977)

along a wave crest. This transfer of energy means that waves can affect the water in the lee of the structure, although their heights are much reduced. The photograph in Figure 1.9 illustrates an example.

1.2.7 **Breaking waves**

Section 1.2.3 noted that the speed of the water particles is slightly greater in the upper segment of the orbit than in the lower part. This effect is greatly magnified in steep waves, so much so that the maximum forward speed may become $7H/T$ not $\pi H/T$ (Stokes, 1847, 1880). Should $7H$ become equal to the wavelength λ ($H/\lambda = 1/7$), the forward speed of the water in the crest would then be equal to the rate of propagation, which is λ/T. There can be no greater forward speed of the water because the water would then plunge forward out of the wave: in other words, the wave would break.

According to Stokes' theory, waves cannot attain a height of more than one seventh of the wavelength without breaking. In reality, the steepness of waves is seldom greater than one tenth of the wavelength. However, at values of that magnitude, the profile of the wave has long ceased to be a simple undulating line and looks more like a trochoid (Figure 1.10). According to Stokes' theory, at the limiting steepness of one seventh, the forward and backward slopes of the wave meet in the crest under an angle of 120° (Figure 1.11).

When waves propagate into shallow water, their characteristics change as they begin to feel the bottom, as already noted in section 1.2.5. The wave period remains constant, but the speed decreases as does the wavelength. When the water depth becomes less than half the wavelength, there is an initial slight decrease in wave height.[1] The original height is regained when the ratio $h/\lambda = 0.06$; thereafter, the height increases rapidly, as does the wave steepness, until the breaking point is reached:

$$h_b = 1.28 H_b, \tag{1.17}$$

where h_b is the breaking depth and H_b the breaker wave height.

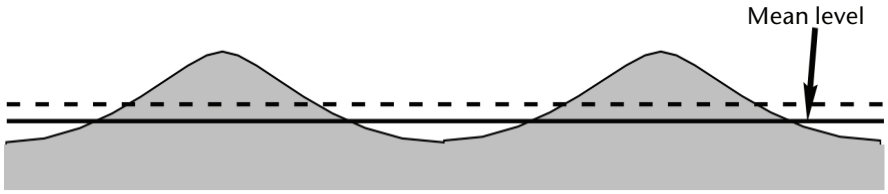

Figure 1.10. Trochoidal wave profile; the crests project farther above the mean level then the troughs sink under it

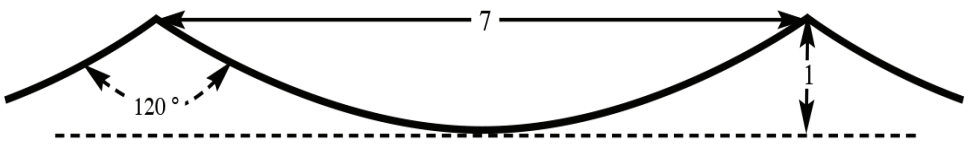

Figure 1.11. Ultimate form that water waves can attain according to Stokes' theory

[1] Tracking a wave into shallow water, the wavelength decreases and the wave slows down but, initially, its energy does not. The energy then spreads over more waves and the height reduces. This is only temporary. The wave energy soon also slows and the height begins to increase.

1.3 WAVE FIELDS ON THE OCEAN

1.3.1 Decomposition of simple waves

Actual sea waves do not look as simple as the profile shown in Figure 1.2. With their irregular shapes, they appear as a confused and constantly changing water surface because waves are continually being overtaken and crossed by others. Waves at sea are therefore often short crested. This is particularly true for waves growing under the influence of the wind (wind sea).

A more regular pattern of long-crested and nearly sinusoidal waves can be observed when the waves are no longer under the influence of their generating winds. Such waves are called swell, and they can travel hundreds and thousands of kilometres after leaving the area in which they were generated. Swell from distant generating areas often mixes with wind waves generated locally.

The simple waves described in section 1.2 can be shown to combine to compose the observed patterns. That is, any observed wave pattern on the ocean can be shown to comprise a number of simple waves, which differ from each other in height, wavelength and direction.

As a first step, consider waves with long, parallel crests but which differ in height (for example, the profile shown in the top curve of Figure 1.12). Although this curve looks regular, it is certainly no longer the profile of a simple sinusoidal wave, because the height is not the same everywhere, nor are the horizontal distances between crests the same. However, this profile can be represented as the sum of two simple wave profiles of slightly different wavelengths (see waves I and II in the bottom curve of Figure 1.12). In adding the vertical deviations of I and II at corresponding points of the horizontal axis, the vertical deviations of the sum of wave I and wave II, represented by the top wave profile in Figure 1.12, can be obtained.

Thus, the top profile can be broken down, or decomposed, into two simple waves of different wavelengths. The reason why the crests are of varying height in the sum of I and II is that at one place, waves I and II are in phase and their heights therefore add up, whereas the resulting height is reduced at those places where the waves are out of phase.

Taking this idea one step further, it can be seen how an irregular pattern of wind waves can be thought of as a superposition of an infinite number of sinusoidal waves, propagating

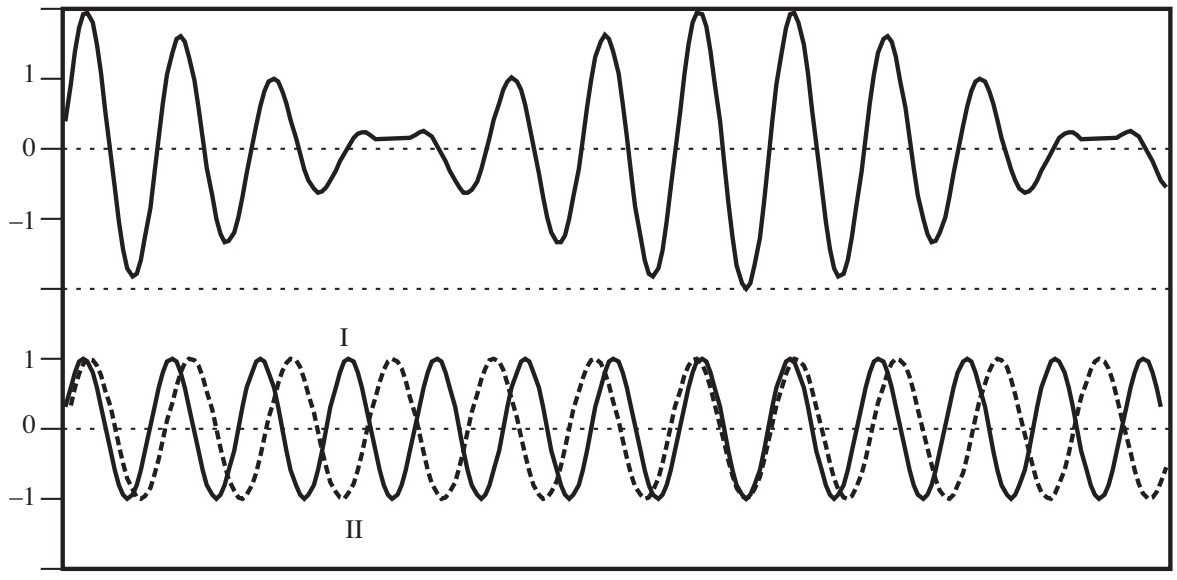

Figure 1.12. Upper profile shows the sum (superposition) of the two simple waves I and II in the lower part of the figure; horizontal dimensions are greatly shortened with respect to vertical ones

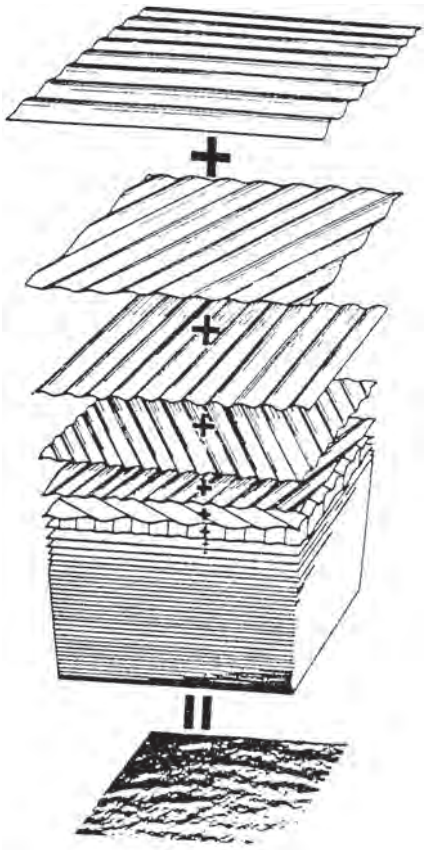

Figure 1.13. Sea surface obtained from the sum of many sinusoidal waves

Source: Derived from Pierson et al. (1955)

independently of each other. Figure 1.13 illustrates this, and shows a great number of sinusoidal waves piled on top of each other. Think, for example, of a sheet of corrugated iron as representing a set of simple sinusoidal waves on the surface of the ocean and caught at an instant in time. Below this, there is another set of simple sinusoidal waves travelling in a slightly different direction from the one on top. Below that again is a third and a fourth , and so on – all with different directions and wavelengths. Each set is a classic example of simple sinusoidal waves.

It can be shown that, as the number of different sinusoidal waves in the sum is made larger and larger and the heights are made smaller and smaller, and the periods and directions are packed closer and closer together (but never the same and always over a considerable range of values), the result is a sea surface just like the one actually observed. Even small irregularities from the sinusoidal shape can be represented by superpositions of simple waves.

1.3.2 Wave groups and group velocity

It has been seen how waves on the ocean are combinations of simple waves. In an irregular sea, the number of differing wavelengths may be large. Even in regular swell, there are many different wavelengths present, but they tend to be grouped together. Figure 1.12 shows how simple waves with close wavelengths combine to form groups of waves. This phenomenon is common. Anyone who has carefully observed waves in the sea will have noticed that in nature, the larger waves tend to come in groups.

Although various crests in a group are never equidistant, there is an average distance and thus an average wavelength. Even though individual crests or wave tops advance at a speed corresponding to their wavelength, the group, as a coherent unit, advances at its own velocity – the group velocity. For deep water, this has magnitude (group speed)

$$c_g = \frac{c}{2}. \tag{1.18}$$

A more general expression also valid in finite-depth water is

$$c_g = \frac{c}{2}\left(1 + \frac{2kh}{\sinh 2kh}\right). \tag{1.19}$$

The general form for the group speed can be shown to be

$$c_g = \frac{d\omega}{dk}. \tag{1.20}$$

Derivations may be found in most fluid dynamics texts (for example, Kinsman, 1965; Crapper, 1984).

It can also be shown that the group velocity is the velocity at which wave energy moves. If the energy flow (flux) due to a wave train is considered, the kinetic energy is associated with the movement of water particles in nearly closed orbits and is not significantly propagated. However, the potential energy is associated with the net displacement of water particles, and this moves along with the wave at the phase speed. Hence, in deep water, the effect is as if half of the energy moves at the phase speed, which is the same as the overall energy moving at half the phase speed. The integrity of the wave is maintained by a continuous balancing act between kinetic and potential energy. As a wave moves into previously undisturbed water, potential energy at the front of the wave train is converted into kinetic energy, resulting in a loss of amplitude. This leads to waves dying out as they outrun their energy. At the rear of the wave train, kinetic energy is left behind and is converted into potential energy, with the result that new waves grow there.

One classical example of a wave group is the band of ripples that expands outwards from the disturbance created when a stone is cast into a still pond. If a person fixes their attention on a particular wave crest, then they will notice that the wave creeps towards the outside of the band of ripples and disappears. Stating this slightly differently, if that person moves along with waves at the phase velocity, then they will stay with a wave crest, but the waves ahead of them gradually disappear. As the band of ripples is made up of waves with components from a narrow range of wavelengths, the wavelength of their particular wave will also increase a little (and there will be fewer waves immediately around). However, if that person travels at the group velocity, the waves ahead of them may lengthen and those behind them shorten, but the total number of waves nearby will be conserved.

Thus, the wave groups can be considered as carriers of the wave energy (see also section 1.3.7), and the group velocity is also the velocity with which the wave energy is propagated. This is an important consideration in wave modelling.

1.3.3 Statistical description of wave records

The confusing pattern seen in Figure 1.13 can also be viewed in terms of Equation 1.6 as the motion of the water surface at a fixed point. A typical wave record for this displacement is shown in Figure 1.14, in which the vertical scale is expressed in metres and the horizontal scale in seconds. Wave crests are indicated with dashes and all zero downcrossings are circled. The wave period T is the time distance between two consecutive downcrossings (or upcrossings[2]), whereas the wave height H is the vertical distance from a trough to the next crest as it appears on the wave record. Another and more commonly used kind of wave height is the zero-crossing wave height H_z, which is the vertical distance between the highest and the lowest value of the

[2] There is no clear convention on the use of either zero upcrossings or downcrossings for determining the wave height and period of zero-crossing waves. Generally, if the record is sufficiently long, no measurable differences will be found among mean values.

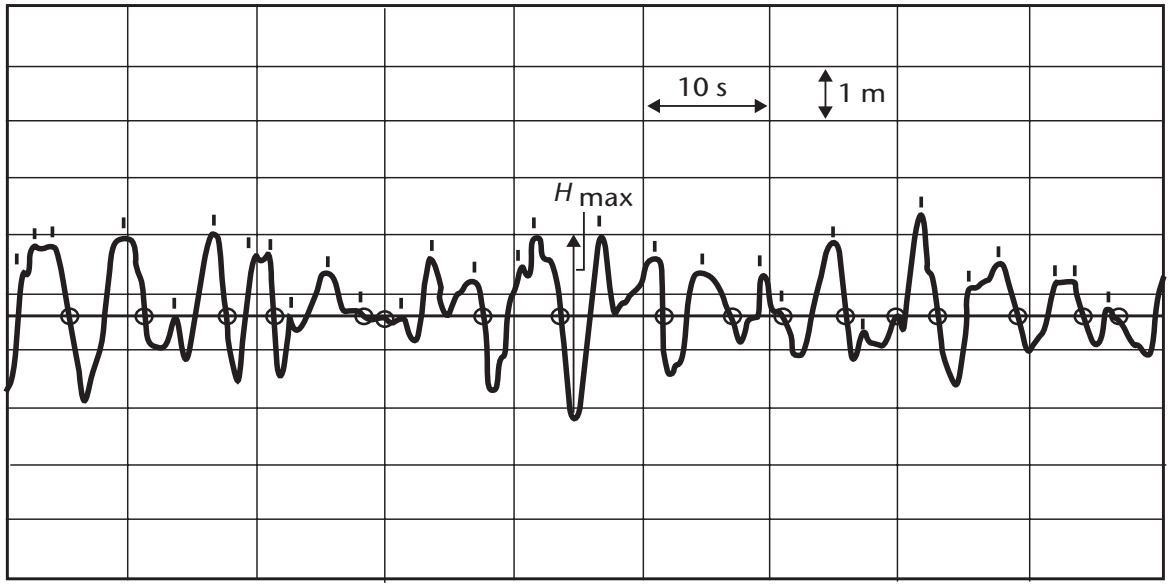

Figure 1.14. Sample of a wave record (dashes show wave crests; circles show zero downcrossings)

wave record between two zero downcrossings (or upcrossings). When the wave record contains a great variety of wave periods, the number of crests becomes greater than the number of zero downcrossings. In that case, there will be some difference between the crest-to-trough wave height and H_z. However, this difference will be neglected in this chapter, and H_z will be used implicitly. A simple and common method for analysing wave records by hand is the Tucker–Draper method, which gives good approximate results (Draper, 1963, 1966).

A measured wave record never repeats itself exactly, due to the random appearance of the sea surface. But if the sea state is "stationary", the statistical properties of the distribution of periods and heights will be similar from one record to another. The most appropriate parameters to describe the sea state from a measured wave record are therefore statistical. The following are frequently used:

- H is the average wave height;
- H_{max} is the maximum wave height occurring in a record;
- T_z is the average zero-crossing wave period; the time obtained by dividing the record length by the number of downcrossings (or upcrossings) in the record;
- $H_{1/n}$ is the average height of the $1/n$ highest waves (if all wave heights measured from the record are arranged in descending order, the one-nth part, containing the highest waves, should be taken and $H_{1/n}$ is then computed as the average height of this part);
- $T_{H1/n}$ is the average period of the $1/n$ highest waves.

A commonly used value for n is 3:

- $H_{1/3}$ is the significant wave height (its value approximates the visually observed wave height);
- $T_{H1/3}$ is the significant wave period (approximately equal to the wave period associated with the spectral maximum, see section 1.3.8).

1.3.4 Duration of wave records

The optimal duration of wave records is determined by several factors. First, for a correct description of the sea state, conditions should be statistically stationary during the sampling period. This will never be achieved completely as wave fields are usually evolving (growing

or decaying). Second, to reduce statistical scatter, the wave record should contain at least 200 zero-downcrossing waves. Hence, the optimal time over which waves are usually measured is 15–35 min, as this reasonably accommodates both conditions.

The manual analysis of analogue "stripchart" records has been introduced. However, most analyses are performed by computer for which digital records are used. That is, the vertical displacement of the ocean surface (or the position of the pen at the chart recorder) is given with a sampling rate of 1–10 times per second (1–10 Hz). For example, a record of 20 min duration with a sampling rate of 4 Hz contains 4 800 values.

When wave records are processed automatically, the analysis is always preceded by checks of the quality of the recorded data points to remove outliers and errors due to faulty operation of sensors, in data recording equipment or in data transmission.

1.3.5 Use of statistical parameters

In this Guide, the term sea state is used as a wave condition described by some statistical parameters. It is common to use the significant wave height $H_{1/3}$ and the average zero-crossing period T_z, or some other characteristic period, to define the sea state. The corresponding maximum wave height can be deduced as shown in section 1.3.6.

The use of the average zero-crossing period T_z has its drawbacks. The distribution of individual zero-downcrossing periods of a record is usually wide and is also sensitive to noise. This is in contrast with the distribution of periods of, say, the highest one third of waves. Moreover, the average period of the highest waves of a record is usually a good approximation of the period associated with the peak of the wave spectrum (see section 1.3.8). It has been found that average wave periods of the $1/n$ highest waves with $n > 3$ are not essentially different from $T_{H1/n}$, but they exhibit a larger scatter.

In this Guide, as elsewhere, various definitions of wave steepness are used. The general form is $\xi = H/\lambda$, which, using Equation 1.12, becomes

$$\xi = \frac{2\pi H}{gT^2}, \tag{1.21}$$

where H represents a wave height (for example, $H_{1/3}$, H_{m_0}, H_{rms} or $\sqrt{m_0}$) and T the wave period (for example, T_z, $T_{H1/3}$, T_p or T_{m02}). Section 1.3.8 introduces some of these parameters.

1.3.6 Distribution of wave heights

The elevation of the sea surface is denoted by $\eta(x,t)$. This formulation expresses the variations of sea surface in space and time for simple waves (see Equation 1.2) and also for more complicated sea states. If the range of wavelengths in a given sea state is not too broad, it has been shown (Longuet-Higgins, 1952) that the elevation η has a Gaussian statistical distribution (normal distribution).

For a normally distributed parameter such as η, the maximum values are known to be distributed with a Rayleigh distribution. For a sea state, these maximum values are directly related to the wave heights. Hence, the distribution of (zero-downcrossing) wave heights can be represented by the Rayleigh distribution. This feature has been shown theoretically and verified empirically. If $F(H_1)$ denotes the probability of heights not exceeding a given wave height H_1 in a sea state characterized by a known value of $H_{1/3}$, then

$$F(H_1) = 1 - \exp\left[-2(H_1 / H_{1/3})^2\right]. \tag{1.22}$$

The probability $Q(H_1)$ of heights exceeding H_1 is

$$Q(H_1) = 1 - F(H_1). \tag{1.23}$$

Example

Problem

Given a sea state for which $H_{1/3} = 5$ m, what is the probability of observing waves higher than 6 m?

Solution

As $F(H_1) = 1 - \exp[-2\,(6/5)^2] = 0.94$, the probability of heights exceeding 6 m is $Q(H_1) = 1 - 0.94 = 0.06$.

If $H_{1/3}$ is computed from a wave record of finite length, the record length or the number of waves used for the computation should be taken into account. If, on a record containing N waves, n waves exceed a given height H_1, the probability of heights exceeding H_1 is

$$Q(H_1) = \frac{n}{N}. \tag{1.24}$$

Inserting the relationships from Equations 1.22 and 1.23 into Equation 1.24 leads to

$$H_{1/3} = H_1 \left(0.5 \ln \frac{N}{n} \right)^{-0.5}. \tag{1.25}$$

Equation 1.25 provides a quick method for the determination of $H_{1/3}$ from a wave record. However, if $H_{1/3}$ is known, the distribution of a wave record can be compared with the Rayleigh distribution using

$$H_1 = H_{1/3} \sqrt{0.5 \ln \frac{N}{n}}. \tag{1.26}$$

For the prediction of the maximum wave height H_{max} for a sequence of N waves with known $H_{1/3}$, it is common to take the mode of the distribution of maximum values,

$$H_{max} = H_{1/3} \sqrt{0.5 \ln N}. \tag{1.27}$$

Alternatively, if the fiftieth percentile of the distribution of maximum values is taken, a more conservative estimate of H_{max} is obtained because of the asymmetry of the distribution, that is, about 5% greater than according to Equation 1.27:

$$H_{max} = H_{1/3} 0.5 \ln \sqrt{1.45 \ln N}. \tag{1.28}$$

The prediction of H_{max} must be based on a realistic duration, for example 6 h, apart from the usual confidence limits of the $H_{1/3}$ forecast. This implies $N = 2\,000$–$5\,000$ (in 6 h, there are about 2 700 waves if the peak period is 8 s). Using Equation 1.27 gives[3]

$$H_{max} \cong 2.0 H_{1/3} \cong 1.9 H_{m_0}. \tag{1.29}$$

While estimates of wave-height probabilities in a given sea state are commonly based on the Rayleigh distribution, it has been demonstrated in some cases that estimates of high wave probabilities from the upper tail of the Rayleigh distribution are overestimated. As a result, some alternative distributions have been devised for use by naval architects interested in high individual waves for design purposes (for example, Forristall, 1978, 2000; Tayfun, 1981, 1983). However, evidence also exists suggesting that the occurrence of seas containing extreme (alternatively termed rogue or freak) waves, with overall or crest heights that are abnormally high relative to background significant wave height, is more common than expected (Liu et al., 2010).

1.3.7 **Wave spectra**

Section 1.3.1 noted that a sea surface with a random appearance may be regarded as the sum of many simple wave trains. A way of formalizing this concept is to introduce the wave spectrum. A wave record may be decomposed by means of harmonic (or Fourier) analysis into a large

[3] See section 1.3.8 for a definition of H_{m_0} and its relation to $H_{1/3}$.

number of sinusoidal waves of different frequencies, directions, amplitudes and phases. Each frequency and direction describes a wave component, and each component has an associated amplitude and phase.

The harmonic (Fourier) analysis thus provides an approximation to the irregular but quasi-periodic form of a wave record as the sum of sinusoidal curves. For a surface elevation varying in time in a single direction.

$$\eta(t) = \eta_0 + \sum_{j=1}^{n} a_j \sin(j\omega_0 t + \phi_j), \tag{1.30}$$

where $\eta(t)$ is the recorded elevation of the water surface at time t, η_0 is the mean elevation (as shown for instance in Figure 1.14), ω_0 is the angular wave frequency of the longest wave fitted to the record, j is the number of wave component, a_j is the amplitude of the jth component, Φ_j is the phase angle of the jth component and n is the total number of components.

The phase angle allows for the fact that the components are not all in phase, that is, their maxima generally occur at different times. The high-frequency components tend to become insignificant and hence there is a reasonable limit to n.

Each wave component travels at its own speed (which depends on the wave frequency – or period – as expressed in Equation 1.10). Hence, the spectrum of wave components is continuously changing across the sea surface as the low-frequency (large-period or long-wavelength) components travel faster than the high-frequency components.

The expected values of the squares of the amplitudes a_j are the contribution to the variance of the surface elevation (η) from each of the wave components (variance is $E[\Sigma_j a_j^2]$). The resulting function is known as the wave-variance spectrum $S(f)$.[4] Typical spectra of wave systems have a form as shown in Figure 1.15 where the squared amplitudes for each component are plotted against their corresponding frequencies. The figure shows the spectrum from a measured wave record, along with a sample of the data from which it was calculated.[5] The wave components are represented by their frequencies on the horizontal axis (0.1 Hz corresponds to a period of 10 s).

Wave spectra can be computed by different methods in practice. The most commonly used algorithm is the fast Fourier transform (FFT), developed by Cooley and Tukey (1965). A much slower method, now superseded by FFT, is the auto-correlation approach according to the Wiener–Kinchine theorem, introduced for practical use by Blackman and Tukey (1959) (see also Bendat and Piersol, 1971). Experience has shown that the difference between spectra computed by any two methods does not exceed the confidence limits of each of them.

As the wave energy E equals $\rho_w g H^2/8$ or $\rho_w g a^2/2$ ($H = 2a$), wave spectra in earlier literature were expressed in terms of E and called wave-energy spectra. However, it has become common practice to drop the term $\rho_w g$ and to plot $a^2/2$ or, simply, a^2 along the vertical axis. The wave-energy spectrum is thus usually regarded synonymously with the "variance spectrum".

Wave spectra are usually given as a continuous curve connecting the discrete points found from the Fourier analysis. Systems typically have a general form like that shown in Figure 1.16. The curve may not always be so regular. Irregular seas give rise to broad spectra that may show several peaks. These may be clearly separated from each other or merged into a broad curve with several humps. Swell will generally give a narrow spectrum concentrating the energy in a narrow range of frequencies (or wavelengths) around a peak value. Such a narrow spectrum is associated with the "clean" appearance of the waves. Recall from section 1.3.2 (and also Figure 1.12) that this was often a condition where wave groups were clearly visible.

Most measurements do not provide information about the wave direction, and therefore only an "energy" distribution over wave frequencies, $E(f)$, can be calculated. On the vertical axis,

---

[4] The variance of a wave record is obtained by averaging the squares of the deviations of the water surface elevation, η, from its mean η_0. In section 1.3.8, this variance is related to the area, m_0, under the spectral curve.

[5] This example shows a case with pure wind sea. However, the spectrum may often have a more complicated appearance, with one or more peaks due to swell.

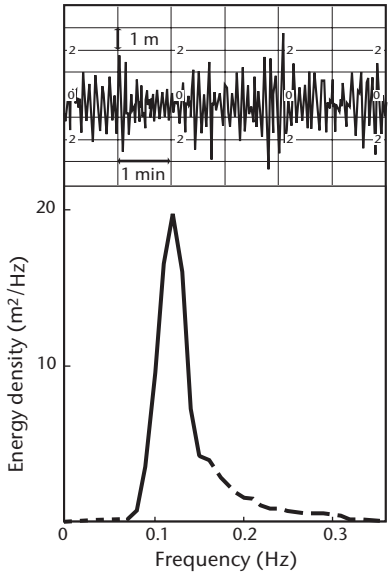

Figure 1.15. Example of a wave spectrum with the corresponding wave record (12 November 1973, 2100 Universal Coordinated Time, 53°25'N, 4°13'E, water depth 25 m, wave height 4.0 m, wave period 6.5 s, west wind 38 knots (19.6 m s^{-1}))

Source: Derived from Royal Netherlands Meteorological Institute

a measure for the wave energy is plotted in units of m^2 Hz^{-1}. This unit is usual for "frequency spectra". Although the spectrum may be continuous in theory, in practice, the variances (or energies) are computed for discrete frequencies. Even when a high-speed computer is used, it is necessary to regard the frequency domain (or the frequency–direction domain) as a set of distinct or discrete values. The value of a^2 at, for instance, a frequency of 0.16 Hz is considered a mean value in an interval that could be 0.155–0.165 Hz. This value, divided by the width of the interval, is a measure for the energy density and expressed in units of m^2 Hz^{-1} (again omitting the factor $\rho_w g$). In fact, the wave spectrum is often referred to as the energy-density spectrum.

Thus, this method of analysing wave measurements yields a distribution of the energy of the various wave components, $E(f,\Theta)$. It was noted in section 1.3.2 that wave energy travels at the group velocity c_g. From Equation 1.19, it can be seen that this is a function of both frequency and direction (or the wave-number vector) and possibly water depth. The energy in each spectral component therefore propagates at the associated group velocity. Hence, it is possible to deduce how wave energy in the local wave field disperses across the ocean.

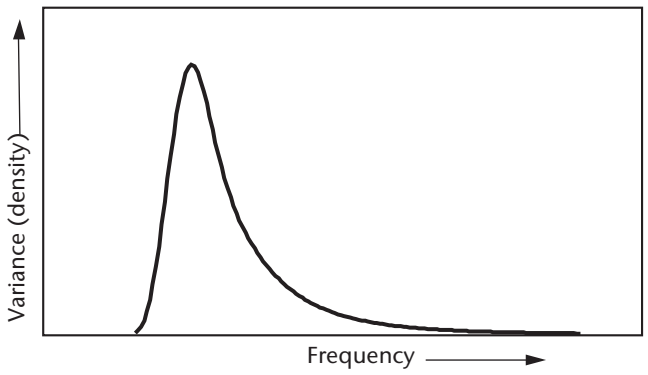

Figure 1.16. Typical wave-variance spectrum for a single system of wind waves; a wave energy $E(f)$ spectrum is obtained by transformation of the vertical axis into units of $\rho_w g S(f)$

A wave record and the spectrum derived from it are samples of the sea state (see section 1.3.4). As with all statistical estimates, it is necessary to investigate how good the estimate is, and how well it is likely to indicate the true state. There is a reasonably complete statistical theory to describe this. Interested readers are referred to other texts such as that of Jenkins and Watts (1968). The validity of a spectral estimate depends on the length of the record, which, in turn, depends on the consistency of the sea state or statistical stationarity (not too rapidly evolving). The spectral estimates can be shown to have a statistical distribution called a χ^2 distribution for which the expected spread of estimates is measured by a number called the "degrees of freedom". The larger the number of degrees of freedom, the better the estimate is likely to be.

1.3.8 Wave parameters derived from a spectrum

A wave spectrum is the distribution of wave energy (or variance of the sea surface) over frequency (or wavelength or frequency and direction, and so forth). Thus, as a statistical distribution, many of the parameters derived from the spectrum are parallel to similar parameters from any statistical distribution. Hence, the form of a wave spectrum is usually expressed in terms of the moments[6] of the distribution (spectrum). The nth-order moment m_n of the spectrum is defined by

$$m_n = \int_0^\infty f^n E(f)\mathrm{d}f. \tag{1.31}$$

(Sometimes $\omega = 2\pi f$ is preferred to f.) In this formula, $E(f)$ denotes the variance density at frequency f, as in Figure 1.16, so that $E(f)\mathrm{d}f$ represents the variance $a_i^2/2$ contained in the ith interval between f and $f + \mathrm{d}f$. In practice, the integration in Equation 1.31 is approximated by a finite sum, with $f_i = i\mathrm{d}f$,

$$m_n = \sum_{i=0}^{N} f_i^n \frac{a_i^2}{2}. \tag{1.32}$$

From the definition of m_n, it follows that the moment of zero order, m_0, represents the area under the spectral curve. In finite form, this is

$$m_0 = \sum_{i=0}^{N} \frac{a_i^2}{2} = \frac{a^2}{2}, \tag{1.33}$$

which is the total variance of the wave record obtained by the sum of the variances of the individual spectral components. The area under the spectral curve therefore has a physical meaning that is used in practical applications for the definition of wave-height parameters derived from the spectrum. Recalling that for a simple wave (section 1.2.4), the wave energy (per unit area) E was related to the wave height by

$$E = \frac{1}{8}\rho_\mathrm{w} g H^2. \tag{1.34}$$

Then, if the actual sea state is replaced by a single sinusoidal wave having the same energy, its equivalent height would be given by

$$H_\mathrm{rms} = \sqrt{\frac{8E}{\rho_\mathrm{w} g}}, \tag{1.35}$$

the root-mean-square wave height. E now represents the total energy (per unit area) of the sea state.

It is desirable to have a parameter derived from the spectrum and corresponding as closely as possible to the significant wave height $H_{1/3}$ (as derived directly from the wave record) and,

[6] The first moment of a distribution of N observations $X_1, X_2, \ldots, X_n$ is defined as the average of the deviations $x_1, x_2, \ldots, x_n$ from the given value X_0. The second moment is the average of the squares of the deviations about X_0; the third moment is the average of the cubes of the deviations; and so forth. When X_0 is the mean of all observations, the first moment is obviously zero, the second moment is then known as the "variance" of X and its square root is termed the "standard deviation".

equally, the characteristic wave height H_c (as observed visually). It can be shown that H_{rms} should be multiplied by the factor $\sqrt{2}$ to arrive at the required value. Thus, the spectral wave-height parameter commonly used can be calculated from the measured area m_0 under the spectral curve as follows:

$$H_{m_0} = \sqrt{2}\sqrt{\frac{8E}{\rho_w g}} = 4\sqrt{m_0}. \tag{1.36}$$

The total variance of the sea state (m_0) is sometimes referred to as the total energy, but the total energy E is really $\rho_w g m_0$. In theory, the correspondence between H_{m_0} and $H_{1/3}$ is valid only for narrow spectra that do not occur often in nature. However, the difference is small in most cases, with $H_{m_0} = 1.05H_{1/3}$ on average. The significant wave height is also frequently denoted by H_s. In that case, it must be indicated which quantity ($4\sqrt{m_0}$ or $H_{1/3}$) is being used.

The derivation of parameters for wave period is a more complicated matter, owing to the great variety of spectral shapes related to various combinations of sea and swell. There is some similarity with the problem of defining a wave period from statistical analysis (see section 1.3.5). The spectral wave frequency and wave period parameters commonly used are:

- f_p, which is the wave frequency corresponding to the peak of the spectrum (modal or peak frequency);
- T_p, which is the wave period corresponding to f_p: $T_p = f_p - 1$;
- $T_{m_{01}}$, which is the wave period corresponding to the mean frequency of the spectrum:

$$T_{m_{01}} = \frac{m_0}{m_1}; \tag{1.37}$$

- $T_{m_{02}}$, which is the wave period theoretically equivalent to the mean zero-downcrossing period T_z:

$$T_{m_{02}} = \sqrt{\frac{m_0}{m_2}}; \tag{1.38}$$

- $T_{m_{-10}}$, which is the energy wave period, so called for its role in computing wave power J in wave-energy studies:

$$T_{m_{-10}} = \frac{m_{-1}}{m_0}, \tag{1.39}$$

where J, the wave power in kW m^{-1} of the wave front, is computed as $J = 0.49H_{m_0}^2 T_{m_{-10}}$.

The wave period $T_{m_{02}}$ is sensitive to the high-frequency cut-off in the integration (Equation 1.31) that is used in practice. Therefore, this cut-off should be noted when presenting $T_{m_{02}}$, in particular, when comparing different datasets. For buoy data, the cut-off frequency is typically 0.5 Hz, as most buoys do not accurately measure the wave spectrum above this frequency. Fitting a high-frequency tail before computing the spectral moments can be a useful convenience when high-frequency information is not available (for example, in a wave-model hindcast).

Goda (1978) has shown that, for a variety of cases, average wave periods of the higher waves in a record, for example $T_{H1/3}$ (see section 1.3.5), remain within a range of $0.87T_p$ to $0.98T_p$.

The width of the spectral peak can be used as a measure of the irregularity of the sea state. The spectral width parameter ε is defined by

$$\varepsilon = \sqrt{\frac{m_0 m_4 - m_2^2}{m_0 m_4}}. \tag{1.40}$$

It varies between 0 (narrow spectrum; regular waves) and 1 (broad spectrum; many different wave periods present; irregular wave pattern).

However, the use of ε is not recommended because of its sensitivity to noise in the wave record due to the higher-order moments, in particular m_4. Rye (1977) showed that the peakedness parameter Q_p (Goda, 1970) is a good alternative,

$$Q_p = \frac{2}{m_0^2}\int_0^\infty fS(f)^2\,df. \tag{1.41}$$

$Q_p = 1$ corresponds with $\varepsilon = 1$, while Q_p becomes large for narrow spectra. Under natural conditions, Q_p usually remains within the interval 1.5–5.

1.3.9 Model forms of wave spectra

The concept of a wave spectrum is commonly used for modelling the sea state. Models of the spectrum enable the spectrum to be expressed as some functional form, usually in terms of frequency, $E(f)$, frequency and direction, $E(f,\Theta)$, or wave number, $E(k)$. As the wave number and frequency are related by the dispersion relation (see Equations 1.3 and 1.4), the frequency and wave-number forms can be transformed from one to the other.

Models of the spectrum are used to obtain an estimate of the entire wave spectrum from known values of a limited number of parameters, such as the significant wave height and wave period. These may be obtained by hindcast calculations, by direct measurement or by visual observation. To give an idea of the various factors that need to be taken into account, a few models are given below as examples. In the first three models, no bottom effects have been taken into account. The Texel–Marsen–Arsloe spectrum is proposed as a general form for a model spectrum in depth-limited waters. In all cases, E is used to represent the variance density spectrum.

The Phillips spectrum describes the shape of the high-frequency part of the spectrum, above the spectral peak. It recognizes that the logarithm of the spectrum is generally close to a straight line, with a slope that is about –5. Hence, the general form is

$$\begin{aligned} E(f) &= 0.005\frac{g^2}{f^5} \quad \text{if } f \geq \frac{g}{u} \\ &= 0 \qquad\qquad \text{elsewhere.} \end{aligned} \tag{1.42}$$

The Pierson–Moskowitz spectrum (Pierson and Moskowitz, 1964) is often used as a model spectrum for a fully developed sea, an idealized equilibrium state reached when duration and fetch are unlimited. This spectrum is based on a subset of 420 selected wave measurements recorded with a shipborne wave recorder – developed by Tucker (1956) – on board British ocean weather ships during a five-year period between 1955 and 1960. In its original form, this model spectrum is

$$E(f) = \frac{\alpha g^2}{(2\pi)^4 f^5} e^{-0.74\left(\frac{g}{2\pi u f}\right)^4}, \tag{1.43}$$

where $E(f)$ is the variance density (in m^2 s^{-1}), f the wave frequency (Hz), u the wind speed (m s^{-1}) at 19.5 m above the sea surface, g the acceleration due to gravity (m s^{-2}) and α a dimensionless quantity, $\alpha = 0.0081$. It can be shown that the peak frequency of the Pierson–Moskowitz spectrum is

$$f_p = 0.877\frac{g}{2\pi u}. \tag{1.44}$$

Equations 1.43, 1.31 and 1.32 allow m_0 to be calculated as a function of wind speed. Hence, H_{m_0} (the significant wave height) for a fully grown sea is

$$H_{m_0} = 0.0246u^2, \tag{1.45}$$

with H_{m_0} in m and u in m s^{-1}, with the wind speed now related to the 10 m height.[7] This agrees well with limiting values of the wave-growth curves in Chapter 4. Equations 1.44 and 1.45 are valid for a fully developed sea only, as is their combination:

$$H_{m_0} = 0.04f_p^{-2}. \tag{1.46}$$

[7] The usual reference height for wind speeds is 10 m. Wind speed at 19.5 m is reduced to 10 m height by applying a correction factor; in this case, the wind speed has been divided by 1.075 (see section 2.4.1).

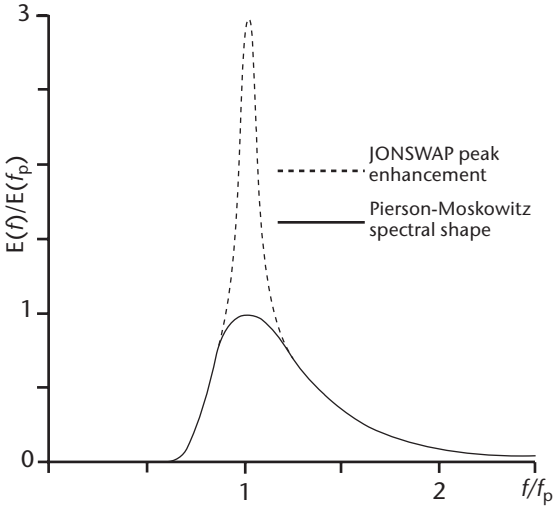

Figure 1.17. General form of a JONSWAP spectrum as a function of f/f_p

The Joint North Sea Wave Project (JONSWAP) spectrum is often used to describe waves in a growing phase. Observations made during JONSWAP (Hasselmann et al., 1973) gave a description of wave spectra growing in fetch-limited conditions, that is, where wave growth under a steady offshore wind was limited by the distance from the shore. The basic form of the spectrum was in terms of the peak frequency rather than the wind speed, that is, as in Equation 1.43 but after the substitution for $g/(2\pi u)$ using Equation 1.44:

$$E(f) = \frac{\alpha g^2}{(2\pi)^4 f^5} e^{-1.25\left(\frac{f}{f_p}\right)^4} \gamma(f). \tag{1.47}$$

The function γ is the peak enhancement factor, which modifies the interval around the spectral peak making it much sharper than in the Pierson–Moskowitz spectrum. Otherwise, the shape is similar. Figure 1.17 illustrates the general form of the JONSWAP spectrum.

Using JONSWAP results, Hasselmann et al. (1976) proposed a relation between wave variance and peak frequency for a wide range of growth stages. Transforming their results into terms of H_{m_0} and f_p,

$$H_{m_0} = 0.0414 f_p^{-2} (f_p u)^{1/3}, \tag{1.48}$$

again with H_{m_0} in m, f_p in Hz and u in m s^{-1} at 10 m above the mean water level. This equation is connected with developing waves and so is not exactly comparable with Equation 1.45 for fully developed waves. The peak frequency can be obtained by reversing Equation 1.48,

$$f_p = 0.148 H_{m_0}^{-0.6} u^{0.2}. \tag{1.49}$$

Equation 1.49 can be applied for estimating the approximate spectrum and characteristic wave periods when wave height and wind speed are known. This is common practice when predicting waves using growth curves relating wave height to wind speed and fetch or duration.

The Texel–Marsen–Arsloe spectrum, proposed as a model in depth-limited waters, takes the form

$$E(f) = E_{\text{JONSWAP}}(f) \Phi(f, h), \tag{1.50}$$

where Φ is a function of frequency f and depth h (for more details see Bouws et al., 1985).

The spectra shown here are all of the type

$$E(f) = E(f, \text{parameters}), \tag{1.51}$$

with no account taken of the directional distribution of the sea state. Section 3.3 provides further information on directionality. Nevertheless, a brief introduction to directional wave spectrum is given next.

1.3.10 Remarks on the directional wave spectrum

Even from a basic idea, such as the one illustrated in Figure 1.13, simple wave components can be thought of as if they are travelling with a certain propagation direction. Describing in some sense the energy density (or variance density) of surface waves as a function of frequency (or wave number) and direction is one of the most complete ways to specify the ocean wave field. In the full description, the sea-surface elevation is represented as a function of space (x,y) and time (t).

In the particular case when an instantaneous description, such as a frozen sea surface, is given by

$$\eta(x, y) = a_{i,j} \cos(k_{x,i}x + k_{y,j}y + \alpha_{i,j}). \tag{1.52}$$

The two-dimensional spectrum can then be expressed describing the distribution of energy density as a function of wave-number components.

The two-dimensional spectrum (as a function of wave-number components) contains directional information, in a similar manner to the two-dimensional spectrum when expressed in terms of frequency and direction. The relation between those two spectra involves the Jacobian

$$J = \mathrm{d}k \,/\, \mathrm{d}\omega = 1 \,/\, c_{\mathrm{g}}, \tag{1.53}$$

which is used to transform information from the wave-number vector domain to the frequency–direction domain assuming the surface-wave dispersion relation holds.

Within a more comprehensive context, the moving three-dimensional sea surface $\eta(x,y,t)$ under the presence of waves is represented by the three-dimensional spectrum (as a function of the wave-number vector and frequency). This general representation does not require the use of the dispersion relation, unless transformation to a particular domain is to be performed. Furthermore, if the waves do behave as linear waves, then the three-dimensional spectrum $E(k_x,k_y,\omega)$ collapses onto a curved plane in the spectral k_x, k_y, ω-space, which are exactly the loci for the well-known dispersion relation. Deviations from the theoretical dispersion relation are then probably due to an ambient current or any non-linear behaviour of the sea surface. In some cases, surface current speed and direction, and even their depth dependence, can thus be inferred from observations of $E(k_x,k_y,\omega)$.

In situ wave directional information is generally estimated from measurements of wave properties, for instance: surface elevation and slope vector at a point, or some property at three or more points, generating a time-series set. In general, the assumption of stationarity of the surface-wave process is adopted and required for the analysis, and various methods are used such as: the classical Fourier transform (Longuet-Higgins et al., 1963), the maximum likelihood method (Capon, 1979), the maximum entropy method (Lygre and Krogstad, 1986) and the wavelet directional method (Donelan et al., 1996).

In some other cases, information on the sea-surface elevation can be available as a snapshot $\eta(x,y)$, and direct FFT analysis might result in the direct estimation of the two-dimensional spectrum as a function of the wave-number vector. A sequence of such sea-surface elevation will comprise the full information, enabling an estimate of the three-dimensional spectrum. This can be achieved from video or stereo video, or from a sequence of marine radar images, allowing the estimation of $E(k_x,k_y,\omega)$.

It is important to mention that due to recent advance in remote sensors, modern synthetic aperture radars (SARs) have proved useful in retrieving ocean wave spectra from the global

oceans (Chapron et al., 2001; Lehner and Ocampo-Torres, 2004). Of course, it is necessary to know details of the full version of the transfer function between the SAR image spectrum and the ocean wave spectrum.

CHAPTER 2. OCEAN-SURFACE WINDS

Editor: W. Gemmill, updated by T. Bruns with contribution from N. Kohno

2.1 INTRODUCTION

The basic force that drives ocean waves is the surface stress imparted by the wind. Thus, the quality of wave forecasts depends on the availability and reliability of wind forecasts. The effects of erroneous wind speeds are cumulative in time, and the effect on forecast wave heights may be appreciable. For example, the wave-growth diagrams in Chapters 3 and 4 show that a wind of 15 m s^{-1} (29 knots) is capable of raising a sea of 4 m height after 12 h and of 5 m height after 24 h. If the wind speed was assumed to be 17.5 m s^{-1} (34 knots), the forecast would indicate wave heights of 4.9 m and 6.3 m, respectively. An initial error of 16% in the wind speed would thus give rise to errors of 25%–30% in the forecast wave heights.

A realistic parameterization of the turbulent momentum transfer within the marine boundary layer is needed to accurately translate wind speed into surface stress. Stratification in the lowest atmospheric layer (up to about 50 m) plays a critical role in the transfer of momentum. Under neutral stability conditions, the mean wind is characterized by a logarithmic increase with height. In this case, surface stress can be derived from the wind speed at a given height using a bulk transfer relation. If the sea is warmer than the overlying air, conditions become unstable in the lower atmosphere and there is more turbulent mixing. This increases the stress on the surface, so for the same wind speed at a given height, waves will become higher under unstable conditions than under stable conditions.

It has become common practice to adjust winds to a pre-assigned height of 10 m over the ocean surface using a suitable boundary-layer parameterization. For wave forecasting, this has the practical advantage that the 10 m wind speed may be treated as "neutral", that is, without considering atmospheric stability. However, in certain situations, the assumption of a neutral wind at 10 m may fail. Consider cases of frontal passages or strong warm advection where the lower atmospheric boundary does not have chance to adjust to the sea-surface temperature. Today, 10 m winds are operationally provided by most numerical weather prediction (NWP) models. Some forecast centres even run coupled models of atmosphere and ocean waves using a modified boundary-layer formulation.

In the early years of wave forecasting, wind fields were determined by manual analysis of the marine meteorological observations. This complex and time-consuming process involved analysis of the surface-pressure distribution, followed by extrapolation in time. Wind fields were then determined using simple dynamic relations among the pressure gradient, Coriolis forces and frictional forces.

With the development of NWP, manual methods have increasingly lost their importance in the analysis of wind fields. However, in certain hindcast studies, where accuracy is particularly important and more time may be available, the combined use of numerical models and manual intervention may provide the most realistic wind fields. Application of manual methods may also have merits for forecasters in remote locations with slow data connections.

Manual methods are also useful for cases where the available models have limitations in resolution and model physics, such as mesoscale events like squall lines, thunderstorms and hurricanes. Sometimes, the models do not initialize well and their output needs enhancement to fit current conditions and short-term trends.

Knowledge of the theoretical and practical backgrounds may also be helpful when using numerical wind and wave forecasts. Therefore, this chapter is structured in the following order. Section 2.2 describes the sources of marine data, because observations and measurements from the ocean surface are used by forecasters as well as for model assimilation and verification.

Section 2.3 reviews the principles of boundary-layer parameterization, section 2.4 gives an overview over the large-scale factors affecting ocean-surface winds and section 2.5 highlights some aspects and examples of NWP.

2.2 SOURCES OF MARINE DATA

Ocean-surface observations are routinely taken by merchant vessels participating in the WMO Voluntary Observing Ship (VOS) Scheme (WMO, 2018), by a few research vessels, by moored and drifting ocean buoys, by platforms, as well as by coastal and island weather stations. The *Manual on the Global Observing System* (WMO, 2015), Part III, section 1, gives a detailed list of the different types of observing stations. Remote wind measurements are provided by active and passive microwave sensors (altimeters, scatterometers and special sensor microwave imagers (SSM/Is)) on board satellites. All these data are disseminated worldwide via the Global Telecommunications System to be used in data assimilation for NWP.

Observation frequency and quality vary widely, depending on the platform and parameter. Wind reports over sea and pressure measurements bear inherent inaccuracies or discrepancies between pressure and wind observations. The following subsections discuss the quality of marine weather reports.

2.2.1 Ship weather reports

Ship weather reports are prepared by deck officers as part of their routine duties. Wind speed and direction are estimated either indirectly, by the observer using sea state and feel of the wind, or directly by anemometer if the vessel is so equipped. Figure 2.1 shows the coverage of VOS reports collected within a year.

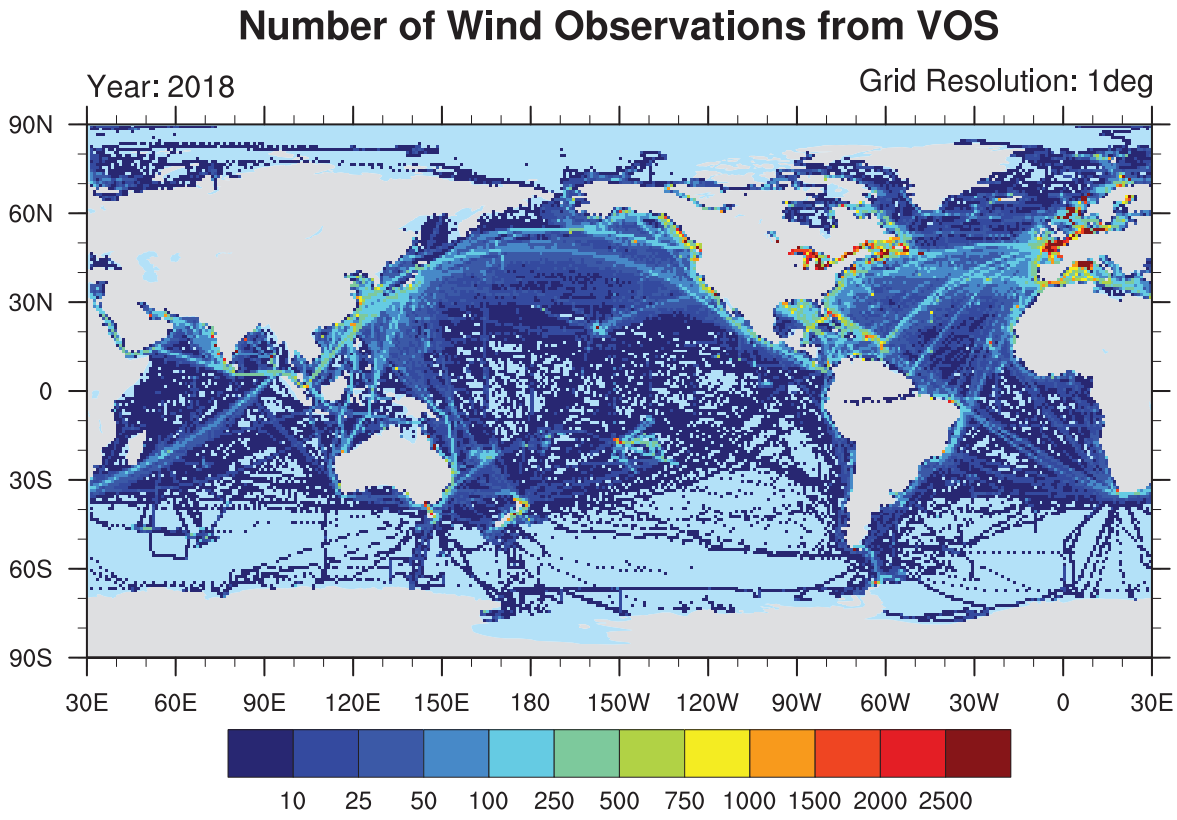

Figure 2.1. Yearly map (2018) of VOS reports

Source: Deutscher Wetterdienst, Marine Data Centre, Hamburg, Germany

2.2.1.1 ***Estimated winds***

Wind observations are subject to a variety of errors. Reports are often made by first determining the wind speed in terms of the well-known Beaufort scale. Each scale number is based on the appearance of the sea state and therefore represents a range of possible wind speeds. Even if an experienced observer is able to distinguish one step from another, a wind observation will be accurate only to within a half of one scale interval.

According to WMO code FM 13, a single wind speed has to be chosen for the report. For this purpose, ships' observers use a conversion table that was introduced internationally in 1948. Table 2.1 shows ranges of wind speed in the right-hand column, which are based on a linear regression of averaged Beaufort values on measured wind speed as the equivalent scale (WMO, 2012).

Numerous attempts have been made to derive the most realistic relationship between Beaufort estimates and equivalent wind speeds using improved linear regression techniques (Kent and Taylor, 1997). For example, a scale proposed for scientific use is shown in the three left columns of Table 2.1 (WMO, 1970). A comparison suggests that observers tend to overestimate high wind speeds and underestimate low wind speeds.

Other errors in wind estimations arise from misinterpretation of the sea state. For example, a substantial time lag may occur for the sea to reach a state that truly reflects the prevailing wind conditions. In addition, it is obvious that night-time wind reports based on visual sea state will be subject to great error because of poor visibility. Due to the increasing size of ships, observers are further removed from the ocean surface and wave estimation is more difficult. Wind effects

Table 2.1. Conversion scales for Beaufort wind force showing the equivalent wind speed for each Beaufort number and equivalent scale intervals in m s^{-1} and in knots

		Scale recommended for use in wave forecasting			*Range of values reported by observers*
Beaufort number	*Descriptive term*	*Equivalent wind speed*	*Intervals*		
		m s^{-1}	*m s^{-1}*	*knots*	*knots*
0	Calm	0.8	0–1	0–2	<1
1	Light air	2.0	1–2	3–5	1–3
2	Light breeze	3.6	3–4	6–8	4–6
3	Gentle breeze	5.6	5–6	9–12	7–10
4	Moderate breeze	7.8	7–9	13–16	11–16
5	Fresh breeze	10.2	9–11	17–21	17–21
6	Strong breeze	12.6	12–14	22–26	22–27
7	Near gale	15.1	14–16	27–31	28–33
8	Gale	17.8	17–19	32–37	34–40
9	Strong gale	20.8	19–22	38–43	41–47
10	Storm	24.2	23–26	44–50	48–55
11	Violent storm	28.0	26–30	51–57	56–63
12	Hurricane	–	31+	58+	64+

Sources: WMO (1970, 2012)

on the sea surface are sometimes modified by other phenomena, of which the observer may be unaware. Surface contaminants of seawater, such as mineral oil or plankton, and even rainfall have an influence on foam forming. Air stability affects the steepness of waves to some extent, and strong currents may change the form of waves and hence the general appearance of the sea state. As a result, the standard deviation of a wind observation is, on average, greater than half of one Beaufort scale interval.

Aside from confused or multimode sea states, the wind direction can easily be determined from the orientation of the crests of wind waves. The standard deviation of an individual observation of wind direction amounts to 10° (Verploegh, 1967) and appears to be independent of wind speed. The direction of constant trade or monsoon winds can be determined with greater accuracy compared to winds in the mid-latitudes.

2.2.1.2 *Measured winds*

Errors of anemometer measurements on board ships are generally introduced by poor instrument exposure, improper reading of wind speed and direction indicators, vessel motion and maintenance problems. The main problem is that a moored anemometer cannot always be properly exposed to all wind directions. The vessel's superstructure may interfere with the flow of air, and consequently the measurement may not be representative of the true air flow over the ocean surface. Moreover, the apparent wind measured by an anemometer on board ship represents the combined effect of the true wind and headwind. However, computing the true wind from the ship's speed and the apparent wind using a vector diagram is an error-prone procedure.

A study by Wilkerson and Earle (1990) demonstrated that the quality of wind reports from ships with anemometers is not much better than those without. Pierson (1990) found that ship reports, with or without anemometers, were inferior to buoy measurements.

On larger ships, anemometers are usually installed at great heights, sometimes up to 40 m above the surface of the sea. The wind speed normally increases with height, but the rate of speed increase depends on the stability of the air. However, routine observations are not corrected for height, which is yet another source of error when comparing wind data from many platforms. For detailed reviews of problems of wind measurements at sea, see those of Dobson (1981) and Taylor et al. (1994, 1999).

Winds measured or observed on ships possess a low priority in the data assimilation process of operational NWP models due to the many error sources. Measurements of sea-level pressure on board ships are much more reliable.

2.2.2 Moored and drifting buoy reports

Moored buoys equipped with meteorological instruments have been used since 1967 to provide surface atmospheric and oceanographic data. Today, a large variety of moored and drifting data buoys cover wide ocean areas. Meindl (1996) gives a description of the moored data network. The International Comprehensive Ocean-Atmosphere Data Set is the largest available set of in situ marine observations (Worley et al., 2005; Woodruff et al., 2011).

Wind measurements by anemometers are available from a few buoys near the coasts. However, surface-pressure measurements from drifting buoys are well distributed over wide oceanic areas.

Buoys can be expected to provide better quality data than those reported by ships for several reasons:

– The sensor's location on the buoy is carefully considered to avoid exposure problems; for example, measurements of high wind speeds can be biased due to the tilt of the mast and shadowing effects in high seas;

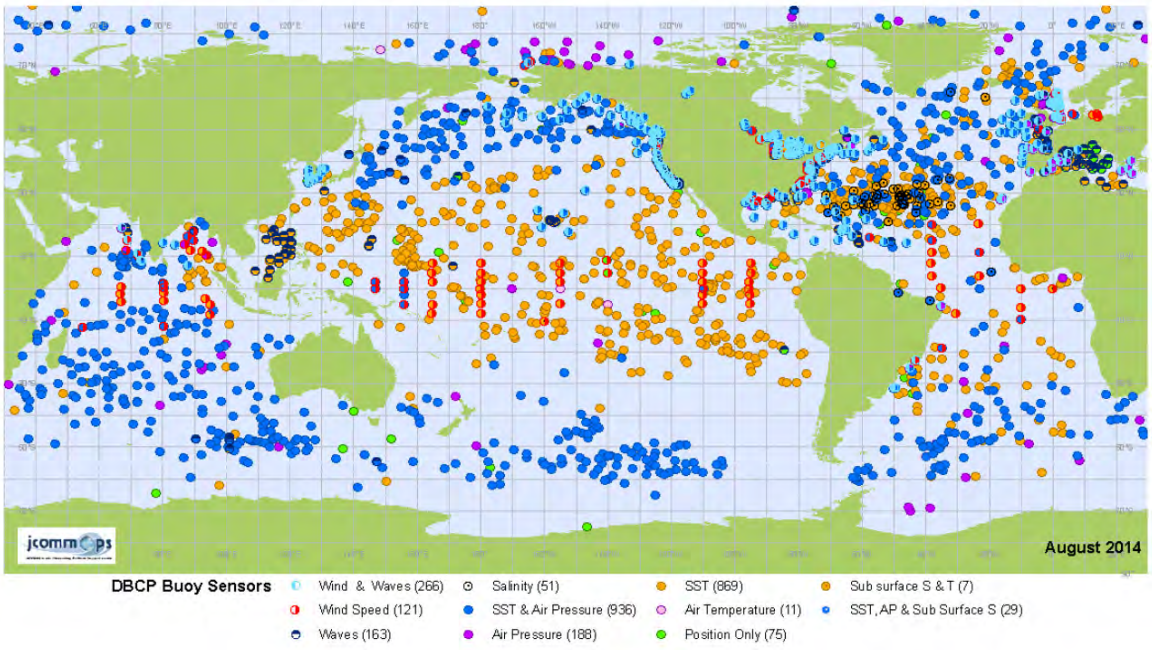

Figure 2.2. Example of a monthly map (August 2014) of active sensors located on drifting and moored buoys published by DBCP (AP = air pressure; SST = sea-surface temperature; S & T = salinity and temperature)

Source: http://www.jcommops.org/dbcp/network/maps.html

- Sampling and averaging periods for the measurements are determined after accounting for buoy motion;
- Duplicate sensors are used for redundancy, and each is calibrated before deployment;
- Buoys are monitored worldwide in near real time by the Data Buoy Cooperation Panel (DBCP), allowing the detection of instrument errors (see Figure 2.2).

2.2.3 Land (coastal) stations

Land (coastal) reporting stations provide data of variable quality and applicability. Using these reports requires knowledge of the exposure, local topography, proximity to the coast and type of station: whether it is a (coastal) buoy, lighthouse or coast-guard station. Consideration should also be given to the time of day (for the possible influence of land–sea breezes) and level of station maintenance.

2.2.4 Common height adjustment of in situ data

To perform wind and pressure analyses, the data must be adjusted to a standard height. However, anemometer heights on moored buoys range between 3 m and 14 m, on ships, they range from 15 m to over 40 m, and on platforms or at coastal stations, they may range up to 200 m or more above sea level.

The theory of Monin and Obukhov (1954) is well known for calculating the vertical wind profile through the lowest part of the atmosphere (known as the constant flux layer). The calculation requires the wind speed at a known height within the layer, and the stability, which is derived from the air–sea temperature difference. Methods for adjusting winds to a standard height are reviewed and wind adjustment ratios are presented in table form in a WMO document by Shearman and Zelenko (1989). In practice, when an ocean-surface wind field is being analysed from observations, the wind field is assumed to be prescribed at 10 m.

See section 2.3 for further discussion of wind profiles in the lower atmospheric boundary layer.

2.2.5 Satellite data

Satellite remote sensing of wind speed and direction over the ocean began with the first satellite microwave scatterometer aboard the Skylab space station in 1973, which measured the backscattered energy from the ocean surface. Many more satellite missions with different types of sensors have been launched since then. Empirical algorithms had to be developed simultaneously to derive near-surface wind parameters from ocean-surface backscatter or brightness temperatures. Nowadays, some satellites on polar orbits provide ocean winds on a near-global scale. There are four types of satellite instruments.

A scatterometer is an active radiometer based on Bragg scattering of capillary waves on the ocean surface. Capillary waves directly reflect the changes in surface wind speed. Scatterometers provide wide swath fields of wind speed and wind direction (Figures 2.3 and 2.4).

Satellite altimeters are downward-pointing radar instruments that determine the distance from the satellite to a target surface by measuring the satellite-to-surface round-trip time of a radar pulse. Depending on the roughness of the sea surface, the pulse will be scattered and deformed. Thus, as a side effect of scanning the oceans, accurate estimates of wave height and wind speed can be derived from the characteristics of the reflected pulse. Empirical relations have been established on the basis of collocated surface buoy observations (for example, Freilich and Challenor, 1994). Many similar studies have also been published as corrections are needed for each new radar instrument.

The SSM/I and the special sensor microwave imager sounder (SSMIS) are passive microwave radiometers that observe the specific "brightness" related to the wind-induced roughness of the ocean surface. The translation of brightness to near-surface wind speed is accurate. However, they fail with sun glint, in the presence of rain, and near ice or land. SSM/I and SSMIS data are produced by remote-sensing systems and sponsored by the National Aeronautics and Space Administration's Earth Science MEaSUREs Program. Data are available from Remote Sensing Systems.

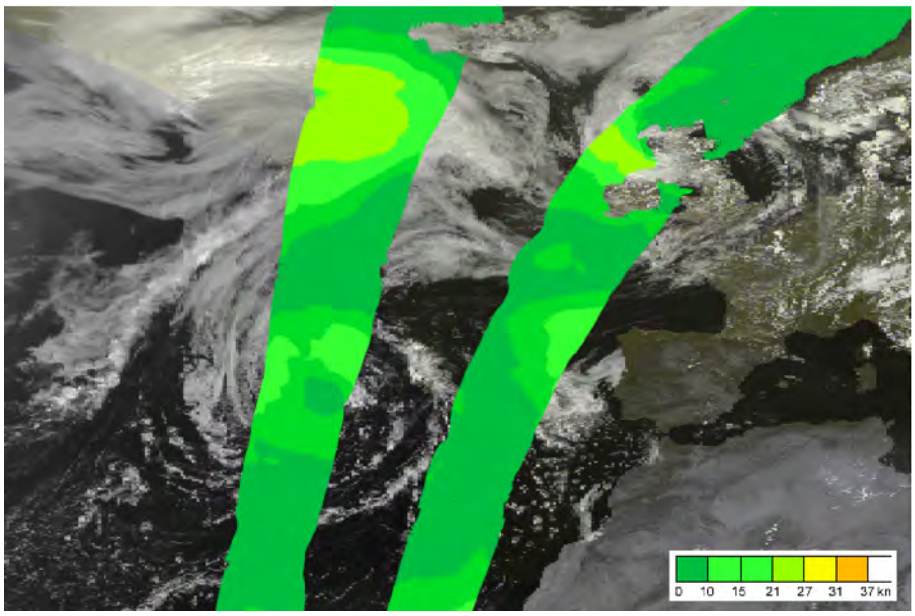

Figure 2.3. Scatterometer wind speeds on 27 July 2014, measured by the MetOp satellite with an infrared METEOSAT image in the background (kn = knots)

Source: German Meteorological Service (Deutscher Wetterdienst)

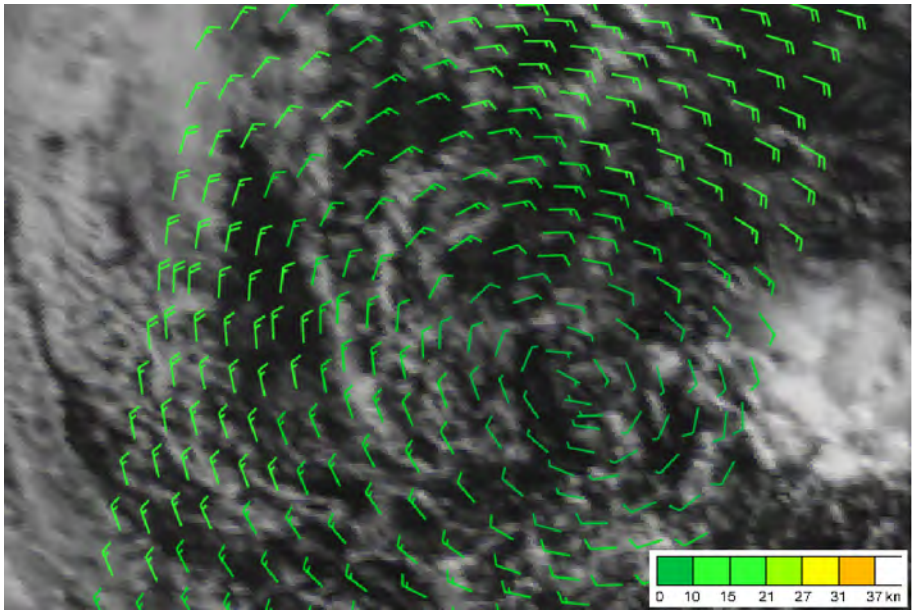

Figure 2.4. Detail of Figure 2.3: scatterometer wind speeds on 27 July 2014, measured by the MetOp satellite with infrared METEOSAT image in the background (kn = knots)

Source: German Meteorological Service (Deutscher Wetterdienst)

The synthetic aperture radar (SAR) and the advanced SAR transmit and receive many successive polarized radar pulses while the satellite is moving. Processing and combining the recordings from multiple antenna locations result in images of land and ocean surfaces that are of high resolution. Empirical algorithms have been developed (for example, by Lehner et al., 2000) to derive wind speed small swaths (imagettes). Wind directions are extracted from wind-induced streaks that are visible in SAR images (Lehner et al., 2012; Figure 2.5).

All sensors respond to changes in the water surface and do not represent 10 m winds due to variations in atmospheric stratification. However, a height adjustment as applied to in situ measurements is not feasible. Therefore, sensors are usually calibrated to match the 10 m "equivalent neutral wind" rather than the true surface wind (see section 2.3.3). Table 2.2 gives an overview of satellite-borne instruments used for wind measurement.

The quality of the wind measurements obtained from satellite-borne sensors depends on the accuracy of the algorithms used to derive wind-related parameters (speed and, if applicable, direction) from the sensor measurements (brightness temperatures from passive microwave sensors, and radar backscatter cross-section and antenna parameters from active microwave sensors) and various corrections that need to be applied for atmospheric water vapour and liquid water contamination. However, application of these algorithms is limited to open ocean areas where measurements are not contaminated by land. Furthermore, the sensor response may drift in time; careful quality-control procedures should be used to monitor the retrievals.

2.3 MARINE BOUNDARY LAYERS

The atmospheric boundary layer extends from the surface to the free atmosphere at approximately 1 km height. Frictional forces dominate at the surface. In the free atmosphere, frictional forces become less important, and, to a first order of approximation, atmospheric flow is close to being in geostrophic balance (see section 2.4.2).

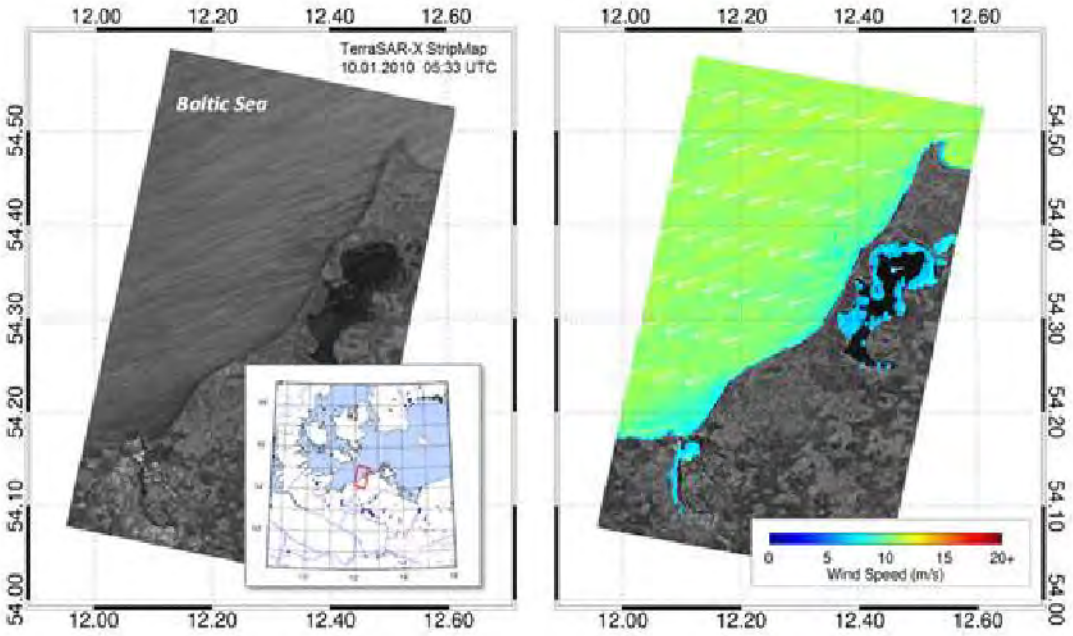

Figure 2.5. Wind speed and direction in the Baltic Sea derived from TerraSAR-X using the XMOD algorithm

Source: A Pleskachevsky, German Aerospace Center, Bremen, Germany

Table 2.2. Satellite-derived wind measurements

Instrument	*Mode*	*Swath*	*Footprint*	*Measurement*
Altimeter	Active microwave	Nadir	5–15 km	10 m wind speed
Scatterometer	Active microwave	500–1 800 km	50 km	10 m wind speed and direction
SSM/I	Passive microwave	1 500 km	25 km	10 m wind speed
SAR and advanced SAR	Active microwave	100–1 000 km aside looking	5–500 km	10 m wind speed and direction

Note: "Nadir" is the point on the Earth's surface directly below the satellite. "Footprint" is the ground area covered by the beam of the sensor. "Swath" is the strip of the Earth's surface from which data are collected by the moving satellite. The swath is usually wider than the footprint (nominal swath) depending on the scan mode of the sensor.

The relevant frictional forces are those arising from turbulent fluctuations – Reynolds stresses. A fundamental difficulty of turbulence theory is to relate these turbulent stresses to the properties of the mean flow.

The influence of turbulent fluxes on prognostic mean variables (momentum, temperature and moisture) can be described through the vertical diffusion equation

$$\frac{\partial C}{\partial t} = -\frac{\partial}{\partial z}\overline{w'c'} = \frac{\partial}{\partial z}\left[K_C\left(\frac{\partial C}{\partial z}\right)\right], \qquad (2.1)$$

where the mixing coefficient K_C describes the turbulent diffusivity of the mean variable C, and c' and w' are the turbulent fluctuations of the variable C and vertical motion, with the overbar representing a timely average.

In a common approach, the marine boundary layer is separated into two regimes (Figure 2.6): the Prandtl layer or constant flux layer (from the surface to about 50 m) and the Ekman layer (Ekman, 1905) (from about 50 m up to the free atmosphere above ~1 km).

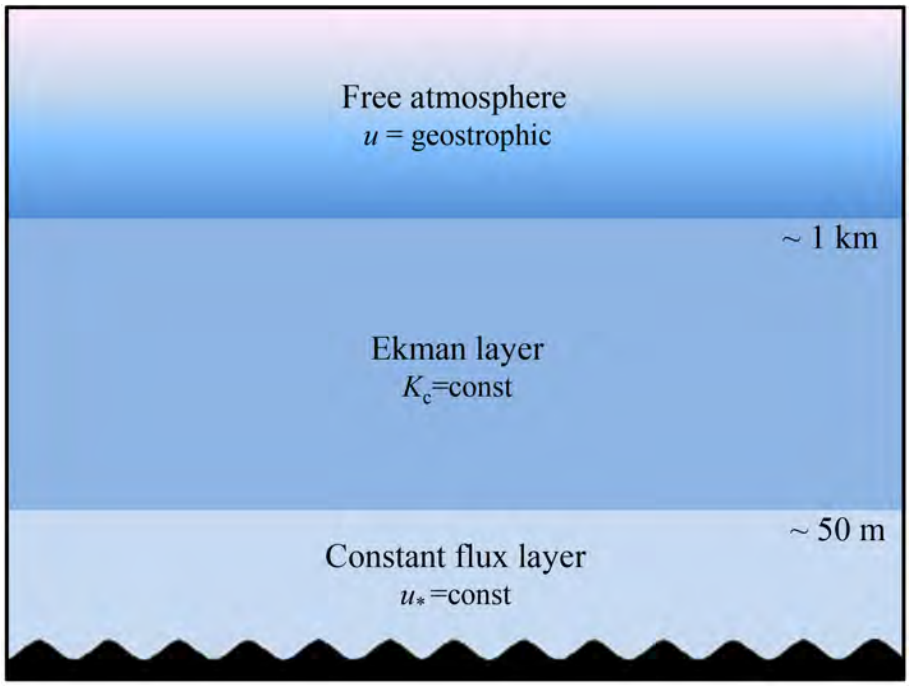

Figure 2.6. Schematic of the two-regime boundary layer; u is the horizontal wind speed and u_* is the friction velocity representing the turbulent vertical momentum flux

Following the mixing length theory developed by Prandtl (for example, Oertel, 2004), it is assumed that the mixing coefficient increases linearly with height in the lowest 50 m. It can be shown that the frictional forces contributing to turbulence are therefore constant with height and the effects of the Coriolis and pressure gradient forces, as well as the horizontal gradient of turbulent fluxes, are negligible. The wind direction is constant with height in this solution. It can also be shown that the mean flow in the constant flux layer depends only on the surface roughness length (Equation 2.2).

However, in the Ekman layer, a constant mixing coefficient is assumed. A transition of wind speed and direction to the geostrophic wind takes place in this layer due to the Coriolis force. The theoretical solution ("Ekman spiral") exhibits an angle of 45° between the geostrophic flow (section 2.4.4) aloft and the wind at the surface. Smaller angles result in theories matching the Ekman and Prandtl layers.

Thermal stratification within the boundary layer is important in determining the wind speed near the ocean surface. Over much of the oceans, the surface air temperature is in equilibrium with the sea-surface temperature so that near-neutral stability dominates. Under these conditions, friction dominates the structure of the wind profile in the constant flux layer, and the profile can be described by a logarithmic form (section 2.3.1).

For unstable cases (air temperature lower than the water temperature), convection becomes active. The higher wind speeds aloft are brought to the surface quickly, reducing dissipation by friction and increasing the stress on the ocean surface. A stable atmosphere (warm air over cold water) acts to increase the friction forces in the boundary layer, resulting in lighter winds and a weaker wind stress (section 2.3.3).

2.3.1 Constant flux layer

Under neutral conditions, Prandtl's solution shows that the horizontal flow over the ocean surface (u) follows the well-known "log" (logarithmic) profile in the vertical direction:

$$u = \frac{u_*}{\kappa} \ln\left(\frac{z}{z_0}\right), \tag{2.2}$$

where κ is the von Kármán constant, z is the height above mean sea level at which the flow is observed, z_0 is the constant of integration (known as the roughness length) and u_* is the vertically constant friction velocity:

$$u_* = \sqrt{\frac{\tau}{\rho_a}}, \tag{2.3}$$

where τ is the magnitude of the surface stress and ρ_a is the density of air. u_* can be thought of as a proxy for the surface stress. It is common to express stress τ through the bulk transfer relation

$$\tau = \rho_a C_d u^2, \tag{2.4}$$

where C_d is the drag coefficient. In general, C_d and u are both functions of height. Determining C_d has been the objective of many field research programmes over the years.

The height and stability dependence of C_d was originally derived by Monin and Obukhov (1954) from profile similarity theory:

$$u = \frac{u_*}{\kappa}\left[\ln\left(\frac{z}{z_0}\right) - \psi\left(\frac{z}{L}\right)\right] \tag{2.5}$$

and

$$C_d(z) = \left(\kappa \Big/ \left[\ln\left(\frac{z}{z_0}\right) - \psi\left(\frac{z}{L}\right)\right]\right)^2. \tag{2.6}$$

The function Ψ has been derived for stable and unstable conditions. L is the Monin–Obukhov mixing length. For neutral conditions, $\Psi(z/L) = 0$. Businger et al. (1971) proposed functional relationships between the non-dimensional wind shear and z/L, which can be used to determine the stability function $\Psi(z/L)$ in Equations 2.5 and 2.6.

2.3.2 **Surface roughness**

One of the problems of specifying the wind in the turbulent layer near the ocean is the formulation of z_0 and its relationship to u_*. Conventionally, z_0 is assumed to be a function of wind speed of a certain height. It is likely that surface roughness is dependent on sea state (waves). Many efforts have been dedicated to determining the relation between waves and roughness by field observations and laboratory experiments. However, all this research has resulted in a wide spread of dependencies on wave age, wave steepness and so forth. Conclusive opinion is yet to be accepted, and Jones and Toba (2001) discussed the complicated status of this topic. More recently, studies have focused on the influence of swell on wind profiles and turbulence properties (Högström et al., 2009; Smedman et al., 2009; Kahma et al., 2016).

Using dimensional arguments, Charnock (1955) related the roughness length of the sea surface to the friction velocity of the wind as follows:

$$z_0 = \frac{\alpha u_*^2}{g}, \tag{2.7}$$

where g is the acceleration due to gravity and α is the Charnock parameter. The common range of α is from 0.01 for swell up to 0.04 for steep young ocean waves, although values up to 0.1 do sporadically occur. A typical value of 0.0185 was determined by Wu (1980). Figure 2.7 illustrates the effect of roughness increasing with 10 m wind speed.

Janssen (1991) examined the feedback of ocean waves on the airflow and introduced a Charnock parameter depending on the sea state. With increasing wave steepness, or low wave age, a considerable enhancement in momentum transfer from air to water was found. Using such a parameterization allows for a two-way coupling of ocean wave and atmospheric models (section 2.5.5).

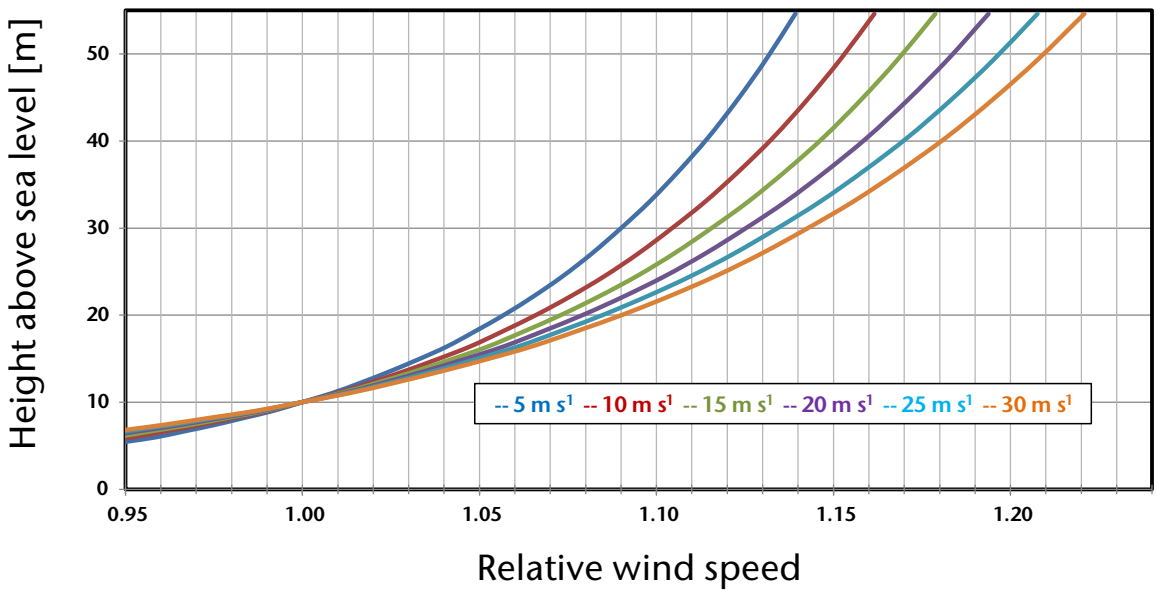

Figure 2.7. Non-dimensional wind profiles scaled by the 10 m wind under neutral conditions $\Psi(z/L) = 0$ over a rough sea surface using the parameterization of Charnock (1955) (Equation 2.7)

2.3.3 Stability effects

In the above discussion in section 2.3.1, the concept of the drag coefficient, as defined in Equation 2.4, was developed. There have been many studies to determine C_d under varying wind speeds and stabilities, and Roll (1965) gave a summary. Wu (1980, 1982) demonstrated through empirical investigations that the drag coefficient at a given height depends linearly on the wind speed, and that the following formulation holds for a wide range of winds under near neutrally stable conditions:

$$10^3 C_{10} = (0.8 + 0.65 U_{10}), \tag{2.8}$$

where C_{10} is the drag coefficient at the 10 m level and U_{10} is the wind speed (m s^{-1}) at the 10 m level.

However, this simple linear empirical relationship needs to be modified when temperature stratification is present. Stratification affects turbulent momentum transport, thereby causing the wind profile to deviate from the logarithmic form.

For moderate wind force regimes, the results of Schwab (1978) suggest a steady increase of the drag coefficient with wind speed. However, this does not seem to be a general law. Other field experiments, for example those of Drennan et al. (1996, 2003) or French et al. (2007), confirmed the wind-speed dependence of the drag coefficient, but also found a large scatter in values. Powell et al. (2003) analysed 331 wind profiles measured by global positioning system dropwindsondes in the vicinity of hurricane eyewalls in the Atlantic, and Eastern and Central Pacific basins. They found that the drag coefficient, friction velocity and roughness length levelled off or even decreased at hurricane wind speeds above 40 m s^{-1}.

Schwab (1978) determined C_d over water for a wide range of wind speeds and atmospheric stabilities. Figure 2.8 shows the results of the calculation. A crucial issue to be addressed concerns the effect of changing stability and wind stress on the prediction of wave growth. It can be inferred from Figure 2.8 that, for a given 10 m level wind speed, unstable conditions result in higher drag coefficients (or surface stress) and hence larger wave growth than stable conditions. Liu et al. (1979) developed a set of equations that computed the surface variables u_*, z_0 and the

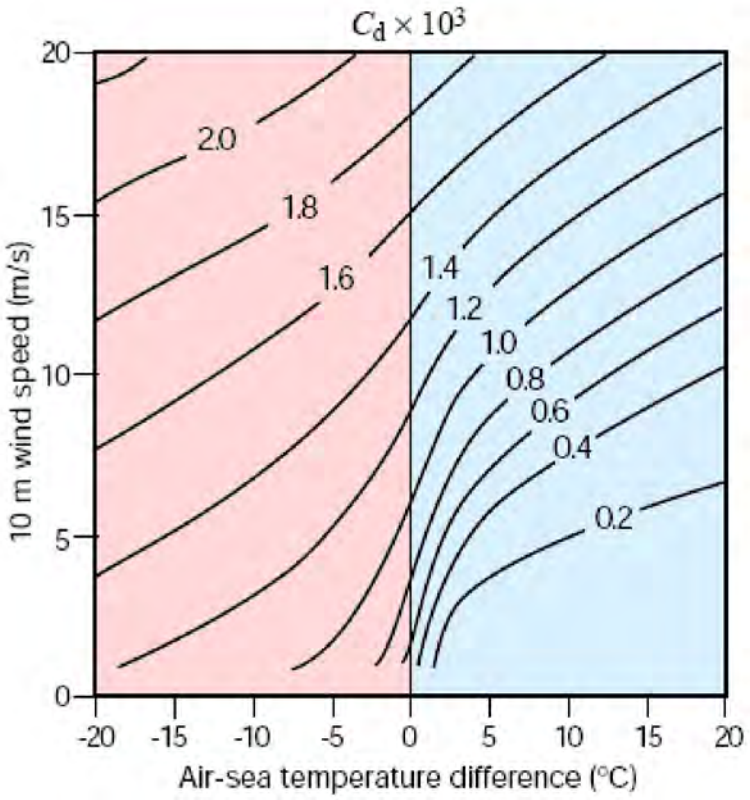

Figure 2.8. Drag coefficient (black contours) as a function of stability (air–sea temperature difference) and 10 m wind speed

Source: Derived from Schwab (1978)

boundary-layer stability length *L*, so that the wind profile of the constant flux layer including stability could be determined. Kara et al. (2008) and Bourassa et al. (1999) calculated the effects of stability on wind profiles as a function of the air–sea temperature difference (Figure 2.9).

For wave forecast models, it appears appropriate to express the input wind in terms of u_*. This is calculated taking stability into account. The wind is then expressed at some nominal height by applying the neutral logarithmic profile (Equation 2.2, given u_* with stability effect already taken into account and $\lambda = 0$). This wind is then called the equivalent neutral wind at that height (Liu and Tang, 1996; Verschell et al., 1999). This definition is, for example, used to derive 10 m equivalent neutral winds from satellite measurements.

Earlier, Geernaert and Katsaros (1986) defined equivalent neutral wind as the mean wind speed that would be observed if there was neutral atmospheric stratification. This definition has been used to calculate neutral drag coefficients and roughness lengths in air–sea interaction models.

If observed winds are given at heights above the constant flux layer (above 50 m), that is, well into the Ekman spiral, the above techniques should not be used. Instead, the more complicated two-regime (constant flux and Ekman) boundary layer needs to be considered.

Several approaches have been developed using the two-regime boundary-layer model, whereby the surface stress and its direction were determined using the free atmospheric parameters. However, analytic models (for example, Cardone, 1969, 1978; Krishna, 1981; Brown and Liu, 1982), as well as Rossby number similarity theory (Clarke and Hess, 1974; Stull, 1988), did not produce satisfactory solutions to the problem.

Today's NWP models (section 2.5) incorporate sophisticated parameterizations of the vertical turbulent transport processes and provide wind speed and direction at the 10 m level by standard.

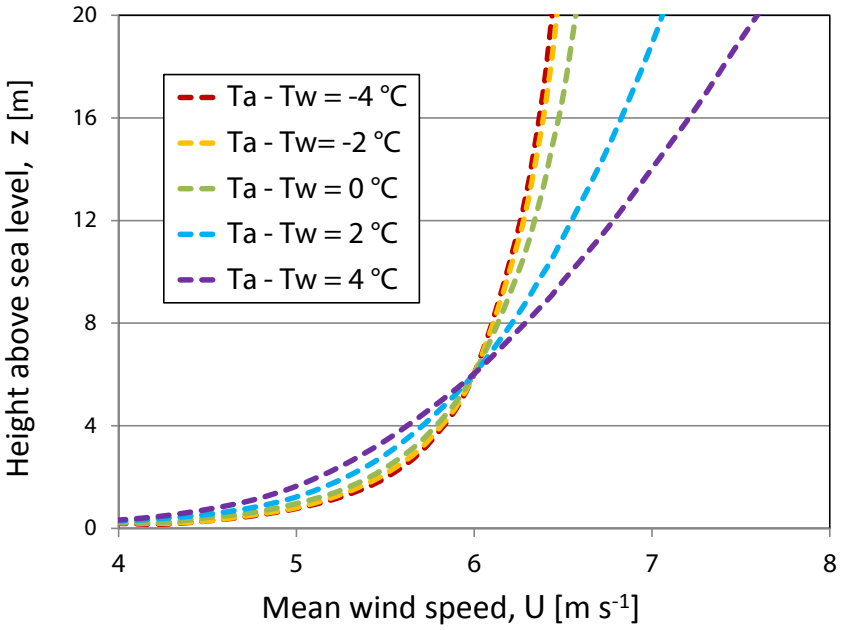

Figure 2.9. Example for wind profiles above sea level (Bourassa et al., 1999; Kara et al., 2008) for stable, neutral and unstable cases in terms of air–water temperature differences for a given wind speed $U = 6$ m s^{-1} at height $z = 6$ m and a given specific humidity difference $\Delta q = 3$ g kg^{-1} between the surface and that level. Stronger winds occur in the low levels in unstable conditions, while stronger winds occur aloft in stable conditions. Unstable conditions cause small differences in the vertical aloft. Profiles are based on Monin–Obukhov's similarity theory (see section 2.3.1) using a flux parameterization scheme for the stability function including the effects of capillary waves and sea state.

Advection is a basic physical process causing a modification of the vertical stratification. For example, stabilization occurs when warm air advection is increasing with height (or cold air advection is decreasing with height). Otherwise, advection of cold air increasing with height (or warm air advection decreasing with height) tends to destabilize the stratification.

Over ocean areas in the vicinity of large land masses, advection plays the dominant role in changing the physical properties of continental air. When air flows over the ocean, its temperature and its stability will be modified by the underlying sea surface. For example, the effect of a cold-air outbreak over warm water will be diminished by the slow increase of stability as the temperature difference between the air and water decreases. Figure 2.10 illustrates the modification of air temperature evaluated by a linear regression (Phillips, 1972; Phillips and Irbe, 1978).

2.4 LARGE-SCALE METEOROLOGICAL FACTORS AFFECTING OCEAN-SURFACE WINDS

This section addresses the circumstance that a forecaster may have to work from a surface weather analysis chart, because prognostic or diagnostic models for producing ocean-surface wind fields are not available or are outdated. Otherwise, if model forecasts are available, they may not have the resolution or physics to properly handle mesoscale features, including squall lines and eyewall features in hurricanes. Moreover, useful observational data may have been received by the forecaster following the generation of the model forecast.

In such cases, a forecaster can subjectively produce an ocean-surface wind chart based on the knowledge of a few principles of large-scale atmospheric motions and some knowledge of boundary-layer theory. In some forecast centres, it is still common practice to draw surface-pressure charts manually (Figure 2.11).

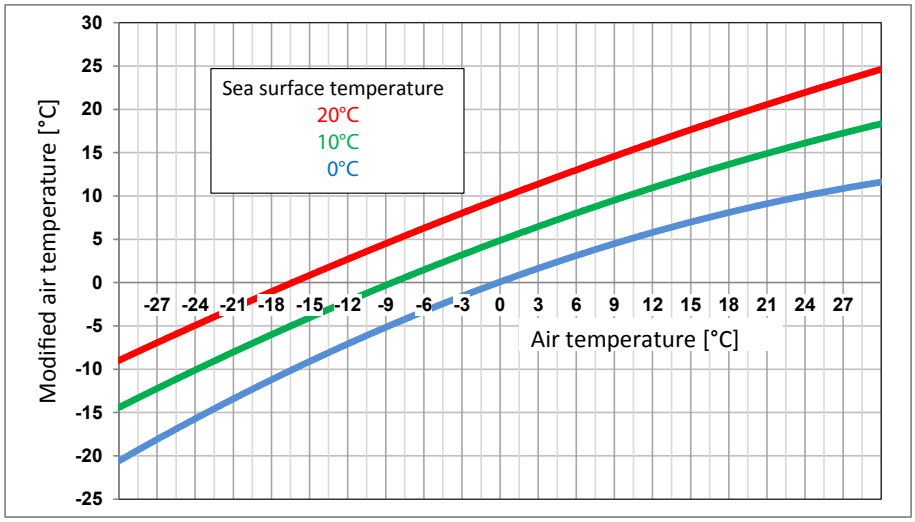

Figure 2.10. Modification of air temperature in 2 m over water after 120 min of advection. More than half of the total modification occurs within the first 10 min, while the major change in conditions takes place in the first metre above the surface. Regression equations were also developed for dewpoint modification. Although the results will occasionally be slightly different, the above diagram may also be used for dewpoint modification and will give an acceptable approximation.

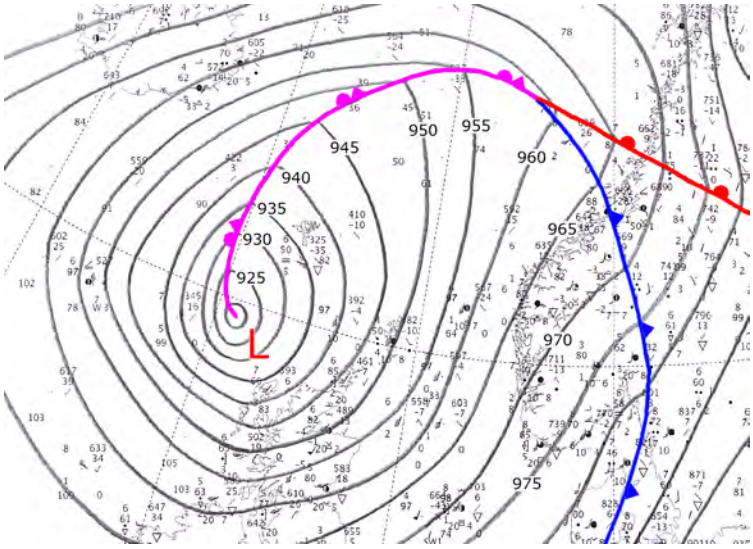

Figure 2.11. Surface analysis (cut-out) of severe storm *Dirk* north of Scotland on 24 December 2013 1800 Universal Time Coordinated (UTC) with a central pressure of 920 hPa (L = low-pressure centre)

Source: Marine Meteorological Service, Hamburg, Germany

2.4.1 Wind and pressure analyses

In middle and higher latitudes, the general approach is to start with a surface-pressure analysis. An isobaric pattern is drawn on a chart of pressure and wind observations. If satellite imagery or even scatterometer winds are available, the centres of pressure systems may be located on the chart (Figures 2.12 and 2.13). Isallobaric tendencies from ship observations will be helpful in the case of moving pressure systems. Attempts have been made to estimate the central pressure of mature low-pressure systems from the shape of their cloud patterns (Turner and Pendlebury,

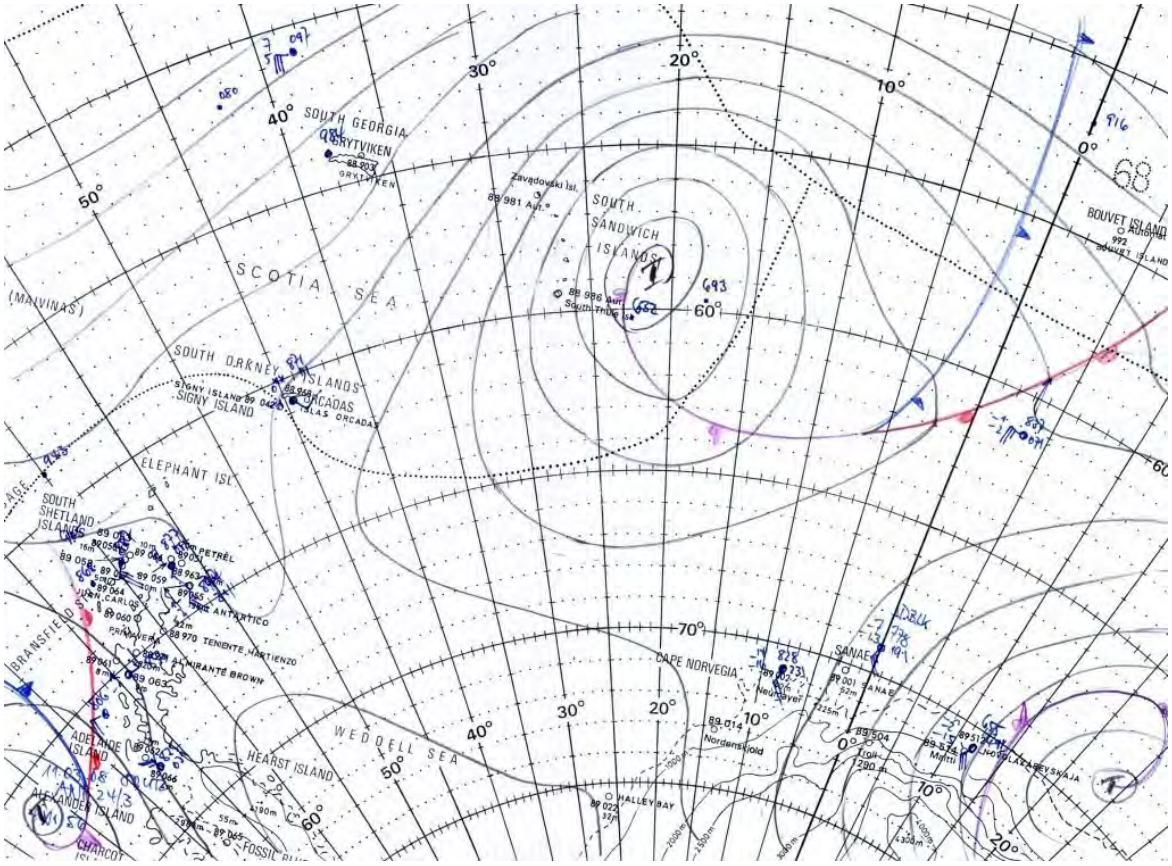

Figure 2.12. Surface analysis in the South Atlantic on 11 March 2008, 0000 UTC, analysed on board German research vessel *Polarstern*

Source: Marine Meteorological Service, Hamburg, Germany

2004). If a previous analysis is available, it may serve as a first guess. The observations of wind speed are used as a check on the pressure gradient, and those of wind direction on the orientation of the isobars.

Once a pressure analysis exists, the easiest way to obtain ocean-surface winds would be to:

- Calculate the geostrophic wind speed.
- Correct it for curvature to derive the gradient wind speed.
- Simulate the effect of friction by reducing this wind to approximately (for neutral stability) 75% and rotating the wind direction by approximately 15° (anti-clockwise in the northern hemisphere and clockwise in the southern hemisphere). In relation to the geostrophic wind, that is towards the region of lower pressure.

This approach may be satisfactory as a quick approximation of ocean-surface winds. However, there are several important factors that should be considered when particular meteorological situations are identified. Some important meteorological relationships that govern the speed and direction of ocean-surface winds are:

- Surface-pressure gradient – geostrophic wind;
- Curvature of isobars – gradient wind;
- Wind profiles in the boundary layer – surface friction effects;
- Vertical wind shear of the geostrophic wind – thermal wind;
- Rapidly changing pressure gradient in time – isallobaric wind;
- Rapidly changing pressure gradient downstream – diffluence and confluence;
- Discontinuity of pressure gradients at fronts – wind shear in frontal zones.

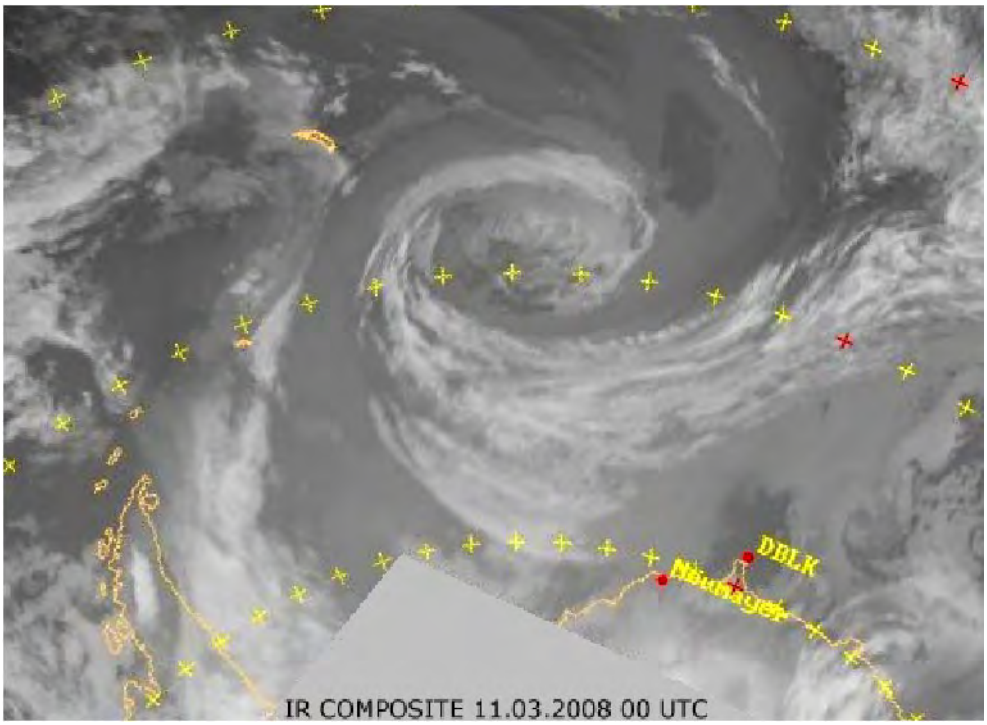

Figure 2.13. Infrared satellite composite image on 11 March 2008, 0000 UTC, corresponding to Figure 2.12 (surface analysis in the South Atlantic on 11 March 2008, 0000 UTC, analysed on board German research vessel *Polarstern*)

Source: Marine Meteorological Service, Hamburg, Germany

These relationships (discussed in the following sections) may be considered independently and then combined to give an estimate of the wind field. This approach is an oversimplification because each relationship yields a wind component that is derived from specific assumptions but then combined under general conditions to approximate the wind field.

2.4.2 Geostrophic wind

The primary driving force for atmospheric motions is the pressure gradient force. One of the most important balances in large-scale atmospheric motions is that between the Coriolis force and the pressure gradient force, with the resulting balanced motion called the geostrophic wind. This balance is generally valid:

- For large-scale flows;
- In the free atmosphere above the friction layer;
- Under steady-state conditions;
- With straight isobars.

The geostrophic flow is parallel to the isobars and is expressed by the following relationship:

$$\left(u_g, v_g\right) = \frac{1}{f\rho_a}\left(-\frac{\delta p}{\delta y}, \frac{\delta p}{\delta x}\right), \tag{2.9}$$

where p is the atmospheric pressure, f is the Coriolis parameter ($f = 2\Omega\sin\Theta$), ρ_a is the density of air, Ω is the angular speed of the Earth's rotation and Θ is the latitude. u_g and v_g are the geostrophic winds in the x (positive towards east) and y (positive towards north) directions, respectively.

Equation 2.9 shows that the wind blows in such a manner that, looking downwind, the high pressure is to the right and the low pressure is to the left in the northern hemisphere ($f > 0$) and

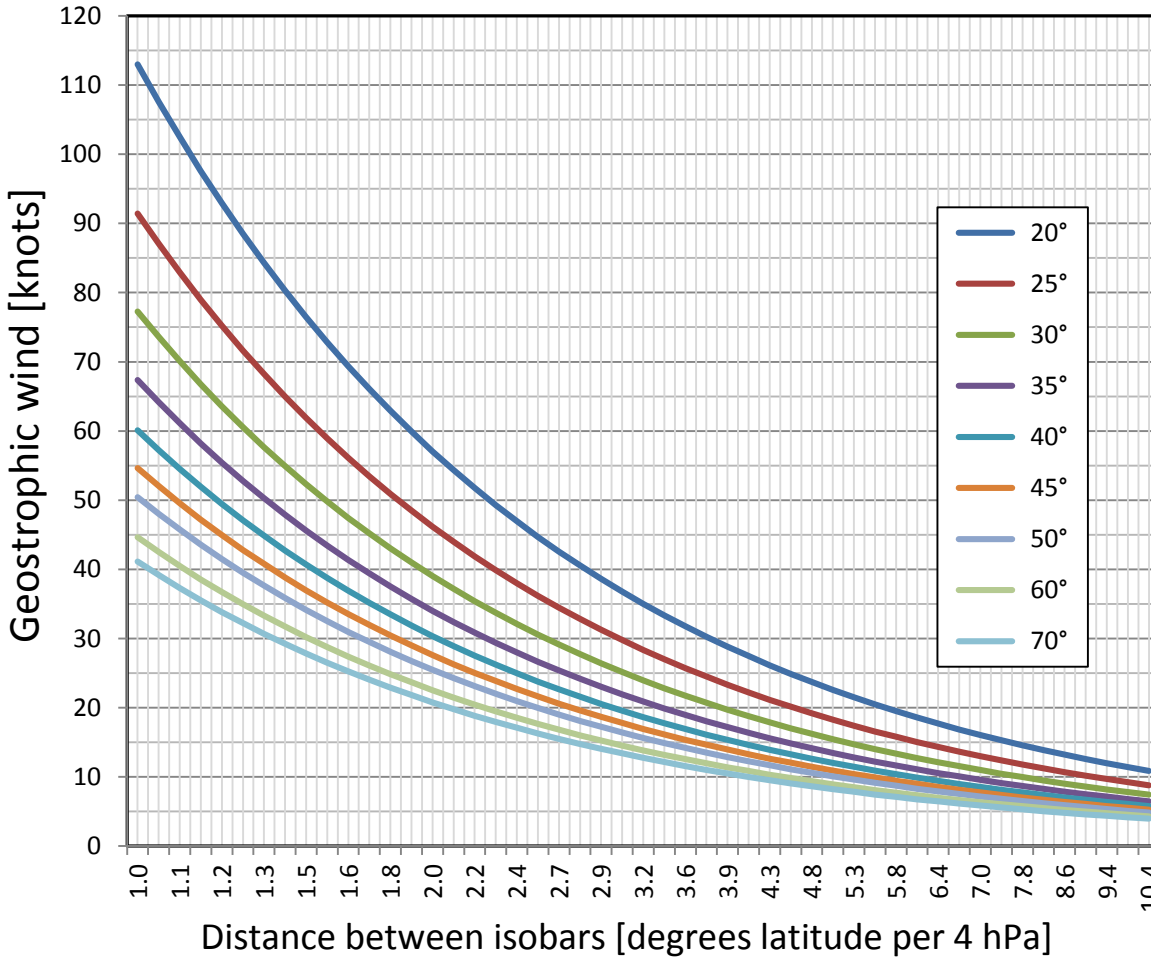

Figure 2.14. Geostrophic wind speed (knots) as a function of isobar spacing in degrees (4 hPa interval) and latitude; pressure 1 015.0 hPa; temperature 285 K; density 1.241 kg m^{-3} (see also Table 2.3)

vice versa in the southern hemisphere ($f < 0$). For a given pressure gradient, the geostrophic wind will increase with decreasing latitude and, in fact, goes to infinity at the Equator. The geostrophic wind relation is assumed to be invalid in low latitudes, between approximately 20°N and 20°S. Also, over the ocean, the density of air may range from 1.3 kg m^{-3} to 0.9 kg m^{-3} between cold high-pressure systems and warm low-pressure systems.[1] The geostrophic wind speed can be estimated from a pressure analysis using Figure 2.14.

Table 2.3. Geostrophic wind speed (knots) as a function of latitude and distance (degrees of latitude) for a 4 hPa change in pressure and constant air density of 1.241 kg m^{-3}, corresponding to 1 015.0 hPa and 285 K

Distance latitude (°)	*Latitude (°)*										
	20	*25*	*30*	*35*	*40*	*45*	*50*	*55*	*60*	*65*	*70*
1.0	113	91	77	67	60	55	50	47	45	43	41
1.1	103	83	70	61	55	50	46	43	41	39	37
1.2	94	76	64	56	50	46	42	39	37	36	34
1.3	87	70	59	52	46	42	39	36	34	33	32

[1] Extreme surface pressures and air temperatures have been assumed, neglecting the influence of the underlying sea surface temperature.

Distance latitude (°)	*Latitude (°)*										
	20	*25*	*30*	*35*	*40*	*45*	*50*	*55*	*60*	*65*	*70*
1.4	81	65	55	48	43	39	36	34	32	30	29
1.5	75	61	52	45	40	36	34	31	30	28	27
1.6	71	57	48	42	38	34	32	29	28	27	26
1.7	66	54	45	40	35	32	30	28	26	25	24
1.8	63	51	43	37	33	30	28	26	25	24	23
1.9	59	48	41	35	32	29	27	25	23	22	22
2.0	56	46	39	34	30	27	25	24	22	21	21
2.1	54	44	37	32	29	26	24	22	21	20	20
2.2	51	42	35	31	27	25	23	21	20	19	19
2.3	49	40	34	29	26	24	22	21	19	19	18
2.4	47	38	32	28	25	23	21	20	19	18	17
2.5	45	37	31	27	24	22	20	19	18	17	16
2.6	43	35	30	26	23	21	19	18	17	16	16
2.7	42	34	29	25	22	20	19	17	17	16	15
2.8	40	33	28	24	21	20	18	17	16	15	15
2.9	39	32	27	23	21	19	17	16	15	15	14
3.0	38	30	26	22	20	18	17	16	15	14	14
3.1	36	29	25	22	19	18	16	15	14	14	13
3.2	35	29	24	21	19	17	16	15	14	13	13
3.3	34	28	23	20	18	17	15	14	14	13	12
3.4	33	27	23	20	18	16	15	14	13	13	12
3.5	32	26	22	19	17	16	14	13	13	12	12
3.6	31	25	21	19	17	15	14	13	12	12	11
3.7	31	25	21	18	16	15	14	13	12	12	11
3.8	30	24	20	18	16	14	13	12	12	11	11
3.9	29	23	20	17	15	14	13	12	11	11	11
4.0	28	23	19	17	15	14	13	12	11	11	10
4.2	27	22	18	16	14	13	12	11	11	10	10
4.4	26	21	18	15	14	12	11	11	10	10	9
4.6	25	20	17	15	13	12	11	10	10	9	9
4.8	24	19	16	14	13	11	11	10	9	9	9
5.0	23	18	15	13	12	11	10	9	9	9	8
5.2	22	18	15	13	12	11	10	9	9	8	8
5.4	21	17	14	12	11	10	9	9	8	8	8
5.6	20	16	14	12	11	10	9	8	8	8	7
5.8	19	16	13	12	10	9	9	8	8	7	7
6.0	19	15	13	11	10	9	8	8	7	7	7

Distance latitude (°)	Latitude (°)										
	20	*25*	*30*	*35*	*40*	*45*	*50*	*55*	*60*	*65*	*70*
6.2	18	15	12	11	10	9	8	8	7	7	7
6.4	18	14	12	11	9	9	8	7	7	7	6
6.6	17	14	12	10	9	8	8	7	7	6	6
6.8	17	13	11	10	9	8	7	7	7	6	6
7.0	16	13	11	10	9	8	7	7	6	6	6
8.0	14	11	10	8	8	7	6	6	6	5	5
9.0	13	10	9	7	7	6	6	5	5	5	5
10.0	11	9	8	7	6	5	5	5	4	4	4

2.4.3 Gradient wind

Atmospheric flow patterns are generally not straight, but move along curved trajectories. This implies an additional acceleration along the radius of curvature, that is, the addition of a centripetal force to balance the flow. This balanced motion is known as the gradient wind. The gradient wind (*Gr*) is given by

$$Gr = \frac{fr}{2}\left[-1 \pm \sqrt{1 + \frac{4G}{fr}}\right], \tag{2.10}$$

where *f* is the Coriolis force, *G* is the geostrophic wind speed (which is used as a proxy for the pressure gradient as seen from Equation 2.9) and *r* is the radius of curvature of an isobar at the point of interest.

For a low-pressure system (cyclone), the circulation is in a counterclockwise direction in the northern hemisphere and a clockwise direction in the southern hemisphere. The sense of direction around a high-pressure system (anticyclone) is opposite to that of a cyclone in each of the hemispheres. The positive sign of the square root in Equation 2.10 describes the cyclonic case ($r > 0$); the negative sign describes the anticyclonic case ($r < 0$).

Around a low-pressure centre, the Coriolis and centrifugal forces act together to balance the pressure gradient force, compared with geostrophic flow where only the Coriolis force balances the pressure gradient. Consequently, the speed of the gradient wind around a cyclone is less than that of a geostrophic wind corresponding to the same pressure gradient. The balance of forces shows that for a high-pressure system, the Coriolis force is balanced by a pressure gradient and centrifugal forces acting together. Hence, the gradient flow around a high-pressure centre is larger (in magnitude) than the geostrophic flow corresponding to the same pressure gradient.

There is an upper limit to the anticyclonic gradient wind, which is obtained when the pressure gradient term reaches

$$\frac{1}{\rho_a}\frac{\delta p}{\delta r} = -\frac{rf^2}{4}. \tag{2.11}$$

When the pressure gradient reaches this value, the quantity in the square root in Equation 2.10 becomes zero, resulting in a maximum (in magnitude) gradient wind speed of

$$Gr = \left|\frac{fr}{2}\right|. \tag{2.12}$$

Using the geostrophic relation with Equation 2.11 and combining with Equation 2.12, the upper limit for the gradient wind speed for anticyclonic flow is twice the geostrophic wind speed,

$$Gr \leq 2G. \tag{2.13}$$

There is no such corresponding lower limit to the cyclonic gradient wind speed in relation to the pressure gradient. Figure 2.15 illustrates the relation between gradient wind speed and

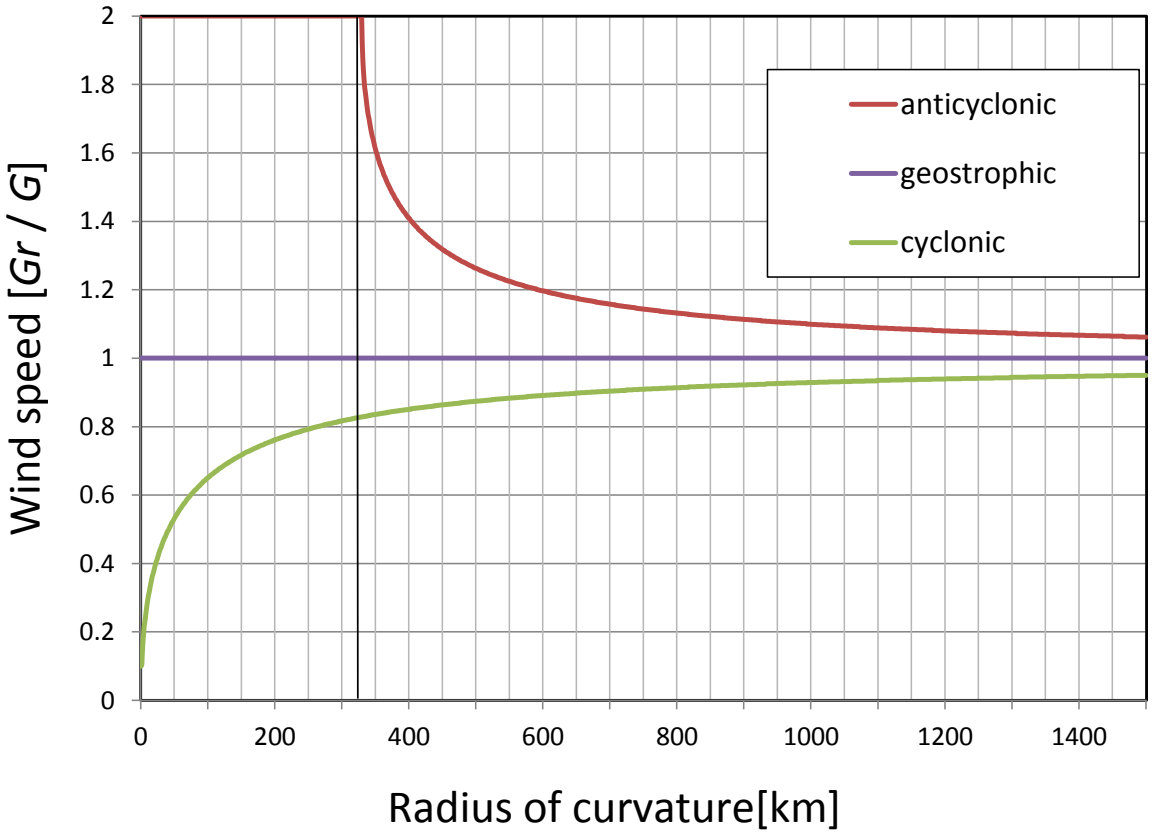

Figure 2.15. Ratio of gradient wind speed to geostrophic wind for anticyclonic and cyclonic flows at latitude 40°N. Geostrophic wind speed is 15 knots in this example. The black solid line marks the area of no winds around a pressure high. For numeric values of gradient wind, see Tables 2.4 and 2.5.

curvature. Numerical values can be taken from Tables 2.4 and 2.5 by measuring the radius of curvature of an isobar from a weather map and using the geostrophic wind speed determined from Equation 2.9. Figure 2.16 illustrates the balance diagrams for the simple frictionless flows reviewed above.

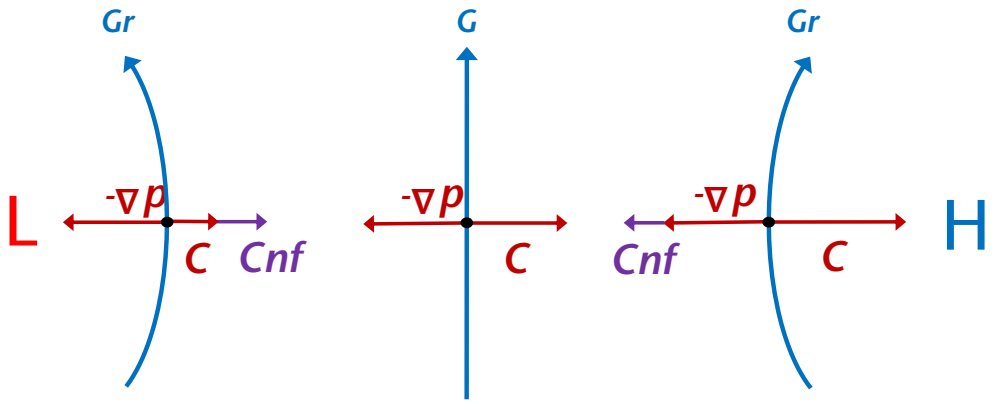

Figure 2.16. Balance of forces for basic types of frictionless flow (northern hemisphere) (*C* = Coriolis force, *Cnf* = centrifugal force, *G* = geostrophic wind, *Gr* = gradient wind, H = high-pressure centre, L = low-pressure centre and $-\nabla p$ = pressure gradient force)

Table 2.4. Gradient wind (anticyclonic flow): wind speeds (knots) are shown at latitude 40°N for given geostrophic wind speed (from Table 2.3) and radius of curvature (° latitude)

Radius of curvature (° latitude)	*Geostrophic wind speed (knots)*														
	5	*10*	*15*	*20*	*25*	*30*	*35*	*40*	*45*	*50*	*55*	*60*	*65*	*70*	*75*
25	5	10	15	21	26	32	38	44	50	56	63	70	77	84	92
24	5	10	15	21	26	32	38	44	50	57	63	70	77	85	93
23	5	10	16	21	27	32	38	44	50	57	64	71	78	86	94
22	5	10	16	21	27	32	38	44	51	57	64	71	79	87	95
21	5	10	16	21	27	32	38	45	51	58	65	72	80	88	97
20	5	10	16	21	27	33	39	45	52	58	66	73	81	90	99
19	5	10	16	21	27	33	39	45	52	59	67	74	83	92	102
18	5	10	16	21	27	33	39	46	53	60	68	76	85	95	106
17	5	10	16	21	27	33	40	46	53	61	69	77	87	98	110
16	5	10	16	21	27	33	40	47	54	62	70	80	90	102	118
15	5	10	16	22	27	34	40	47	55	63	72	82	94	109	135
14	5	10	16	22	28	34	41	48	56	65	75	86	101	126	
13	5	10	16	22	28	35	42	49	58	67	78	93	117		
12	5	10	16	22	28	35	42	51	60	70	84	108			
11	5	10	16	22	29	36	43	52	63	76	99				
10	5	11	16	23	29	37	45	55	68	90					
9	5	11	16	23	30	38	47	59	81						
8	5	11	17	23	31	40	51	72							
7	5	11	17	24	32	43	63								
6	5	11	18	25	35	54									
5	5	11	18	27	45										
4	5	12	20	36											
3	5	13	27												
2	6	18													
1	9														

Note: For any other latitude, Φ, the winds should be scaled by the ratio $f_{\Phi}/f_{40°}$, where f is the value of the Coriolis parameter.

2.4.4 **Surface friction effects**

As discussed in section 2.3, the effect of friction is to reduce the speed of the free air flow. As a result of the balance of forces, this will turn the direction of flow towards lower pressure, which is to the left in the northern hemisphere and to the right in the southern hemisphere. As the surface of the Earth is approached, the wind speed tends to zero, and the inflow angle tends to reach a maximum. The impact of surface friction decays to zero at the top of the atmospheric boundary layer. A simple balance between the pressure gradient and the Coriolis and frictional

Table 2.5. Gradient wind (cyclonic flow): wind speeds (knots) are shown at latitude 40°N for given geostrophic wind speed (from Table 2.3) and radius of curvature (° latitude)

Radius of curvature (° latitude)	*Geostrophic wind speed (knots)*														
	5	*10*	*15*	*20*	*25*	*30*	*35*	*40*	*45*	*50*	*55*	*60*	*65*	*70*	*75*
25	5	10	15	19	24	28	33	37	42	46	50	54	58	62	66
24	5	10	15	19	24	28	33	37	41	46	50	54	58	62	66
23	5	10	15	19	24	28	33	37	41	46	50	54	58	62	66
22	5	10	15	19	24	28	33	37	41	45	49	54	58	62	65
21	5	10	15	19	24	28	33	37	41	45	49	53	57	61	65
20	5	10	14	19	24	28	32	37	41	45	49	53	57	61	65
19	5	10	14	19	24	28	32	37	41	45	49	53	57	60	64
18	5	10	14	19	23	28	32	36	40	45	49	52	56	60	64
17	5	10	14	19	23	28	32	36	40	44	48	52	56	60	63
16	5	10	14	19	23	28	32	36	40	44	48	52	55	59	63
15	5	10	14	19	23	28	32	36	40	44	48	51	55	59	62
14	5	10	14	19	23	27	31	36	39	43	47	51	55	58	62
13	5	10	14	19	23	27	31	35	39	43	47	50	54	57	61
12	5	10	14	19	23	27	31	35	39	43	46	50	53	57	60
11	5	10	14	18	23	27	31	35	38	42	46	49	53	56	59
10	5	10	14	18	22	27	30	34	38	41	45	48	52	55	58
9	5	10	14	18	22	26	30	34	37	41	44	48	51	54	57
8	5	9	14	18	22	26	30	33	37	40	43	47	50	53	56
7	5	9	14	18	22	25	29	33	36	39	42	45	48	51	54
6	5	9	13	17	21	25	28	32	35	38	41	44	47	50	52
5	5	9	13	17	21	24	28	31	34	37	40	42	45	48	50
4	5	9	13	17	20	23	26	29	32	35	38	40	43	45	47
3	5	9	12	16	19	22	25	28	30	33	35	37	39	42	44
2	4	8	12	15	17	20	22	25	27	29	31	33	35	37	38
1	4	7	10	12	15	17	18	20	22	23	25	26	28	29	30

Note: For any other latitude, Φ, the winds should be scaled by the ratio $f_{\Phi}/f_{40°}$, where f is the value of the Coriolis parameter.

forces (Figure 2.17) describes this effect through the well-known Ekman spiral, which predicts a 45° angle of turning at the surface. In nature, this angle is too large, and predicted speeds near the surface are too low.

To represent the effects of friction in a more realistic manner, several approaches have been developed that relate the free atmospheric wind to a stress at the ocean surface. These often use the concept of a two-regime boundary layer; a constant flux layer at the surface and the Ekman layer above. Observations fit much better with this representation of the planetary boundary layer, with a turning angle of 10°–15° predicted over the ocean for a neutrally stable atmosphere in contact with the ocean.

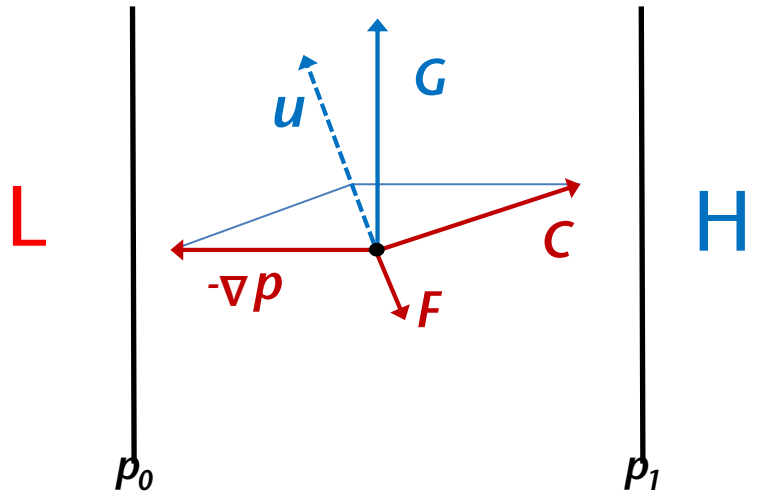

Figure 2.17. Balances of friction, pressure gradient and Coriolis forces (northern hemisphere) (*C* = Coriolis force, *F* = friction, *G* = geostrophic wind, H = high-pressure centre, L = low-pressure centre, $-\nabla p$ = pressure gradient force and *u* = surface wind; p_0 and p_1 represent isobars)

2.4.5 Thermal wind

So far, the sea-level pressure field has been considered constant from the ocean surface to the top of the boundary layer. However, if there are non-zero horizontal temperature gradients at the surface, it can be shown through the thermal wind equation that the pressure gradient will change with height. This results from the well-known fact that the vertical distance between two pressure levels is proportional to the mean temperature of that layer. Therefore, the geostrophic wind at the top of the boundary layer may differ from that at the surface. The vertical shear of the geostrophic wind is given by

$$\left(\frac{\delta u_g}{\delta z}, \frac{\delta v_g}{\delta z}\right) = \frac{g}{T}\left(-\frac{\delta T}{\delta y}, \frac{\delta T}{\delta x}\right). \qquad (2.14)$$

In the southern hemisphere, the left-hand side of the equation needs to be multiplied by –1. It is clear from Equation 2.14 that the geostrophic wind increases with height if higher pressure coincides with higher temperatures (as in the case of mid-latitude westerlies) and decreases with height if higher pressure coincides with lower temperatures. Furthermore, if the geostrophic wind at any level is blowing towards higher temperatures (cold advection), the wind turns to the left (backing) as the height increases and the reverse happens (veering) if the geostrophic wind blows towards lower temperatures (warm advection).

The vector difference in the geostrophic wind at two different levels is called the "thermal wind". It can be shown geometrically that the thermal wind vector represents a flow such that high temperatures are located to the right and low temperatures to the left. The thermal wind, through linear vertical wind shear, can be incorporated directly into the solution of the Ekman layer, and thus incorporated in the diagnostic models described in more detail below.

The effects of friction on the geostrophic flow in the Ekman layer are further influenced by the thermal wind discussed above. Studies have shown the importance of the thermal wind in explaining deviations from the typical Ekman spiral (Mendenhall, 1967). A result of the thermal wind influence is larger surface cross-isobaric (inflow) flow angles during cold advection and smaller inflow angles during warm advection, as described above. An illustration of the effect of thermal wind on the wind in the Ekman layer is shown for a low-pressure system in Figure 2.18.

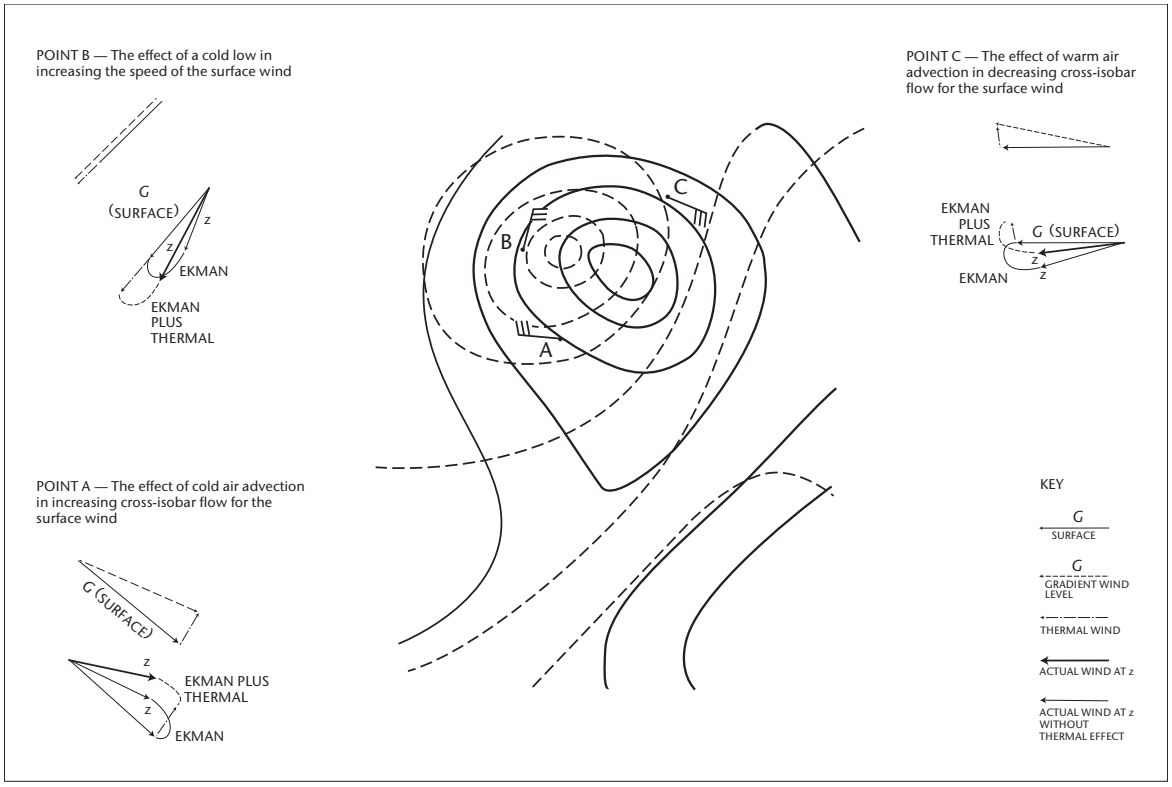

Figure 2.18. Thermal wind: sketch of surface winds, surface isobars (solid contours) and a constant pressure surface (dashed contours) for an extratropical cyclone

Source: Pierson (1979)

2.4.6 **Isallobaric wind**

In the above discussions, the wind systems have been considered to be evolving slowly in time. However, when a pressure system is deepening (or weakening) rapidly, or moving rapidly, so that the local geostrophic wind is changing rapidly, an additional wind component becomes important. This is obtained through the isallobaric wind relation. An isallobar is a line of equal pressure tendency (time rate of change of pressure). The strength of the isallobaric wind is proportional to the isallobaric gradient, and its direction is perpendicular to the gradient – away from centres of rises in pressure and towards centres of falls in pressure. Normally, this component is less than 5 knots (2.5 m s^{-1}), but can become greater than 10 knots (5 m s^{-1}) during periods of rapid or explosive cyclogenesis.

The isallobaric wind component is given by

$$(u_i, v_i) = -\frac{1}{\rho_a f^2}\left[\frac{\delta\left(\frac{\delta p}{\delta t}\right)}{\delta x}, \frac{\delta\left(\frac{\delta p}{\delta t}\right)}{\delta y}\right]. \qquad (2.15)$$

Figure 2.19 illustrates the modification of the geostrophic wind field around a moving low-pressure system.

2.4.7 **Diffluence of wind fields**

Diffluence (confluence) of isobars also creates flows that make the winds deviate from a geostrophic balance. When a diffluence of isobars occurs (isobars spread apart), the pressure gradient becomes weaker than its upstream value, so that as an air parcel moves downstream, the pressure gradient is unbalanced by the Coriolis force associated with the flow speed. This results in the flow being deflected towards high pressure in an effort to restore the balance of

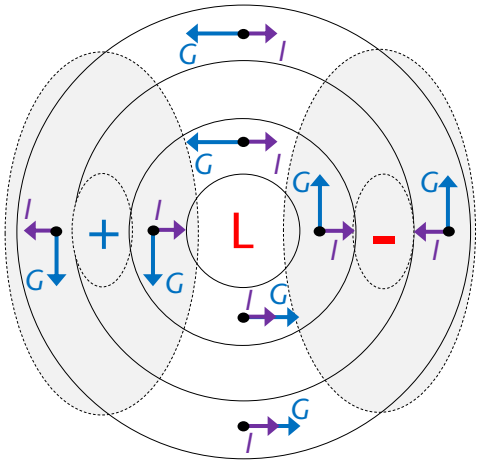

Figure 2.19. Example of the isallobaric wind field of a moving low-pressure system. Solid line = isobar, dashed line = isallobar, $G = (u_g, v_g)$ = geostrophic wind, H = high-pressure centre, L = low-pressure centre and $I = (u_i, v_i)$ = isallobaric wind, which is always directed towards areas of pressure decrease. This results in a wind decrease/increase north/south of the depression. Wind direction is affected in the front and rear of the system.

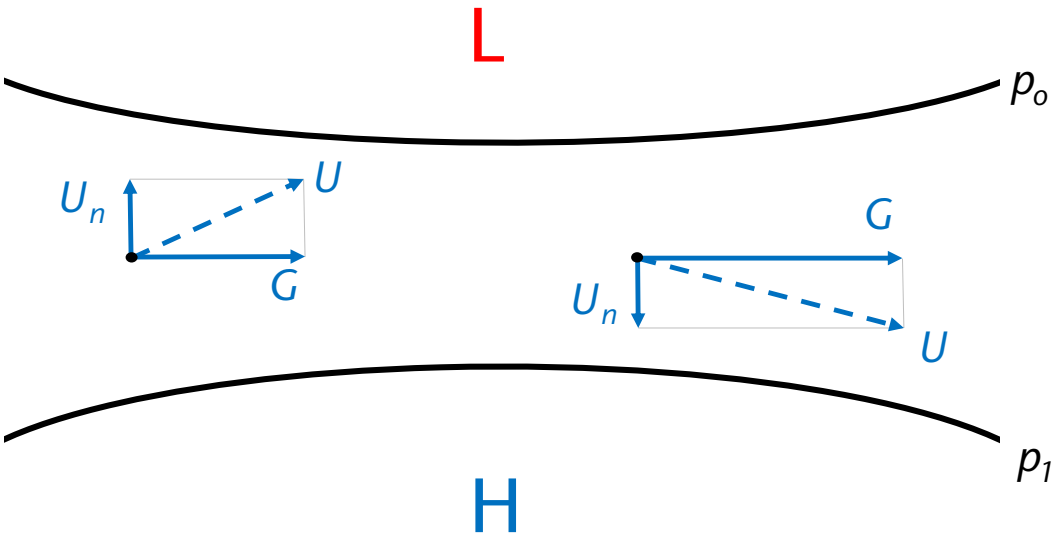

Figure 2.20. Examples of confluent/diffluent wind fields (p_0 and p_1 are isobars, U_n is the non-geostrophic wind component, G and U are the geostrophic and surface winds, H = high-pressure centre and L = low-pressure centre)

forces through an increase in the pressure gradient force. In the case of converging isobars, the pressure gradient increases from its upstream value. Hence, the pressure gradient force becomes larger than the Coriolis force, and the flow turns towards low pressure in an effort to decrease the pressure gradient force. In either case, a non-geostrophic component normal to the geostrophic flow develops with a magnitude $U_n = (G/f)\, dG/ds$ (Haltiner and Martin, 1957), where G is the geostrophic speed, f is the Coriolis parameter and s is the vector in the direction of the geostrophic flow.

In reality, as surface friction turns the flow towards low pressure, confluence will increase the inflow angle over the effect of friction alone, and diffluence will decrease the inflow angle, with the result that flow towards high pressure will seldom exist. Figure 2.20 illustrates the modification to the geostrophic wind due diffluence and confluence effects.

2.4.8 Wind shear in frontal zones

Front lines on surface weather charts (Figures 2.11 and 2.12) represent the boundaries between air masses of different temperature. The dynamics of fronts is closely related to the development of extratropical low-pressure systems (Bjerknes and Solberg, 1922). Fronts actually consist of narrow transition zones where a mixing of air masses occurs. A discontinuity of parameters at the frontal planes that extend high into the atmosphere can be assumed for simplicity. In a state of equilibrium, potentially warmer air is generally located over the colder air such that the frontal zone is tilted in the vertical. As the vertical decrease of pressure is less in warm air than in cold air, the pressure gradient and the geostrophic wind will change discontinuously at the front. The sudden wind shifts at fronts are often associated with confused or crossing seas.

The relationship between the vertical tilt α of the front, the horizontal temperature difference $T' - T$ and the horizontal shear of geostrophic wind components $V'_g - V_g$ parallel to the front was first derived by Margules (1906):

$$\tan\alpha = \frac{f\bar{T}}{g}\frac{V'_g - V_g}{T' - T}, \tag{2.16}$$

where f denotes the Coriolis parameter, $\bar{T}$ the mean temperature and g the acceleration due to gravity. It is obvious that a large wind shear will be found at a steep front between air masses of large temperature difference. This is a typical phenomenon at cold fronts. Figure 2.21 shows cross-sections of warm and cold fronts schematically. The structure of frontal systems can be complex and shows a large variety. In the mature state of a cyclone, a cold front generally moves faster than the warm front ahead. Successively, the warm sector between the fronts gets narrower and, finally, an occlusion is formed in which warm air is lifted by the underlying cold air masses.

The propagation of a front and the associated vertical circulation processes will act to modify the discontinuities of the surface pressure and wind distribution near the front line. An experienced forecaster will therefore start their surface-pressure analysis by carefully identifying air masses to locate surface front lines. In the analysis of the pressure field, the forecaster will construct isobars with sharp bends at the front lines depending on the dynamics of the synoptic system (Figure 2.11).

Furthermore, when warm (cold) air is being advected over relatively cold (warm) water, changes in stratification must be considered (see section 2.3.3). For example, after the passage of a warm front, stabilization will typically decrease surface wind speed relative to the geostrophic wind. Otherwise, cold air over warm water will destabilize the boundary layer and thus increase mean wind and gustiness.

2.4.9 Streamline analyses in the tropics

It is not possible to determine the wind field directly from the pressure analyses in the tropics. This is because the geostrophic relationship is weaker in the lower latitudes and breaks down completely at the Equator. Also, errors in pressure measurements can become significant compared with the often weak pressure gradients that are to be analysed. Direct analysis of the wind in the form of streamlines and isotachs gives a useful depiction of the low-level wind field.

The procedure for streamline analysis is similar to pressure analysis in that all weather systems have consistency over time and they need to be located and tracked from chart to chart. Each system should be followed from genesis, through maturity and to decay, and its movement tracked. Knowledge of conceptual models of weather systems is required to carry this out so that streamlines and isotachs can be better analysed where there are few observations. It is particularly important for an analyst to monitor the evolution of subtropical anticyclones, as sudden increases in intensity can result in surges of wind penetrating well into the tropics, with resultant increases in wave and swell height. A useful reference for analysis in the tropics is the *Forecasters Guide to Tropical Meteorology* (Air Weather Service, 1995).

2.4.10 Tropical cyclone analysis

Tropical cyclones (TCs) have their origin over the warm water areas of the tropical and subtropical oceans. In their extreme stages of development (hurricanes), TCs are one of the most hazardous phenomena at sea. A sea-surface temperature of 27°C is a well-known empirical lower threshold for the formation of a TC. Evaporation from a warm water surface usually initiates the formation of cumulus clouds. If the upper level atmospheric stratification is potentially unstable, the release of latent heat caused by condensating water vapour will further intensify the upward motion within the clouds and eventually may lead to high reaching (deep) and thundery convection.

Additionally, the basic mechanism for the formation of TCs, known as conditional instability of the second kind (CISK), involves the presence of an incipient large-scale cyclonic vortex. Such weak tropical depressions are characterized by a small Coriolis parameter but strong convergence in the lower levels, which maintains the supply of moisture into the vortex. In turn, the upper level latent heat release will intensify convection and also the vortex. This CISK was first described by Charney and Elliasen (1964). The theory has been discussed and advanced by many others (for example, Smith, 1997).

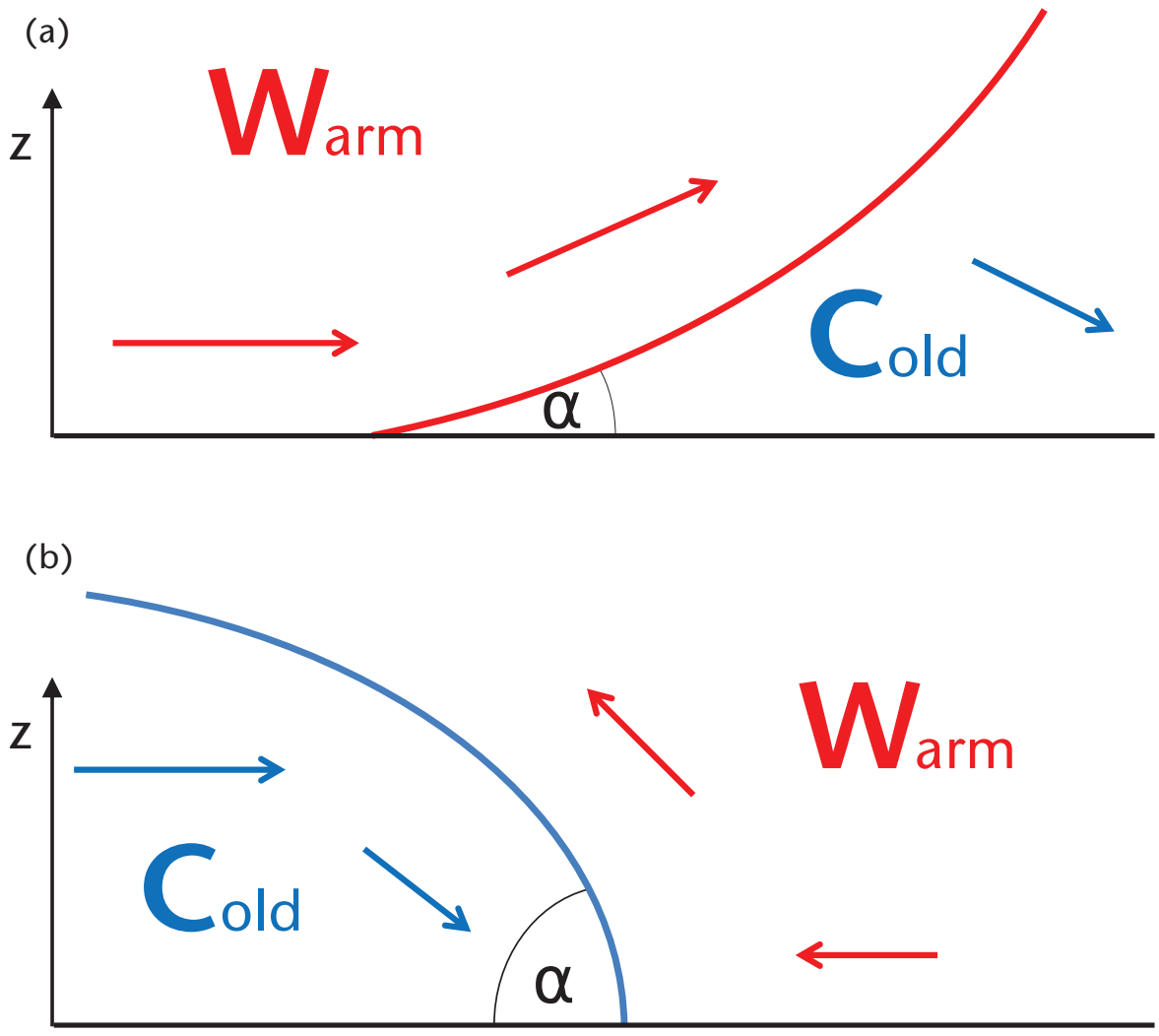

Figure 2.21. Schematic vertical cross-section. (a) At a warm front, warm air is gliding over colder air under a small angle. This results in stabilization of the vertical stratification. (b) At a cold front, cold air is lifting the warm air. This results in a vertically steeper frontal zone and a destabilization of the vertical stratification, often enhanced by the condensation of water vapour in upper levels.

As the Coriolis force vanishes at the Equator, TCs have not been observed in the belt between 5°S and 5°N. Track and intensity of TCs are strongly affected by the distribution of sea-surface temperatures. Therefore, TCs travel westward slowly (different from mid-latitude cyclones) until they change course to north-west to north (in the northern hemisphere) or south-west to south (in the southern hemisphere), or eventually fall into land. A TC climatology for the Atlantic Ocean and eastern Pacific Ocean is available at the National Hurricane Center.

Table 2.6. Classification and nomenclature of TCs in terms of maximum sustained (10 min) winds. The Saffir–Simpson scale classifies hurricane winds beyond the maximum Beaufort scale.

Classification of TCs	*Maximum sustained winds*
Tropical depressions	≤33 knots
Tropical storms	34–63 knots
Hurricanes ("typhoons" in the Western North Pacific, "cyclones" in the Indian Ocean and South Pacific)	≥64 knots (categories 1 and 2 on the Saffir–Simpson scale)
Major hurricanes	≥96 knots (categories 3–5 on the Saffir–Simpson scale)

As surface observations of TCs are rare, Dvorak (1975, 1984) developed a practical method to analyse TCs from geostationary satellite imagery. Many weather centres have used Dvorak's method for decades to operationally analyse and monitor TCs.

Dvorak classified the intensity of TCs by detailed analyses of cloud patterns and their relation to kinematic and thermodynamic properties (see Table 2.6). The current intensity (CI) number is therefore directly related to maximum sustained wind speed and central pressure as shown in Table 2.7. Velden et al. (2006) gave a review of the technique.

Dvorak (1984) determined the relationship between CI number and TC intensity differently in the North-western Pacific (typhoons) and Atlantic (hurricanes). A different classification was proposed by Koba et al. (1990) using Japan Meteorological Agency (JMA) best track data and aeroplane reconnaissance data between 1981 and 1986. The maximum wind speeds (MWSs) of Koba et al. tended to be weaker than those of Dvorak. This is partly because Koba et al. defined MWS as a 10 min sustained wind (WMO standard), while Dvorak defined MWS as a 1 min sustained wind (common in the United States of America).

As Dvorak's technique is a subjective analysis of TC intensity, it depends on the experience of the analyst. Objective Dvorak techniques have also been developed and used operationally (Velden et al., 2006; Kishimoto et al., 2013). In addition, microwave sensors of orbital satellites can directly observe surface wind and details of the TC structure such as a warm core. Such data have become a powerful tool for recent TC intensity analysis (Tang and Sui, 2014; Oyama et al., 2016). However, orbital satellites observe an area around their path only, and do not always catch a TC. Therefore, Dvorak's technique is still useful for operational analysis, because it makes use of geostationary satellite images that cover a wide range and is available at any analysis time.

The wind field of a strong TC vortex is basically governed by the gradient wind relation of Equation 2.10. Several attempts have been made to derive the sea-level pressure field inside the vortex from Dvorak's TC intensity:

$$\begin{cases} p(r) = p_\infty - \dfrac{p_\infty - p_c}{\sqrt{1 + (r / r_0)^2}} & \text{(Fujita, 1952),} \\ p(r) = p_c - (p_\infty - p_c) \cdot \exp(-r / r_0) & \text{(Schloemer, 1954),} \\ \text{and} \\ p(r) = p_c - (p_\infty - p_c) \cdot \exp\left(-(r / r_0)^B\right) & \text{(Holland, 1980),} \end{cases} \tag{2.17}$$

Table 2.7. Relationship between the CI number, the minimum sea-level pressure (MSLP) and the maximum sustained 10 min wind speed (MWS), determined by Dvorak (1984) (MWS: 1 min sustained wind) and Koba et al. (1990)

CI number	*North-western Pacific*				*Atlantic*	
	Koba et al. (1990)		*Dvorak (1984)*		*Dvorak (1984)*	
	MWS (knots)	*MSLP (hPa)*	*MWS (knots)*	*MSLP (hPa)*	*MWS (knots)*	*MSLP (hPa)*
1	22	1 005	25	–	25	–
1.5	29	1 002	25	–	25	–
2	36	998	30	1 000	30	1 009
2.5	43	993	35	997	35	1 005
3	50	987	45	991	45	1 000
3.5	57	981	55	984	55	994
4	64	973	65	976	65	987
4.5	71	965	77	966	77	979
5	78	956	90	954	90	970
5.5	85	947	102	941	102	960
6	93	937	115	927	115	948
6.5	100	926	127	914	127	935
7	107	914	140	898	140	921
7.5	115	901	155	879	155	906
8	122	888	170	858	170	890

where r is the distance from a TC centre, and p_c and p_∞ represent central pressure and environmental pressure, respectively. The radius r_0 of maximum wind defines the horizontal diameter of the TC.

The formula of Fujita (1952) is based on typhoons of the North-western Pacific Ocean, while Schloemer (1954) analysed North Atlantic hurricanes. The additional parameter B introduced by Holland (1980) ranges between 1 (Schloemer's formula) and 2.5, taking into account regional characteristics. However, the asymmetry of observed cyclonic wind fields caused by the movement and environmental conditions around the TC cannot be represented by these simple formulae. Asymmetric components have to be added to consider those factors to some degree (Yoshizumi, 1968; Konishi, 1995).

2.5 NUMERICAL WEATHER PREDICTION

The physical processes that determine the ocean-surface wind field are described by the basic non-linear equations of motion and thermodynamics, which can be solved using numerical methods on high-performance computers. This approach, known as NWP, was pioneered originally by Richardson (1922). See Haltiner and Williams (1980) for a description of the basic principles.

The first operational NWP models date back to the 1960s when model physics was restricted to the dynamics of barotropic and quasi-geostrophic atmospheric flows. These models were capable of simulating just the vertically integrated winds in the mid-latitudes. The availability of 1 d forecasts of the long-wave structures in the upper troposphere enabled meteorologists to estimate the track of the embedded surface-pressure systems. However, a challenge remained in deriving the corresponding temperature and wind fields.

With the introduction of baroclinicity, prognostic humidity, boundary-layer parameterizations and so forth, NWP became increasingly sophisticated in the following decades. Simultaneously, the explosive progress in computer technology enabled new physics parameterizations and

horizontal and vertical resolution increases to be applied to models, leading to significant improvements in NWP. Advanced data assimilation techniques are applied today to obtain a physically self-consistent three-dimensional initial state (analysis) of the entire troposphere and most of the stratosphere, which is based on multiple observational datasets.

Various global and limited-area NWP models are used worldwide. The models differ in the way they handle a multitude of physical processes, like the condensation of raindrops, the absorption and scattering of solar radiation, and the heat and momentum fluxes in the atmospheric boundary layer. Distinctions among forecast systems also consist of the amount and type of data involved in the assimilation process. The development of new model generations is still rapidly ongoing. Therefore, the following sections briefly cover some basics and the main developments of today's NWP.

2.5.1 Grid-point models

Richardson's first numerical experiment failed because the stability of numerical methods had not yet been explored. When solving partial-differential equations on a discrete grid, the distance between the grid points determines the maximum time step to be chosen for any kind of physically realistic advection from one point to another. To avoid numerical instability, the time step must satisfy the Courant–Friedrichs–Lewy condition (Courant et al., 1928). This implies that for a global model, a small time step and extremely large computer time would be required on a regular latitude–longitude grid due to the convergence of meridians towards the poles. Therefore, many of today's global grid-point models make use of grid architectures with a quasi-isotropic horizontal resolution on the sphere, which can be realized for example with an icosahedral grid (Figure 2.22). Advanced grids may have variable resolution in space and time. Running a numerical wave model on the same grid offers the possibility of a direct two-way coupling without interpolation of wind fields.

Figure 2.22. Schematic depiction of an icosahedral grid with regional refinement over Europe as implemented at the German Meteorological Service (Deutscher Wetterdienst)

2.5.2 Spectral models

Expanding the dynamic equations in terms of spherical harmonics is the classical approach for avoiding numerical instability of the type described above. Spectral models calculate the linear propagation of momentum, temperature and moisture fields in wave-number space and provide a much better approximation of spatial derivatives. However, at each time step, a transform into grid space is necessary to evaluate the non-linear advection terms, the grid-scale physical processes and the forcing of a wave model. As computational costs of the forward and backward transforms increase rapidly with resolution, the spectral method is not as efficient as an equivalent grid-point model. Today's spectral models therefore require an increasing amount of computer power to compensate for this handicap. But, supercomputer architecture has shifted from vector processing to parallel processing, thereby increasing the efficiency of grid-point models.

2.5.3 Limited-area models

Parallel to the progress of NWP, many non-hydrostatic limited-area models have been developed to study the mesoscale structures of atmospheric flow. The Mesoscale Meteorology Model 5 (MM5), maintained by Penn State University and the National Center for Atmospheric Research in the United States of America, was the first freely available model for the scientific community. In 2008, MM5 was replaced by the Weather Research & Forecasting Model (WRF), which was designed to serve atmospheric research and operational forecasting needs over a wide range of spatial scales. For example, WRF is run twice daily within the Antarctic Mesoscale Prediction System (AMPS) (Figure 2.23). Many national weather services run limited-area models as a link in operational forecast chains, for example, HIRLAM, ALADIN or COSMO, which all developed from research cooperation of European meteorological institutes and national weather services.

When limited-area models are applied to weather forecasting, boundary values must be provided by a model of larger scale. Many weather forecast centres run limited-area models in combination with a global model. Global models with regional or even movable grid refinements are now state of the art.

2.5.4 Boundary-layer parameterization

Today's NWP models include complex parameterizations of the two-regime boundary layer. In the surface layer – typically extending from the surface to the lowest model level (ranging from 10 to 40 m among models) – turbulent transfer of momentum, temperature and moisture is parameterized on the basis of the Monin–Obukhov similarity theory as described in section 2.3.1.

In the "outer" layer above the surface layer, subgrid-scale turbulent fluxes are described using prognostic mean variables through vertical diffusion equations (see Equation 2.1).

However, the parameterizations used in NWP differ in the way diffusivity is expressed as a function of the mean flow. In first-order-closure parameterizations, the mixing coefficient K_C is commonly expressed as a function of wind shear and Richardson number (Louis, 1979). Thus, no additional prognostic equations are needed to describe the influence of turbulence on mean variables.

In the one-and-a-half-order closure, K_C is expressed as a function of the mixing length and the turbulent kinetic energy. Closure schemes used in NWP differ in the definition of these variables depending on the vertical stratification within the boundary layer. A hierarchy of turbulence closure models was discussed by Mellor and Yamada (1974). Special attention is paid in these schemes to modelling the depth of shallow convection.

Stull (1988) gave an overview of turbulence closure schemes. Holt and Raman (1988), Garrat (1994) and Hurley (1997) reviewed first- and higher-order-closure schemes. Hu et al. (2010) and Shin and Hong (2011) compared different boundary-layer parameterizations using the WRF model with case studies.

2.5.5 **Coupled models**

Wave models are conventionally driven by 10 m winds taken from the output of an atmospheric model. As the wind cannot "feel" the waves in the wave model, assumptions need to be made of how wind increases the surface roughness of the sea, which, in turn, reduces the 10 m wind speed. However, the parameterization of the marine boundary layer discussed in section 2.3 does not consider the duration and fetch laws (see section 4.2) of wind-wave growth. A direct two-way coupling of atmospheric and wave models can overcome this deficiency by modifying the common parameterization.

The European Centre for Medium-Range Weather Forecasts (ECMWF) has run a coupled atmosphere–ocean wave forecasting system operationally since 1998. The two-way-interaction has significantly improved atmospheric forecast scores (Janssen, 2004; Chen et al., 2013). An even higher degree of accuracy – at the cost of higher complexity – is achieved with the coupling of atmosphere, waves and ocean currents (for example, Liu et al., 2011; Janssen et al., 2013).

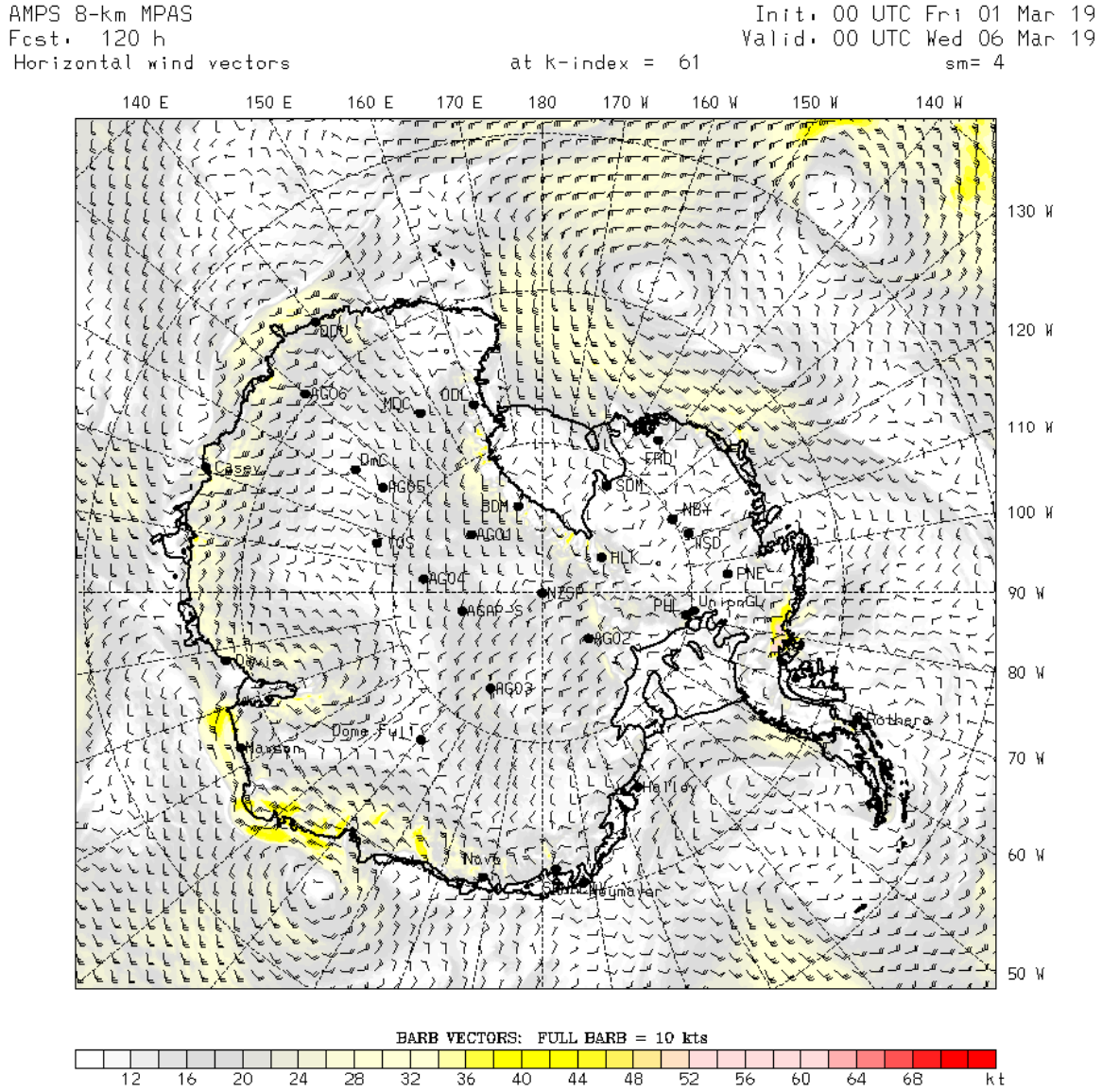

Figure 2.23. Five-day wind forecast of 1 March 2019

Source: Interactively created at the AMPS website; courtesy of Antarctic Mesoscale Prediction System (AMPS) / University Corporation for Atmospheric Research (UCAR)

2.5.6 Data assimilation

NWP is an initial-value problem. Lorenz (1963) was the first to recognize the chaotic behaviour of atmospheric flows. It is the non-linearity of the governing equations that may lead to an exponential growth of small errors in the initial field. As a practical consequence, it was realized that deterministic models have a naturally limited forecast horizon.

Modern data assimilation techniques incorporate surface observations, upper-air soundings, aircraft reports, and a large variety of satellite and other remote-sensing data. Sophisticated mathematical methods are used to interpolate observations on the three-dimensional model grid. As a first guess, the preceding model forecast is used to avoid numerical instabilities in the forward integration. Common variational methods involve the minimization of a cost function that summarizes the squared deviations between the analysis and the observations weighted by the empirically estimated accuracy of the observations. This allows measurements from platforms and instruments of different accuracy to be combined. For example, in situ measurements of temperature may be exact, but may not be representative of the grid cell of the model. The limitations of data assimilation become obvious in regions where observations are rare and thus the first guess of the model dominates the analysis. This entails the risk of missing a sudden development – although it may have been observed by a single ship.

In four-dimensional variational analysis (Lorenc, 2003), data assimilation was extended over a time interval of 6 or 12 h. The cost function also summarized the squared deviations of the forecast fields and the analysed fields weighted by the accuracy of the forecast. Consequently, time-dependent analysis satisfied dynamical equations and did not drift too far away from the forecast.

Some NWP models, fine-mesh regional models in particular, have the ability to simulate TCs. However, models sometimes fail to adequately resolve TC intensity, in the case of small or intense TCs and in the formation stage. Therefore, several operational models assimilate bogus pressure and wind fields derived from observed TC intensity (see section 2.4.10) to create realistic initial conditions.

2.5.7 Reanalyses

Climatologists have recognized the potential value of numerical analyses in the early stages of NWP. However, the operational analyses archived by weather centres are not appropriate for deriving reliable climatologies, because of model changes in spatial resolution and physical parameterizations. Moreover, assimilation techniques have changed over the years, along with incorporation of new data sources. In the 1990s, leading weather centres started projects to reanalyse past weather on the basis of "the best possible assimilation" to overcome the inhomogeneity of operational analyses. Datasets covering 15–40 years or even the complete twentieth century are available on the Internet, for example, from the National Center for Atmospheric Research (CAS), ECMWF (ERA), National Centers for Environmental Prediction (NCEP) (CFSR), National Oceanic and Atmospheric Administration (PSD) or JMA (JRA). Descriptions of datasets can, for example, be found in Kalnay et al. (1996), Uppala et al. (2005), Swail et al. (2000, 2006) and Kobayashi et al. (2015). However, a common deficiency of all datasets is still the inhomogeneity of the basic observational material.

2.5.8 Ensemble prediction

A new era of exploring the meteorological forecast uncertainty started in 1994 with the introduction of the ECMWF Ensemble Prediction System (ENS, formerly named EPS). The fundamental idea of ENS is to run an ensemble of $N + 1$ forecasts, with each starting from individually perturbed initial conditions while one member starts from the "best possible" unperturbed analysis. Spatial resolution is reduced in these runs owing to limited computer resources. As a result, $N + 2$ forecasts are obtained, including the standard high-resolution forecast and the undisturbed reduced resolution forecast. Due to error growth, the forecasts

begin to diverge rapidly depending on the dynamic stability of the initial state. The spread of forecasts and the ensemble mean provide a lot more information than a single deterministic forecast. Up-to-date forecasts (ENS) are available for registered users.

Meteograms like the one shown in Figure 2.24 illustrate the expected range of meteorological parameters in the forecast period. Thus, forecasters have the potential to combine deterministic wind forecasts with the predicted probability of exceeding certain thresholds. An example of a probability forecast chart of high wind speed is shown in Figure 2.25. As ENS is based on the coupled ocean wave–atmosphere model, and probabilities of wave parameters are also available (see section 6.6).

Global ensemble prediction systems are also run by the Met Office (MOGREPS), NCEP (GEFS) and JMA (GEPS). Moreover, regional ensemble prediction systems are run by an increasing number of forecast centres.

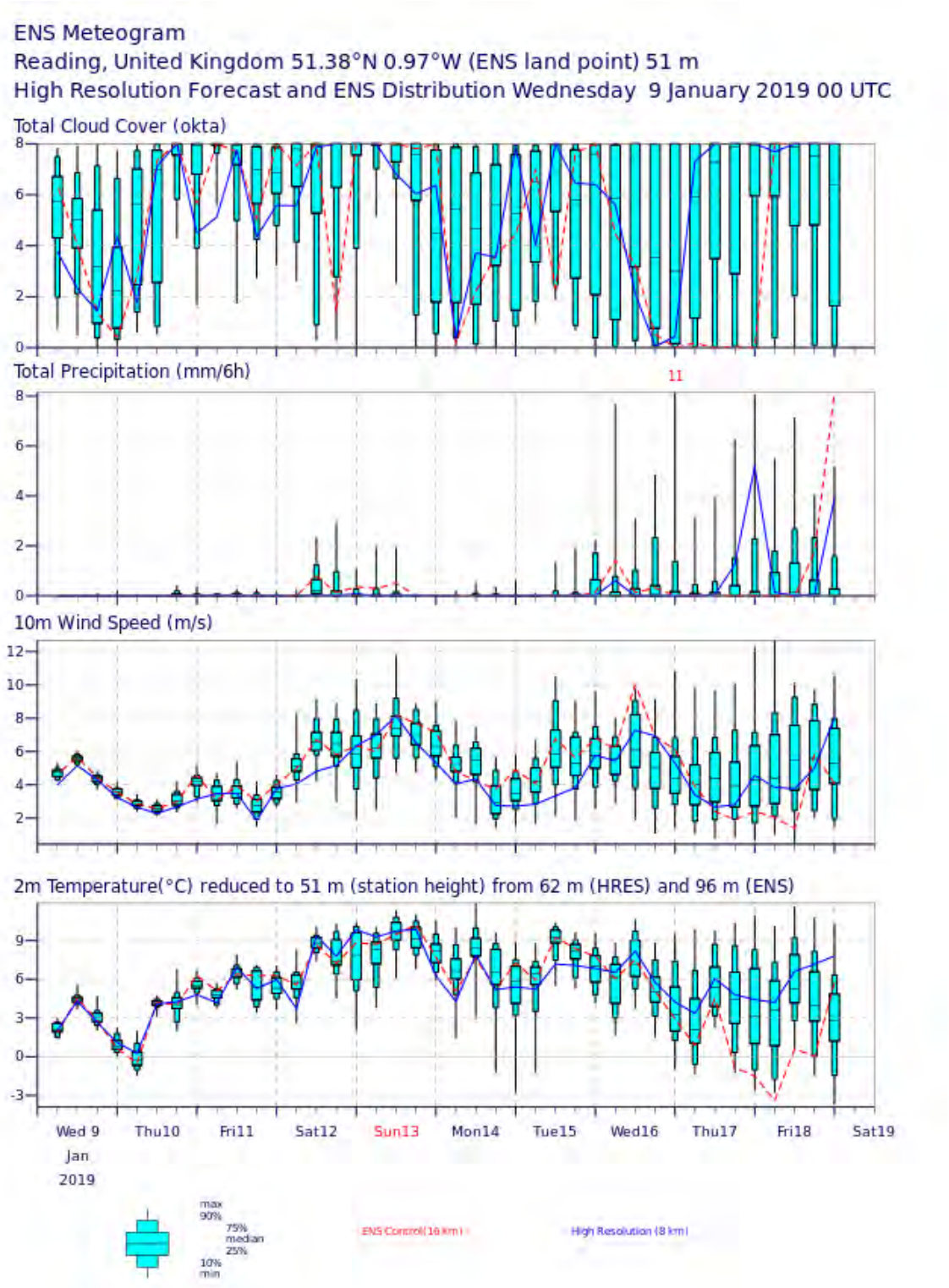

Figure 2.24. Example of an ENS meteogram comparing the high-resolution model run (blue curves) with the frequency distribution of 50 ensemble runs and the undisturbed control run (red curves)

Source: Interactively created at the website of the European Centre for Medium-Range Weather Forecasts, https://www.ecmwf.int/en/forecasts/charts/web/classical_meteogram (registered users only)

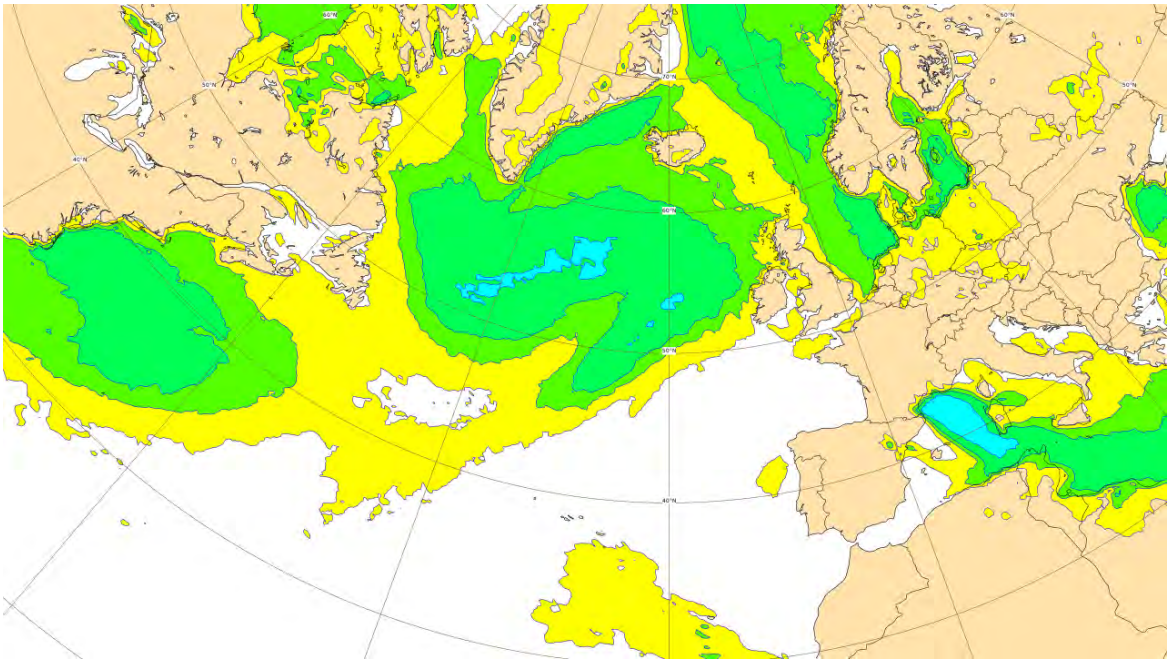

Figure 2.25. Chart of the T + 5 d forecast probability (colour shading: yellow < 35%, light green > 35%, green > 65%, blue > 95%) to exceed a wind-speed threshold of 10 m s^{-1} (ENS)

Source: Interactively created at the website of the European Centre for Medium-Range Weather Forecasts, https://www.ecmwf.int/en/forecasts/charts/web/classical_meteogram (registered users only)

CHAPTER 3. WAVE GENERATION AND DECAY

Editors: M. Reistad with A.K. Magnusson, updated by A. Chawla

3.1 INTRODUCTION

This chapter gives an overview of the processes involved in wave generation and decay. It provides an indication of how these processes are formulated for the purposes of wave prediction.

Wave forecasting is the process of estimating how waves evolve as changing wind fields act on the surface of the ocean. To understand this, the processes affecting the energy of the waves need to be identified. In simple terms, wave energy at a given location is changed through advection (rate of energy propagated into and away from the location), the wave-energy gains from the external environment (forcing by the wind) and wave-energy losses due to dissipation. In wave modelling, the usual approach is to represent these influences as a wave-energy conservation equation, as presented in Chapter 5 (Equation 5.1), and then to solve it. The sources of wave energy (gains and losses) are identified as three major processes: the external gains (S_{in}), the dissipative loss (S_{ds}) and the shifting of energy within the spectrum due to weakly non-linear wave–wave interactions (S_{nl}). This chapter presents a description of these terms as well as of propagation.

3.2 WIND-WAVE GROWTH

The only input of energy to the sea surface over the considered timescales comes from the wind. Transfer of energy to the wave field is achieved through the surface stress applied by the wind. This transfer varies roughly as the square of the wind speed. Thus, as already noted in section 2.1, an error in wind specification can lead to a large error in the wave energy and subsequently in parameters such as significant wave height.

After the onset of a wind over a calm ocean, there are thought to be two main stages in the growth of wind waves: an initial linear growth and a subsequent exponential growth. The small pressure fluctuations associated with turbulence in the airflow above the water are sufficient to induce small perturbations on the sea surface and to support a subsequent linear growth as the wavelets move in resonance with the pressure fluctuations. This mechanism is called the Phillips resonance (Phillips, 1957), and Barnett (1968) and Ewing (1971) gave formulations. However, this mechanism is only significant early in the growth of waves on a calm sea.

Most of the development commences in the subsequent exponential growth when the wavelets have grown to a sufficient size to start affecting the flow of air above them. The wind now pushes and drags the waves with a vigour that depends on the size of the waves. This growth is usually explained by what is called a “shear flow instability”: the airflow sucking at the crests and pushing on the troughs (or just forward of them). Miles (1957) presented a useful theory in this regard. The rate of this growth is exponential as it depends on the existing state of the sea. This is usually described in terms of the components of the wave-energy-density spectrum (see section 1.3.7).

From the formulation of Miles (1960),

$$E(f,\theta) = \frac{\boldsymbol{k}}{4\pi\rho_w^2 \mu g} P(\boldsymbol{k}, f)(e^{2\pi f t \mu} - 1) \tag{3.1}$$

or

$$S_{in}(f,\theta) = \frac{\delta E(f,\theta)}{\delta t} = 2\pi f \mu E(f,\theta), \tag{3.2}$$

where $E(f,\theta)$ is a frequency (f)–direction (θ) component, $\boldsymbol{k}$ is the wave number, $P(\boldsymbol{k},f)$ is the spectrum of wave-induced turbulence, μ is a coupling coefficient to be defined, g is the acceleration due to gravity, ρ_w is the density of water and S_{in} is the spectral energy input due to winds.

It has been noted that the rates of growth predicted by Miles are much smaller than growth rates observed from laboratory and field studies. Snyder and Cox (1966) proposed a simple form based on a field experiment:

$$\mu = \frac{\rho_a}{\rho_w}\left[\frac{u}{c}\cos(\theta-\psi)-1\right], \tag{3.3}$$

where c and θ are the phase speed and the direction, respectively, of the component being generated, Ψ and u are the direction and speed of the wind, respectively, and ρ_a is the density of air.

Measurements made in the Bight of Abaco in the Bahamas in 1974 enabled Snyder et al. (1981) to propose a revision,

$$S_{in}(f,\theta) = E(f,\theta)\max\left[0, K_1 2\pi f \frac{\rho_a}{\rho_w}\left[\frac{U_5}{c}\cos(\theta-\psi)-1\right]\right], \tag{3.4}$$

where U_5 is the wind speed at 5 m and K_1 is a constant determined empirically. The height at which the wind speed was specified in the original work was 5 m. As application of this to other situations can be affected by the structure of the lower part of the atmospheric boundary layer (see section 2.3), it may be better to express the wind input in terms of the friction velocity u_* with magnitude

$$u* = \sqrt{\frac{\tau}{\rho_a}} = u\sqrt{C_d}, \tag{3.5}$$

where τ is the magnitude of the wind stress and C_d is the drag coefficient.

The drag coefficient, which relates u_* to u, varies with u. Komen et al. (1984) used an approximate form to write the wind input term as

$$S_{in}(f,\theta) = E(f,\theta)\max\left[0, K_1 2\pi f \frac{\rho_a}{\rho_w}\left[K_2\frac{u*}{c}\cos(\theta-\psi)-1\right]\right]. \tag{3.6}$$

The constants K_1 (~0.25) and K_2 (~28) allow for some flexibility in specifying this term.

Later research has shown that the aerodynamic drag on the sea surface depends on the state of the waves. Janssen (1991) and Jenkins (1992), using quasi-linear theories, found that the drag coefficient depended on the wave age parameter defined as c_p/u_*, where c_p is the phase velocity of the peak frequency of the wave spectrum. These theories imply that the aerodynamic drag and the growth rate of the waves are higher for young wind sea (lower wave age) than for old wind sea (higher wave age). This result is in good agreement with the experimental data of Donelan (1982) and Maat et al. (1991).

Winds have a subgrid variability (in time and space) that cannot be resolved by meteorological models. This is referred to as wind gustiness, and it can have a significant impact on wave growth (Abdalla and Cavaleri, 2002). Consider a wind field with a wind speed such that the friction velocity along the direction of the waves matches the phase speed of the wave. Then, according to Equation 3.6, when wind gusts exceed the phase speed, waves would grow; however, when they are less than the phase speed, there would not be a negative impact. Abdalla and Cavaleri (2002) likened this to the "diode effect" in analogy with the filtering capability of an electronic diode. The limitation of this explanation is that it does not take into account a process referred to as the "negative wind effect" in which waves transfer energy back to the atmosphere when they move slower than the wind. That process is a matter of much debate in the scientific community, but it is well acknowledged that, even if this process exists, the dissipation during wind slowdown is smaller than the growth during wind speed up.

Friction velocity has a non-linear relationship with the wind speed. A mean friction velocity based on a fluctuating wind field is larger than the friction velocity from a mean wind speed.

Furthermore, the quasi-linear theories of Janssen (1991) demonstrated that wind input source terms are a non-linear function of friction velocity. All of these suggest that wind gustiness will have a net positive impact on wave growth. The problem is in practically quantifying the level of gustiness. Higher growth rates in unstable boundary layers, which are related to the air–sea temperature difference, were observed by Kahma and Calkoen (1992). The work of Abdalla and Cavaleri (2002) made the corresponding connection with wind gustiness. Thus, the impact of wind gustiness can be incorporated by including the effect of air–sea temperature difference in wave-growth terms (Tolman, 2002; Bidlot, 2012).

Empirical formulae and wind-wave growth curves

There are also many empirical formulae for wave growth that have been derived from large datasets. These formulae make no attempt to separate the physical processes involved. They represent net wave growth from known properties of the wind field (wind speed and direction, fetch and duration). In representing such relations, it simplifies comparisons if the variables are all made dimensionless:

- Peak frequency $f_p^* = uf_p/g$;
- Fetch $X^* = gX/u^2$;
- Duration $t^* = gt/u$;
- Height $H^* = gH/u^2$;
- Energy $E^* = Eg^2/u^4$.

For example, from the Joint North Sea Wave Project (JONSWAP) 1973 data (see Hasselmann et al., 1973, 1976; and section 1.3.9), the peak frequency and total energy in the spectrum are related to the fetch (X) and wind speed at 10 m (U_{10}) by the following:

$$f_p^* = 3.5X^{*-0.33} \text{ and } E^* = 1.6 \times 10^{-7} X^*. \quad (3.7)$$

Operationally useful graphical presentations of such empirical relations have existed since the mid-1940s and the Sverdrup and Munk (1947) and Pierson et al. (1955) curves have been widely used (see Annex 1). Such relationships may also need to consider the depth. As wave growth is affected by depth, with additional dissipative processes in play, the deep-water curves will overestimate the wave growth in shallow water.

Gröen and Dorrestein (1976) developed a more recent set of curves. These comprised a variety of formats for calculating wave height and period, given the wind speed, fetch length and wind duration, and the effects of refraction and shoaling. The basic non-dimensional graphs are displayed in Figure 3.1, showing characteristic height and period versus fetch and duration. These graphs have been constructed to fit visually assessed wave heights and periods and are thus called "characteristic" height (H_c) and period (T_c), as distinct from significant height ($H_{1/3}$) and mean period (T_z). Section 4.1 gives the set of curves and their applications.

There is uncertainty about the relationship between the visually and instrumentally derived quantities, but it appears that some bias (H_c and T_c both being slightly higher than $H_{1/3}$ and T_z, respectively) may need to be kept in mind when using this type of graph. However, the systematic errors are generally small compared with the random errors in individual observations.

In situations with moderate variations in the wave field (at some distance from the coast, or in the idealized case of a constant wind blowing perpendicularly off a long, straight coast over water with uniform depth), the frequency spectrum of the waves seems to have a universal shape in shallow water in the same sense as it seems to have in deep water (where the Pierson–Moskowitz and the JONSWAP spectra have been proposed, see section 1.3.9). The assumption of a k^{-3} spectral tail in the wave-number spectrum (Phillips, 1958) leads, in deep water, to the corresponding f^{-5} tail in the Pierson–Moskowitz and JONSWAP spectra. The same assumption in shallow water leads to another shape of the frequency tail, as the dispersion relationship is different. For shallow water, the result is an f^{-3} frequency tail. This assumption led Bouws et al.

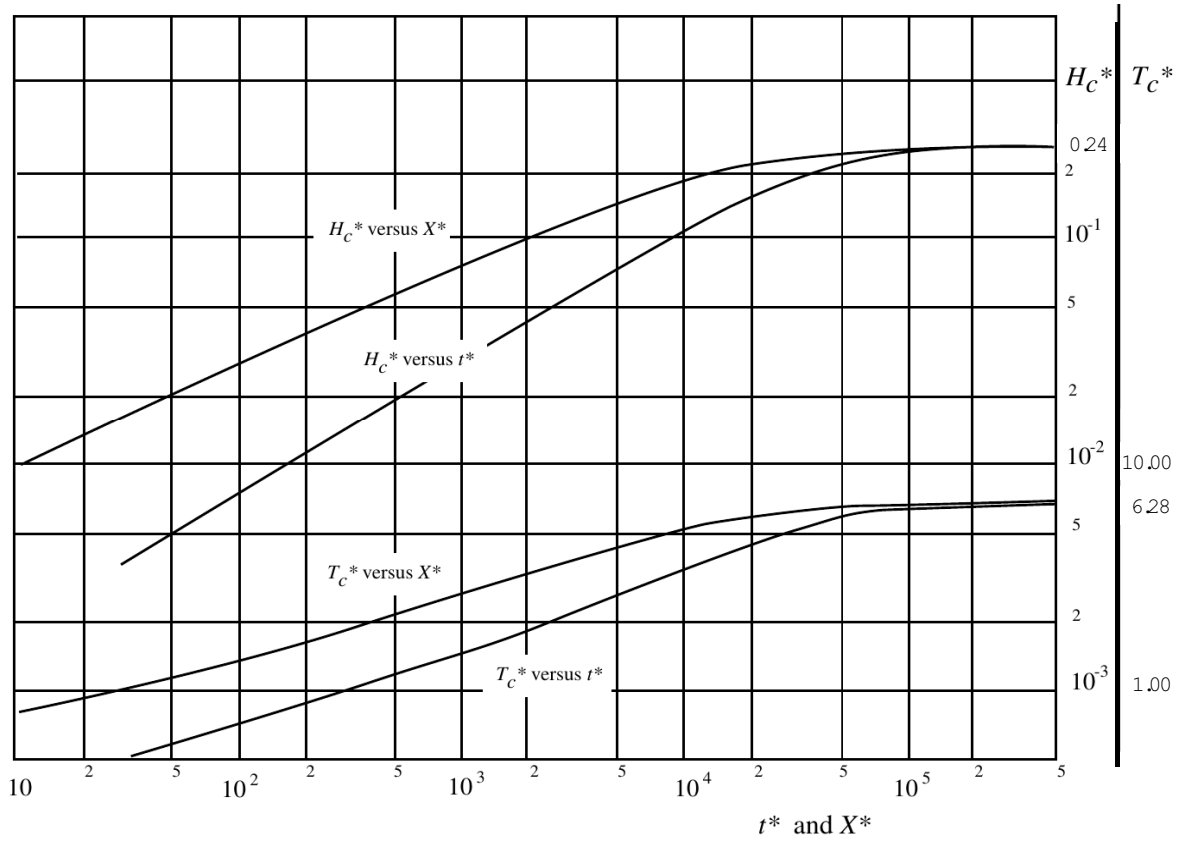

Figure 3.1. Basic diagram for manual wave forecasting. The curves are drawn for non-dimensional parameters ($H_c^* = gH_c/u_2^2$; $T_c^* = gT/u$)

Source: Derived from Gröen and Dorrestein (1976)

(1985) to propose a universal shape of the spectrum in shallow water that is similar to the JONSWAP spectrum in deep water (with the f^{-5} tail replaced with the transformed k^{-3} tail). It is called the Texel–Marsen–Arsloe spectrum.

The evolution of the significant wave height and the significant wave period in the described idealized situation is parameterized from observations in deep and shallow water with the following formulations:

$$H^* = A \tanh(\kappa_3 h^{*m_3}) \tanh\left[\frac{\kappa_1 X^{*m_1}}{\tanh(\kappa_4 h^{*m_4})}\right] \text{ and}$$
$$T^* = 2\pi B \tanh(\kappa_4 h^{*m_4}) \tanh\left[\frac{\kappa_2 X^{*m_2}}{\tanh(\kappa_4 h^{*m_4})}\right], \quad (3.8)$$

where the dimensionless parameters for significant wave height H^*, significant wave period T^*, fetch X^* and depth h^*, are, respectively: $H^* = gH_s/u^2$, $T^* = gT_s/u$, $X^* = gX/u^2$ and $h^* = gh/u^2$ (fetch is the distance to the upwind shore). Many investigators have estimated the values of the coefficients. Those of CERC (1973) are:

$A = 0.283$, $B = 1.2$;
$\kappa_1 = 0.0125$, $\kappa_2 = 0.077$, $\kappa_3 = 0.520$, $\kappa_4 = 0.833$;
$m_1 = 0.42$, $m_2 = 0.25$, $m_3 = 0.75$, $m_4 = 0.375$.

Corresponding growth curves are plotted in Figure 3.2.

Wind waves in the process of growing have been considered so far. When the wind stops or when the waves propagate out of the generating area, they are often called “swell”. Swell looks different from an ordinary running sea. The backs of the waves are smoother and the crests are

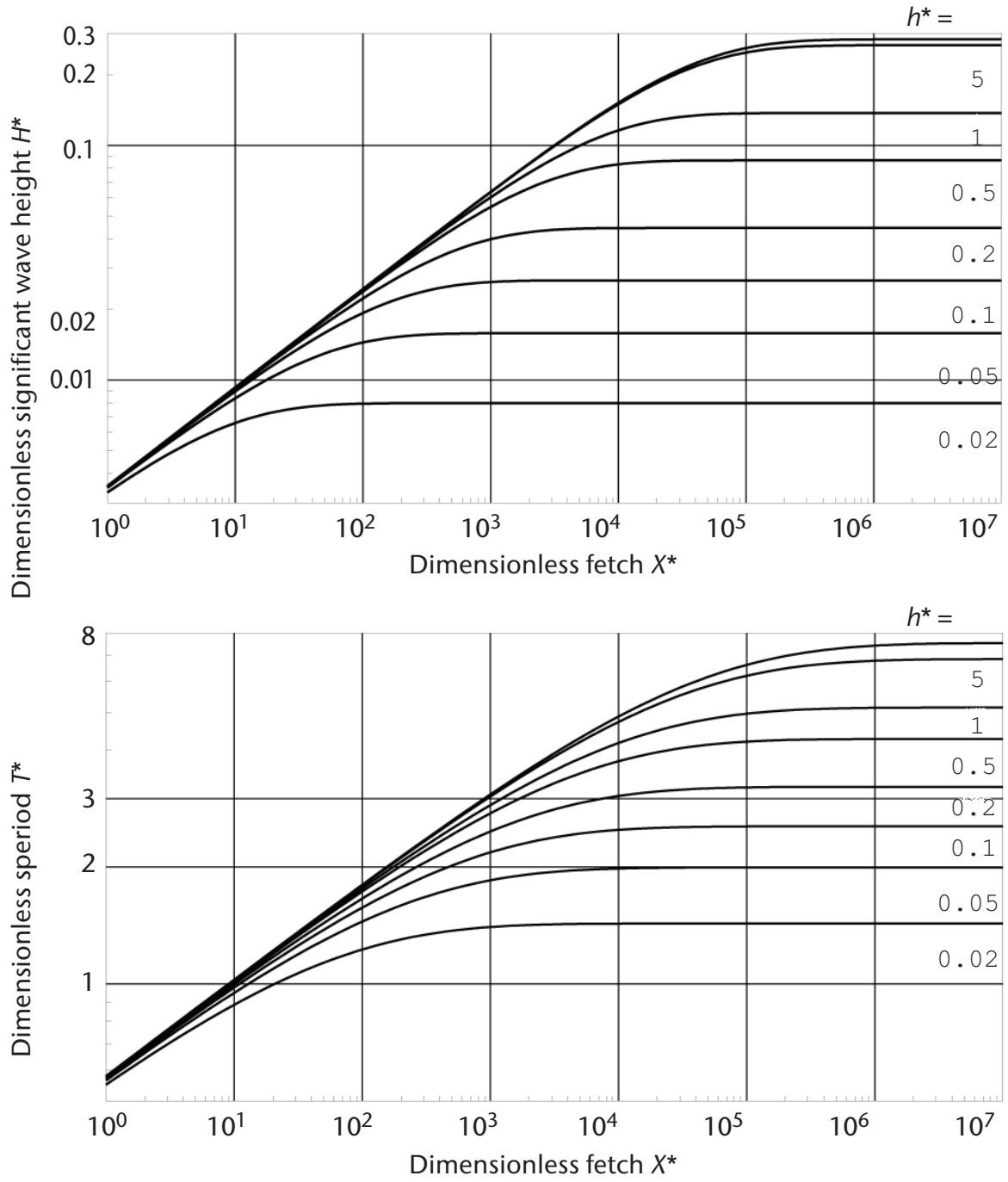

Figure 3.2. Shallow-water growth curves for dimensionless significant wave height (upper) and period (lower) as functions of fetch, plotted for a range of depths

long. Whereas wind waves grow under the influence of the wind, swell waves decrease in its absence. The spectra of swell waves need not be narrow. For points close to large generating areas, faster waves from further back in the generating area may catch up with slower waves from near the front. The result is a broad spectrum. The dimensions of the wave-generating area and the distance from it are therefore also important in the type of swell spectrum observed. Propagation is the most important characteristic of swell waves.

3.3 WAVE PROPAGATION

A disturbance on the water will travel away from the point at which it was generated. For a wave train with period T (frequency $f = 1/T$) and wavelength λ, the wave speed (phase speed) is $c = \lambda/T$. This can also be written as ω/k, where ω is the angular frequency ($2\pi f$) and k is the wave number $2\omega/\lambda$ (the number of crests per unit distance). Wave energy travels at the group velocity, which is not generally the same. For dispersive waves in deep water, the group velocity (c_g) is only half of the phase velocity. This can be worked out from the dispersion relation using $c_g = \mathrm{d}\omega/\mathrm{d}k$, as given in section 1.3.2. In shallow water, the waves are non-dispersive because the bottom dominates the fluid's response to a perturbation and the group velocity equals the phase velocity.

In general, for water of finite depth h, the dispersion relation is

$$\omega^2 = gk \tanh kh, \tag{3.9}$$

and the group speed is

$$c_g = \frac{\omega}{2k}\left(1 + \frac{2kh}{\sinh 2kh}\right). \tag{3.10}$$

For large h, this reduces to $\omega/2k$ and, for small h, to $\omega / k = \sqrt{gh}$.

How a local average of the energy moves is interesting in wave modelling. This is not as simple as moving the energy at one point in a straight line (or more correctly a great circle path) across the ocean. For any one location, the energy is spread over a range of directions. Also, waves at different frequencies will propagate at different speeds. Thus, from a point source, each component of the spectrum $E(f,\theta)$ can be propagated in the direction θ with speed $c_g(f,h)$.

3.3.1 Angular spreading

It is often assumed that the directional part of the wind-wave distribution has a $\cos^2(\theta - \Psi)$ form, where ψ is the predominant direction of the waves and θ is the direction of the spectral component concerned. Most of the energy is propagated in the mean direction of the sea. At deviating angles, less energy is transported, and, for all practical purposes, the energy propagated at right angles to the mean direction is negligible. There is considerable evidence indicating that the spread is dependent on the lengths of the waves. There are several such formulations for the directional distribution based on observations. Using the form $\cos^2(\theta - \Psi)/2$, Mitsuyasu et al. (1975) and Hasselmann et al. (1980) gave functional forms for the directional distribution spectrum $s(f,\theta)$ that are dependent on the ratio of frequency to peak frequency. These indicate the narrowest spread at the peak of the spectrum, with widening at both lower and higher frequencies. However, there is still uncertainty in the real functional form of the s parameter in simple sea states (for example, wind-sea generation and long swells). This is because different directional wave instruments located close to one another give widely different results (for example, Allender et al., 1989).

Waves that have left the generating area (swell) are reduced, in terms of energy density along their crest length, by the angular spreading. Numerical models automatically take care of this by splitting the spectrum into components and propagating each of the components independently. Manual methods require more action by the operator. Angular spreading and dispersion factors must be applied.

As illustrated in Figure 3.3, a point P will receive wave energy from points all along the front of the fetch. It is possible to compute the sum of all the contributions. Figure 3.4 shows results for a cosine-squared distribution of energy at the fetch front. At any fixed frequency, the curved lines in this diagram represent the percentages of the wave energy from the fetch front that reaches there. These are the angular spreading factors. The spatial coordinates are expressed in terms of the width AB of the fetch area. For example, at a distance of 2.5AB along the predominant swell

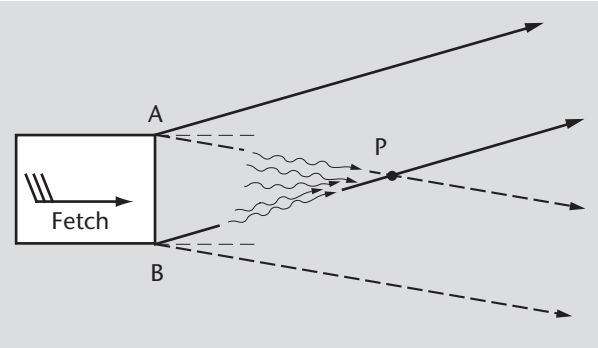

Figure 3.3. Possible directions for swell originating at a storm front AB and incident on a point P

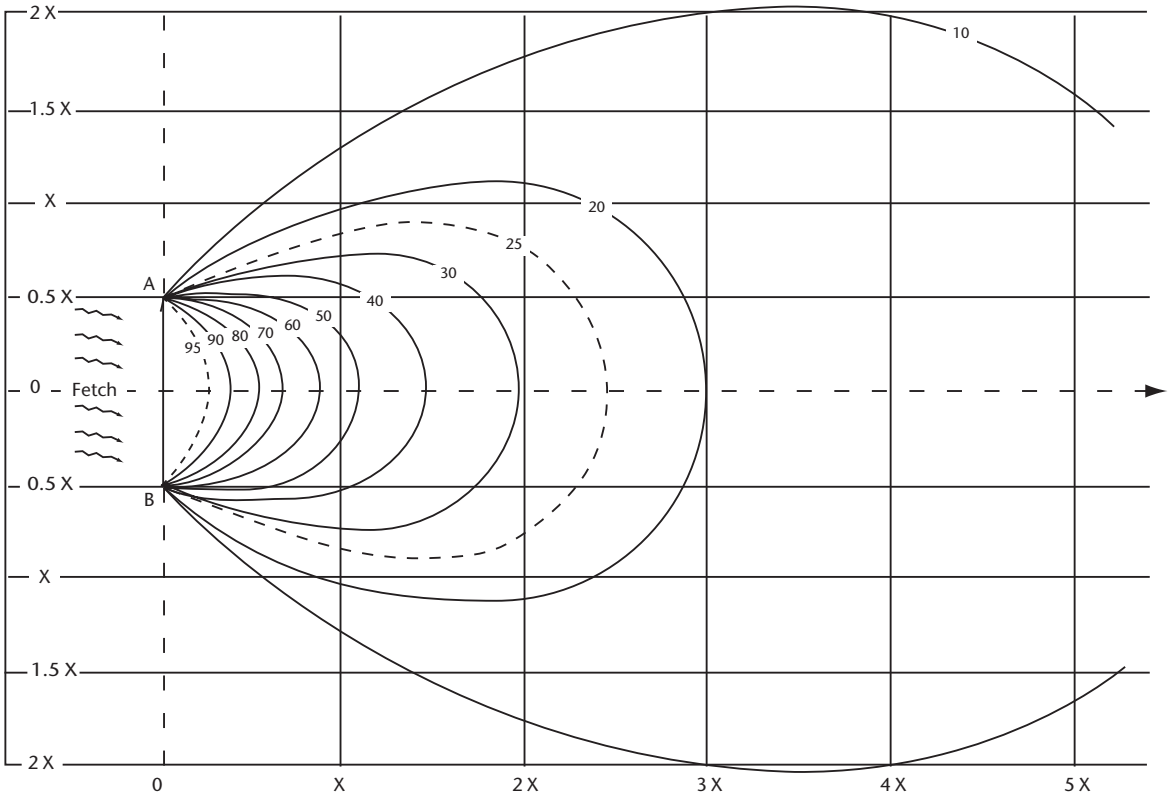

Figure 3.4. Angular spreading factors (as percentages) for swell energy

direction, the wave energy has decreased to about 25% of the energy per unit area that was present at the fetch front AB. The reduction in wave height due to angular spreading is by the square root of this percentage. These heights are the maximum heights that the swell may attain.

3.3.2 **Dispersion**

A further reduction needs to be applied to account for dispersion. It has been explained how long waves and their energy travel faster than short waves and their energy. The wave field leaving a generating area has a mixture of frequencies. At a large distance from the generating fetch, the waves with low frequencies (long waves) will arrive first, followed by waves of increasing frequency.

If the spectrum at the front edge of the generating fetch is that represented in Figure 3.5, then, given the distance from this edge and the time elapsed, it is easy to work out the speed of the

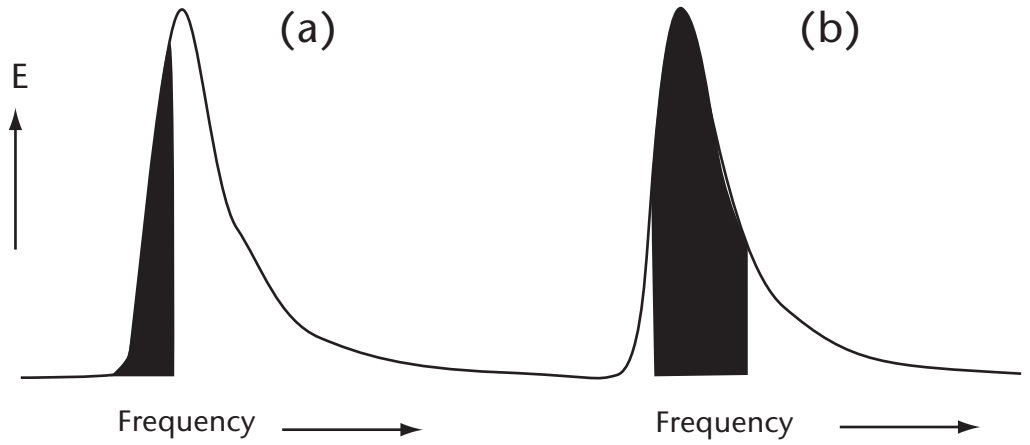

Figure 3.5. Effect of dispersion on waves leaving a fetch, showing the spectrum at the fetch front. The first components to arrive at a point far downstream constitute the shaded part of the spectrum in (a). Higher frequencies arrive later, by which time some of the fastest waves (lowest frequencies) have passed by as illustrated in (b).

slowest wave that could possibly reach the point of observation. Hence, the maximum frequency that could be observed is known. The length of fetch and the time at which generation ceases may limit the low frequencies. Similarly, after a certain time, all the fastest waves may have passed through the monitoring point. In these cases, the swell spectrum is limited to a narrow band of frequencies (indicated by the shaded areas in Figure 3.5). The shaded portion of the spectrum is the maximum that can be expected at the point of observation. The ratio of this area to the total area under the spectrum is called the wave-energy dispersion factor. A consequence of this dispersion effect is that by analysing the way in which swell arrives at an observing point, and noting the changes in the frequencies in the swell spectrum, it is possible to get an idea of the point of origin of the waves.

Dispersion and spreading can be considered the main causes of a gradual decrease of swell waves. Thus, given the spectrum of wave energy exiting a generating area and a point at which it is desirable to calculate the swell, the angular spreading factor and the dispersion factor can be calculated to obtain an estimate of the swell. Other processes affect swell heights where propagation distances are large; for example, some energy is also lost through internal friction and air resistance. Such swell dissipation has long been considered negligible, but recent studies (Ardhuin et al., 2009) have shown that even though this process may be small, the distances travelled by swells mean that it can have a significant impact (more on this in section 3.4). Interesting observations of the propagation of swell were made by Snodgrass et al. (1966) when they tracked waves right across the Pacific Ocean from the Southern Ocean south of Australia and New Zealand to the Aleutian Islands off Alaska. Chapter 5 gives more detail on how to determine the spectrum of wind waves and swell and on how to apply the above ideas.

Other considerations in propagating waves are the water depth and currents. It is not too difficult to adapt the advection equation to take account of shoaling and refraction. Currents have often been ignored for operational modelling purposes. The influence of currents on waves depends on local features of the current field and wave propagation relative to the current direction. Although current modulation of mean parameters may be negligible in deep oceans, and even in shelf seas for ordinary purposes, the modulation of spectral density in the high-frequency range may be significant (for example, Tolman, 1990). Waves in these frequency ranges may even be blocked or break when they propagate against a strong current, as in an estuary. The steepening of waves coupled with non-linear processes can have a significant impact on wave spectra near the blocking region (Chawla and Kirby, 2002). See Komen et al. (1994) for a general treatment of this subject.

3.4 WAVE DISSIPATION

Wave energy can be dissipated by four different processes: whitecapping, wave–bottom interaction, surf breaking and swell dissipation. Surf breaking occurs in extremely shallow water only, where depth and wave heights are of the same order of magnitude (for example, Battjes and Janssen, 1978). This mechanism is not relevant for shelf seas. Some mechanisms may be involved in the dissipation of wave energy due to wave–bottom interactions. Shemdin et al. (1978) reviewed these mechanisms, including bottom friction, percolation (water flow in the sand and the seabed) and bottom motion (movement of the seabed material itself).

3.4.1 Deep-water-wave dissipation

The primary mechanism of wave-energy dissipation in deep and open oceans is whitecapping. As waves grow, their steepness increases until a critical point when they break (see section 1.2.7). This process is highly non-linear. It limits wave growth, with energy being lost into the underlying ocean currents.

The limitation with whitecapping is that it is an episodic process which can occur over some wavelengths, and measurements of dissipation have to be done in regions that are sometimes wet (under the crest of waves) and sometimes dry (above the trough of waves). Hence, field measurements of this process are difficult and hard to quantify in spectral terms. In most models, dissipation terms due to whitecapping are used as "tuning knobs" to close the spectral balance, without limited theoretical/observational-based formulations. The WISE Group (2007) gave a detailed review on whitecapping dissipation formulations. There is no consensus in the literature on the form of dissipation due to whitecapping, with the dissipation function ranging from varying linearly with spectral energy E, to different powers of E.

The most common approach is the "random pulse" whitecap model by Hasselmann (1974). This dissipation depends on the existing energy in the waves and on the wave steepness, and can be written as

$$S_{\mathrm{ds}}(f,\theta) = -\psi(E)\frac{f^2}{\overline{f}}E(f,\theta), \tag{3.11}$$

where $\Psi(E)$ is a property of the integrated spectrum E. Ψ may be formulated as a function of a wave steepness parameter ($\xi = Ef^4/g^2$, where f is the mean frequency). Hasselmann (1974) and Komen et al. (1984) suggested forms for Ψ. Though this formulation is commonly used, it has some significant shortcomings like spurious amplification of wind seas under swell conditions (Van Vledder and Hurdle, 2002) and decreasing dissipation of swell with increasing swell steepness (Ardhuin et al., 2010).

In recent years, there have been several developments in the theory of wave-dissipation processes that are based on physical observations. These include considering wave breaking based on a threshold saturation spectrum (Alves and Banner, 2003) and dissipation of high-frequency waves due to wave breaking of the dominant waves (Banner et al., 1989; Young and Babanin, 2006). Dissipation formulations based on new understandings of the dissipative processes have been developed (Ardhuin et al., 2010; Babanin et al., 2010).

There are also processes of microscale breaking and parasitic capillary action through which wave energy is lost. However, there is still much to learn about dissipation; usually, no attempt is made to distinguish the dissipative processes. The formulation of S_{ds} in deep water therefore requires further research.

3.4.2 Shallow-water-wave dissipation

When a wave progresses into shallow water (with a depth of the order of the wave height), the upper part of the wave tends to increase its speed relative to the lower part. At some point, the crest attains a speed sufficiently high to overtake the preceding trough. The face of the wave becomes unstable, and water from the crest "falls" along the forward face of the wave (spilling).

In extreme cases, the crest falls freely into the trough (plunging). In all cases, a high-velocity jet of water is injected at some point into the area preceding the crest. This jet creates a submerged whirl, and in severe breaking, it forces the water up again to generate another wave (often seen as a continuation of the breaking wave). This wave may break again, resulting in an intermittent character of the breaker (Jansen, 1986).

Breaking of the waves is, of course, visible in the white water generated in the surf zone. It appears to be possible to model this by treating each breaker as a bore with a height equal to the wave height. The dissipation in such a bore can be determined analytically. By assuming a certain random distribution of the wave heights in the surf zone, the total rate of dissipation can be estimated. This model (for example, Battjes and Janssen, 1978) has been successful in predicting the decrease of the significant wave height in the surf zone. Using the bore formulation, the dissipation rate due to depth-limited breaking is given by

$$S_{\text{breaking}}(\omega,\theta) = -\alpha \frac{Q_{\text{b}}\bar{\omega}H_{\text{m}}^2}{8\pi}\frac{E(\omega,\theta)}{E_{\text{total}}}, \tag{3.12}$$

where α is an empirical coefficient of order 1, $\bar{\omega}$ is the mean wave frequency, and Q_{b} is the fraction of breaking waves determined from

$$\frac{1-Q_{\text{b}}}{\ln Q_{\text{b}}} = -8\frac{E_{\text{total}}}{H_{\text{m}}^2}. \tag{3.13}$$

H_{m} is the maximum possible wave height (determined either as a fixed fraction of the local depth, or as a limit on wave steepness) and E_{total} is the total wave energy. Other formulations of depth-limited wave breaking have been proposed, but for monotonic beaches, the bore formulation approach works as well as any.

The breaking wave dissipation forms in deep water (whitecapping formulation) and shallow water (bore formulation) are inherently different. Wave breaking can also occur due to waves steepening over an opposing current. In all of these cases, the waves steepen, become unstable and break. While studying wave breaking against an opposing current in deep water, Chawla and Kirby (2002) showed that a modified form of the bore formulation could be used to explain the energy dissipation over opposing currents. However, the dissipation constant α was different to the one used for shallow-water breaking (which is not surprising because they are different physical processes). More recently, using a scaled dissipation constant, Filipot et al. (2010) showed a unified formulation for wave dissipation that transitions seamlessly from deep to shallow water. There have been alternative formulations developed for shallow-water breaking, but unlike deep-water breaking where dissipation can be intermittent (in space, direction and frequency), shallow-water waves (at least for monotonic beaches) dissipate energy all the way through the surf zone. Furthermore, the directional spreading is significantly reduced due to refraction, which explains the success of simple energy-removing models like that of Battjes and Janssen (1978).

Energy dissipation in shallow water is not limited to depth-limited wave breaking. There are two other processes that occur due to wave and bathymetry interactions: frictional damping and wave scattering. Technically, wave scattering is not a wave dissipation process, but a mechanism for redistribution of wave energy. Apart from these two processes, there are also wave dissipation due to percolation (for example, waves dissipating over a coral reef), interactions with a mud layer and interactions with vegetation (for example, waves propagating over sea grass). The discussion here will be limited to the more prevalent wave dissipation over a sandy bottom. Bottom friction is usually the most relevant form of wave dissipation in intermediate water depths outside the surf zone where the waves can still feel the bottom. It is essentially the effort of the waves to maintain a turbulent boundary layer just above the bottom.

Several formulations have been suggested for the bottom friction. A simple expression, in terms of the energy balance, is that of Hasselmann et al. (1973) in the JONSWAP project:

$$S_{\text{bottom}}(\omega,\theta) = -\Gamma\frac{\omega^2}{g^2\sinh kh}E(\omega,\theta), \tag{3.14}$$

where Γ is an empirically determined coefficient. Tolman (1994) showed that many different formulations can be written in the generic form above, with the differences being in the way the

coefficient Γ is computed. A dimensional analysis shows that Γ has a velocity scale and thus can be represented as the product of a non-dimensional frictional coefficient and a velocity measure near the bottom. Using previous studies, Tolman (1994) developed a frictional formulation for a moving bed where the friction coefficient changed due to the formation and destruction of ripples on the bottom floor. Tolman showed that most wind seas occurred in regimes when the ripples were washed out, leading to a sheet flow regime where the friction factor reduced with increasing bottom velocity in such a way that their effects cancelled out, leading to a constant value for Γ. This explains the success of the simple JONSWAP formulation above. However, this is not true for swell conditions where the bottom floor is generally in ripple formulation leading to enhanced bottom roughness and consequently increased frictional dissipation. Using field measurements, Ardhuin et al. (2003*a*, 2003*b*) showed that a movable bed friction formulation was essential to describe swell attenuation over the continental shelf, and was the dominant process in swell transformation across the shelf.

3.4.3 Swell dissipation

Until recently, swell dissipation processes in deep water (not due to bottom dissipation) have been the subject of significant debate in the scientific community. Donelan (1990) found evidence of swell damping in laboratory experiments. However, the dissipation rates obtained were too large to be applicable to swell propagation in the field. Tolman (2002) introduced a "negative wind" swell dissipation term, but that was more as a tuning term to reduce errors. The problem with observing swell dissipation in the field has been that the process is weak, and swells have to be tracked over long distances to make any significant observations. Using synthetic aperture radar datasets, Ardhuin et al. (2009) were able to track swells across the Pacific Ocean and show that swell dissipation is a real physical process. The underlying causes of swell dissipation are still topics of considerable scientific debate. Nonetheless, Ardhuin et al. (2010) have shown that accounting for swell dissipation processes using semi-empirical formulations removes the large biases in model simulations over swell-dominated areas.

Manual wave calculations do not need to pay specific attention to dissipative processes. The dissipation of wind waves is generally included implicitly in the overall growth curves used.

3.5 NON-LINEAR WAVE–WAVE INTERACTIONS

The introduction to this Guide noted that simple sinusoidal waves, or wave components, are linear waves. This is an approximation. The governing equations admit more detailed analysis. While the theory is restricted by a requirement that the waves do not become too steep, the weakly non-linear interactions have been shown to be important in the evolution of the wave spectrum.

Weakly non-linear, resonant, wave–wave interactions transfer energy among waves of different frequencies, redistributing the energy within the spectrum in such a way that preserves some characteristics of the spectral shape (a self-similar shape). The process is conservative, it is internal to the wave spectrum and it does not result in any change to the overall energy content in the wave field.

The resonance that allows this transfer among waves can be expressed by imposing the conditions that the frequencies of the interacting waves must sum to 0, and likewise the wave numbers. This first occurs at the third order of a perturbation analysis in wave energy (as shown by Hasselmann, 1962) and the integrals that express these energy transfers are complicated cubic integrals:

$$S_{\mathrm{nl}}(f,\theta) = f \iiint \mathrm{d}\boldsymbol{k}_1 \mathrm{d}\boldsymbol{k}_2 \mathrm{d}\boldsymbol{k}_3 \delta\left(\boldsymbol{k}_1 + \boldsymbol{k}_2 - \boldsymbol{k}_3 - \boldsymbol{k}\right)) \delta(f_1 + f_2 - f_3 - f) \left[n_1 n_2 (n_3 + n) - n_3 n (n_1 + n_2)\right] K\left(\boldsymbol{k}_1, \boldsymbol{k}_2, \boldsymbol{k}_3, \boldsymbol{k}\right). \tag{3.15}$$

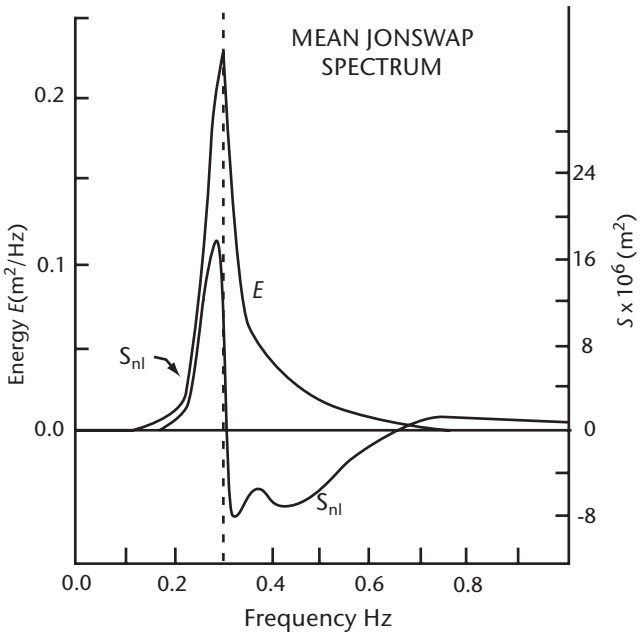

Figure 3.6. Growth from non-linear interactions (S_{nl}) as a function of frequency for the mean JONSWAP spectrum (E)

In this integral, the delta functions, δ, enforce the resonance conditions, the $(f_i,\boldsymbol{k}_i)$ for $i = 1, 2, 3$ are the frequency and wave-number pairs for the interacting wave components, the $n_i = E(f_i,\theta_i)/f_i$ are the wave action densities and the Kernel function K gives the magnitude of the energy transfer to the component $\boldsymbol{k}$ (or (f,θ)) from each combination of interacting wave components.

This interactive process is responsible for the downshift in peak frequency as a wind sea develops. Figure 3.6 illustrates the non-linear transfer function $S_{nl}(f)$ calculated for a wind sea with an energy distribution, $E(f_i,\theta_i)$, given by the mean JONSWAP spectrum (see section 1.3.9). The positive growth just below the peak frequency leads to this downshift. As the interaction involves four components, this type of interaction is also referred to as a "quadruplet interaction". These non-linear interaction terms are the lowest-order terms that can simulate this spectral downshift. Hence, it is important to include their effect even in a linear wave formulation.

Another feature of the non-linear wave–wave interactions is the "overshoot" phenomenon. Near the peak, the non-linear wave–wave interaction dominates the growth at a given frequency. As a wind sea develops (or moving out along a fetch), the peak frequency decreases. A given frequency f_e will first be well below a peak frequency, resulting in a small amount of growth from the wind forcing, some non-linear interactions and a little dissipation. As the peak becomes lower and approaches f_e, the energy at f_e comes under the influence of a large input from non-linear interactions. This can be seen in Figures 3.6 and 3.7 in the large positive region of S or S_{nl} just below the peak. As the peak falls below f_e, this input reverses, and an equilibrium is reached (known as the saturation state). Figure 3.8 illustrates the development along a fetch of the energy density at such a given frequency f_e.

Although the non-linear theory can be expressed as in Equation 3.15, evaluation is a problem. The integral in Equation 3.15 requires a great deal of computer time; it is not practical to include it in this form in operational wave models. Some wave models use the similarity of spectral shape, which is a manifestation of this process, to derive an algorithm so that the integral calculation can be bypassed. Having established the total energy in the wind-sea spectrum, these models will force it into a predefined spectral shape. Alternatively, it is now possible to use integration techniques and simplifications that allow evaluation of a reasonable approximation to the integral (see the discrete interaction approximation of Hasselmann and Hasselmann (1981, 1985) and Hasselmann et al. (1985), or the two-scale approximation of Resio et al. (1992)). These efficient computations of the non-linear transfer integral made it possible to develop third-generation wave models that compute the non-linear source term explicitly

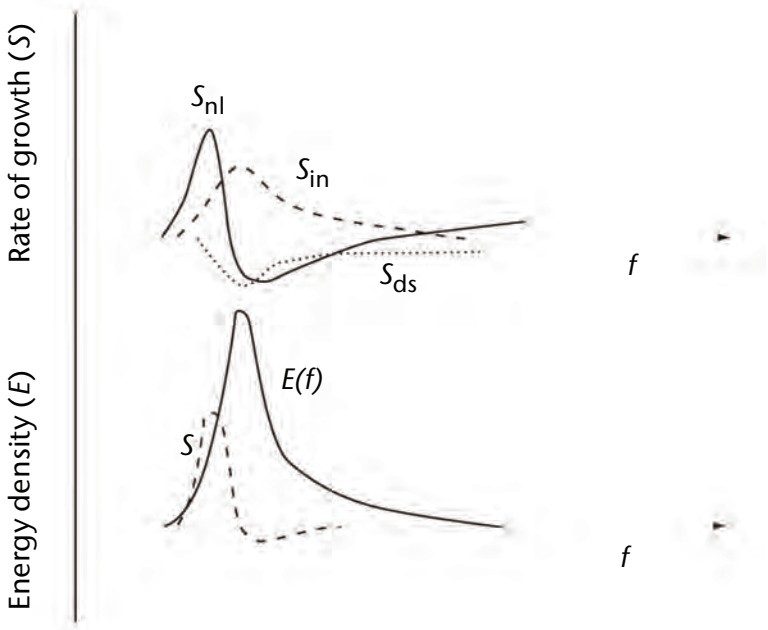

Figure 3.7. Structure of spectral energy growth: the upper curves show the components S_{nl}, S_{in} and S_{ds}, and the lower curves are the frequency spectrum $E(f)$ and the total growth curve S

without a prescribed shape for the wind-sea spectrum. Resonant weakly non-linear wave–wave interactions are just one facet of the non-linear problem. When the slopes of the waves become steeper and the non-linearities become stronger, modellers are forced to resort to weaker theories and empirical forms to represent processes such as wave breaking. Section 3.4 has mentioned these aspects.

Three wave interaction terms (also referred to as "triads") become important in shallow waters. In deeper water dispersive waves, these terms are non-resonant and hence do not play a role in the interaction process. But in shallow waters, as the waves become non-dispersive, these

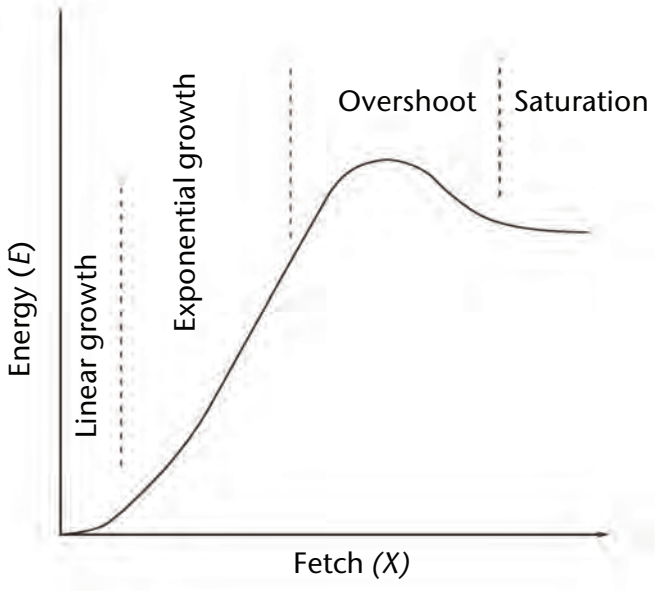

Figure 3.8. Development of wave energy at a single frequency along an increasing fetch, illustrating the growth stages

terms play an important role in skewing the waves and pitching them forward (Elgar and Guza, 1985). These interaction terms lead to the generation of super- and sub-harmonic components. Although some semi-empirical formulations have been developed (Eldeberky and Battjes, 1995; Eldeberky, 1996), this is still an area of active research for phase-averaged wind-wave models (see WISE Group (2007) for a comprehensive review).

3.6 GENERAL NOTES ON SOURCE TERMS

The overall source term is $S = S_{in} + S_{ds} + S_{nl}$. Ignoring the directional characteristics (looking only at the frequency dependence), a diagram for S can be constructed, such as in Figure 3.7. This gives an idea of the relative importance of the various processes at different frequencies. For example, it can be seen that non-linear transfer is the dominant growth agent at frequencies near the spectral peak. Also, for the mid-frequency range (from the peak to about twice the peak frequency), the direct input from the atmosphere dominates the growth. The non-linear term relocates this energy mostly to the lower-frequency range. The dissipation term, so far as is known, operates primarily in the mid- and high-frequency ranges.

Figure 3.9 illustrates the development of a frequency spectrum along a fetch, with a set of spectra measured during the JONSWAP experiment. The downshift in peak frequency and the overshoot effect at each frequency are evident.

Application of the source terms is not always straightforward. The theoretical–empirical mix in most wave models allows for some "tuning" of the models. This also depends on the grid, the boundary configuration, the type of input winds, the time step, the influence of depth, the computer power available and so forth. However, manual methods conform to what may be regarded as universal rules and can usually be applied anywhere without modification.

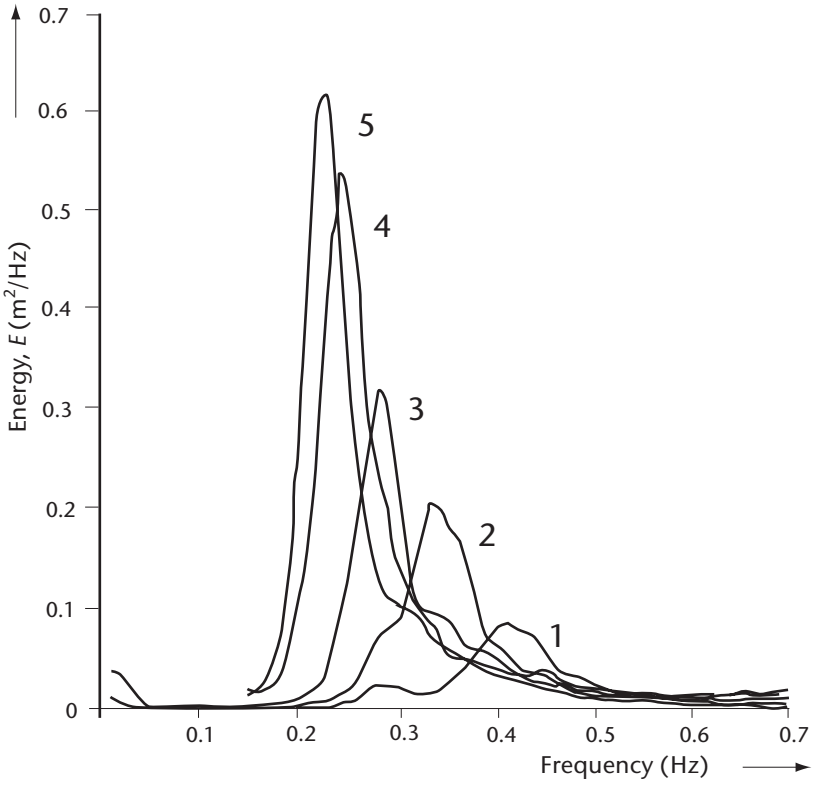

Figure 3.9. Growth of a frequency spectrum along a fetch. Spectra 1–5 were measured at distances of 9.5, 20, 37, 52 and 80 km, respectively, offshore. The wind was 7 m s^{-1}.

Source: Hasselmann et al. (1973)

For manual calculations, the distinction between wind sea and swell is real and an essential part of the computation process. It is necessary for the hybrid parametric models (see section 5.5.2), although the problem of interfacing the wind-wave and swell regimes arises. The definition of swell is arbitrary for numerical models that use spectral components for all the calculations (discrete spectral models). From the spectrum alone, there is no hard and fast rule for determining the energy that was generated locally and that which was propagated into the area. This can pose problems when attempting to interpret model estimates in terms of features traditionally understood by the "consumer". Many users are familiar with, and often expect, information in terms of "wind sea" and "swell". One possible algorithm is to calculate the Pierson–Moskowitz spectrum (section 1.3.9) for fully developed waves at the given local wind speed, and, specifying a form for directional spreading (section 3.3.1), allocate energy in excess of this to a swell spectrum. Sophisticated algorithms assess a realistic cut-off frequency for the local generation conditions. These may be considerably higher than the peak frequency from the Pierson–Moskowitz spectrum and hence also designate as swell excess low-frequency wave energy at directions near the wind. Spectral partitioning algorithms have been developed in recent years to identify the underlying sea states that make up the ocean spectrum (see section 6.2 for details).

CHAPTER 4. MANUAL WAVE FORECASTING

Editor: L. Burroughs, updated by D. Mercer, J. Mclean and S. Desjardins

4.1 INTRODUCTION

There are many empirical formulae for wave growth that have been devised from large, visually observed datasets. There are also formulae, more recently derived, that are based on wave measurements. These formulae make no attempt to separate the physical processes involved. They represent the net wave growth from known properties of the wind field (wind speed and direction, fetch and duration).

There are some inherent differences between visually and instrumentally observed wave heights and periods that affect wave prediction. In general, the eye concentrates on the nearer, steeper waves and so the wave height observed visually approximates the significant wave height ($H_{1/3}$), while the visually observed wave periods tend to be shorter than instrumentally observed periods. There are several formulae that have been used to convert visual data to $H_{1/3}$ accurately. For almost all practical meteorological purposes, it is unlikely to be worth the transformation. Operationally useful graphical presentations of such empirical relations have existed since the mid-1940s.

The curves developed by Sverdrup and Munk (1947) and Pierson, Neumann and James (PNJ) (1955) are widely used. The two methods are similar in that the basic equations were deduced by analysing a great number of visual observations by graphical methods using known parameters of wave characteristics. However, they differ fundamentally in the way in which the wave field is specified. The former method describes a wave field by a single wave height and wave period ($H_{1/3}$ and $T_{1/3}$), while the latter describes a wave field in terms of the wave spectrum. The most obvious advantage of the PNJ method is that it allows for a more complete description of the sea surface. Its major disadvantage is the time necessary to make the computations.

Gröen and Dorrestein (GD) later developed another set of curves (Gröen and Dorrestein, 1976). These comprise a variety of formats for calculating wave height and period given the wind speed, fetch length, wind duration, and the effects of refraction and shoaling. These curves differ little from the PNJ curves, except that the wave height and period are the characteristic wave height (H_c) and period (T_c) rather than $H_{1/3}$ and $T_{1/3}$, and the International System of Units is used rather than units of feet and knots. The PNJ and GD curves are derived from visually assessed data. The only difference between "characteristic" and "significant" parameters (H_c and $H_{1/3}$, and T_c and $T_{1/3}$) is that H_c and T_c are biased slightly high when compared to $H_{1/3}$ and $T_{1/3}$, which are assessed from instruments. However, the differences are insignificant for all practical purposes.

Breugem and Holthuijsen (BH) refined previous results and produced a new set of equations (Breugem and Holthuijsen, 2007). The main differences with previous work were the additions of the significant wave height H_{m0} and the peak period T_p, adjusting the typical hyperbolic tangent function fit to give more flexibility to fitting the intermediate zone between fully developed seas (Pierson and Moskowitz, 1964) and the initial growth zones (Kahma and Calkoen, 1992), and incorporation of data from newer field studies. Mercer (2008) took these new equations and generated a nomogram structured like that of GD, but reformatted slightly for ease of operational use. Winds were in knots, fetch in nautical miles, peak period in seconds and wave heights in metres.

Figure 4.1 shows the BH curves for deep water. This figure is of the form introduced in Figure 3.1 (section 3.2) and will be used in wave calculations in this chapter. The GD curves are presented in Annex 1 for comparison. In Figure 4.1, thick red lines represent the growth of waves along increasing fetch, which is shown by green oblique lines. Each thick red line corresponds to a constant wind speed. The significant wave height H_{m0} is obtained from the horizontal black lines and the peak period T_p from the blue lines. The vertical lines indicate the duration in hours

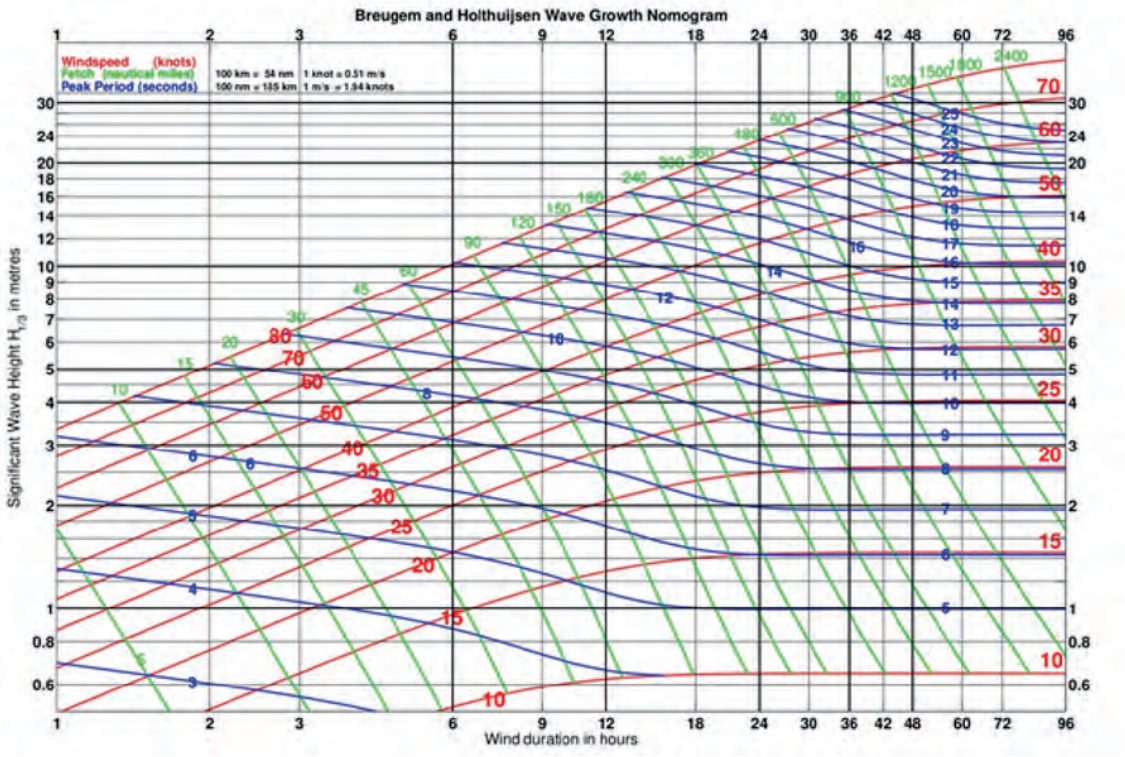

Figure 4.1. Manual wave-growth nomogram

Source: Breugem and Holthuijsen (2007)

at which that stage of development will be reached from zero wave height. If the duration is limited, waves will not develop along the thick dark lines beyond that point, irrespective of the fetch length.

The curves are nearly horizontal on the right-hand side of the diagram. This implies that for a given wind speed, the waves stop growing and reach a fully developed state when the duration and fetch are long enough.

Of the formulae that have been devised from measured wave data, the most notable are those from the Joint North Sea Wave Project (JONSWAP) experiment that was introduced in section 1.3.9 (see also Figure 1.17 and Equation 1.49).

This chapter presents some manual forecasting examples. Each example is designed to show how to make a forecast for a given set of circumstances and/or requirements. Section 4.2 mentions some empirical working procedures. These procedures have proved their value in practice and are alluded to in sections 4.3 and 4.4. Section 4.3 gives examples highlighting the various aspects of computing wind-wave growth. Section 4.4 gives examples of swell computations. Sections 4.3 and 4.4 give examples related to deep-water conditions. Shallow-water effects on waves were discussed in Chapter 3, and section 4.5 presents a few examples of manual applications related to shallow-water (finite-depth) conditions. Table 4.1 provides a summary of each example given, and shows where it can be found. Section 4.6 discusses how to determine when to use manual techniques to modify wave forecasts generated by wind and wave models, and also an approach for how to do it. Section 4.7 describes considerations and tips in rip current forecasting.

The explanations given in this chapter and in Chapter 2 provide, in principle, all the material necessary to forecast waves for a particular location and also to perform a spatial wave analysis (analyse a wave chart) by manual methods. A great deal of experience is necessary to analyse an entire chart within reasonable time limits, mainly because there are constantly changing wind conditions.

Table 4.1. Specific examples of manual forecasting presented in Chapter 4

Description	*Subsection no.*
Determining sea-state characteristics for a given wind speed and fetch	4.3.1
Determining sea state for an increasing wind speed	4.3.2
Extrapolating an existing wave field with further development from a constant wind	4.3.3
Extrapolating an existing wave field with further development from an increasing wind	4.3.4
Estimating wave growth due to dynamic fetch in three cases	4.3.5
Computing when swell will arrive, what periods it will have and how these periods will change for 36 h after arrival begins	4.4.1
Same as 6, except for a long fetch in the generation area	4.4.2
Computing swell characteristics at Casablanca for a storm of nearby origin	4.4.3
Estimating the swell heights for the cases described in 6, 7 and 8	4.4.4
Determining wave number and shoaling factor for two wave periods and several representative depths	4.5.1.1
Finding the shallow-water refraction factor and angle, for a given deep-water wave angle with the bottom, shallow depth and wave period	4.5.1.2
Finding the refraction factor by Dorrestein's method	4.5.1.3
Finding the shallow-water height and period for a given wind speed, shallow-water depth and fetch	4.5.2

It is usual to start from known wave and wind conditions, say 12 h earlier, and then compute the corresponding wave chart using the present analysed wind chart. In cases of sudden wind changes, the intermediate wind chart from 6 h earlier may also be needed. The forecast wind in the generation area and the forecast movement of the generation area are also necessary to produce the best wave forecast over the next 24–36 h.

With the current availability of several wave models, including ensembles with global coverage, most forecasters normally use numerical guidance, some of which may have significant differences, and come up with the most likely solution. Section 4.6 discusses a typical strategy to use available observations and manual techniques to address any biases or potential errors in the numerical guidance, and then to modify the model forecast accordingly.

4.2 EMPIRICAL WORKING PROCEDURES

This section briefly discusses several empirical procedures. They cover variable winds, wave growth and decay, speed and motion of wave fields, fetch length and others. These procedures are useful when time is short for preparing a forecast or as a reality check on numerical guidance. The main variables addressed in wave forecasting are wind velocity, duration of winds, fetch length and width, and initial wave characteristics. The objective is to forecast wave heights, periods and directions. A summary of the tips and techniques from this section and previous chapters is given in Annex 2.

4.2.1 Variable winds

- If the wind direction changes by 30° or less, wave heights and periods are computed as if no change had occurred; the wave direction is assumed to be aligned with the mean direction. With greater directional changes, the existing waves are treated as swell, and the newly generated waves are computed with the new wind direction.
- Freshening wind at constant direction is a frequent occurrence, and the procedure described in section 4.3.4 should be used. For quick calculations, subtract one quarter of the amount the wind has increased by from the new wind speed, and work with the value thus obtained.
  Example:
  The wind speed has increased from 10 to 20 knots (1.94 knots = 1 m s^{-1}) over the last 12 h; to compute the characteristic wave height, use a wind speed of 17.5 knots over a duration of 12 h. When sharp increases of wind speed occur, it is advisable to perform the calculation in two stages.
- When the wind speed drops below the value needed to maintain the height of existing waves, or there is a change in wind direction greater than 30°, the waves turn into swell and should be treated as such. Thus, it would be necessary to calculate waves for the new lower wind speed, and combine them with the swell generated by the earlier higher winds.
- Winds on currents. For opposing currents, add the current speed to the wind speed to get the effective wind speed. For currents moving in the same direction as the wind, subtract the current speed from the wind speed instead.

4.2.2 Estimating fetch

- Fetch is the distance over which a wave field is forced by an approximately constant wind velocity. A fetch box is defined by the length and width of an area of roughly constant wind velocity, with the length aligned with wind. Wind directions should be within about 30° of the mean wind, and wind speeds within the box should be within 5–10 knots of the mean. When the wind field is forecast to change significantly in direction and/or speed, the fetch box is adjusted in position, orientation and dimensions. Figure 4.2 shows examples of fetch boxes, including how to determine which ones will affect a given point. Normally, the task will be to calculate the wave field at a point, so the fetch boxes needed would be those that will send significant waves to the target point. Section 4.2.3 discusses wave growth within the boxes, and section 4.2.4 summarizes swell propagation after the waves leave the boxes.
- For tropical cyclones (TCs), if the wind field is roughly symmetrical about a system, the fetch box length is defined as in Figure 4.3. The fetch width is defined as before, using the radial bandwidth of similar wind velocities. The fetch length is simply equal to the radial distance to the band of winds selected.
- For dynamic or trapped fetch, if the area of forcing winds moves along with the waves, this is equivalent to a longer fetch box forcing the waves. For example, a fetch box 50 nautical miles long is moving east at 10 knots, over a wave field of the same size moving in the same direction at an average group velocity of 20 knots. After 5 h, the fetch box moves 50 nautical miles while the wave field moves 100 nautical miles, and after that the entire wave field is ahead of the wind field. If the fetch box (or wind field) was stationary, the maximum fetch for the wave field would be 50 nautical miles. But for the moving case, the maximum fetch would be 100 nautical miles. This is common for TCs at mid-latitudes, and for some frontal passages. Section 4.3.5 gives an example.

4.2.3 Wave growth

- Accurate wind forecasts are essential. Wave energy is proportional to the square of the wave height, which, in turn, is proportional to the square or cube of the wind speed.
- For a fully developed sea, $H_{1/3} \cong (U_{10}/12.5)^2$, where U_{10} is the 10 m wind in knots.

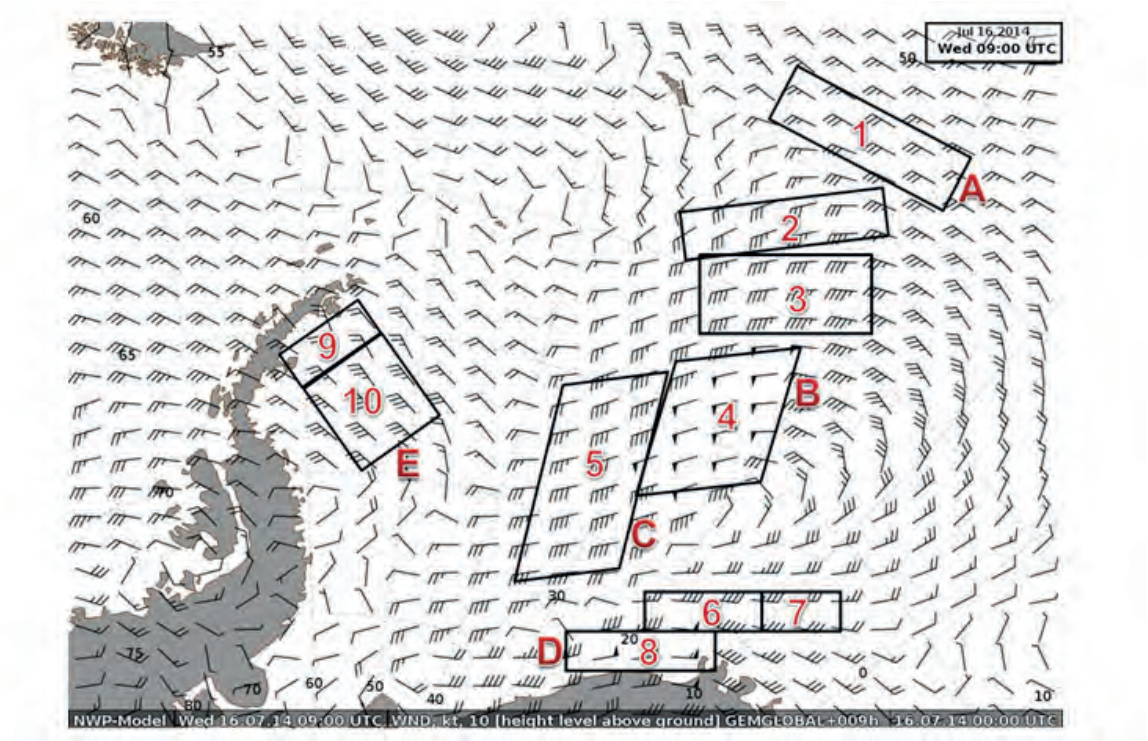

Figure 4.2. Fetch boxes for a storm in the Weddell Sea, Antarctica. This shows examples of how to choose fetch boxes for given points, such as a ship location. The fetch boxes here are determined by wind speeds being within 5 knots of the mean wind speed in the box, and by wind direction being within 30° of the mean wind direction. Point A is affected by Boxes 1 and 2. Point B is affected by Boxes 4 and 5, point C is affected by Box 5 only and point E is affected by Boxes 9 and 10. Point D is affected by Box 8, and also by north-westerlies from Boxes 9 and 10. Boxes 3, 6 and 7 do not directly affect any of the points, but Box 3 might become important if point A moves south, and Boxes 6 and 7 may affect point D if it moves north.

- For the nomogram basic method, see Figure 4.1. For a given wind speed, follow the wind speed line from the left until the desired fetch length or duration is reached. Then, read off the wave height and the peak period:
  - If the waves are fetch limited, the fetch line will be reached before the desired duration line. Stop at the maximum fetch and read the wave height and period. As a bonus, the duration needed to reach that fetch will also be obtained.
  - Similarly, if the wave height is duration limited, the maximum duration line will be reached before the desired fetch. Again, stop at the duration line and read off the wave height and period, and the fetch needed for that duration will be obtained.
  - If starting with an existing sea state, follow the appropriate wind-speed line until that wave height is reached, then continue on for the required duration and/or fetch. For example, there are seas of 2 m and a wind speed of 25 knots, and the seas after 12 h need to be calculated. Follow the 25 knot line to the 2 m wave height (at 6 h on the nomogram) then continue along the line for another 12 h. This will give a wave height of 3.5 m with a period near 8.5 s.

4.2.4 Swell decay

- Swell height usually decays about 25% in 12 h, and 40% in 24 h.
- Swell heights are almost unaffected by opposing winds.
- For distant swell, angular spreading usually dominates over dispersion effects. See section 3.3.1.

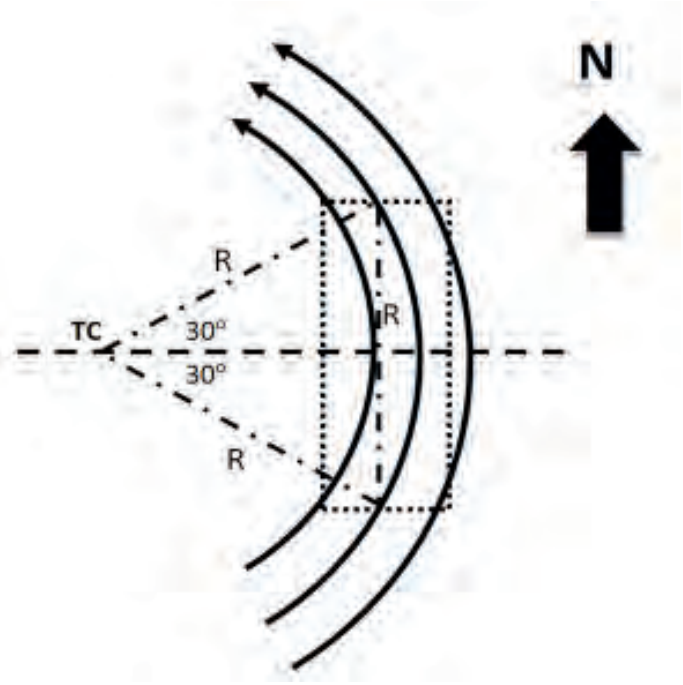

Figure 4.3. Fetch for an idealized TC. TC indicates the storm centre, R is the radial distance to the band of winds indicated by the curving arrows and the dotted rectangle is the fetch box for waves moving north. As the fetch box is defined by winds blowing within 30° mean wind velocity in the box, the triangle formed by the dash-dotted lines is equilateral, and therefore the fetch length is approximately equal to the radial distance to the band of winds. For a rapidly moving storm, this fetch relation would need adjustment for dynamic fetch.

4.2.5 Speed and motion of wave groups

- Wave group speed c_g (in knots) $\cong 1.5T_p$ where T_p is the peak period (in seconds). Similarly, the 12 h movement in degrees is $0.3T_p$. Remember that waves travel along great circles.

- For wind-wave movement, average the peak period. Example: A wave grows during 12 h going from an 8 s wave to a 12 s wave. A 10 s average gives a movement of 3° in 12 h using $0.3T_p$.
- For swell movement, do not use the average peak period. Swell increases in peak period over time, as does the swell group velocity. Dispersion of deep-water waves will spread the swell field over a growing area with distance from the source; averaging the period will overestimate propagation time for the longer swells. Swell decay nomograms take this into account.

4.2.6 Miscellaneous

- Combine wave heights by summing the squares then take the square root:

$$H_{\text{tot}} = \sqrt{H_1^2 + H_2^2 + H_3^2 \cdots}.$$

- Waves moving into currents moving in the same direction increase in wavelength and reduce steepness. Waves moving into opposing currents reduce wavelength and steepen. In fact, if the group velocity of the waves ($c_g = 1.52T_p$ in knots) is near the speed of the opposing current, wave breaking is likely. Most currents are much slower than typical wave speeds, but look for shallow water and strong tidal currents, and major ocean currents such as the Gulf Stream.
- There are two cases to consider for waves approaching sea ice. For a solid ice sheet, short-period waves are dissipated or are partially reflected near the ice edge, and waves with long periods may be transmitted as flexural waves into the ice sheet. In either case,

assume the waves keep their amplitude until hitting the edge, then drop to zero. For ice floes or pans partially covering the surface upon moving into the main pack, wave energy is dissipated and/or scattered, which usually occurs over less than 4–8 km. So again, assume the waves diminish quickly. For waves generated downwind of an ice field, assume initial wave heights of zero and that they grow normally (maybe drop the wave heights slightly if there are some ice floes downwind of the pack).

– High/low stability in the lower boundary layer will reduce/enhance surface wind stress, resulting in lower/higher waves. Lower temperatures result in higher density air at constant pressure. This effect is linear with absolute temperature. It can be significant at middle to high latitudes, where winter temperatures can often be 30°C or more colder than those in summer, and can give surface wind-stress levels higher by 10% or more for the same wind speeds in winter.

4.3 COMPUTATION OF WIND WAVES

Unless otherwise specified, wave heights are assumed to be significant wave heights, $H_{1/3} \cong (H_{m0}$, and the period for the wave field is assumed to be the peak period T_p.

4.3.1 Determination of sea-state characteristics for given wind speed and fetch

Problem

Determine the characteristics of the sea state for a wind speed of 15 m s^{-1} (about 30 knots), with a fetch of 600 km (about 325 nautical miles), after a duration of 36 h.

Solution

The fetch is the limiting factor according to the diagram in Figure 4.1. For a fetch of 600 km, the significant wave height (H_{m0}) is 5 m and the peak period (T_p) is 10.3 s.

To determine the significant wave period $T_{H1/3}$, the results of Goda (1978) are used in an approximate form: $T_{H1/3} \cong 0.9T_p \cong$ x 10.3 $\cong$ 9.3 s.

The range of important wave periods can be determined from Figure 1.17, where peak frequency f_p (= $1/T_p$) varies from $0.7f_p$ to $2.0f_p$. This translates to a range of 5–15 s. The maximum energy in the spectrum will be near the period of 10 s.

To estimate maximum wave height, and recalling Equation 1.27, $H_{max} \cong H_{m_0}\sqrt{(\ln N)/2}$ where N is the number of waves in a given time period. For a duration of 6–48 h, $H_{max} \cong 2H_{m0} \cong$ x 10 m, but for an hour, the typical period between wave observations from buoys and ships, it is less. In that case, for 10.3 s waves, $N \cong 350$, then $H_{max} \cong 1.7H_{m0} \cong 8.5$ m. In summary, H_{m0} =5.0 m, T_p = 10.3 s m, the range of periods of significant wave height is 5–15 s, and the maximum expected wave height in an hour is 8.5 m (over a long period, it would be 10 m).

4.3.2 Determination of sea state for increasing wind speed

Problem

An aeroplane had to ditch at sea 100 nautical miles from shore. The closest ship is positioned 400 nautical miles from shore. The wind speed over the last 24 h has been steady at 35 knots. During the preceding 24 h, it gradually increased from 25 to 35 knots. The wind direction remained constant for the entire period and blew towards 240° (30° offshore of the coast). Figure 4.4 illustrates the situation.

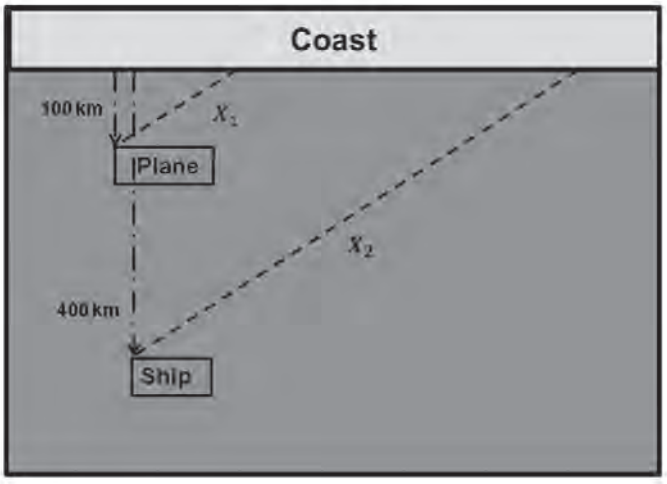

Figure 4.4. Illustration of the situation in problem 4.3.2

Forecast the sea conditions for:

- The point at which the aeroplane ditched, to determine whether a search and rescue seaplane could land and rescue the pilot, or whether the nearest vessel should be dispatched – which would take more time?
- The position of the ship.

Solution

The effective fetch for the landing place of the aeroplane is

$$X_1 = \frac{100}{\sin 30} = 200 \text{ nautical miles,}$$

and the fetch for the ship is

$$X_2 = \frac{400}{\sin 30} = 800 \text{ nautical miles.}$$

This is an example of complicated wind duration conditions. During the first full 24 h period, the wind increased steadily from 25 to 35 knots, then stayed constant for the second 24 h. Recalling section 4.2.1, the first 24 h period is divided into two 12 h periods with the wind increasing from 25 to 30 knots in the first 12 h and from 30 to 35 knots in the second. Using the tip for increasing winds, and subtracting one quarter of the difference gives 28.75 knots followed by 33.75 knots; then, rounding off gives 29 knots for the first 12 h followed by 34 knots.

Use of the diagram in Figure 4.1 shows that, for a wind speed of 29 knots, wind waves reach a height of 3.7 m after 12 h. Now, for the second 12 h, the 34 knot wind speed starting at the 3.7 m height is used, and then for another 12 h from there. Note that because at 34 knots, 3.7 m would be reached after 8 h, the final "duration" would be 20 h using the 34 knot line. The diagram shows that at 20 h with a wind speed of 34 knots, the wave height is 5.9 m. At the beginning of the second full 24 h period, wave heights are 5.9 m; the wind speed is 35 knots and remains constant throughout the period. To work with a wind speed of 35 knots, the equivalent duration necessary to raise waves to a height of 5.9 m needs to be determined. It is 18 h. Thus, the equivalent duration for a 35 knot wind speed is 18 h + 24 h or 42 h. For these conditions, H_{m_0} = 7.5 m and T_p = 13.5 s.

For these conditions to occur, a minimum fetch of about 700 nautical miles is required. At the position of the nearest ship, there is no fetch limitation (800 nautical miles), but there is a fetch limitation at the position of the ditched aeroplane (200 nautical miles). Figure 4.1 shows that a fetch of 200 nautical miles would be reached after about 18 h, so the winds would have been constant at 35 knots for the entire time needed for waves from the shore to reach the fetch limit

at the ship. Winds blowing longer would not increase the waves at the ship. So for a wind speed of 35 knots and a 200 nautical miles fetch, H_{m_0} = 5.8 m and T_p = 11 s. Finally, the maximum wave heights would be about twice the height of H_{m_0} at both locations.

4.3.3 Extrapolation of an existing wave field with further development from a constant wind

Problem

Figure 4.5 shows a wave field at time t_0. Forecast the characteristics of the sea state at point B at the time t_0 + 12 h, with a constant west wind of 35 knots blowing at and to the west of point B.

Solution

The starting point for the calculation cannot be at point B because the waves currently there move away from it. A starting point must be sought upwind at a point where waves have travelled from time t_0 to arrive at B at time t_0 + 12 h.

To estimate how far upwind A should be from B, a point where the wave height is roughly 4 m (probably 4.2 m at A) should be chosen. Figure 4.1 shows that waves with H_{m_0} = 4 m and u = 35 knots have T_p = 8 s. After 12 h, T_p increases to about 11 s, and the mean period is about 10 s. The wave propagation rate is given by $c = gT / 2\pi$ and the group velocity is given by $c_g = c/2$ in deep water. As $g / 2\pi = 1.56$ m s^{-1} (or 3.03 knots), then the group velocity $c_g \approx 0.8T_p$ m s^{-1} or $\approx 1.5T_n$ knots . Waves with T_p = 10 s have c_g = 15 knots and, in 12 h, cover a distance of 180 nautical miles, or 3° of latitude. Dividing 3 by T_p = 10 gives 0.3. This example shows that the travel distance over 12 h, expressed in degrees of latitude, is $0.3T_c$. This is an easy formula to use to determine how far upwind to put A.

H_c equals 4.2 m at time t_0 at point A. To produce waves of that height, a wind of 35 knots needs an equivalent duration of 10 h. H_{m_0} at point B at t_0 + 12 h can be determined by taking a total duration of 10 h + 12 h = 22 h. From Figure 4.1, H_{m_0} = 6.5 m and T_p = 11.5 s. The maximum wave height over 2 000 waves would be about 13 m, and the maximum in any given hour would be about $1.7T_p$ = 11 m.

4.3.4 Extrapolation of an existing wave field with further development from an increasing wind

Problem

The situation at t_0 is the same as in Figure 4.5, but now the wind increases from 35 knots at t_0 to 55 knots at t_0 + 12 h over the area that includes the distance AB. Forecast the sea state at point B.

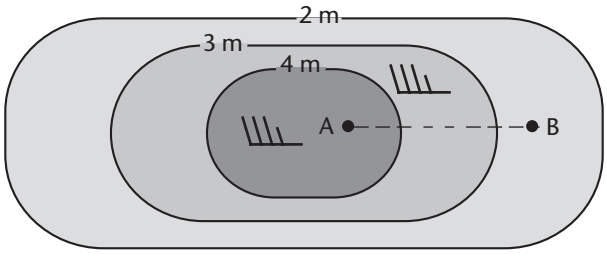

Figure 4.5. Wave field at time t_0 indicated by lines of equal wave height

Solution

As the increase in wind speed is so great, divide the time period into two 6 h periods with winds increasing from 35 knots at t_0 to 45 knots, and then from 45 knots to 55 knots. Recalling section 4.2.1, the corresponding speeds used to compute the waves are 43 knots (rounding from 42.5) and 53 knots (rounding from 52.5).

At t_0, H_{m_0} equals 4.2 m. Waves grow to this height with 43 knot winds after 5 h. Over the first period, the equivalent duration with wind speed u = 43 knots is 5 h + 6 h = 11 h. At the end of the first interval, H_{m_0} = 6.2 m. Waves would reach the 6.2 m height after an equivalent duration of 7 h with a wind of 53 knots. Over the second 6 h period, it is possible to work with an equivalent duration of 13 h and a wind of 53 knots. Thus, H_{m_0} = 9.0 m and T_p = 12.2 s.

4.3.5 Determination of the effects of a dynamic or trapped fetch for a tropical cyclone moving at different speeds

This exercise will show the effects of dynamic fetch using three cases involving a tropical storm, to demonstrate the impact of dynamic fetch on the wave field generated by a moving storm.

Problem

Consider a TC with maximum winds of 50 knots and a radius of maximum winds of 20 nautical miles. Using Figure 4.1, calculate the significant wave height generated by the highest winds in the storm and the fetch length for three cases (shown in Figure 4.6). Case A assumes the storm is stationary, case B assumes the storm then moves in a straight line at 5 knots for at least 6 h, and case C assumes that the storm then moves at the group velocity of the wave field for 24 h.

Solution

Case A: first the fetch length needs to be determined. The storm-relative fetch is easily calculated from the requirement that the wind be within 30° of the wave direction of interest. For a circle of radius 20 nautical miles, the fetch F is $F = 2R\sin(30)$ where R is the radius of maximum winds, and is trivially 20 nautical miles. For slowly moving or stationary TCs, the relation for fetch length $F = R$ is a good general rule (see Figure 4.3).

Given a fetch of 20 nautical miles and 50 knot winds, 3.3 m waves are generated with a period of 6.5 s. From the nomogram, this would have taken 2.75 h; after this, the waves generated would be fetch limited and would stay at 3.3 m height. The group velocity of the largest waves would be about 1.5 × 6.5 = 9.8 knots. Round this to 10 knots, for convenience.

Case B: the waves are moving faster than the fetch area under the storm (5 knots), and will eventually move out ahead of the storm and become swell. However, they will spend more time being forced than if the fetch area was stationary. If the group velocity is assumed constant, then relative to the storm, the waves are moving forward at 5 knots across a fetch box of 20 nautical miles, implying that the wave can continue to grow for a maximum of 4 h. On the nomogram, on the 50 knot line, start at 3.3 m then move right for another 4 h to get 5.5 m and 9 s.

However, this would be an overestimate, as the period (and hence the group speed) increased from 6.5 to 9 s, and the lowest speed was used, thus giving more time under the fetch area. To improve this slightly, use an average period of about 8 s, giving a group speed of 12 knots, allowing an additional 1.7 h under the fetch. Again, starting at 3.3 m on the 50 knot line, move right another 1.7 h, reaching 4.4 m.

So, the fetch moving in the same direction as the waves it generates prolongs the period of time that the waves are being forced, which is equivalent to the waves being forced by a longer fetch length. This is called dynamic fetch or trapped fetch. The most extreme dynamic fetch occurs when the storm's fetch area stays over the waves being generated, and accelerates as the growing waves accelerate, thus maximizing the effective fetch for wave generation.

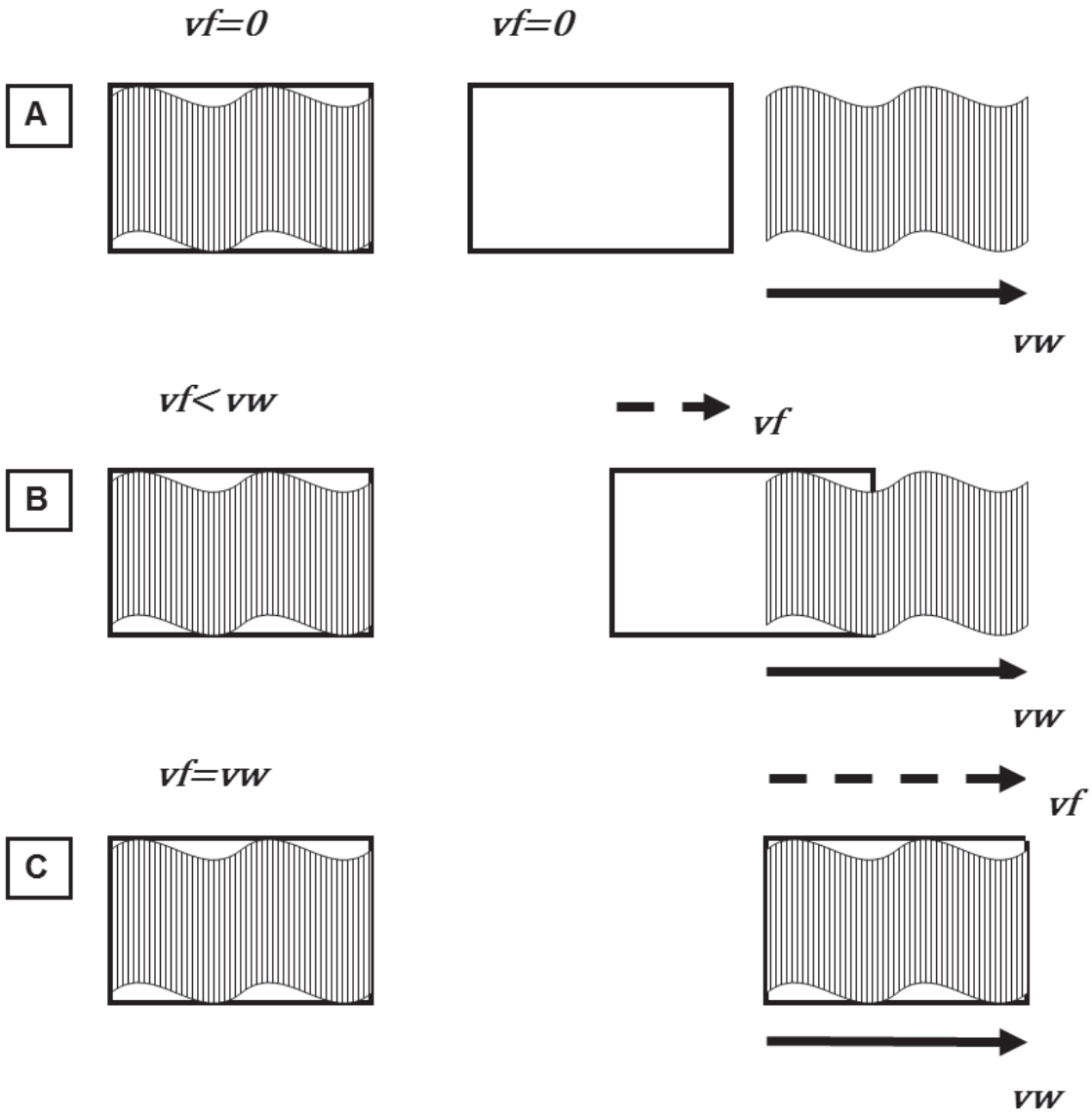

Figure 4.6. Cases A, B and C for trapped fetch exercise. Rectangles are the fetch area under the storm. Wavy areas are the wave fields initially generated under the storm. Solid arrows indicate wave speed (*vw*), dashed arrows show the speed of the fetch area (*vf*). The left-hand side shows the initial state and the right-hand side the final state. For case A, the fetch is stationary and the waves move out of the fetch box. For case B, the fetch box is slower, but the rear side of the wave field is still being forced. For case C, the entire wave field is still in the fetch box and continuing to be forced, giving an optimal dynamic fetch.

Case C: as the waves are being continuously forced, the calculation is simple. Start at 3.3 m on the 50 knot line on the nomogram, then move to the right 24 h. The resultant significant wave height is 12.2 m with a period of 15.5 s. From the nomogram, this is equivalent to about a 480 nautical mile fetch, and from the period, the group speed is 23 knots. The final wave field is almost four times as high as that of a stationary storm, and the dynamic fetch length is 24 times as long as the storm-relative fetch length of 20 nautical miles.

Ideal growth situations seldom occur. The trajectory and speed of the storm must closely parallel those of the wave field being generated, and storms usually do not stay on a great circle for more than a day. If the storm is slower than the wave field, waves move out ahead of the storm and become swell, gradually spreading and dispersing. If the storm is faster than the wave field, the waves fall behind and diminish. Waves generated by dynamic fetch often give little warning as they approach a point. Recall that as waves grow, the peak period grows and the distribution of

energy in the spectra shifts to lower frequencies, becoming more highly peaked near the longest periods. This implies that for a good dynamic fetch case, there will be little indication of high waves approaching ahead of a storm, especially from a TC.

4.4 COMPUTATION OF SWELL

For most practical applications, two different situations need to be considered:

- Swell arriving at the point of observation from a storm at a great distance (600 nautical miles or more). In this case, the dimensions of the wave-generating area of the storm (for example, a TC) can be neglected for most swell forecasting purposes, so that the storm is regarded as a point source. The important effect to be considered is wave dispersion.
- Swell arriving at the point of observation from a nearby storm. Swell fans out from the points along a storm edge. Because of the proximity of the storm edge, swell may reach the point of observation from a range of points on the storm front. Therefore, the effect of angular spreading should be considered in addition to wave dispersion. The propagation of wave energy is of interest in swell computations. Therefore, the group velocity of individual wave components should be considered. As large distances are often involved, it is convenient to measure distances in units of nautical miles and group velocities in knots. The wave period T is measured in seconds as usual. This gives (as in section 1.3.2)

$$c_g = \frac{c}{2} = \frac{gT}{4\pi} = 1.517T \text{ (knots)}. \qquad (4.1)$$

4.4.1 Distant storms

In the case of a distant storm (Figure 4.7), the questions to be answered in swell forecasting are:

- When will the first swell arrive at the point of observation from a given direction?
- What is the range of wave periods at any given time?
- What wavelengths are involved?
- What will the height of the swell be?

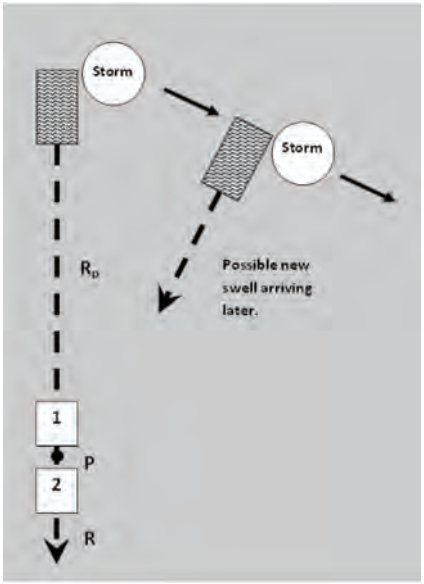

Figure 4.7. Swell from a distant storm. Waves travelling in the direction of P have been generated over a time period D_p

The known data to start with are the distance R_p (in nautical miles) from the nearest storm edge to the point of observation P, the duration D_p of wave generation in the direction of P and the maximum wave period in the storm area.

Because they travel faster, the wave components with the maximum period are the first to arrive at P. Their travel time (in hours) is

$$t = \frac{R_p}{c_g} = \frac{R_p}{1.517T} = 0.659\frac{R_p}{T}. \tag{4.2}$$

These components continue to arrive over a period of D_p hours, then they disappear. D_p is determined from weather charts by examining how long a given fetch remained in a given area. In the meantime, slower wave components have arrived, and in the present example, each component is assumed to last for D_p hours. There is a wave component so slow that it starts to arrive at the moment when the fastest wave component present is about to disappear (compare Boxes 1 and 2 in Figure 4.7). The first wave of the slow component (Box 2) with period T_2 has travelled over a time of t hours; the last wave of the fast component (Box 1) with period T_1 has started out D_p hours later and has thus travelled over a time of $(t - D_p)$ hours. For the slow component,

$$T_2 = \frac{R_p}{1.517t} = 0.659\frac{R_p}{T}, \tag{4.3}$$

and for the fast component,

$$R_p = c_g(t - D_p) = 1.517(t - D_p)$$

or

$$T_1 = \frac{R_p}{1.517(t - D_p)} = 0.659\frac{R_p}{t - D_p}. \tag{4.4}$$

R_p is measured in nautical miles, t and D_p in hours, and T_1 and T_2 in seconds.

T_1 and T_2 are the limits of all wave periods that can possibly be present at P at a given time of observation. Some periods within this range may not be present in the observed wave spectrum; the components could be dissipated during their long travel outside the storm area. It can easily be shown from the above equations that the range of possible wave frequencies is given by

$$f_1 - f_2 = 1.517\frac{D_p}{R_p}. \tag{4.5}$$

This means that the maximum bandwidth (range) of frequencies of wave components that exist at a given point of observation is a constant for that point and depends on the duration of wave generation D_p. The range of frequencies becomes smaller at greater distances from the storm. This result, obtained from a schematic model, is indeed observed. Thus, as for the result of wave dispersion, swell attains a more regular appearance at greater travel distances.

Example of swell from a distant storm

Problem

Waves were generated in the direction R for 18 h. The longest wave period generated in the storm was 15 s. Forecast swell for point A at 600 nautical miles from the area of generation. Compute when the first waves arrive and which periods could possibly be present during the subsequent 36 h.

Solution

At point A, R_p = 600 nautical miles, D_p = 18 h and T_{max} = 15 s.

From Equation 4.2, the first waves arrive at $t = 0.660 \times 600/15 = 26.4$ h after the beginning of the storm. Waves of this period continue for 18 h after they first arrive.

Table 4.2. Range of swell periods and wavelengths at point A for arrival times after the beginning of the storm

Arrival time (h)	*Period (s)*	*Wavelength (m)*
30	15.0–13.2	351–272
36	15.0–11.0	351–189
42	15.0–9.4	351–138
48	13.2–8.2	272–105
54	11.0–7.3	189–83
60	9.4–6.6	138–68
66	8.2–6.0	105–56

The range of periods ($T_1 - T_2$) at point A are computed for the 36 h after the arrival time of the first wave at 6 h intervals beginning with 30 h after the storm as shown in Table 4.2. The range of wavelengths can also be given using the relation $\lambda = 1.56T^2$ (m). The wave components with a period of 15 s disappear after $t = 44.4$ h.

Long forecast times have been given to demonstrate the gradual change of wave periods. In practice, the shorter waves may not be noticeable after 2–3 d of travel time, and also after displacement of the storm in the case of a TC. However, a cyclone does not generate equal swell in all directions; this depends on the structure of the wind fields in the cyclone and the motion of the storm.

4.4.2 Distant storms with long fetch

Forecasting the waves from a distant storm with long fetch is a more complicated case, as the distance travelled by individual wave components inside the wave-generating area will generally not be the same for the various components. The longer and larger waves will usually be found in the downwind part of the storm area. For all practical purposes, an appropriate mean value for the distance S (see Figure 4.8) may be chosen and a corrected duration D'_p applied by adding to D_p the time needed by wave components to cover the "mean fetch" S:

$$D'_p = D_p + \frac{S}{c_{gi}} = D_p + \frac{S}{1.517T_1}, \tag{4.6}$$

where c_{gi} is the group speed of the component considered. It can be shown that in this case, the range of wave frequencies of the swell does not remain constant for a given point P but increases slightly as the larger components disappear, and the spectrum consists of progressively smaller components.

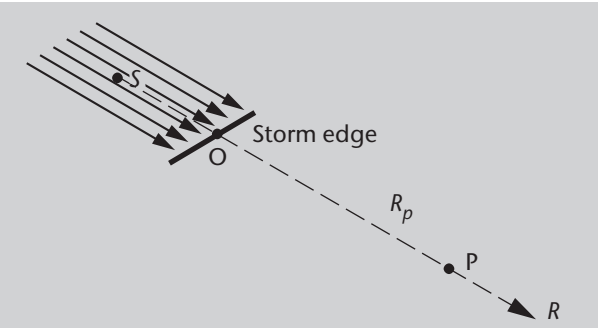

Figure 4.8. Swell from a quasi-stationary, distant storm, in which the waves travel over a distance *R*, and the generation area has a long fetch

Example of swell from a distant storm with long fetch

Problem

Referring to Figure 4.8, waves are generated in the direction *R*. The "mean" generation fetch is 180 nautical miles for waves with periods between 12 and 15 s; R_p = 600 nautical miles; D_p = 18 h. Find the wave conditions at P.

Solution

The corrected duration for waves with T = 15 s is D_p = 18 h + (0.66 × 180/15) ≦ 18 h + 8 h = 26 h. This component arrives at P 26.4 h after the storm as before, but disappears 26 h later. Likewise, the corrected duration for generation of waves with T = 12 s is D_p = 27.9 h. The travel time for this component to arrive at point P is t = 0.66 × (600/12) = 33 h. The last waves with T = 12 s pass point P at t = 33 h + 27.9 h = 60.9 h.

Table 4.3 gives the range of periods and wavelengths.

Comparison of the examples in sections 4.4.1 and 4.4.2 shows that, in the latter, the wave spectrum remains broader for a longer period. Because of the wide range of energetic periods, the swell will also have a less-regular appearance.

4.4.3 Swell arriving at point of observation from a nearby storm

As pointed out in the introduction to section 4.4, swell fanning out from different points of a nearby storm edge (less than 600 nautical miles) may reach the observation point. Therefore, when forecasting swell from a nearby storm, the effect of angular spreading should be considered in addition to wave dispersion.

For swell estimates:

- The sea state in the fetch area that has influence on the forecast point should be computed;
- The distance from the leading edge of the fetch area to the observation point should be measured;
- The period of the spectral peak and the range of wave periods about the peak should be found;
- The arrival time of the swell at the forecast point should be determined;
- The range of periods present at different times should be calculated;
- The angular spreading factor and the wave dispersion factor at each forecast time should be determined.

Table 4.3. Range of swell periods and wavelengths at point P for arrival times after the beginning the storm

Arrival time (h)	*Period (s)*	*Wavelength (m)*
30	15.0–13.2	351–272
36	15.0–11.0	351–189
42	15.0–9.4	351–138
48	15.0–8.2	351–105
54	14.1–7.3	310–83
60	12.0–6.6	225–68
66	10.4–6.0	169–56

The angular spreading can be calculated using the width of the fetch area and the distance from the leading edge of the fetch area to the forecast point in Figure 3.4 (see also section 3.3). This factor is a percentage of the energy, so when applied to a wave height, the square root must be taken.

From the JONSWAP results, Hasselmann et al. (1976) proposed a relation between sea-surface variance (wave energy) and peak frequency for a wide range of growth stages. Transforming their results into terms of H_{m_0} and f_p gives

$$H_{m_0} = 0.414 f_p^{-2} (f_p u)^{1/3}. \quad (4.7)$$

Equation 4.7, the JONSWAP spectrum (Figure 1.17) and the PNJ method can be used to find the wave dispersion factor at each forecast time at the forecast point. Figure 3.5 illustrates how the wave spectrum disperses over time. The following example also illustrates this.

Example

Figure 4.9 shows the storm that produced waves to be forecast at Casablanca. A review of previous weather charts showed that, in the past 24 h, a cold front had been moving eastwards. It travelled slowly, but with sufficient speed to prevent any waves from moving out ahead of the fetch. At chart time, the front was slowing down, and a secondary low started to develop. The forecast indicated that, as the secondary low intensified, the wind in the fetch area would change to become a cross-wind from the south. It was also expected that the front would continue its movement, but the westerly winds in the rear would decrease in strength. At chart time, the well-developed sea that existed in the fetch area would no longer be sustained by the wind.

Problem

The fetch area (hatched area in Figure 4.9) was 480 nautical miles long and 300 nautical miles wide at chart time. The winds in the area were west-north-west. The distance to Casablanca from the leading edge of the fetch (R_c) was 600 nautical miles. Determine all of the swell characteristics at Casablanca and their direction. For this exercise, use the Gröen and Dorrestein wave nomogram in Annex 1.

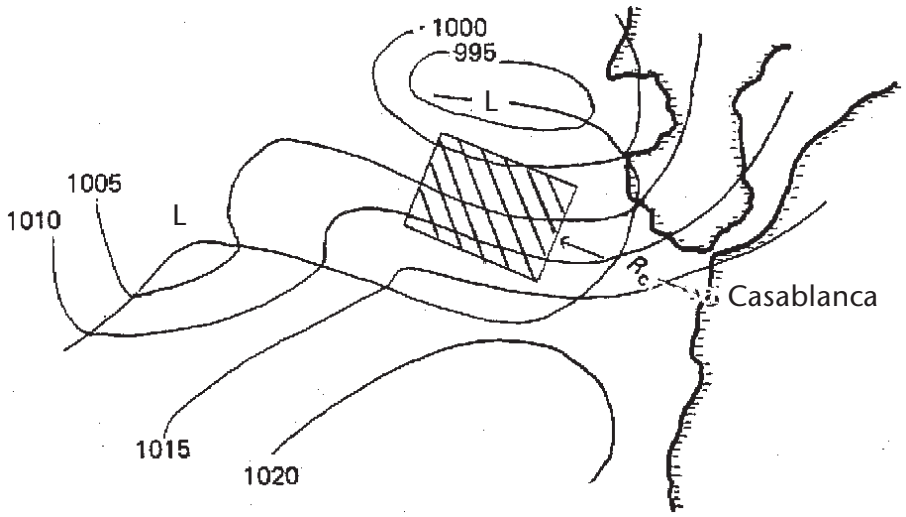

Figure 4.9. Weather situation over the North Atlantic at $t = 0$

Solution

During the past 24 h, the average wind speed was $u = 15$ m s^{-1} in the fetch area; for that wind, $H_c = 4.8$ m and $T_c = 8.6$ s. From Equation 1.49, $T_p = 10.1$ s and the range of important wave periods was from 14.4 s down to 5.0 s ($2.0f_p$ to $0.7f_p$). The first waves with a period of 14.4 s will arrive at the coast at.

$$t = \frac{0.659 \times 600}{14.4} = 27.5 \text{ h}$$

after chart time. Also, the waves with a period of 14.4 s cease to arrive at the coast in

$$t = \frac{0.659 \times (480 + 600)}{14.4} = 49.4 \text{ h.}$$

As the time to get from the rear of the fetch area for the wave components with $T = 14.4$ s was less than 24 h, Equations 4.3 and 4.4 can be used to determine the range of frequencies at each forecast time at Casablanca. Table 4.4 shows these ranges.

The angular spreading factor is determined from the ratio of R_c to the fetch width, 600/300 = 2. For this situation, the angular spreading factor is 30% (from Figure 3.4). This means that the height of swell observed at the shore of Casablanca should be less than $\sqrt{0.3 \times 4.8}$ or 2.6 m, or about half the initial wave height.

The wave dispersion factor at any given forecast time is the most difficult part of the forecast. A model spectrum must be chosen, and the mathematical integration of the frequency spectrum $S(f)$ should be carried out for the range of frequencies at each forecast time. In this example, Equation 1.49 is used in conjunction with the JONSWAP spectrum (Figure 1.17) to determine the range of important frequencies corresponding to $f_p = 1/T_p = 0.099$, that is, between $0.7f_p$ and $2.0f_p$ (1/14.4 = 0.069 Hz and 1/5.04 = 0.198 Hz), and the PNJ method is used to determine the fraction of energy in given ranges of frequencies (dispersion factor) arriving at any given time at Casablanca.

To determine the energy values, use the distorted co-cumulative spectra for wind speeds 10–44 knots as a function of duration from the PNJ curve (shown in Annex 1). The wind speed is 15 m s^{-1} (~30 knots). Determine where the upper and lower frequencies intersect the 30 knot

Table 4.4. Forecast of swell periods, wavelengths and heights at Casablanca for various times after the arrival of the longest period waves. H_c and angular spreading and dispersion multipliers are also shown (bracketed values in the last two columns are based on an approximation where the energy is assumed uniformly distributed over the range of periods).

Arrival time (h)	*Period (s)*	*Wavelength (m)*	H_c	*Angular spreading multiplier*	*Dispersion multiplier*	*Arriving wave height (m)*
30	14.4–13.2	323–272	4.8	0.55	0.35 (0.23)	0.9 (0.6)
36	14.4–11.0	323–189	4.8	0.55	0.63 (0.41)	1.7 (1.1)
42	14.4–9.4	323–138	4.8	0.55	0.75 (0.54)	2.0 (1.4)
48	14.4–8.2	323–105	4.8	0.55	0.90 (0.64)	2.4 (1.7)
54	13.2–7.3	272–83	4.8	0.55	0.84 (0.70)	2.2 (1.8)
60	11.0–6.6	189–68	4.8	0.55	0.73 (0.69)	1.9 (1.8)
66	9.4–6.0	138–56	4.8	0.55	0.62 (0.68)	1.6 (1.8)
72	8.2–5.5	105–47	4.8	0.55	0.40 (0.68)	1.1 (1.8)

curve, and find the E values that intersect with those points. For $f = 0.069$ Hz, $E = 51$. For $f = 0.198$, $E = 2.5$. The difference is 48.5. To calculate the dispersion factor at 36 h, find the E values for the periods arriving at that time and divide by the total energy: $(51 - 31.5)/48.5 = 0.402$.

The PNJ curves are used to find the proportion of energy in the given frequency ranges; for the significant wave height, it is preferable to use the BH curves (Figure 4.1).

The wave height is determined by multiplying the square root of the dispersion factor (the dispersion multiplier) by the square root of the angular spreading factor (angular spreading multiplier) by H_c. For 36 h, this is $\sqrt{0.042 \times 0.3} \times 4.8 = 1.7$ m.

At $t = 48$ h, a much larger part of the wave spectrum is still present with periods shifted to lower values (wave frequencies to higher values). The dispersion factor is $(51 - 12)/48.5 = 0.804$, and the wave height is given by $\sqrt{0.804 \times 0.3} \times 4.8 = 2.4$ m. Table 4.4 gives the various wave heights computed in this way.

A shorter method is that of Bretschneider (1952), who developed two empirical nomograms to predict swell period change and swell height change as a function of the fetch length and the propagation distance from the fetch area. They implicitly include decay from angular spreading and dispersion. While not as exact as the PNJ technique, they are fast and simple to use.

Using the initial wave height of 4.8 m (~16 feet) and Figure 4.10, a swell height factor near 0.475 is obtained, then $4.8 \text{ m} \times 0.475 \cong 2.3$ m. The maximum from the PNJ method shown in Table 4.4 was 2.4 m. The match was close, but it does not show the evolution of the swell heights at the observation point nor the time the peak waves would occur. To calculate the change in peak period, using Figure 4.11 shows that the peak period grows from 10 s to 13 s, at about the time the peak wave height occurred. The period spread in the table would be calculated as before.

This example has shown the common features of swell development as a function of time: a general increase in wave height at first and, over a long period of time, a constant height as the spectrum reaches its greatest width. Angular spreading, even for nearby fetch areas, is important. For more distant storms, angular spreading becomes the dominant decay term.

4.4.4 Further examples

Problem

Assuming that swell originates from a small fetch area of hurricane winds in a TC, and that the wind waves have a characteristic height of 12 m over a width of 120 nautical miles, estimate the swell heights in the cases described in sections 4.4.1 and 4.4.2 with the experience gained from section 4.4.3.

Solution 4.4.1

In section 4.4.1, the distance to point A was 600 nautical miles, or five times the fetch width. From Figure 3.3, the angular spreading factor is about 12%. Thus, the characteristic height of swell arriving at A should be less than $\sqrt{0.12} \times 12 = 4.2$ m.

The dispersion factor can be determined from the same PNJ graph as before (see Annex 1), but an effective wind speed needs to be determined because only the wave height is known. The effective wind speed is determined by following the line for a 15 s period on the PNJ graph to where it intersects the given wave height. The effective wind speed can be determined from the intersection point, in this case 21.5 m s^{-1} (43 knots). Then the E values can be determined, and the dispersion factors computed as in section 4.4.3. As the swell spectrum is broadest at 42 h, the wave heights are highest at that time. The dispersion factor is 0.8, giving a multiplier of 0.9, which leads to a characteristic wave height of 3.7 m when angular spreading is included in the computation.

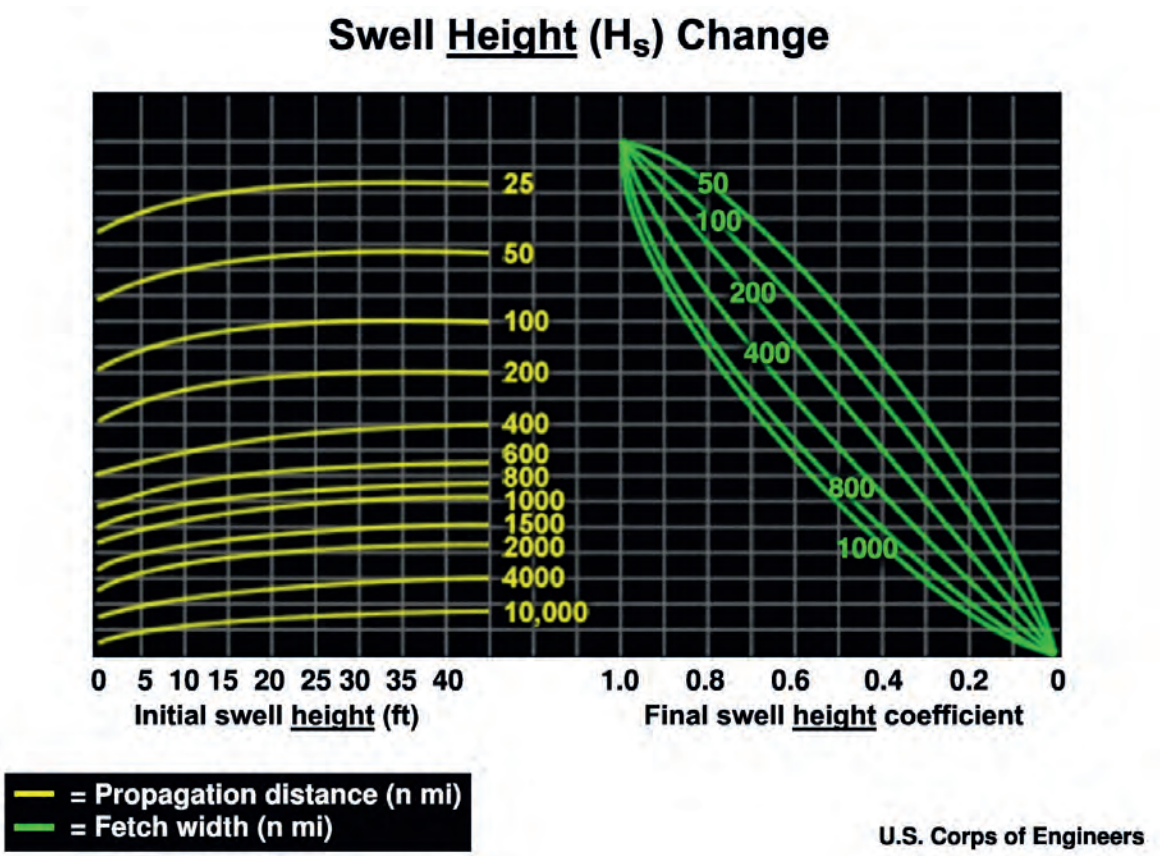

Figure 4.10. Bretschneider swell height decay nomogram. To calculate: choose the initial swell height(in feet) on the left horizontal axis, move vertically up to the propagation distance line in yellow (in n mi = nautical miles), then horizontally across to the correct fetch width line in green (really defined as fetch length, in n mi), then vertically down to the swell height coefficient. Multiply the initial swell height by this coefficient.

Sources: Bretschneider (1952), CERC (1977) and COMET (2011)

The height is small at first, when only long waves arrive at A. The wave heights are highest in the period between 40 h and 50 h (see Table 4.2), as the swell spectrum has its greatest width during that period.

The distance to point B is about eight times the width of the fetch area, which leads to an angular spreading factor of about 6%; therefore, the swell heights at point B should be no more than 2.9 m. Considering that the wave dispersion must have progressed further from point A to point B and that the smaller components may have been dissipated on their long journey as a result of internal friction and air resistance, wave dispersion factors can be computed from the PNJ curve, for each arrival time. The widest part of the spectrum, with the highest heights, passes point B about 60 h after generation. The dispersion factor for this time is 0.6, so the multiplier is 0.8; therefore, the characteristic swell height will be 2.3 m.

Solution 4.4.2

In section 4.4.2, the swell spectrum at point A was more complex. There was a range of generation wave periods from 12 to 15 s. There was also a limited fetch (180 nautical miles). The highest characteristic waves possible differ for each of these wave limits.

The distorted co-cumulative spectra for wind speeds of 10–44 knots as a function of fetch from the PNJ curve can be used to determine these wave period limits. To ascertain the maximum characteristic wave height for the 15 s waves, trace the 15 s period line to where it intersects the 180 nautical mile fetch line and read the wave height (4.5 m = 14.8 feet). An effective wind speed

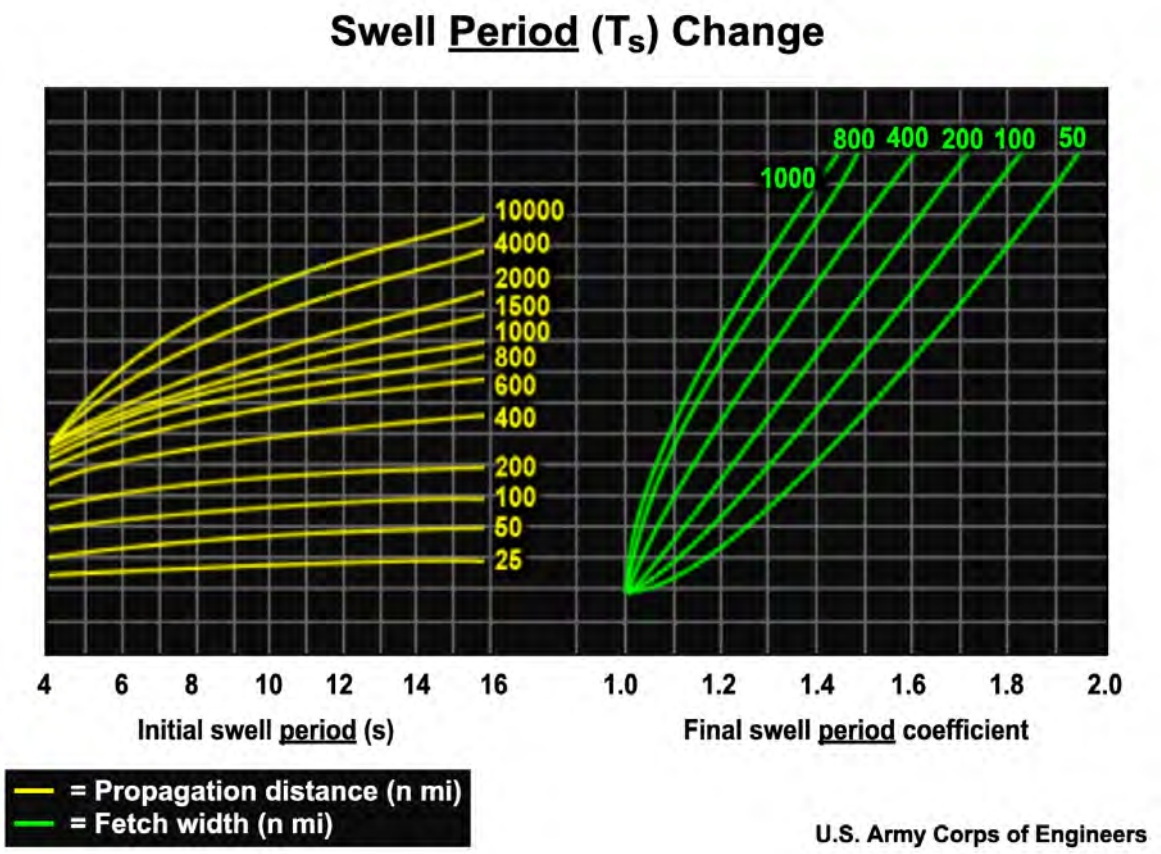

Figure 4.11. Bretschneider swell period decay nomogram. To calculate: choose the initial swell period (in s) on the left horizontal axis, move vertically up to the correct propagation distance line in yellow (in n mi = nautical miles), then horizontally across to the correct fetch width line in green (really defined as fetch length, in n mi), then vertically down to the swell period coefficient. Multiply the initial swell period by this coefficient.

Sources: Bretschneider (1952), CERC (1977) and COMET (2011)

can also be found for these waves (13 m s^{-1} = 26 knots). Likewise for the 12 s waves (characteristic wave height = 4.8 m = 15.8 feet, and effective wind speed = 14 m s^{-1} = 28 knots). The *E* values (energy proportions) are determined in the same way as before. By comparing the 15 s and 12 s wave heights after the dispersion factors have been taken into account for each forecast hour, it can be shown that the waves arriving at 60 h have the greatest characteristic heights. Recall that the angular spreading factor at point A was 12%; this means the highest characteristics possible for these conditions had a height of 1.7 m. The dispersion factor at 60 h is 0.82 with the multiplier being 0.9; thus, the waves arriving at point A at 60 h can have a characteristic height of no more than 1.5 m.

4.5 COMPUTATION OF SHALLOW-WATER EFFECTS

Several kinds of shallow-water effects (shoaling, refraction, diffraction, reflection and bottom effects) are described elsewhere in this Guide. This section describes a few practical methods taken from CERC (1977) and Gröen and Dorrestein (1976). In absolute terms, a useful general

rule is to disregard the effects of depth greater than about 40 m unless the waves are long, that is, if a large portion of the wave energy is in waves with periods greater than 10 s. Distinction is made between:

- Swell originating from deep water entering a shallow area with variable depth;
- Wind waves with limited wave growth in shallow water with constant depth.

More complicated cases with combinations of the above two will generally require the use of numerical models.

Section 4.5.1 deals with shoaling and refraction of swell whose steepness is sufficiently small to avoid wave breaking after shoaling and focusing due to refraction. Section 4.5.2 presents a diagram for estimating wave heights and periods in water with constant depth.

4.5.1 Shoaling and refraction of swell in a coastal zone

Wave decay due to dissipation by bottom friction and wave breaking is neglected in this section. Shoaling and refraction generally occur simultaneously; however, they will be considered separately.

4.5.1.1 *Variation in wave height due to shoaling*

To obtain the shoaling factor K_s, which represents the change of wave height H due to decreasing depth (without refraction), the basic rule that energy flux must be conserved needs to be considered. As energy is related to the square of the wave height (sections 1.2.4 and 1.3.8) and wave energy travels at the group velocity, the energy flux is $c_g H^2$. This is a constant for a normally incident wave. Hence, the shoaling factor depends on the ratio between the deep-water group velocity c_{g0} and the group velocity c_g at depth h, and is given by

$$K_s = \frac{H}{H_0} = \sqrt{\frac{c_{g0}}{c_g}} = \sqrt{\frac{c_0}{2c_g}}, \tag{4.8}$$

where $c_0 = \sqrt{g / k_0}$ is the phase velocity in deep water, and k_0 and H_0 are the wave number and the wave height in deep water, respectively. As the group velocity c_g is given by

$$c_g = \beta\sqrt{\frac{g}{h}\tanh kh}, \quad \beta = \frac{1}{2}\left(1 + \frac{2kh}{\sinh 2kh}\right),$$

and the dispersion relationship $\omega^2 = k\tanh(kh)$ can be used to show that $k_0 = k\tanh(kh)$, the shoaling factor can also be expressed as

$$K_s = \frac{1}{\sqrt{2\beta\tanh kh}}. \tag{4.9}$$

The wave number $k = 2\pi/\lambda$ at depth h is usually solved iteratively, but can be approximated as follows:

$$k \oplus \frac{k_0}{\tanh k_0 h}. \tag{4.10}$$

The approximation is valid for $k_0 \oplus k$ only. To find the shoaling factor and the change in wavelength at various depths, the deep-water wave number k_0 or wavelength are needed. Then, the following figures can be used to obtain the desired results. Figure 4.12 shows various curves involved in the transformation of properties of a wave propagating from deep to shallow water. The curve labelled λ / λ_0 equals k_0 / k, so for a given depth, read the value off that curve, invert and multiply by k_0. The shoaling factor K_s is also shown in this figure. For the convenience of users interested in obtaining the shoaling factor K_s associated with a deep-water wave of a given wave number k_0 (= $2\pi/\lambda_0$), the curve of K_s versus h/λ_0 is presented in Figure 4.13 on an expanded scale.

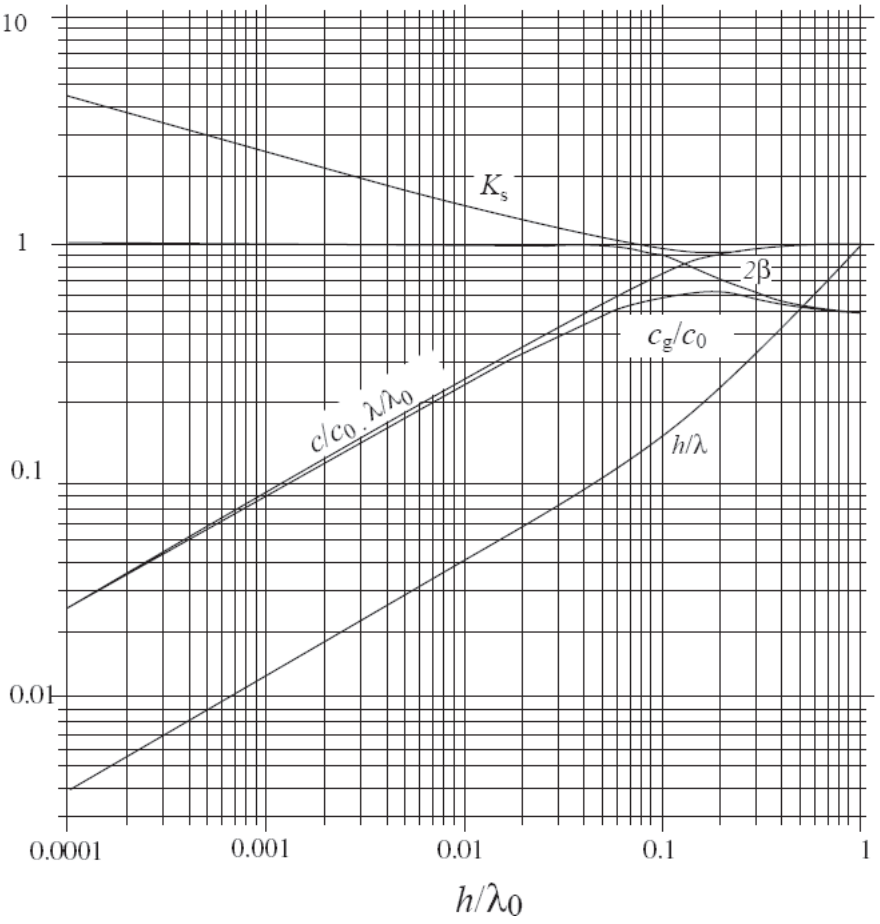

Figure 4.12. Illustration of various functions of h/λ_0

Source: Derived from CERC (1984)

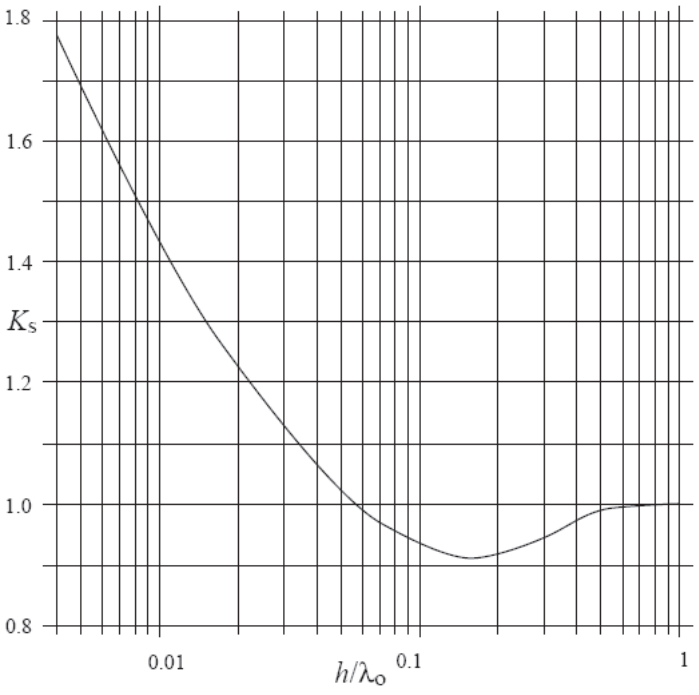

Figure 4.13. Graph of shoaling factor K_s versus h/λ_0

Source: Derived from CERC (1984)

Example

For a deep-water wave of period $T_0 = 10$ s, $\lambda_0 = 1.56\ T_0^2 = 156$ m, then $k_0 = 0.04$ m^{-1}, and similarly for $T_0 = 15$ s, $\lambda_0 = 351$ m and $k_0 = 0.018$ m^{-1}. For each depth, find h/λ_0, then find the value of λ/λ_0 to calculate k from Figures 4.12 and 4.13, and also obtain K_s from Figure 4.13.

Table 4.5 gives the shoaling factor K_s for some shallow depths. It shows that the height of shoaling waves is reduced at first, but finally increases up to the point of breaking, which also depends on the initial wave height in deep water (see also Figures 4.12 and 4.13).

The initial drop in wave energy is not due to friction as the wave starts to "feel" the bottom. It is due to an initial increase in group velocity causing a slight dispersion of wave energy; as the depth continues to decrease, the group velocity will eventually drop, giving a convergence of wave energy and an increase in wave height.

4.5.1.2 *Variation of wave height due to refraction*

In the previous example, no refraction was taken into account, which implies propagation of waves perpendicular to parallel bottom depth contours. In natural conditions, this will rarely occur. So the angle of incidence with respect to the bottom depth contours usually differs from 90°, which is equivalent to α (the angle between a wave crest and the local isobath) being different from 0°. This leads to variation of the width between wave rays. Using Snell's law,

$$\frac{H}{H_0} = \sqrt{\frac{c_{g0}}{c_g}}\sqrt{\frac{\cos\alpha_0}{\cos\alpha}}.$$

The refraction factor is

$$K_r = \sqrt{\frac{\cos\alpha_0}{\cos\alpha}}, \tag{4.11}$$

where α_0 is the angle between a wave crest and a local isobath in deep water. Figure 4.14 taken from CERC (1977), is based on Equation 4.11. For a given depth and wave period, the shallow-water angle of incidence (solid lines) and the refraction factor (broken lines) can be read off easily for a given deep-water angle of incidence α_0. It is valid for straight parallel depth contours only.

Problem

Given an angle $\alpha_0 = 40°$ between the wave crests in deep water and the depth contours of the sloping bottom, find α and the refraction at $h = 8$ m for $T = 10$ s.

Table 4.5. Wave number k and shoaling factor K_s for two wave periods, at several depths h, using Equations 4.9 and 4.10

h (m)	$T = 10$ s, $k_0 = 0.04$ m^{-1}		$T = 15$ s, $k_0 = 0.018$ m^{-1}	
	k (m^{-1})	K_s	k (m^{-1})	K_s
100	0.040	1.00	0.018	0.94
50	0.041	0.95	0.021	0.92
25	0.046	0.91	0.028	0.98
15	0.055	0.94	0.035	1.06
10	0.065	1.00	0.043	1.15
5	0.090	1.12	0.060	1.33
2	0.142	1.36	0.095	1.64

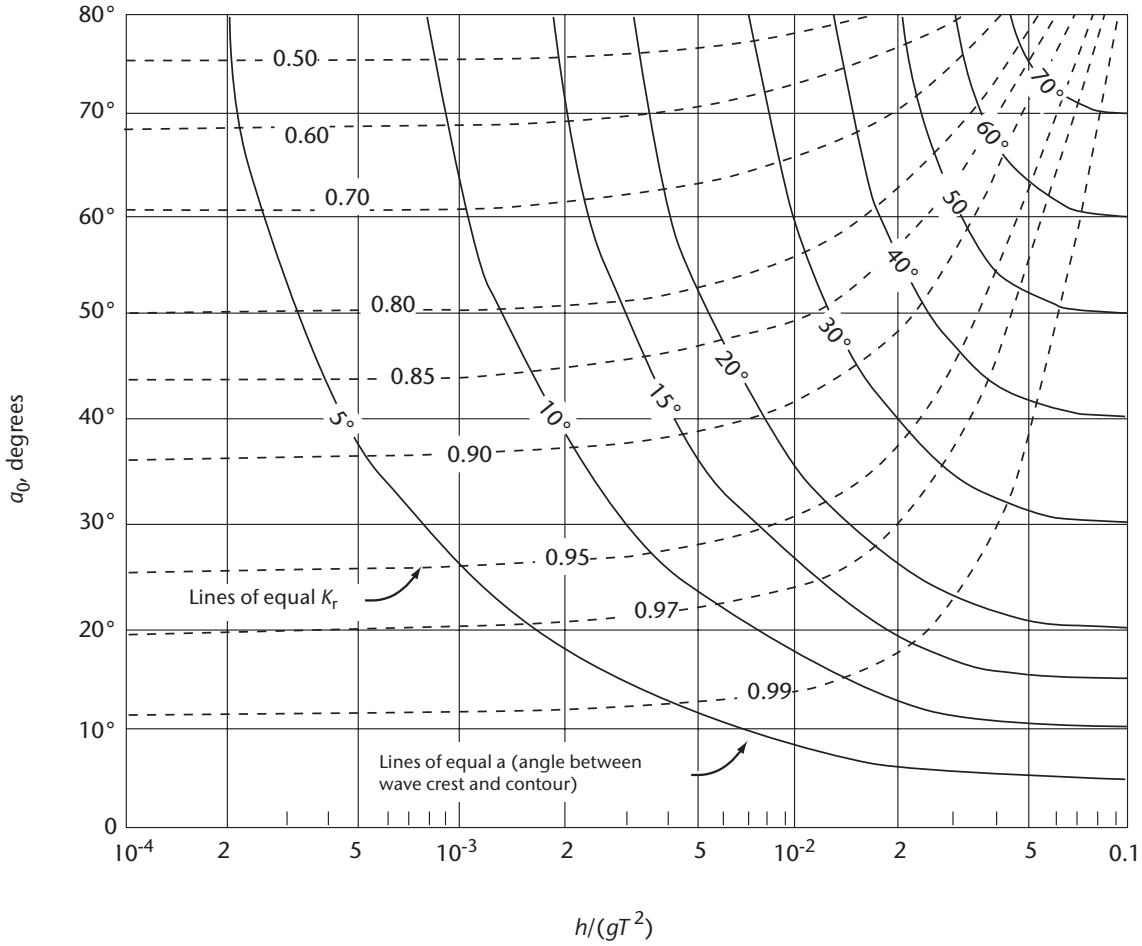

Figure 4.14. Changes in wave direction and height due to refraction on slopes with straight parallel bottom contours. α_0 is the deep-water angle of incidence, measured between the wave crest and the local isobath. The continuous curves are lines of equal incidence for various combinations of period and depth. To estimate the refraction as a wave moves into shallower water, starting from a given α_0 follow a horizontal line from right (deep water) to left. The broken lines are lines of equal refraction factor K_r.

Source: Derived from CERC (1977)

Solution

$h/(gT^2) = 8/(9.8 \times 100) = 0.0082$; from Figure 4.14, the refraction factor is 0.905 and $\alpha = 20°$.

4.5.1.3 ***Dorrestein's method for determining refraction factor***

As bottom depth contours are rarely straight in reality, there are generally sequences of convergence and divergence (see also sections 1.2.6 and 3.3.2). Dorrestein (1960) devised a method for manually determining refraction where bottom contours are not straight. This method requires the construction of a few wave rays from a given point P in shallow water to deep water, including all wave directions that must be taken into account according to a given directional distribution in deep water.

It is assumed that in deep water, the angular distribution of wave energy is approximately a uniform distribution in the azimuthal range α_1'. These and α_2' angles correspond, respectively, to

the angles of incidence α_1 and α_2 at point P. Rays must at least be constructed for waves at these outer limits of the distribution. It may be sufficient to assume straight isobaths and use Figure 4.14 to calculate these angles. Then, according to Dorrestein, the refraction factor is

$$K_r = \sqrt{\frac{c_0}{c} \cdot \frac{\alpha_1 - \alpha_2}{\alpha_1' - \alpha_2'}}, \tag{4.12}$$

where c_0 and c are the phase velocities in deep water and at point P, respectively.

Problem

As in the example in section 4.5.1.2, $h = 8$ m at point P. $T = 10$ s, so $h/(gT^2) = 0.0082$. With the help of Figure 4.9, $\alpha = 20°$ for $\alpha_0 = 40°$. Find K_r by Dorrestein's method.

Solution

Snell's law gives

$$\frac{c_0}{c} = \frac{\sin\alpha_0}{\sin\alpha} = \frac{\sin 40}{\sin 20} = 1.88.$$

It is prudent to use a small window. $\alpha = \alpha_1 - \alpha_2$ centred around α (= 20° in this case) in applying the ideal linearly sloping bottom results to obtain the answers to a real case of bottom topography. If $\alpha_1 = 21°$ and $\alpha_2 = 19°$, then from Figure 4.14, $\alpha_1 \approx 42°$ and $\alpha_2 \approx 37.5°$. Equation 4.12 thus gives $K_r = 0.904$.

In general, the results for K_r are sensitive to the choice of spread between α_1 and α_2 (or α_1' and α_2').

4.5.2 **Wind waves in shallow water**

In shallow water, the bottom topography and composition have a dissipative effect on waves. A simple manual method is presented here for prediction of the significant wave height H_c and the associated wave period in shallow water with constant depth. Figure 4.15 is used based on the same deep-water growth nomogram, but modified to take the limitation of wave growth by the bottom into account. As in the previous sections of this chapter, it is assumed that H_c is approximately equal to the significant wave height $H_{1/3}$ or H_{m_0} , and T_c is approximately equal to the significant wave period T or T_p (see Chapter 1). For the sake of compactness, only ratios are shown: H_c/h and $T_c/\sqrt{h}$, both as a function of $u/\sqrt{h}$. u denotes wind speed at the standard level (usually 10 m above water) in m s^{-1}. Wave height H_c and depth h are expressed in metres, and wave period T_c in seconds. The solid curves show H_c/h and $T_c/\sqrt{h}$ for sufficiently long fetches, for example, an X/h ratio much greater than 3 000. Then a sort of balance between wind input and bottom dissipation can be assumed. The effect of limited fetch is shown for $X/h = 3\,000$.

Problem

Find H_c and T_c for $u = 20$ m s^{-1}, $h = 10$ m and fetch $X = 200$ km and 30 km.

Solution

From section 3.2, non-dimensionalize as follows: $H^* = gH_s/u^2$, $T^* = gT_s/u$, $X^* = gX/u^2$, $h^* = gh^*/u^2$. Then, $h^* \cong h/40 \cong 0.25$ and $X^* \cong X/40 \cong 5\,000$ and 750. Then go to Figure 3.2 and get $T^* \cong 2.8$ and 2.1 and $H^* \cong 0.060$ and 0.045. Converting back to dimensional units gives $T = 5.6$ and 2.4 s and $H = 2.4$ m and 1.8 m, respectively, for fetches of 200 and 30 km. Fetches are either from the upwind shore or the upwind edge of the fetch box, whichever is shorter.

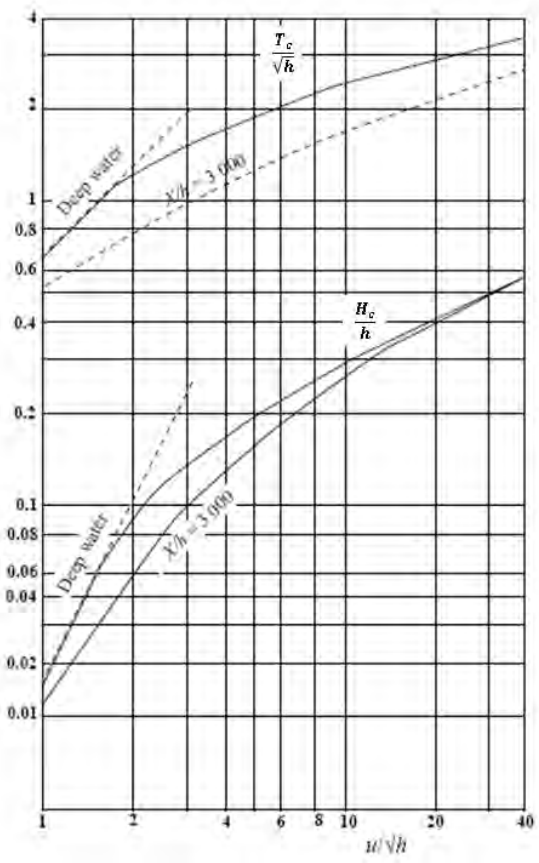

Figure 4.15. Diagram to estimate characteristic wave heights and period of wind waves in shallow water of constant depth. Solid lines indicate limiting values for sufficiently long fetches, denoted *X*. Broken lines indicate conditions with short fetches, specified by $X/h = 3\,000$.

Source: Gröen and Dorrestein (1976)

4.6 MODIFICATION OF NUMERICAL GUIDANCE

Wave models currently have high skill in forecasting, at least when the wind models forcing them are accurate. Model output from most major wave models are also widely available (via the Internet for example) to most forecast centres around the world. As a result, wave forecasting has become a process of using the model guidance as a good first guess, and then looking for weaknesses or biases in the wave model and in the wind model forcing it. A 10% error in wind speed is often associated with a 20%–30% error in wave heights. Manual techniques as discussed previously can be used as a "reality check" of model results, and as a guide on how to modify model results to improve the forecast. The following sections discuss a general approach to forecasting, emphasizing how to combine observations, model guidance and manual techniques to improve the forecast. Section 4.6.1 looks at the models, including possible issues, and is followed in section 4.6.2 by verification of the model initialization and ongoing performance against observations. Section 4.6.3 discusses the classic analysis, diagnosis and prognosis loop as applied to this environment.

4.6.1 Possible model issues

Different models have unique strengths and weaknesses; it is important as a forecaster to be aware of them. There are also generic issues that apply to all numerical models. Waves, and wave forecasting models, are extremely sensitive to wind forcing, and this is the most important thing

to consider first. Deep-water wave models are good, but shallow-water effects, and the effects due to tides and currents, may not be handled well or at all depending on the configuration of the model.

For wind models, the most common thing to look for are boundary-layer stability issues, especially from 10 m to the surface. Finding biases here is usually a matter of experience, but the largest errors tend to occur in stable environments (strong warm advection over cold water) and in unstable environments (strong cold advection over warm water). Model resolution may not properly resolve some local effects such as channelling winds or tip jets. If initialization errors are found, finding the cause is vital, as it will determine what changes to make in the forecast, and how long to keep them going.

For the wave model itself, there are some possible issues, but they will often differ among the models, so it is vital to know them for each model used, especially for the main wave forecasting model. Issues related to shallow water include wave breaking, set up and run up. Factors that may be parameterized or neglected are refraction and diffraction effects. Many wave models do not account for wave–current or wave–tidal interactions, and those that do may not be coupled to ocean models to get realistic energy and momentum exchanges. Finally, there are wave–ice and wave–ice–current interactions, which include issues of wave dissipation and growth in regions with ice floes or solid ice.

Other concerns with wave models are the presentation and interpretation of data. In general, wave fields are combinations of several or many components, including wind waves and various swell components generated nearby or from great distances, each with its own spectral characteristics. Some models give full wave spectra, others only the significant wave height, peak period and direction, and the same for one or more swell components. Models have algorithms to try to identify the major wind-wave and swell components and partition them in a simple manner, but are sometimes in error. There are also issues with wave masking, where the smaller of two large wave components could be missed. Associated with this is a problem where the peak period displayed may not be representative of the significant wave, but of another wave component.

A general concern for all models is their resolution, especially how they match up between the wave and wind model, bathymetry including good near-shore bathymetry, and coast-lines. Interactions with sea ice, currents, tides or combinations are issues for the wind models and the wave models. Chapters 5 and 6 give information on wave models, and also provide guidance on other sources of relevant information.

There are two main messages here. Get to know the models, then watch how they behave in realistic situations to get a feeling for biases and errors. Finally, it is always vital to get the correct wind field.

4.6.2 Model operational verification

Common concerns or issues with model guidance are discussed below, as well as some simple ways to address these issues, starting with verification against observations. For further information on observations and their characteristics, see Chapter 2 on marine winds and Chapter 7 on wave data.

4.6.2.1 *Wind*

As mentioned previously, check available wind data and compare to the wind model data. To do so, it is necessary to consider that most wave models input 10 m winds, and many assume neutral stability when extrapolating to the surface and calculating the wind stress actually driving the model. The neutral stability assumption should be checked for the wave model type and version. This also needs to be accounted for when using various instruments. Buoys and near-shore anemometers and ships are at different elevations, which must be corrected to 10 m; many have

air and sea temperatures to help estimate stability and correct for it. Many remote sensors do not measure wind speed directly, but ocean-surface features, and most then use an algorithm that gives 10 m winds assuming neutral stability.

After these have all been compared with the model, biases and hopefully causes can then be identified. If the cause is not clear, it might be necessary to keep the bias correction initially then taper it off over 6–12 h. If it is clear, it is sometimes possible to do much better. For example, if a storm is approaching and the model underestimates the winds in a sector of the storm, it might be possible to keep the bias correction for the areas that the sector wind field is approaching, until it passes. Squall lines and TCs are examples of such cases.

If the wind forcing seems accurate, wave observations should be checked against the model. If there are discrepancies and there is confidence in the wind forcing, then other possible sources of differences need to be investigated. Swell is a common source of differences. Regional wind and wave models may not resolve swell generated outside the high-resolution part of the model domain. Global models might resolve the cause, but typically lower resolution might weaken or distort the wave field generated. For strong mesoscale features including squall lines and TCs, even regional models might have a problem with wind waves and swell. Finally, there may have been swell or wind waves generated before the data assimilation cycle and still in the forecast area that were not modelled correctly. Many major wave models do not have data assimilation.

4.6.2.2 ***Waves***

To cope with an area of anomalous swell in the forecast domain that will move out in a given direction, bias the results high near and ahead of the swell field, and drop back to the model forecast behind it. For swell due to an approaching squall line, bias high ahead of the gust front then drop to zero behind the line (if the line overtakes waves and there is a surface flow opposing the waves behind the line, it might even be possible to diminish the waves a little). For TCs, keep an eye on waves generated to the right of the storm track, especially if the storm is moving at a significant speed or accelerating in a straight line. This could create a dynamic fetch that would generate higher waves than expected from such a system. As discussed previously, this is due to the waves being forced for a long period of time, sometimes approaching fully developed waves. It is necessary to estimate how long the waves are forced before the waves leave the fetch area. For example, waves with an average speed of 25 knots, in a fetch box of length 100 nautical miles under a storm moving at 20 knots would be forced for up to 20 h, but for a stationary storm, the waves would be forced for up to 4 h. For 60 knot winds, this would be the difference between 4.5 m and 14 m (using the BH nomogram).

4.6.2.3 ***Other effects***

For wind waves or swell in shallow water, there are several effects that may not be noticeable on the model scale (for shallow straits or shelf areas). Refraction towards shallower areas, shallow-water wave breaking and tidal current–wave interactions may have to be considered. For ice floes and continuous ice fields, some models assume that the initial ice field does not move during the forecast period. For strong winds and longer model runs, this may make a difference, exposing areas to wave effects that do not exist initially. The initial ice analysis used in the model may also have position errors. For waves approaching ice, unless the model is high resolution, assume the wave height does not change right up to the ice edge, then it drops to zero. The length scale for wave decay is usually at most one or two grid boxes.

4.6.3 **Forecast cycle: analysis, diagnosis and prognosis**

This is a typical sequence followed by a wave forecaster:

1. Analysis: check current observed conditions and recent observed trends and compare to the model initialization:
   (a) Check the winds first. If model winds are off, the wave field almost certainly will be. Look for error magnitudes and spatial patterns. This will give guidance on how to modify the model forecast.
   (b) Check all wave observations:
      (i) For buoys, ships and offshore platforms, look for other wave components from manual observations or wave spectra. Directional wave spectra are best. With this, it might be possible to identify wave fields not resolved by other sources, and compare with the way the model partitioned the wave fields. This can also uncover wave masking effects, and show which wave components are the highest threat.
      (ii) Most of the satellite and other remote sensors will give a good estimate of significant wave heights in space, either along lines (radar altimeters) or over areas (synthetic aperture radars).
2. Diagnosis and prognosis:
   (a) For wind discrepancies in the forecast domain, finding the cause should give a strategy for modifying the forecast. For example, an approaching hurricane that was underforecast should imply a low bias to wave height or peak period in the model, which may grow in magnitude as the storm approaches.
   (b) For wave discrepancies without associated wind discrepancies in the forecast domain:
      (i) Observed waves are too weak for the winds – a likely cause would be higher than forecast stability. Then it might be necessary to keep waves weak until the stability is likely to reduce. Other causes might include oceanic or tidal currents moving with the wind and thus reducing the wind stress on the water. Large ocean currents such as the Kuroshio Current or Labrador Current also have associated strong sea-surface temperature gradients, so there is a possible combination of stability and current effects on the surface wind stress.
      (ii) Observed waves are too strong for the winds – a likely candidate might be due to non-locally generated swell moving into the forecast domain, or already there and leaving/dissipating. If the cause of the swell and the recent behaviour can be isolated, this should give a strategy to modify the forecast. If it is a strong weather system, either stationary or approaching the forecast domain, it might be necessary to keep higher waves throughout the forecast. If it is a weakening field moving out, it might be possible to gradually trend back to the model forecast. Again, stability and currents could easily play a part, especially as some wave models still assume neutral stability. Most larger-scale models do not account for currents, so tidal or larger-scale oceanic currents may be a concern.
   (c) For mixed cases where part of the model error is due to errors in the wind forcing, there are also problems with other factors that may be affected directly by the winds and which can feed back. Here it is necessary to either try to account for the dominant cause of the error (the best case) or be forced to account for two or more causes. Likely processes that need to be accounted for along with the winds would be tidal effects, which include currents, and mixing of colder water to the surface as well as coastal upwelling of colder water, both of which have a stabilizing effect. Hurricanes can also create strong upwelling to the right of their track, often cooling the surface waters over a large area. These upwellings might have to be considered because many atmospheric models are not coupled to an ocean model, and would have problems modelling cooling due to upwelling or wind-current feedback. When this is used to force the wave model, which does not account for these factors, the problem could be exacerbated.
3. Monitor and repeat the cycle as necessary.

4.7 RIP CURRENT FORECASTING

There is growing interest in developing forecasting schemes to predict rip current activity, given that it is one of the largest causes of swimming fatalities. This is an area of recent development in several countries, and there is limited direct numerical guidance. Given the dynamic nature of beach morphology and its sensitivity to weather and other factors, good numerical guidance might not be available for a while yet. A common approach in the United States of America and other areas is to use observations and anecdotal data to determine correlations between objective predictors and observed rip current events. Then, a worksheet for each beach being forecast is developed based on the predictors and their individual levels of significance, and objective scores to each risk factor are assigned. When the combined score is high enough, advisories are issued for low, medium or high risk of rip currents along beaches.

The main factors that contribute to rip currents include:

- Bathymetry and coast-line shape/orientation, which make certain locations vulnerable to rip currents;
- Waves or swell that affect the beach at an angle near normal incidence;
- Wind waves resulting from persistent onshore flow;
- Tidal stage and amplitude, especially middle to low tides;
- Forcing mechanisms such as wave set-up, coastal human-made structures, sandbars and near-shore bathymetry, and coral reefs.

4.7.1 Basic forecasting method

After the worksheet for a given beach or beaches is developed, the forecaster's task is to determine the levels of the predictors, using observations, numerical guidance, previous experience, knowledge of local effects and pattern recognition. Figure 4.16 shows an example worksheet for Pender and Brunswick (United States) beaches, the first facing east and the second south.

Problem

Consider Pender Beach and a simple case. There have been winds of between 15 and 20 knots from 135° for the last 2 d, and these are expected to continue for at least another 30 h. An offshore buoy is showing 3 foot swell from the east with a period of 12 s from a distant nearly stationary storm. It is near a full moon and the low tide will be about 2 p.m. local time, but not below the mean lower low water (the mean of the lowest daily tide each day during the recording period).

Solution

Filling in the worksheet from top to bottom gives: 2.5 for the wind (it is onshore at 135°), 1 for persistence (2 d plus 30 h > 48 h), 3.5 for swell and 0.5 for the tide level, giving a total of 7.5. This gives a high risk for rip currents according to the bottom of the chart.

For Brunswick Beach under the same conditions, the following are obtained: 0 for winds (north of the onshore directions of 150° to 220°), 0 for the last 48 h of wind (winds were not onshore during the period), 0 for swell (as the swell was from the east, and south-east or south winds are needed) and 0.5 for the tides. This gives a total of 0.5 and thus presents a low risk for rip currents.

4.7.2 Forecasting considerations

The main forecasting considerations are analysis of the swell, wind waves, the wind, tidal levels and possibly known local effects such as preferred areas for rip currents.

Wind analysis is important for two key reasons: analysing wind waves and ensuring that the wave model used is driven by a good wind field. Chapter 2 discussed the analysis of winds.

For forecasting rip currents, there might be an issue with the 48 h persistence rule used in the worksheet. If the winds are particularly strong, it might be a good idea to give a score for shorter periods of wind. Alternatively, for significantly light winds, a longer period might be required.

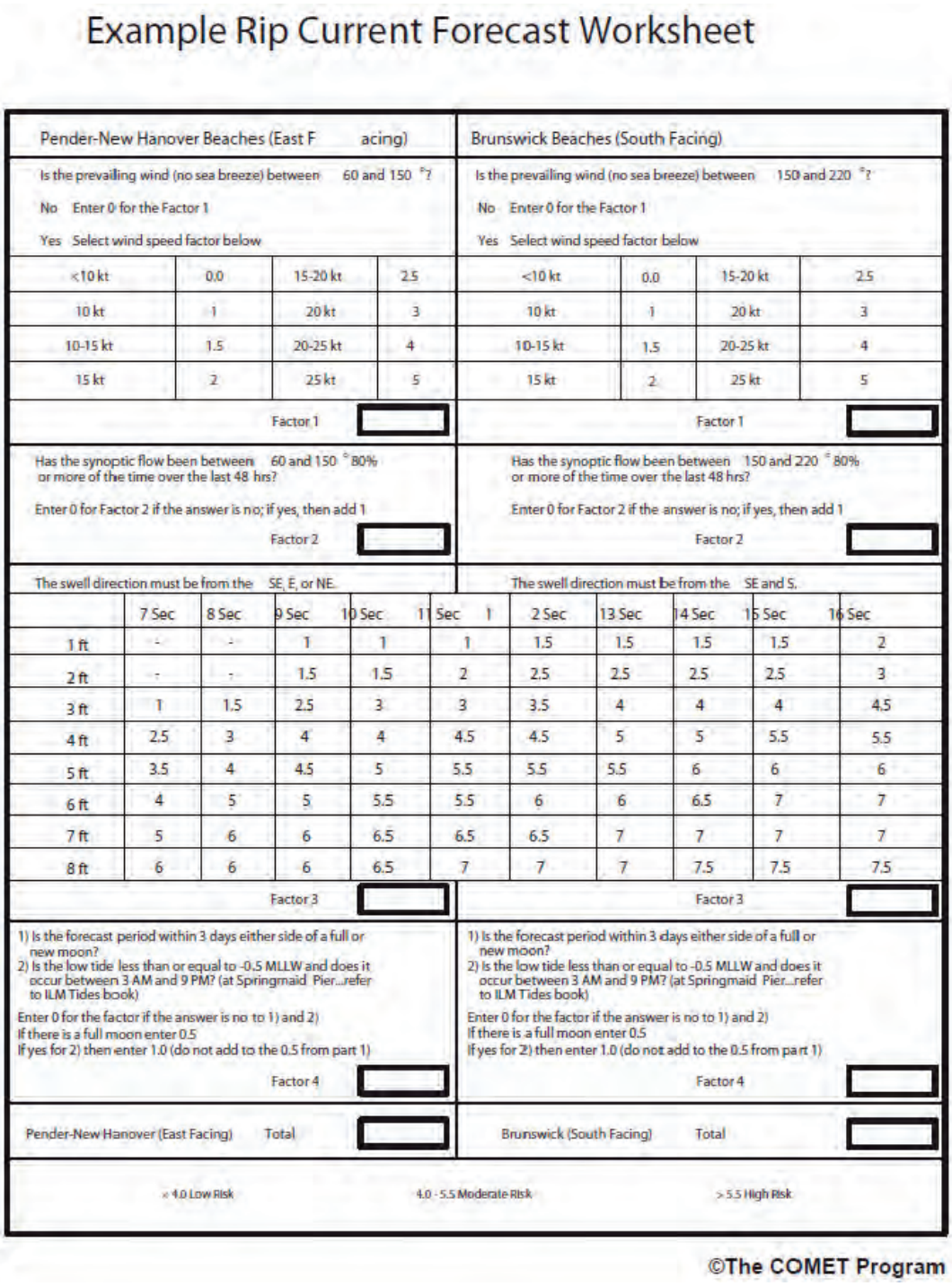

Example Rip Current Forecast Worksheet

Pender-New Hanover Beaches (East F acing)				Brunswick Beaches (South Facing)			
Is the prevailing wind (no sea breeze) between 60 and 150 °?				Is the prevailing wind (no sea breeze) between 150 and 220 °?			
No Enter 0 for the Factor 1				No Enter 0 for the Factor 1			
Yes Select wind speed factor below				Yes Select wind speed factor below			
<10 kt	0.0	15-20 kt	2.5	<10 kt	0.0	15-20 kt	2.5
10 kt	1	20 kt	3	10 kt	1	20 kt	3
10-15 kt	1.5	20-25 kt	4	10-15 kt	1.5	20-25 kt	4
15 kt	2	25 kt	5	15 kt	2	25 kt	5
Factor 1				Factor 1			
Has the synoptic flow been between 60 and 150 ° 80% or more of the time over the last 48 hrs?				Has the synoptic flow been between 150 and 220 ° 80% or more of the time over the last 48 hrs?			
Enter 0 for Factor 2 if the answer is no; if yes, then add 1				Enter 0 for Factor 2 if the answer is no; if yes, then add 1			
Factor 2				Factor 2			
The swell direction must be from the SE, E, or NE.				The swell direction must be from the SE and S.			

	7 Sec	8 Sec	9 Sec	10 Sec	11 Sec	1	2 Sec	13 Sec	14 Sec	15 Sec	16 Sec
1 ft	-	-	1	1	1		1.5	1.5	1.5	1.5	2
2 ft	-	-	1.5	1.5	2		2.5	2.5	2.5	2.5	3
3 ft	1	1.5	2.5	3	3		3.5	4	4	4	4.5
4 ft	2.5	3	4	4	4.5		4.5	5	5	5.5	5.5
5 ft	3.5	4	4.5	5	5.5		5.5	5.5	6	6	6
6 ft	4	5	5	5.5	5.5		6	6	6.5	7	7
7 ft	5	6	6	6.5	6.5		6.5	7	7	7	7
8 ft	6	6	6	6.5	7		7	7	7.5	7.5	7.5

Factor 3	Factor 3
1) Is the forecast period within 3 days either side of a full or new moon? 2) Is the low tide less than or equal to -0.5 MLLW and does it occur between 3 AM and 9 PM? (at Springmaid Pier...refer to ILM Tides book) Enter 0 for the factor if the answer is no to 1) and 2) If there is a full moon enter 0.5 If yes for 2) then enter 1.0 (do not add to the 0.5 from part 1)	1) Is the forecast period within 3 days either side of a full or new moon? 2) Is the low tide less than or equal to -0.5 MLLW and does it occur between 3 AM and 9 PM? (at Springmaid Pier...refer to ILM Tides book) Enter 0 for the factor if the answer is no to 1) and 2) If there is a full moon enter 0.5 If yes for 2) then enter 1.0 (do not add to the 0.5 from part 1)
Factor 4	Factor 4
Pender-New Hanover (East Facing) Total	Brunswick (South Facing) Total

< 4.0 Low Risk 4.0 - 5.5 Moderate Risk > 5.5 High Risk

©The COMET Program

Figure 4.16. Rip current forecast worksheet for Pender and Brunswick Beaches, North Carolina, United States

Source: COMET. The source of this material is the COMET® Website at http://meted.ucar.edu/ of the University Corporation for Atmospheric Research (UCAR), sponsored in part through cooperative agreement(s) with the National Oceanic and Atmospheric Administration (NOAA), U.S. Department of Commerce (DOC). ©1997-2017 University Corporation for Atmospheric Research. All Rights Reserved.

Rip current risk might remain for a while after the winds die down. During the event, rip current channels develop or are increased in size, allowing the currents to persist for a while. In addition, a small change in wind direction near the end may cause wave–wave interference, thus increasing the chance of rip currents persisting.

Observations of swell direction, period and height are first needed for swell analysis observations. The best sources are weather buoys in the vicinity, either privately or government owned. One issue is identifying swell that might be masked by other wave components. Some buoys transmit wave spectra, either directional or averaged, and these are excellent resources. Some others give the significant wave height, the wind-wave component and the largest swell component. Finally, some only give the significant wave height. Many do not give wave directions. In many cases, the observations will need to be supplemented by numerical guidance. Finally, there are some observations from satellite, especially synthetic aperture radars, and various other types of radar such as light detection and ranging and coastal ocean dynamics applications radar instruments.

Given a buoy that generates spectra, the wind-wave and significant swell components can be identified. Otherwise, significant onshore swell may be masked in the buoy report by wind waves or swell components that will not affect the beach. If the spectra are non-directional, they could be compared with model spectra nearby, and the different components and their directions identified. There may also be ship observations nearby that might help with identifying swell and correlating with buoy data.

As mentioned above, before using numerical wave guidance, the wind guidance for the wave model has to be analysed for error. Wave models usually give good results, but are extremely sensitive to the winds. The swell and wave analysis must be compared with model results, so that the model wave guidance can be modified if necessary.

Many models will give the wind wave and the primary swell component, including height, period and direction. Some also routinely plot directional wave spectra at various points (the National Oceanic and Atmospheric Administration Wave Watch III model uses buoy positions to plot the spectra). This helps identify the components that will be moving towards the beach of interest. There may also be an associated table of wave components and their parameters, including direction, identified and extracted from the spectra. These spectra can help to catch wave masking from observations and correct for it.

Other forecast situations include tide stage, situational awareness and lake effects. Near and at low tide, conditions for rip currents and their effects can be enhanced. For beaches with sandbars, offshore water driven towards the shore can be partially “trapped”, enhancing longshore currents and rip currents. If wave conditions persist, the threat can return for the next few tidal cycles because the sandbars and bathymetry usually evolve slowly.

4.7.3 Tips for creating a forecasting scheme

Look for other similar beaches where a forecast system is in place, as a candidate for adjustment to the current conditions. Look for historical and meteorological/oceanographic data for previous events to get likely situations and criteria for wind and wave parameters. Sources could include emergency measures organizations (EMOs), local lifeguard networks, law enforcement reports and coroner offices. Create links with local lifeguards, EMOs, the coast-guard, local coastal engineers or specialists. Try to establish regular contact with lifeguards and the like to obtain a regular log of incidents, rescues, fatalities or rip current activity. Finally, keep up to date with recent research work especially in the local region.

Research on forecasting rip currents operationally is active. One approach is to use lifeguard reports of rip current incidents over a period of time, possibly supplemented with other reliable anecdotal data, then get physical data on predictors for the events, such as water levels, winds, wind wave and swell activity. These are then correlated with the observed incidents, often using regression analysis. Then a worksheet is developed similar to Figure 4.16 but using the best predictors for that beach. An example is the modified east central Florida (ECFL) Lushine

Modified ECFL LURCS Checklist

Example computations appear in ***bold***.

Wave Period	
Period, T (s)	Factor
T < 6	0
6 <= T < 9	***0.5***
9 <= T < 11	1
11 <= T <12	2
T >=12	3
Wave Period Factor =	***0.5***

Wave Direction	
Direction, θ (deg)	Factor
θ < -35 or θ > 20	0
–35 <= θ < -30 or 20 >= θ > 15	1
–30 <= θ < -25 or 15 >= θ > 10	2
–25 <= θ < -15 or 10 >= θ > 5	3
-15 <= θ <= 5	***4***
Wave Direction Factor =	***4***

Wave Height	
Height, Ho (ft)	Factor
Ho < 1	0
1 <= Ho < 2	0.5
2 <= Ho < 3	***1***
3 <= Ho < 5	2
5 <= Ho < 8	3
Ho >= 8	4
Wave Height Factor =	***1***

Tide	
Tide, h (m)	Factor
h > -0.2	0
- 0.5 < h <= -0.2	***1***
- 0.75 < h <= -0.5	2
h <= -0.75	1
Tidal Factor =	***1***

Directional Spreading	
Dspr, (θ°)	Factor
θ > 35	0
30 < θ <= 35	***3***
θ < 30	4
Dspr Factor =	***3***

Sum the factors: The Modified ECFL LURCS rip current threat =	***9.5***

Figure 4.17. Modified ECFL LURCS worksheet

Source: Engle et al. (2002)

rip current scale (LURCS) checklist, developed by Lascody (1998). This was modified from a previous worksheet to give greater weight to winds, swell period and larger-amplitude tides. Using a larger dataset, Engle et al. (2002) found that a better correlation was obtained using a greater emphasis on wave direction and angular spread, and de-emphasized the wind direction (Figure 4.17).

This method has the advantage that it is designed to forecast conditions likely to cause an incident that requires emergency response. A possible caveat is that it may miss conditions where historically the emergency responders should have reacted but did not. It is also biased due to attendance patterns at beaches, which is combined with typically low attendance during bad weather. However, it should cover periods where attendance is good. It is also obviously modifiable using recent or new data. But it does not directly address the physics of the situation, nor changes in beach morphology, which modify rip current patterns.

A related approach is to process photographic imagery to identify rip current events, then correlate with predictors as before (Gallop et al., 2011). This is more objective than lifeguard reports, but again will not directly account for changes in near-shore bathymetry, and it may not

give a good estimate of current strength. Gallop et al. also noted that for their case study, the rip current response was primarily driven by wave energy over about the previous 10 d, and was less sensitive to present conditions. They also noted several changes in beach morphology affecting rip current occurrence in the 3.3 year course of their study.

There is also significant research on modelling rip currents to forecast them directly (for example, Austin et al., 2013; van Dongeren et al., 2013). One major problem is that it is necessary to frequently update the near-shore bathymetry in the model. This is because it often changes gradually, but during severe and/or long-duration weather events, it can change drastically. Rip current forecasting also often requires nested wave models driving a high-resolution model giving set-up, set-down and rip currents.

CHAPTER 5. NUMERICAL WAVE MODELLING

Editors: M. Reistad with A.K. Magnusson, updated by J.-R. Bidlot

5.1 INTRODUCTION

National Meteorological and Hydrological Services in maritime countries have experienced a rapidly growing need for wave forecasts and wave climatology. In particular, the offshore oil industry needs wave data for many purposes such as design sea states, fatigue analysis, operational planning and marine operations. Furthermore, consulting companies operating in the maritime sector have an increasing need for wave information in their projects.

To meet this growing requirement for wave information, wave conditions must be estimated over large tracks of ocean at regular intervals, often many times a day. The volume of data and calculations makes computers indispensable. Furthermore, measured wave data are often sparse and not available when and where they are desired. Using atmospheric and oceanic information and by application of the basic physical principles described in Chapters 1 and 3, numerical models are continually improving to provide the required estimates of sea-state conditions.

In wave modelling, it is necessary to organize theoretical and observational knowledge about waves into a form that can be of practical use to forecasters, engineers, mariners or the general public. A key input parameter to the wave models is the surface stress exercised by the wind; therefore, the accuracy of the wave-model output is dependent on the quality of the wind fields. Chapter 2 was devoted to the specification of marine winds. Other important parameters that influence the environment in which the waves evolve include sea ice, surface current and changing water depth.

The *Handbook on Wave Analysis and Forecasting* (WMO, 1976) described one particular model in detail to exemplify the structure and methodology of numerical wave models. Rather than giving details of one or a few particular models, this chapter covers general descriptions of the three model classes that were defined in the Sea Wave Modeling Project (SWAMP) (SWAMP Group, 1985). "Third-generation" models are now widely in use due to advances in computational capabilities.

Section 5.2 gives an introduction to the basic concepts of wave modelling. Section 5.3 discusses the wave-energy-balance equation. Section 5.4 contains a brief description of some elements of wave modelling. Section 5.5 defines and discusses the most important aspects of the model classes.

5.2 BASIC CONCEPTS

On the temporal–spatial scales at which wave data are predicted, the mathematical representation of surface waves has a large random element that requires a statistical description to characterize sea conditions. Formally, over these scales, it is necessary to assume stationarity (steadiness in time) and spatial homogeneity of the process describing the sea surface. Obviously, no such conditions will hold over the larger scales that characterize wave growth and decay. To model changing waves effectively, these scales (time step or grid length) must be small enough to resolve the wave evolution, but it must be recognized that, in time or space, there are always going to be smaller scale events that have to be overlooked.

The most common representation of the wave field is the sea-surface variance density spectrum $E(f,\theta)$, which discretizes the wave field in frequency f and direction θ under the assumption of linear wave theory (see section 1.3.7). This representation is particularly useful because it is already known how to interpret knowledge about wave physics in terms of the spectral components $E(f,\theta)$. (The energy-density spectrum can also be defined as a function of wave

number along coordinate axes, with a simple transformation connecting the two definitions.) Each component can be regarded as a sinusoidal wave for which there is a reasonably well-understood theory. Sea-state parameters can be derived from this spectrum, namely the significant wave height, the frequency spectrum, the peak frequency and secondary frequency maxima, the directional spectrum, the primary wave direction, any secondary wave directions, the zero-crossing period and the directional spreading (see Chapter 1).

Not all models use this representation. Simpler models may be built around direct estimation of the significant wave height, or on the frequency spectrum, with directional characteristics often diagnosed directly from the wind.

There is a reasonable conception of the physical processes that are thought to control wave fields. To be of general use in wave modelling, these processes are described by the response of useful statistical quantities such as the wave spectrum. Not all the processes are fully understood; empirical results are therefore used to varying degrees within wave models. Although the current research trend is to develop good physics-based representation of these processes, such representations still allow a certain amount of "tuning" of wave models (where the model performance can be adjusted by altering empirical constants). Although models for different purposes may differ slightly, the general format is the same. See Figure 5.1 for a schematic representation.

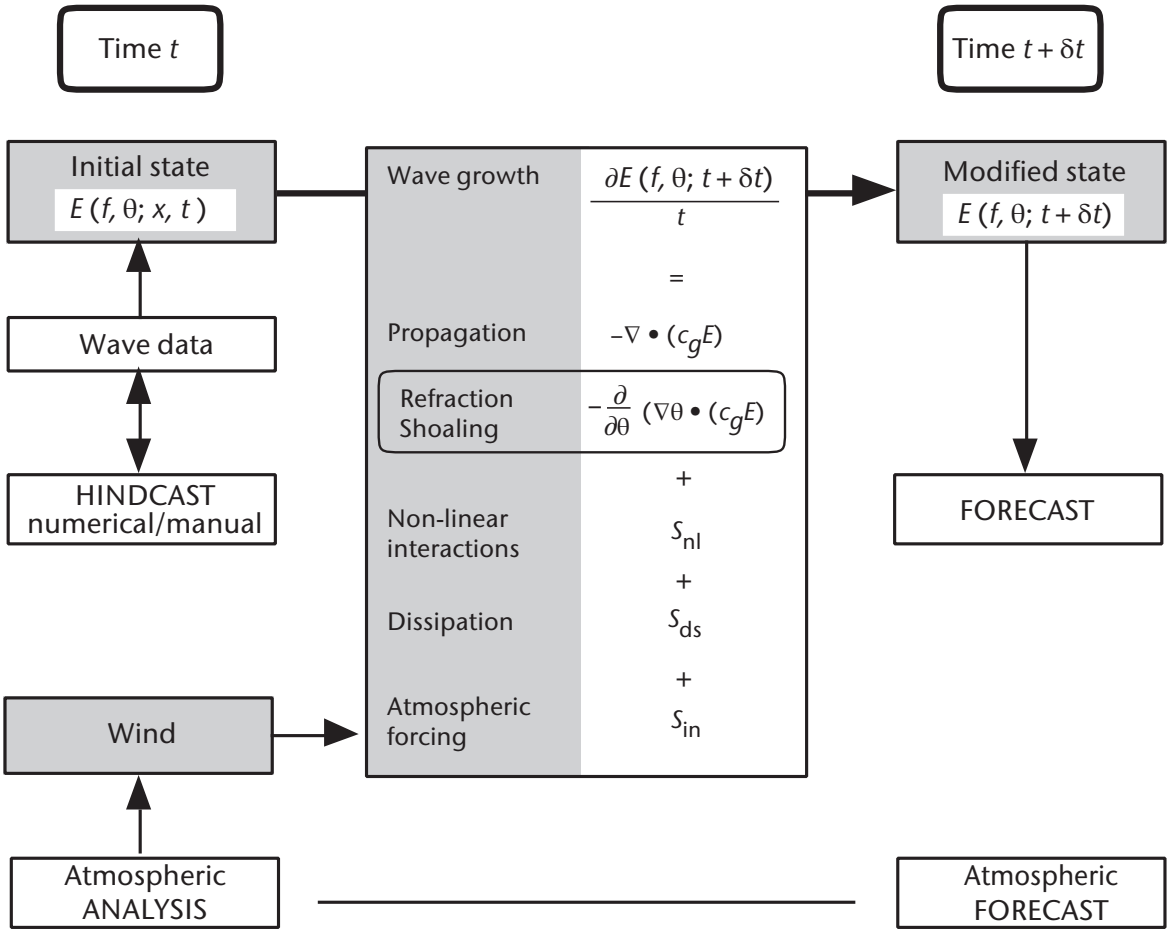

Figure 5.1. Elements of wave modelling

5.3 WAVE-ENERGY-BALANCE EQUATION

The concepts described in Chapter 3 are represented in wave models in a variety of ways. The most general formulation for computer models based on the elements in Figure 5.1 involves the spectral energy-balance equation, which describes the development of the surface gravity wave field in time and space:

$$\frac{\partial E}{\partial t} + \nabla \bullet (\boldsymbol{c}_g E) = S = S_{in} + S_{nl} + S_{ds}, \quad (5.1)$$

where $E = E(f,\theta,\boldsymbol{x},t)$ is the five-dimensional wave spectrum, which is a function of the two-dimensional sea-surface variance spectrum, time t and space $\boldsymbol{x}$, and $\boldsymbol{c}_g = \boldsymbol{c}_g(f)$ is the deep-water group velocity associated with its discrete intrinsic frequency f. S is the net source function, consisting of its simplest deep-water form of three terms: S_{in} the energy input with the wind, S_{nl} the non-linear energy transfer by wave–wave interactions and S_{ds} the dissipation (S_{ds} can be split into a set of terms based on the different dissipation processes being modelled).

This form of the equation is valid for deep water with no refraction and no significant currents or sea ice.

5.4 ELEMENTS OF WAVE MODELLING

The essence of wave modelling is to solve the energy-balance equation given as Equation 5.1. This first requires the definition of starting values for the wave energy, or initial conditions, which requires definition of the source terms on the right-hand side of Equation 5.1 and a method for solving changes as time progresses.

5.4.1 Initial conditions

As they predict a "forced-dissipative" system, wave-model forecasts are dependent on the quality of driving wind and ocean fields, particularly at long range. However, at short range, the quality of the wave forecast will also be strongly influenced by how well the model's starting conditions estimate the real-world wave field. In numerical weather prediction, the process of data assimilation, where model "first-guess" fields are blended with observations to provide a best estimate of these starting conditions (termed the "analysis"), is a critical step in forecast production.

In some ocean areas in the northern hemisphere, there is sufficient density of observations to make a direct field analysis of the parameters observed (such as significant wave height or period). Available in situ data are those provided from ships, buoys and platforms, which are of variable quality (see Chapter 7). This makes initialization of computer models based on in situ observations challenging. Phase-averaging models use spectral representations of the wave field, and it is difficult to reconstruct a full spectral distribution from a height, period and direction. However, the possibility of high-quality wave data from satellite-borne sensors with good ocean coverage has prompted attempts to find methods of assimilating these data into wave models. The first tested methods have been those using significant wave heights measured by radar altimeters on the GEOSAT and ERS-1 satellites. It has been shown that a positive impact on the wave-model results can be achieved by assimilating these data into wave models (for example, Breivik and Reistad, 1992; Lionello et al., 1992), and improvements in skill have been demonstrated at least 24–36 h into a forecast (see Figure 5.2). Successive altimeter missions have proven to be an invaluable source of information for operational analyses (Janssen et al., 2008; Abdalla et al., 2010) and reanalyses (Dee et al., 2011). Methods to assimilate spectral information, for example, wave spectra derived from synthetic aperture radar (SAR) images, have also been implemented (Abdalla et al., 2006). The effect of assimilating this type of data should be particularly beneficial in models that simulate long-range propagation of swell (for example, through the tropics, Figure 5.2), as the energy can be resident in the model forecast for several days.

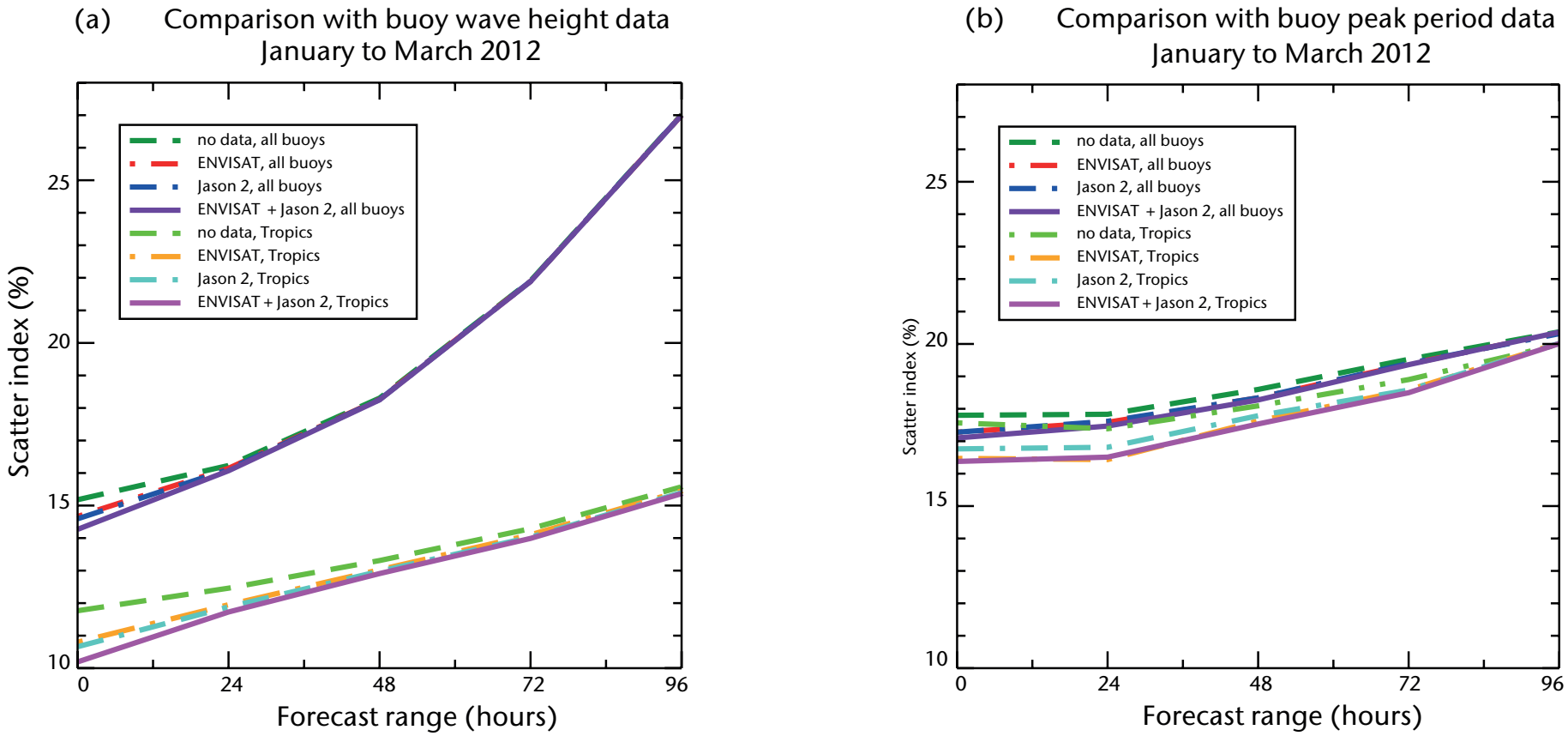

Figure 5.2. Impact of using altimeter wave-height data in a global model analysis. Verification is made against all available buoy data and buoy data from the tropics for wave height (a) and peak period (b). A set of 3 months stand-alone runs at 28 km resolution, forced by operational analysis winds were performed: a reference run with no data, one with Envisat data, another one with Jason-2 data and a final run with Envisat and Jason-2 data. Scatter index is the standard deviation of the difference normalized by the mean of the observations

Source: European Centre for Medium-Range Weather Forecasts (ECMWF)

Methods for generating the analysis (see Vilolante-Carvalho and Ramos (2006) for a summary) are described as "sequential", when the first guess and observation combination is made at a given time using observations made at a similar time to the first guess. A "variational" analysis minimizes the error variance through a predefined time window. Variational methods are generally more sophisticated than sequential methods and are in common use for numerical weather and ocean forecast applications. However, many variational methods can incur a higher computational cost. Lefèvre and Aouf (2012) noted that in wave data assimilation, more-sophisticated methods have not proven significantly advantageous over a well-refined sequential method such as optimal interpolation (for example, Lionello et al., 1992; Greenslade and Young, 2004, 2005*a*).

The key observations in global wave-model assimilation are sourced from satellite remote-sensing instruments, due to the wide geographical coverage given by their data. More-localized models will be reliant on in situ platforms providing a regularly updated source of observations. Observations from altimeter instruments enable assimilation based on significant wave-height values, while data from advanced SARs (ASARs) provide a truncated estimate of the wave spectrum. For application in the model, corrections to the first-guess field using these parameters must be converted to a correction over the two-dimensional wave spectrum. Where significant wave heights are assimilated, the full wave spectrum, or wind-sea part only, can be adjusted to preserve either mean wave steepness or an empirical relationship between dimensionless significant wave height and mean wave period (Lionello et al., 1992). For ASAR data assimilation, the correction is applied to specific partitions of the wave spectrum (Lefèvre and Aouf, 2012).

Common practice for estimating significant wave-height observation errors is to use a "triple collocation" method (for example, Janssen et al., 2007) in which three (or more) independent estimators of sea state (for example, a model, a satellite-borne sensor and an in situ network) are cross-compared in pairs to provide a (linear) bias and random error estimate for each data type. In the data assimilation scheme, local corrections at model-observation collocation points are propagated into the surrounding model cells via a spatial error covariance matrix. Choices are available for derivation of this matrix. For example: the method of Lonnberg and Hollingsworth (1986) uses the difference between the model output and observations; the National Meteorological Centre method (Greenslade and Young, 2005*b*) examines the differences among forecasts of different ranges that are valid at the same time; and the Canadian quick covariance method (Polavarapu et al., 2005) estimates the background error structure from the difference between the time-varying model state and the mean model state averaged over all time steps. The spatial correlation function can be simplified to a relationship defined by correlation length scale but requires assumptions about the spatial uniformity of these scales ("isotropy"). In the open ocean, these scales have been demonstrated to be in the region 200–500 km (Greenslade and Young, 2005*a*), although shorter scales and non-isotropic behaviour might reasonably be expected in shelf seas where topographic sheltering, shallow-water effects and interaction with tides will modify the wave field over shorter distances. Delpey et al. (2010) also demonstrated non-isotropic behaviour of swell wave fields in the open ocean.

Even if wave observations are available, wave-model initial conditions are tied to the availability of good-quality winds fields (see next section) for the generation of the initial conditions used at the start of any forecast.

5.4.2 **Winds**

An important element in wave modelling is the motion of the atmosphere above the sea surface. The only input of energy to the sea surface over the considered timescales comes from the wind. Transfer of energy to the wave field is achieved through the surface stress applied by the wind, which varies roughly as the square of the wind speed. Thus, an error in wind specification can lead to a large error in the wave energy and subsequently in parameters such as significant wave height.

The atmosphere has a complex interaction with the wave field, mean and gust wind speeds, wind profile, atmospheric stability, density of air, influence of the waves themselves on the atmospheric boundary layer and so forth, all of which should be considered. Chapter 2 discussed specification of the winds required for wave modelling.

For a computer model, a wind history or prognosis is given by supplying the wind field at a series of time steps from an atmospheric model, either directly as part of the active coupling among the different models (Janssen, 2004; Chen et al., 2013) or through input fields following the run of a given atmospheric model. This takes care of the problem of wind duration. Similarly, considerations of fetch are accounted for by the wind field specification and by the boundary configuration used in the propagation scheme. Forecasters using manual methods must make their own assessment of fetch and duration.

5.4.3 Input and dissipation

The atmospheric boundary layer is not completely independent of the wave field. In fact, a feedback mechanism, which depends on the energy in the wave field, dominates the input to the waves. S_{in} designates the rate at which energy is fed into the wave field.

This wind input term, S_{in}, is generally accepted as having the form

$$S_{in} = A(f,\theta) + B(f,\theta)E(f,\theta). \tag{5.2}$$

$A(f,\theta)$ is the resonant interaction between waves and turbulent pressure patterns in the air suggested by Phillips (1957), whereas the second term on the right-hand side represents the feedback between growing waves and induced turbulent pressure patterns as suggested by Miles (1957). The Miles theory has limits and cannot explain all features that have been observed, for example, change in wind direction or decay of wind speed (Donelan et al., 2006).

Equation 5.2 is often defined in terms of the friction speed $u_* = \sqrt{(\tau / \rho_a)}$, where τ is the magnitude of the wind shear stress and ρ_a is the density of air. From a physical point of view, scaling wave growth to u_* is preferable to scaling with wind speed U_z at level z (commonly taken to be 10 m)

$$U_{10} = \frac{u_*}{\kappa} \ln\left(\frac{10}{z_0}\right), \tag{5.3}$$

where z_0 is the surface roughness and κ is the von Kármán constant.

Komen et al. (1984) approximated such a scaling, as illustrated in Equation 3.5. However, a lack of wind-stress data precluded more-rigorous treatments. U_z and u_* do not appear to be linearly related, and the drag coefficient C_d, used to determine τ ($\tau = \rho_a C_d U_z^2$), has been found to be an increasing function of U_z (for example, Large and Pond, 1981; Wu, 1982; Hersbach, 2011; Edson et al., 2013). Scaling is an important part of wave modelling, but is far from resolved. Note that C_d also depends on z (from U_z) (see, for example, Equation 2.5). Recent advances with a quasi-linear theory, which includes the effects of growing waves on the mean air flow, have enabled further refinement of the formulation (Janssen, 2004).

Alternative formulations to Equation 5.3 exist and are at the core of active research in the field (Tolman and Chalikov, 1996; Donelan et al., 2006; WISE Group, 2007; Ardhuin et al., 2010; Chalikov and Rainchilk, 2011; Stopa et al., 2016). The general form of Equation 5.2 remains, albeit, negative wind input is modelled and $B(f,\theta)$ can become a function of the spectrum itself (Zieger et al., 2015).

The term S_{ds} describes the rate at which energy is lost from the wave field. In deep water, this is mainly through wave breaking and whitecapping. Originally, this source term was treated as a random process at the sea surface. However, recent in situ and SAR observations have provided insights into the magnitude of the wave dissipation term. This has shown the multiple aspects of the problem, such as the threshold behaviour of the breaking, the cumulative impact of longer

waves on the breaking of short waves and the dissipation of non-breaking waves (Ardhuin et al., 2010; Babanin, 2011; Jiang et al., 2016). In shallow water, waves may also be dissipated through interaction with the seabed (bottom friction and bottom-induced breaking). Chapter 3 gave more details.

5.4.4 Non-linear interactions

Any strong non-linearities in the wave field and its evolution are generally accounted for in the dissipation terms. Input and dissipation terms can be regarded as complementary to those linear and weakly non-linear aspects of the wave field that are possible to describe dynamically. Into this latter category fall the propagation of surface waves and the redistribution of energy within the wave spectrum due to weak non-linear interactions among wave components, which is designated as a source term, S_{nl}. Section 3.5 discussed non-linear interactions.

The effect of the term S_{nl} is briefly as follows. In the dominant region of the spectrum near the peak, the wind input is greater than the dissipation. The excess energy is transferred by the non-linear interactions towards higher and lower frequencies. At the higher frequencies, the energy is dissipated. The transfer to lower frequencies leads to growth of new wave components on the forward (left) side of the spectrum. This results in migration of the spectral peak towards lower frequencies. The non-linear wave–wave interactions preserve the spectral shape. As a consequence, spectra of growing seas are shaped by these non-linear interactions to conform to a self-similar spectrum (for example, the Joint North Sea Wave Project (JONSWAP); see section 1.3.9).

The source term S_{nl} can be computed explicitly, but the requirement on computing power is still significant. In third-generation models, the non-linear interactions among wave components are computed explicitly using special integration techniques and with the aid of simplifications introduced by Hasselmann and Hasselmann (1985) and Hasselmann et al. (1985). With these simplifications, modern computers are now well able to produce real-time wave forecasts. More-exact methods like the multiple discrete interaction approximation (DIA) (Tolman, 2013) and two-scale approximation (Perrie et al., 2013) for wave–wave interaction computation have yet to be used in large applications but are available for model developments (Tolman et al., 2012). Before the advent of power computers, second-generation numerical wave models were developed, in which the non-linear interactions were parameterized or treated in a simplified way. This difference in the treatment of non-linear interactions may give rise to significant differences among models of different generations. A simplified illustration of the three source terms in relation to the wave spectrum was shown in Figure 3.7.

5.4.5 Propagation

Wave energy propagates at the group velocity (see section 1.3.2), not at the velocity of the waves or wave crests (which is the phase velocity: the speed at which the phase is constant). Wave modelling deals with descriptors such as energy density and so it is the group velocity that is important.

The propagative effects of water waves are quantified by noting that the local rate of change of energy is equal to the net rate of flow of energy to or from that locality (divergence of energy-density flux). The practical problem encountered in computer modelling is to find a numerical scheme for calculating this. In manual models, propagation is considered only outside the generation area, and attention is focused on the dispersion and spreading of waves as they propagate.

Propagation affects the growth of waves through the balance between energy leaving a locality and that entering it. It is the propagation of wave energy that enables fetch-limited growth to be modelled in a numerical model. Energy levels over land are zero, and so, downwind of a coast, there is no upstream input of wave energy. Hence, energy input from the atmosphere is propagated away, keeping total energy levels near the coast low.

5.4.5.1 *Discrete-grid methods*

The energy-balance equation (Equation 5.1) is often solved numerically using finite-difference schemes on a discrete grid as exemplified in Figure 5.3. Δx_i ($i = 1, 2$) is the grid spacing in the two horizontal directions. Equation 5.1 may take a form such as

$$E(\boldsymbol{x}, t + \Delta t) = E(\boldsymbol{x}, t) - \Delta t \sum_{i=1}^{2} \left[\frac{(c_{g_i} E)_{x_i} - (c_{g_i} E)_{x_i - \Delta x_i}}{\Delta x_i} \right] + \Delta t S(\boldsymbol{x}, t), \tag{5.4}$$

where Δt is the time step, and E and S are functions of wave number ($\boldsymbol{k}$) or frequency and direction (f,θ).

Using the spectral representation $E = E(f,\theta)$, the energy density is an array of frequency–direction bins (f,θ). The above approach collects a continuum of wave components travelling at slightly different group velocities into a single frequency bin. That is, it uses a single frequency and direction to characterize each component. Due to the dispersive character of ocean waves, the area of a bin containing components within ($\Delta f,\Delta\theta$) should increase with time as the waves propagate away from the origin. The wave energy in this bin will spread out over an arc of width $\Delta\theta$ and stretch out depending on the range of group velocities. In the finite-difference approach, all components propagate at the mean group velocity of the bin, so that eventually the components separate as they propagate across the model's ocean. This is called the "garden sprinkler" effect, as it resembles the pattern of droplets from a garden sprinkler, and is an artefact of the method of modelling. All discrete-grid models in the inventory suffer from the sprinkler effect (see Figure 5.4), although usually the smoothing effect of continual generation diminishes the potential ill effects, or it is smoothed over as a result of numerical error (numerical diffusion).

There are many finite-difference schemes in use: from first-order schemes, which use adjacent grid points only to work out the energy gradient, to fourth-order schemes, which use five consecutive points. The choice of time step Δt depends on the grid spacing Δx. For numerical stability, the distance moved in a time step ($\Delta t c_g$) must be less than one grid space (Δx). Models typically use 10–100 km grid spacing and time steps of several minutes to 1 h.

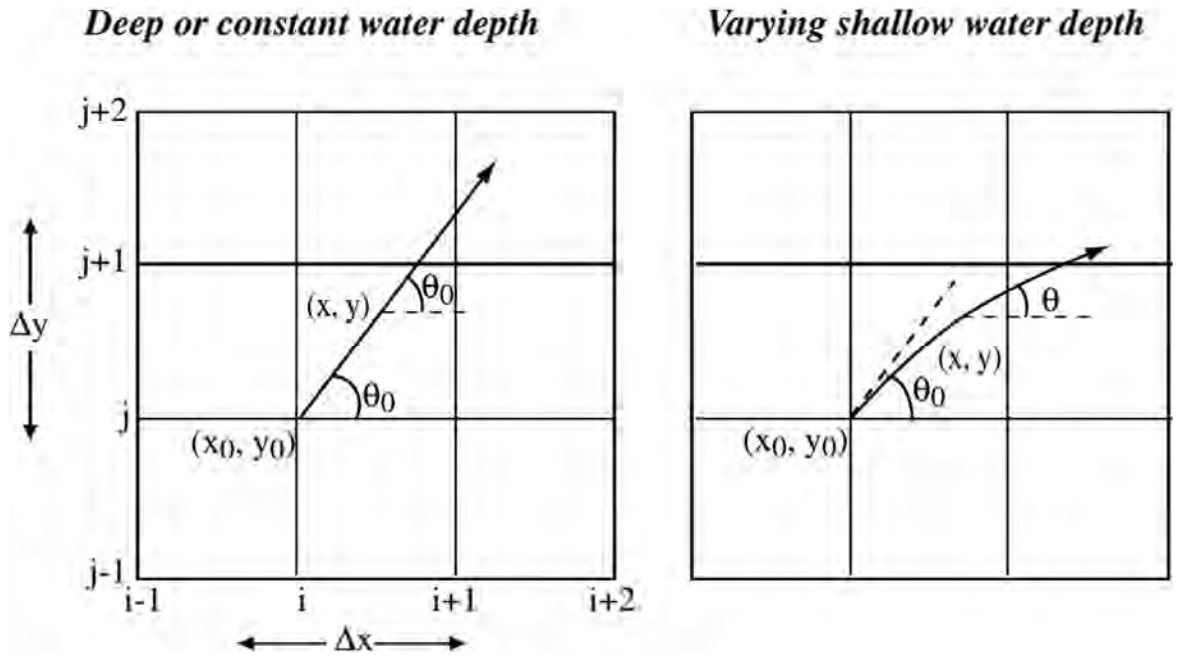

Figure 5.3. Typical grid for numerical wave models (x stands for x_1 and y for x_2). In grid-type models, the energy in (f,θ) bins is propagated between points according to an equation like Equation 5.4. In ray models, the energy is followed along characteristic lines.

Frequency	Period	Distance travelled in km	Length of disturbance in km
0.050	20	3630	556
0.067	15	2722	232
0.083	12	2185	333
0.100	10	1815	278
0.167	6	1092	167

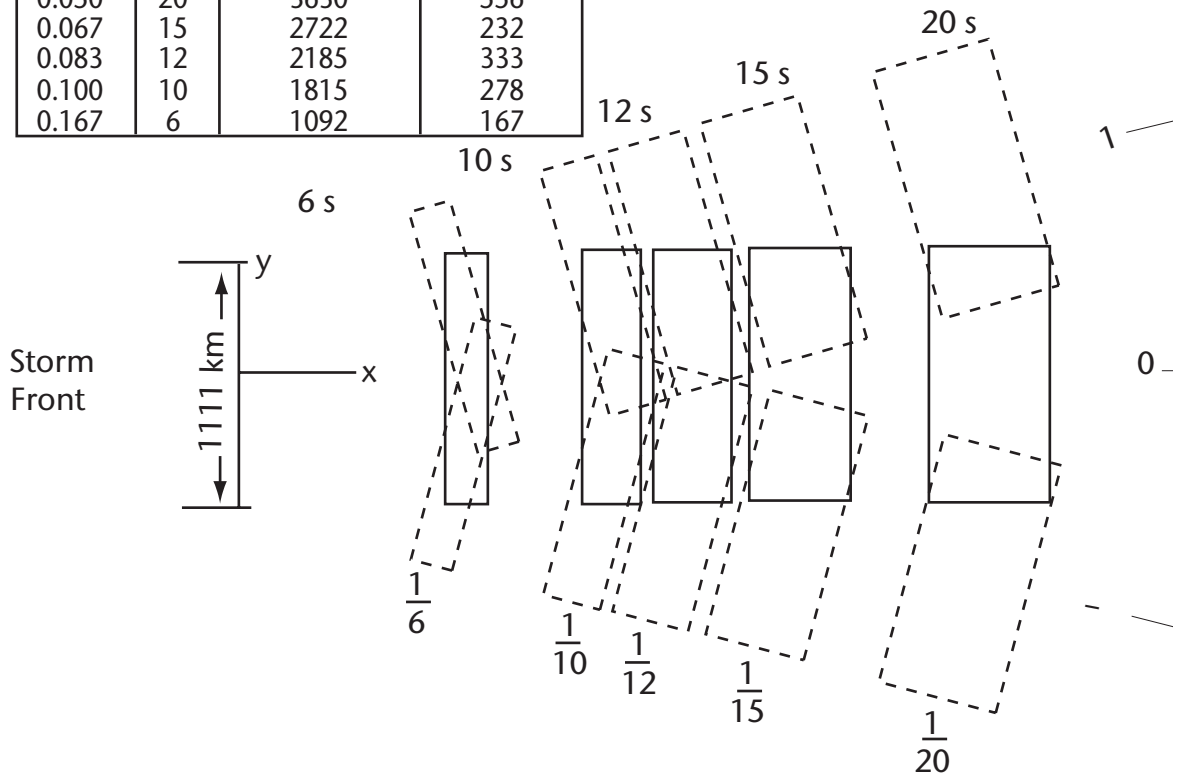

Figure 5.4. Propagation of discrete spectral components from a storm front. This illustrates the effects of angular spreading and dispersion on the wave energy. The garden sprinkler effect resulting from the discretization of the spectrum can be seen.

Discrete-grid models calculate the complete (f,θ) spectrum at all sea points of the grid at each time step.

5.4.5.2 *Ray-tracing methods*

An alternative method is to solve the energy-balance equation (Equation 5.1) along characteristics or rays. Time integration is still performed by finite differencing, but the spatial integration is not needed and the sprinkler effect is avoided. However, the number of output points is usually reduced for reasons of computational costs.

For ocean waves, there is a dispersion relation, relating the wave frequency to the wave number (see Equations 1.3 and 1.4), of the form

$$f(\boldsymbol{x},t) = \sigma\left[\boldsymbol{k}(\boldsymbol{x},t)\psi(\boldsymbol{x},t)\right]. \tag{5.5}$$

Here, σ is used to denote the particular frequency associated with wave number $\boldsymbol{k}$, and the property of the medium Ψ, which in this context will be the bottom depth and/or currents. Characteristic curves are then obtained by integration of

$$\frac{\mathrm{d}x}{\mathrm{d}t} = c_{\mathrm{g}} = \frac{\delta\sigma}{\delta k}. \tag{5.6}$$

In an ocean with steady currents, these curves need be obtained only once. Figure 5.3 shows examples including refraction due to bottom topography. See LeBlond and Mysak (1978) for more details on ray theory.

Thus, starting from the required point of interest, rays or characteristics are calculated to the boundary of the area considered necessary to obtain reliable wave energy at the selected point. As the history of a particular wave frequency is being considered, the reference frame moves with the component and all that needs to be considered is the source function along the rays:

$$\frac{\delta E}{\delta t} = S. \tag{5.7}$$

Rays are calculated according to the required directional resolution at the point of interest; along each ray, Equation 5.7 may be solved either for each frequency separately or for the total energy. In the former approach, S_{nl} is not considered at all. In the latter case, interactions in the frequency domain are included, but the directions are uncoupled.

The ray approach has been extensively used in the past in models where wind sea and swell are treated separately. In such cases, swell is propagated along the rays subjected only to frictional damping and geometric spread. Interactions with the wind sea may take place where the peak frequency of the Pierson–Moskowitz spectrum ($f_{PM} = 0.13g/U_{10}$) is less than the swell frequency.

5.4.6 Directional relaxation and wind-sea–swell interaction

Before the wide acceptance of third-generation wave models, many of the differences among numerical wave models resulted from the way in which they catered for the weakly non-linear wave–wave interactions (S_{nl}). The differences are particularly noticeable in the case of non-homogeneous and/or non-stationary wind fields. When the wind direction changes, the existing wind sea becomes partly swell, and a new wind sea develops. The time evolution of these components results in a relaxation of the wave field towards a new steady state that eventually approaches a fully developed sea in the new wind direction.

Three mechanisms contribute to the directional relaxation:

1. Energy input by the wind to the new wind sea;
2. Attenuation of the swell;
3. Weak non-linear interactions, resulting in energy transfer from swell to wind sea.

The way these mechanisms are modelled may yield significant deviations among models. The third mechanism appears to be dominant in this respect.

5.4.7 Depth

Water depth can considerably affect the properties of waves and how they are modelled. It is known that waves feel the seabed and are changed significantly by it at depths less than about one quarter of the deep-water wavelength (see also section 1.2.5). In a sea with a wide spectrum, the longer waves may be influenced by the depth without much effect on the short waves.

One major effect of depth is on the propagation characteristics. Waves are slowed down, and may be refracted if the seabed is not flat. The slowing of the waves leads to an increase in wave energy (see Equation 5.1). There are also more dissipative processes involved through interaction with the seabed. The framework described here for wave modelling is broad enough in its concept to be able to cope with depth-related effects without drastic alterations to the form of the model outlined in Figure 5.1. Chapters 1 and 3 discussed the effects of shallow water in more detail.

5.4.8 Effects of boundaries, coast-lines and islands

With the exception of global models, most existing wave models have an open ocean boundary. Wave energy may then enter the modelled area. The best solution is to obtain boundary data from a model operating over a larger area, for example, a global model. If there is no knowledge

of the wave energy entering the model area, a possible boundary condition is to let the energy be zero at the boundaries at all times. Another solution may be to specify zero flux of energy through the boundary. It will be difficult to get a true representation of distantly generated swell in either case. The area should therefore be sufficiently large to catch all significant swell that affects the region of interest.

In operational global models, with a grid resolution in the range 10–100 km, it is difficult to get a true representation of coast-lines and islands. A coarse resolution will strongly affect the shadowing effects of islands and capes. Special precautions need to be taken to obtain a faithful representation of the sea state near such a feature. One solution may be to use a finer grid for certain areas, a "nested" model, where results from the coarse grid are used as boundary input to the fine grid. It may also be necessary to increase the directional resolution so as to model limited depth and shadowing effects better. Another way may be to evaluate the effects of small-scale topographic features for affected wave directions and pass that subgrid information as part of the wave advection (Chawla and Tolman, 2008). A more elegant way is to refine the grid where needed. This can be achieved using a two-way nested multigrid approach (WAVEWATCH III Development Group, 2016), whereby subdomains with finer resolution are interacting with the coarser grid, or by solving the problem on a smoothly varying mesh using unstructured grids (Roland et al., 2009; Zijlema, 2010; Li, 2012).

5.5 MODEL CLASSES

Wave models compute the wave spectrum by numerical integration of Equation 5.1 over a geographical region. The models may differ in several respects, for example, the representation of the spectrum, the assumed forms of S_{in} and S_{ds}, the representation of S_{nl}, and whether the integration is carried out in natural characteristic coordinates along individual rays or in terms of a discretized advection operator in a grid-point system common to all wave components.

During the development of wave models, the treatment of the non-linear source term S_{nl} required some attention. Differences among the categories were found in the specification of S_{nl}. Even within third-generation models, the choice of the treatment of S_{nl} is still a topic of debate. However, it is recognized that the choice should not dictate the development of more physics-based parameterizations for the other source terms (Tolman et al., 2012).

In the energy-balance equation (Equation 5.1), the interactive term S_{nl} couples the components. Models based on discrete spectral components with a non-linear term formulated in terms of several (if not all) components are called coupled discrete (CD) models. In such models, estimates of all components are needed just to be able to compute the evolution of any one component.

Computations for these models can be time-consuming. Some modellers prefer to dispense with the coupling term and include the weak non-linear interactions implicitly in their formulation for $S_{in} + S_{ds}$. Such models are decoupled propagation (DP) models. Each component can then be calculated independently. Advanced models in this class may include a simple parametric form for S_{nl}, but they are nevertheless distinguished by the pre-eminence of S_{in} and S_{ds} in the source term.

The third type of model uses the evidence that spectra of growing seas are shaped by the non-linear interactions to conform to a self-similar spectrum (for example, JONSWAP – see section 1.3.9). The spectral shape is characterized by a few parameters and the energy-balance equation can then be written in these terms. This gives an evolution equation for each of a small number of parameters rather than one for each of a large number of components. However, this parametric representation is valid for the self-similar form of the wind-sea spectrum only, and waves outside the generating area (swell) require special treatment. This is usually achieved by interfacing the parametric model for wind sea with a DP model for swell through a set of algorithms by which wind-sea energy and swell energy are interchanged, hence the naming of this class as coupled hybrid (CH) models. SWAMP Group (1985) gave a thorough description and discussion of the model classes.

5.5.1 Decoupled propagation models

Models of this class generally represent the wave spectrum as a two-dimensional discretized array of frequency–direction cells in which each cell or component propagates at its appropriate group velocity along its own ray path. The components are grown according to a source function of the form

$$S = A + B\ E(f, \theta). \tag{5.8}$$

As non-linear energy transfer is basically neglected, the factors A and B are usually determined empirically.

Each component is grown independently of all the other components up to a saturation limit, which is also independent of the other spectral components and is represented by a universal equilibrium distribution. If non-linear coupling is considered at all, it is parameterized in a simple way, for example, by one or two spectral parameters. The saturation limit may be given by the energy of a fully developed sea, often represented by the Pierson–Moskowitz spectrum (see section 1.3.9). Let the fully developed sea spectrum be given by E_∞. A modification of S_{in} may then appear as

$$S = \frac{\delta E}{\delta t} = \left[A\sqrt{1 - \left(\frac{E}{E_\infty}\right)^2} + BE \right] \left[1 - \left(\frac{E}{E_\infty}\right)^2 \right] \tag{5.9}$$

(Pierson et al., 1966; Lazanoff and Stevenson, 1975), or

$$S = \frac{\delta E}{\delta t} = (A + BE)\left(1 - \frac{E}{E_\infty}\right)^2 \tag{5.10}$$

(Ewing, 1971). It is also possible to use the Phillips saturation range

$$E_\infty = \frac{\alpha g^2}{(2\pi)^4} f^{-5} \tag{5.11}$$

as the saturation limit (Cavaleri and Rizzoli, 1981).

The introduction of a saturation limit also works as an implicit representation of wave-energy dissipation, except for dissipation due to bottom friction and dissipation of swell. None of these effects is specific to DP models and may vary from model to model.

For strictly decoupled models, and for weakly coupled models, the differential time and space scales dt and ds are related through the group velocity c_g for a wave component, ds = c_gdt. From this, it follows that for DP models, the laws for fetch-limited waves under uniform stationary wind conditions are immediately translated into the corresponding duration-limited growth laws by replacing the fetch X with $c_g t$ for each wave component.

Another feature of DP models that can be traced to the decoupling of wave components is that the spectrum generally develops a finer structure in both frequency and direction than coupled models, which continually redistribute energy and smooth the spectrum.

5.5.2 Coupled hybrid models

The independent evolution of individual wave components is effectively prevented by non-linear energy transfer. Unless the wind field is strongly non-uniform, the non-linear transfer is sufficiently rapid (relative to advection and other source functions) that a quasi-equilibrium spectral distribution is established. The distributions appear to be of the same shape for a wide variety of generation conditions and differ only with respect to the energy and frequency scales. Hasselmann et al. (1973, 1976) confirmed theoretically the quasi-self-similarity.

A universal relationship appears to exist between the non-dimensional total energy and frequency parameters ε and ν, respectively. The non-dimensional scaling incorporates g and

some wind-speed measure, for example the wind speed at 10 m U_{10}, or the friction speed u_*. Hence, $\varepsilon = Eg^2/u^4$ and $\nu_p = f_p g/u$, where $u = U_{10}$ or u_*, and E is the total energy (from the integrated spectrum).

As the evolution of the developing wind-sea spectrum is so strongly controlled by the shape-stabilizing non-linear transfer, it appears reasonable to express the growth of the wind-sea spectrum in terms of one or a few parameters (for example ε, the non-dimensional wave energy). In such a one-parameter, first-order representation, all other non-dimensional variables (for example ν_p, the non-dimensional peak frequency) are uniquely determined and hence diagnosed.

Thus, in one extreme, the parametric model may predict as few as one parameter (for example, the total spectral energy), with the wind-sea spectrum being diagnosed from that. For such a model, the evolution equation is obtained by integrating Equation 5.1 over all frequencies and directions,

$$\frac{\delta E}{\delta t} + \nabla \bullet (\bar{c}_g E) = S_E, \tag{5.12}$$

where $\bar{c}_g$ is the effective propagation velocity of the total energy,

$$\bar{c}_g = \frac{\int c_g E(f,\theta) \mathrm{d}f \ \mathrm{d}\theta}{\int E(f,\theta)}, \tag{5.13}$$

and S_E is the projection of the net source function S onto the parameter E,

$$S_E = \int S(f,\theta) \mathrm{d}f \ \mathrm{d}\theta. \tag{5.14}$$

$\bar{c}_g$ is uniquely determined in terms of E by a prescribed spectral shape. S_E must be described as a function of E and U_{10} or u_*, and is usually determined empirically.

If additional parameters are introduced, for example the peak frequency f_p, the Phillips parameter α or the mean propagation direction θ, the growth of the wind-sea spectrum is expressed by a small set of coupled transport equations, one for each parameter. Hasselmann et al. (1976) gave a general method for projecting the transport equation in the complete (f,θ) representation onto an approximate parameter space representation.

In slowly varying and weakly non-uniform wind, parametric wave models appear to give qualitatively the same results. The more parameters that are used, the more varied are the spectral shapes obtained. In particular, if the mean wave direction θ is used, directional lag effects become noticeable in rapidly turning winds.

The fetch–duration relation for a parametric wave model will differ from that of a DP model in that a mean propagation speed takes the place of the group speed for each frequency band:

$$\boldsymbol{X} = A c_g t, \tag{5.15}$$

where $\boldsymbol{X}$ is the fetch, t is the duration and A is a constant (typically $A = 2/3$). Thus, it is not possible to tune the two types of model for both fetch- and duration-limited cases.

Once the non-linear energy transfer ceases to dominate the evolution of the wave spectrum, the parametric representation breaks down. This is the case for the low-frequency part of the wave spectrum that is no longer actively generated by the wind (the swell part). The evolution of swell is controlled primarily by advection and some weak damping. It is therefore represented in parametric wave models in a discrete DP model. The combination of a parametric wind-sea model and a DP swell model is termed a CH model.

Such CH models may be expected to encounter problems when sea and swell interact. Typical transition regimes arise:

– In decreasing wind speed or when the wind direction turns, in which cases, wind sea is transformed to swell;

– When swell enters areas where the wind speed is sufficiently high that the Pierson–Moskowitz peak frequency $f_p = 0.13g/U_{10}$ is lower than the swell frequency, in which case, the swell suddenly comes into the active wave growth regime.

These transitions are modelled simply in CH models. For turning winds, it is common that the wind sea loses some energy to swell. The loss may be a continuous function of the rate of change of wind direction or take place only when the change is above a certain angle.

When the wind decreases, the CH models generally transfer frequency bands that travel faster than the wind to swell. Some models also transfer the energy that exceeds the appropriate value for fully developed wind sea into swell.

Swell may be reabsorbed as wind sea when the wind increases, and the wind-sea peak frequency becomes equal to or less than the swell frequency. Some CH models allow reabsorption only if the angle between wind-sea and swell propagation directions fulfil certain criteria.

Some models allow swell to propagate unaffected by local winds to destination points. Interaction takes place only at the destinations. If wind sea exceeds swell at a point, the swell is completely destroyed. Thus, the reabsorption of swell into wind sea is non-conservative.

Generally, CH models use characteristics or rays to propagate swell. The CH class may include many semi-manual methods. The parametric approach allows empirical relationships for the evolution of spectral parameters to be used. These can often be evaluated without the assistance of a computer, as can the characteristics of the swell.

5.5.3 Coupled discrete models

The problem of swell–wind-sea interaction in CH models may be circumvented by retaining the discrete spectral representation for the entire spectrum and introducing non-linear energy transfers. These interactions are parameterized in different ways in the models in operational use today. However, the number of parameters are often limited, creating a mismatch among the degrees of freedom used in the description of the spectrum (say, for example, 24 directions and 30 frequencies) and the degrees of freedom in the representation of the non-linear transfer (for example, 10 parameters).

In CD models, a source function of the Miles type, $S_{in} = BE$ is common, as in DP models. However, the factor B is strongly exaggerated in the DP models to compensate for the lack of explicit S_{nl}. A Phillips forcing term may also be included so that $S_{in} = A + BE$, but the value of A is usually significant only in the initial spin-up of the model.

The difference between present CH and CD models may not be as distinct as the classification suggests. In CD models, the non-linear transfer is sometimes modelled by a limited set of parameters. The main difference is in the number of degrees of freedom. The CD models usually parameterize the high-frequency part of the spectrum. However, some of the latest observation-based formulations are trying to move away from the need to parameterize the high frequencies (Zieger et al., 2015).

The non-linear source term S_{nl} may be introduced in the form of the simple redistribution of energy according to a parameterized spectral shape, for example the JONSWAP spectrum. Another solution can be to parameterize S_{nl} in a similar way to the spectrum. This approach is generally limited because each spectral form will lead to different forms of S_{nl}. This problem may be avoided by using a value of S_{nl} parameterized for a limited number of selected spectral shapes. The shape most resembling the spectrum is chosen. Further approaches include sophisticated calculations of S_{nl}, such as DIA (Hasselmann and Hasselmann, 1985), generalized multiple DIA (Tolman, 2013) and near exact calculations (Van Vledder, 2006, 2012) that result from numerical integration of Equation 3.15.

The individual treatment of growth for each frequency–direction band in CD models provides certain inertia in the directional distribution. This allows the mean wind-sea direction to lag the

wind direction and makes the models more sensitive to lateral limitations of the wind field or asymmetric boundary conditions. The CD models also develop more directional fine structure in the spectra than CH models.

5.5.4 Third-generation models

Classification of wave models into first-, second- and third-generation wave models is also used. This takes into account the method of handling the non-linear source term S_{nl}:

- First-generation models do not have an explicit S_{nl} term. Non-linear energy transfers are implicitly expressed through the S_{in} and S_{ds} terms.
- Second-generation models handle the S_{nl} term by parametric methods, for example, by applying a reference spectrum (for example, the JONSWAP or the Pierson–Moskowitz spectrum) to reorganize the energy (after wave growth and dissipation) over the frequencies.
- Third-generation models calculate the non-linear energy transfers explicitly, although it is usually necessary to make analytic and numerical approximations to expedite the calculations.

Results from many of the operational first- and second-generation models were intercompared in the SWAMP Group (1985) study. Although the first- and second-generation wave models can be calibrated to give reasonable results in most wind situations, the intercomparison study identified some shortcomings, particularly in extreme wind and wave situations for which reliable wave forecasts are most important. The differences among the models were most pronounced when the models were driven by identical wind fields from a hurricane. The models gave maximum significant wave heights in the range 8–25 m.

As a consequence of the variable results from the SWAMP Group study, and with the advent of more powerful computers, scientists began to develop a new, third generation of wave models that explicitly calculated each of the identified mechanisms in wave evolution. This led to the development of WAM (Komen et al., 1994), followed by WAVEWATCH III (WAVEWATCH III Development Group, 2016) and SWAN (Holthuijsen, 2007). WAM has shown good results in extreme wind and wave conditions. Figure 5.5 shows a comparison between observed significant wave heights and significant wave heights from WAM during Hurricane *Camille*, which occurred in the Gulf of Mexico in 1969. The grid spacing was 1/4° in latitude and longitude. The comparison demonstrates good performance of the model in a complicated turning wind situation.

The main difference between the second- and third-generation wave models is that, in the latter, the wave-energy-balance equation is solved without constraints on the shape of the wave spectrum. This is achieved by attempting to make an accurate calculation of the S_{nl} term. As mentioned in section 3.5, a simplified integration technique to compute the non-linear source term S_{nl} was developed by Hasselmann at the Max Planck Institute in Hamburg, Germany. Efficient computation of the non-linear source term together with more powerful computers made it possible to develop third-generation spectral wave prediction models (WAM; WAMDI Group, 1988). Third-generation wave models are similar in structure, representing state-of-the-art knowledge of the physics of the wave evolution. Methods for exact computation of this term are now becoming more widely used (Van Vledder, 2012), finally unleashing the full potential of third-generation modelling.

Other models may differ in the propagation schemes used, in the method for calculating the non-linear source term S_{nl}, in the manner in which they deal with shallow-water effects and the influence of ocean currents on wave evolution, and whether or not they are coupled to an atmospheric model and/or to a hydrodynamical or an ocean circulation model.

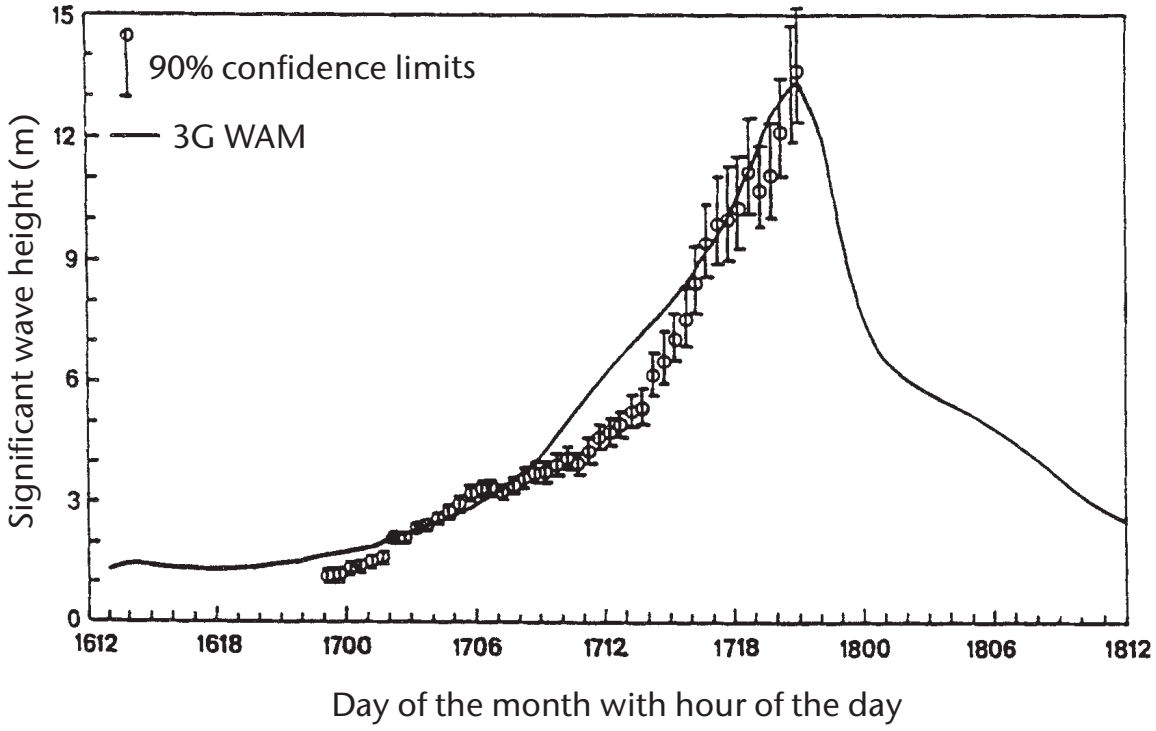

Figure 5.5. Comparison of calculated and observed wave heights during Hurricane *Camille* (1969). The wave sensor failed at the height of the storm.

Source: WAMDI Group (1988)

5.6 NEW DEVELOPMENTS

Improving the parameterization of wave growth, dissipation, non-linear wave–wave interactions and the ocean's interaction with the atmosphere are key to continued development of wave model accuracy. As discussed in Chapters 3 and 5, a significant body of recent research has led to the proposal of new formulations for wind sea, swell and depth-limited breaking wave dissipation (for example, Ardhuin et al., 2010; Filipot and Ardhuin, 2012; Zieger et al., 2015), which are gradually being introduced to operational forecast models. Stopa et al. (2016) assessed the model performance for the most recently developed source terms. An increased body of data from imaging systems measuring wave whitecapping processes and remote-sensed observations of open ocean swell mean that further advances and refinements are expected in this field.

A major control on the model specification of the two-dimensional wave spectrum in third-generation wave models comes from the DIA scheme (Hasselmann et al., 1985), which is commonly used to parameterize non-linear four-wave interactions. Numerous other schemes with a closer match to the analytical solution exist, from quasi-analytical techniques (Masuda, 1980; Van Vledder, 2006; Gagnaire-Renou et al., 2010) to more-generalized forms of DIA (Tolman, 2013) and the two-scale approximation of the wave–wave interaction term (Perrie et al., 2013). However, the DIA scheme has persisted as an operational tool due to its computational efficiency. As computing power increases, the use of other schemes in operational models may become plausible. The challenge with alternatives for the non-linear interaction term is that it has not been fully balanced with existing input and dissipation terms, meaning that the tuning parameters and coefficients in these source terms would need some attention.

The most fundamental control on wave-model forecast skill lies in the quality of the driving atmospheric winds (Cavaleri and Bertotti, 2006; Janssen, 2008). Numerical weather prediction has traditionally seen ongoing improvements in the skill of marine wind fields, which have positively affected wave prediction. A development that is believed to be fundamental to the

continued improvement of wave and atmospheric systems is the adoption of fully coupled atmosphere–wave–ocean modelling systems, in which the feedback among the atmosphere, surface waves and the ocean are explicitly calculated. A growing evidence base exists of experimental work testing coupling parameterizations in extreme cases (for example, in tropical storms by Moon et al., 2004; Chen et al., 2013). Janssen and Viterbo (1996) and Janssen (2004) documented an improvement to the ECMWF operational model forecasts that has resulted from coupling the atmosphere to waves.

In the open ocean, the requirement to improve spatial resolution in wave models is restricted to adopting a scale that is compatible with the available forcing winds. However, in the coastal zone, models must account for (often fine-scale) changes in bathymetry and effects of sheltering behind headlands. Beyond the use of traditional one- or two-way nesting schemes, some wave models have been developed to work using unstructured grid schemes (for example, Sorensen et al., 2004; Roland, 2008; Zijlema, 2009), locally refined grids (for example, Tolman, 2008; Popinet et al., 2010; Li, 2012) and adoption of numerical techniques that deal efficiently with spatial and intraspectral propagation of energy on high-resolution grid cells (for example, Booij et al., 1999; Van der Westhuysen and Tolman, 2011; Li, 2012). The challenge in the future will be to provide products that exploit the benefits of such models at ocean and at coastal scales.

From a forecasting perspective, the main outcome from progress in wave-model science over recent years is that the wave spectrum is sufficiently well forecast to consider using a richer set of wave parameters with which to describe the characteristics of a given sea state. In particular, the opportunity exists to add “advisory” parameters that highlight tough or dangerous sea conditions, for example, where operability or manoeuvrability of a vessel may be severely restricted. Examples of operational or pre-operational services using maximum wave-height estimation (Janssen and Bidlot, 2009), crossing sea indices (Savina and Lefèvre, 2004; Kohno, 2013), critical steepness (Viggosson and Bernodusson, 2009) and the full wave spectrum as an input to vessel response (Lai et al., 2006) currently exist. These examples do not represent a complete body of work, but it is believed that enough research is ongoing in the wave modelling community to assume that further improvements to the science and forecast products underpinning dangerous sea-state prediction will continue to be made.

CHAPTER 6. OPERATIONAL WAVE MODELS

Editor: A. Saulter, based on original material by M. Khandekar

6.1 INTRODUCTION

Operational wave analysis and forecasting has reached a sophisticated level following the pioneering development of wave forecasting methods by Sverdrup and Munk (1947) and with the advent of modern high-performance computing facilities. National Meteorological and Hydrological Services (NMHSs), oceanographic institutions and some commercial weather forecasting companies now operationally run numerical wave models that provide detailed sea-state information at given locations.

Chapter 5 provided an introduction to modern numerical wave models, the parameterizations they use to represent wave-development processes and blending of observations and model fields, via the data assimilation process. The purpose of this chapter is to now describe the types of product a forecaster might generally expect from these models (sections 6.2–6.4) and approaches to determining uncertainty in forecasts, either using long-term model verification (section 6.5) or ensemble prediction systems (EPSs) (section 6.6).

6.2 TWO-DIMENSIONAL SPECTRAL WAVE MODELS

Sea state is described in the form of two-dimensional (frequency–direction) wave-energy density spectra within numerical models. Figure 6.1 shows wave spectra generated at two locations in the Met Office global wave model at the same time on the same day. Both contain similar levels of wave energy, but show a different distribution. In the wind-sea-dominated spectrum (case 1, left panel), the waves will be short crested and steep, predominantly directed from close to east-south-east. As the waves are well developed for the local wind conditions, they will have begun to take on an organized, "groupy", structure. In the multiple-component spectrum (case 2, right panel), wave energy approaches the location from three different direction sectors (north-east, south-south-west and south-south-east). Lower-frequency (longer-period) components representing swell energy from north-east and south-south-west will have low steepness and an organized, groupy, structure. The higher frequency wind-sea waves from the south-south-east will be choppy and appear more random. For operations in these conditions, the crossing seas may cause an unpredictable vessel motion, particularly when high waves from different directions coincide.

A spectrum provides a detailed portrayal of wave conditions. However, although they are utilized in a few specific applications, spectral data are generally considered too voluminous and in need of detailed interpretation to be communicated within marine forecasts. Various sea-state characteristic parameters, which are derived from the spectrum, are instead presented to users. The choice of parameters that are most relevant to marine operations can vary, depending upon the type of activity and whether it is conducted offshore or in a coastal region. Significant wave height may be regarded as the most commonly used sea-state parameter. As defined earlier (in section 1.3.8), the significant wave height (H_s, although more strictly this is H_{m_0} due to its derivation from the zeroth moment of the modelled wave spectrum) describes the population of wave heights in a sea in a statistical sense and is therefore of universal interest to most offshore and coastal activities.

In addition to significant wave height, two other characteristics of sea state that are commonly presented in operational forecasts are the wave period and the direction in which waves are propagating. Wave periods commonly derived from the spectrum are the peak period (T_p), zero-up/downcrossing period (T_z, more strictly this is the second frequency moment of the spectrum $T_{m_{02}}$) or mean period (T_m, strictly the first frequency moment $T_{m_{01}}$). The convention of

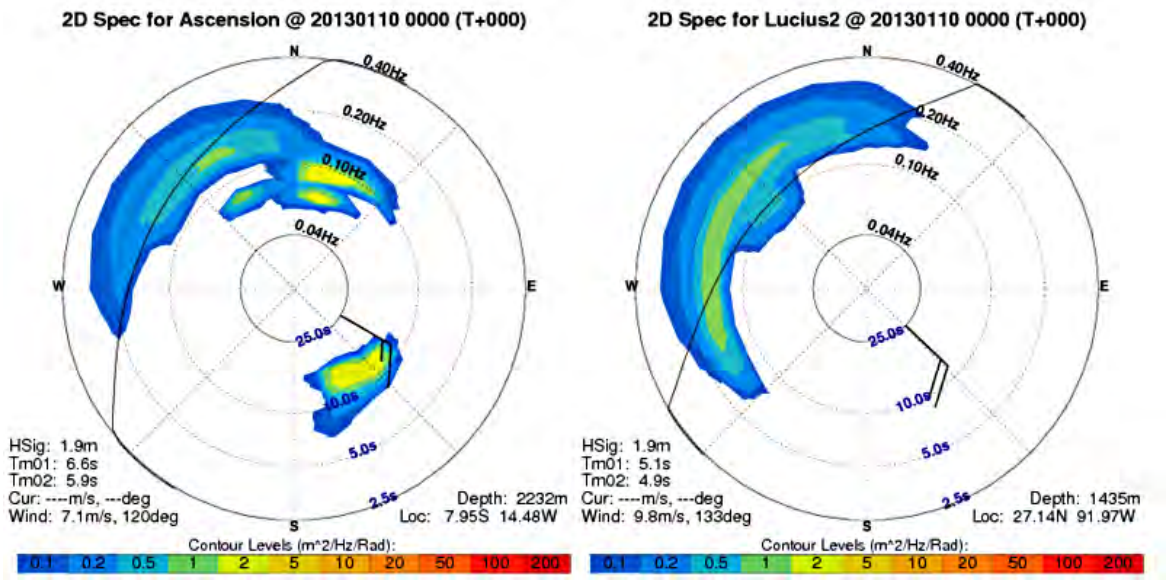

Figure 6.1. Two-dimensional (frequency–direction) wave-energy density spectra developed for: (case 1, left) wind-sea-dominated conditions in the Gulf of Mexico; (case 2, right) multimodal wind-sea and swell conditions in the South Atlantic (near Ascension Island). Direction in the polar plots indicates the direction towards which the waves will be travelling. While overall spectrum significant wave-height values are identical, and mean and zero-upcrossing and mean periods are within 1–1.5 s, the spectra show different distributions.

Source: Met Office (© British Crown copyright, Met Office)

wave direction from wave models can vary ("from which" direction or "towards which" direction), whereas measured data are invariably presented as the direction "from which" waves travel, to be consistent with the meteorological convention for wind direction. The direction parameter presented generally takes the form of either a "principle direction" associated with the most energetic spectral frequency, or a mean direction derived from the full spectrum. A further useful characteristic parameter is a measure of directional spread. When used in association with the wave period (to derive wavelength), this gives some guide as to whether the waves will be long or short crested.

Some care may be needed when interpreting period and direction forecasts derived from the full wave spectrum. Where two or more "wave systems" are present in a given sea, the overall values may end up as a physically meaningless average. For example, the overall mean direction from the multiple-component wave spectrum in Figure 6.1 will be influenced by all components, including a swell system that propagates in the opposite sense to the wind sea. In such cases, a large directional spread and a major discrepancy between wind and wave directions may indicate an issue. For a more precise assessment of the wave conditions, parameters for significant height, period, direction and spreading can also be derived for discrete wind-sea and swell components. This is achieved by "partitioning" the wave spectrum. Figure 6.2 presents a time-series evolution of partitioned data and shows the localized development of short-period wind seas (waves of high frequency, where the frequency decreases with time) and the arrival of longer-period, remotely generated swells.

Some methods for partitioning the wave spectrum into components are found in operational practice. These include a frequency-based cut-off that identifies swell as long-period energy (for example in SWAN, Booij et al., 1999), a wind-dependent frequency cut-off that identifies swell as the part of the spectrum not directly influenced by the wind (for example, the WAMDI Group, 1988) or topographic partitioning that identifies multiple wave systems based on the shape of the wave spectrum (for example, in WAVEWATCH III following Hanson and Phillips (2001)). To aid the forecasting process, the United States Army Corps of Engineers and the National

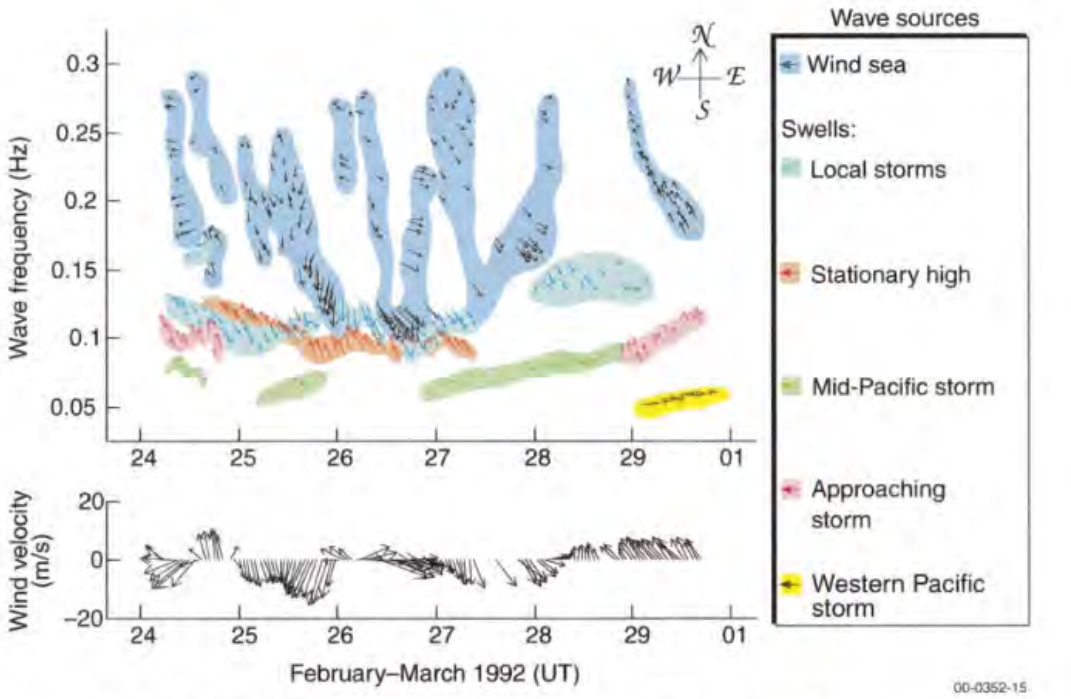

FIG. 15. Wind and wave vector history from Gulf of Alaska observations. To simplify presentation of data, observations were subsampled at a 1-h interval. Gaps in the record apparent on 27 Feb are a result of the WAVEC buoy drifting out of telemetry range. See text for further explanation.

Figure 6.2. Clustering of partitioned wave data in time series. The diagram shows evolution of data from a complex sea comprising short-period (high-frequency) wind seas superimposed on moderate- to long-period swells generated in other parts of the ocean basin.

Source: Hanson and Phillips (2001). © American Meteorological Society. Used with permission.

Centers for Environmental Prediction (NCEP) have developed a process for tracking partitions so forecasters can trace swell back to originating storms (Figure 6.3; WAVEWATCH III Development Group, 2016).

For the sake of completeness, and to aid assessment of confidence in the wave-model products, wave parameters are commonly accompanied by parameters related to atmospheric forcing of the ocean surface, namely wind speed and wind direction (and sometimes surface pressure). In cases where the wave field is significantly modified by currents and changes in water level, these oceanographic boundary condition data may also be supplied.

6.3 WAVE CHARTS

A map (or chart) showing the spatial distribution of wind and wave parameters is called a wave chart. The chart may provide sea-state information in a diagnostic (analysed) or prognostic (forecast) form. A wave chart should be simple and uncluttered for efficient transmission. Almost all wave charts show isopleths of significant wave height suitably labelled and a few additional parameters like peak period, wave direction and so forth. Charts viewed over the Internet can have the added facility to display more detailed data at given locations, for example, charts provided by NCEP include clickable locations that display wave spectra and partition data. Numerous meteorological or oceanographic service providers issue wave charts. The examples of charts in this section are not intended to be an exhaustive list of chart types, but are used to illustrate some of the options in current usage.

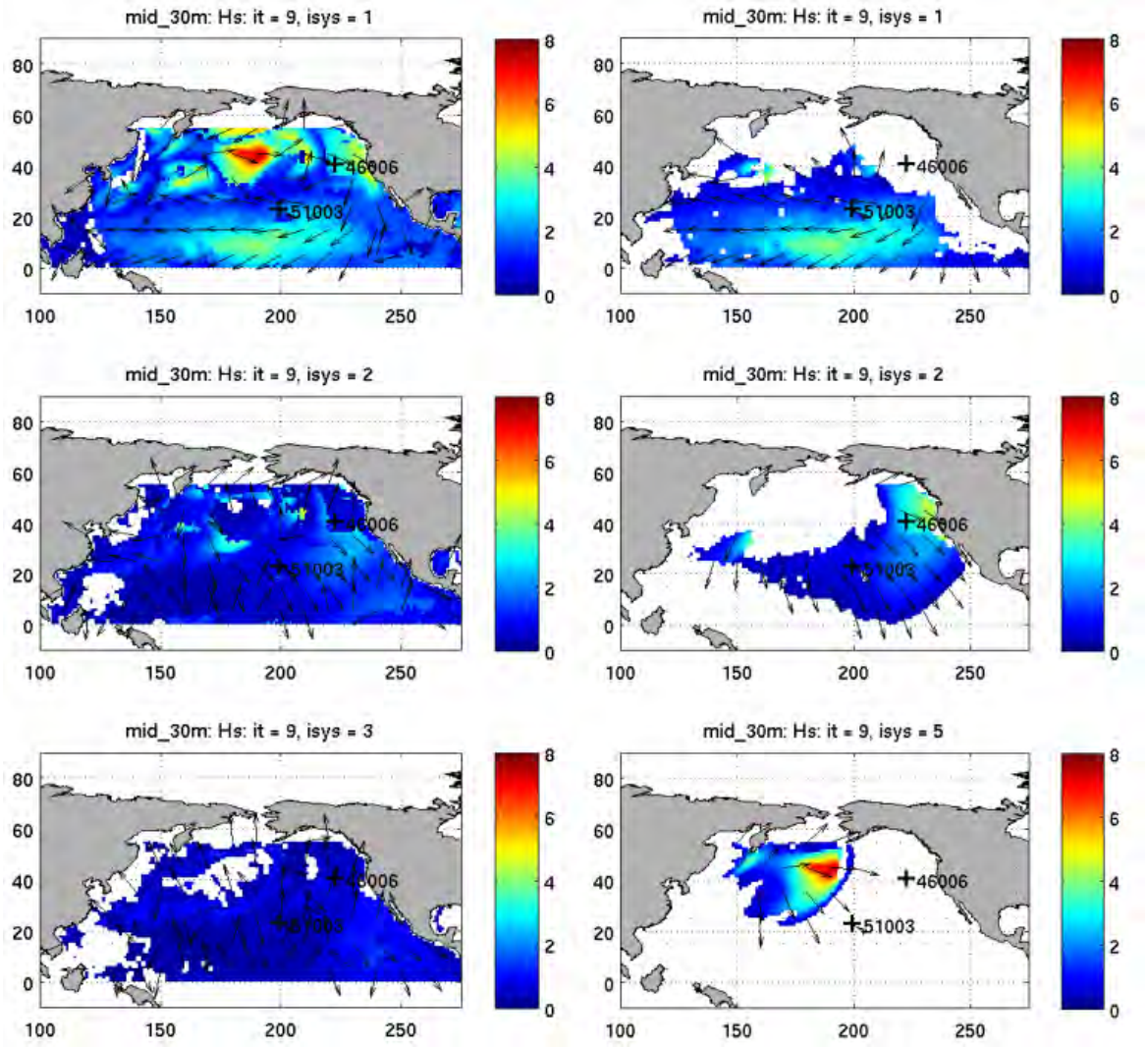

Figure 6.3. Transformation of topographically partitioned North Pacific significant wave-height data (left) into systems (right) by the NCEP swell tracking routine

Source: NCEP (https://polar.ncep.noaa.gov/waves/workshop/pdfs/wwws_2013_wave_tracking.pdf)

In the example in Figure 6.4, significant wave-height contours have been overlaid by "station diagrams" that describe the wave field and driving wind conditions in more detail. For charts of this type, the wave-height contours generally refer to the total significant wave height H_s, which is defined as

$$H_s^2 = H_{wi}^2 + H_{sw}^2, \tag{6.1}$$

where H_{wi} and H_{sw} are, respectively, the wind-sea and swell significant wave heights as described in positions 2 and 4 of the station diagrams. Wind speed and direction are displayed using the standard meteorological barb convention: integer values are supplied to define wave peak period, swell period, and wind-sea and swell wave height; the arrows define the direction of travel of the swell waves.

In the example in Figure 6.5, wave information is simplified to estimates of significant wave height, period and direction from the overall spectrum. Significant wave height is displayed using marked contours, direction of wave propagation is denoted by an arrow and wave period is given as a number. Wind barbs are overlaid to illustrate the atmospheric forcing conditions. Forecast values of wave period and height, and wind speed and direction, are given for selected

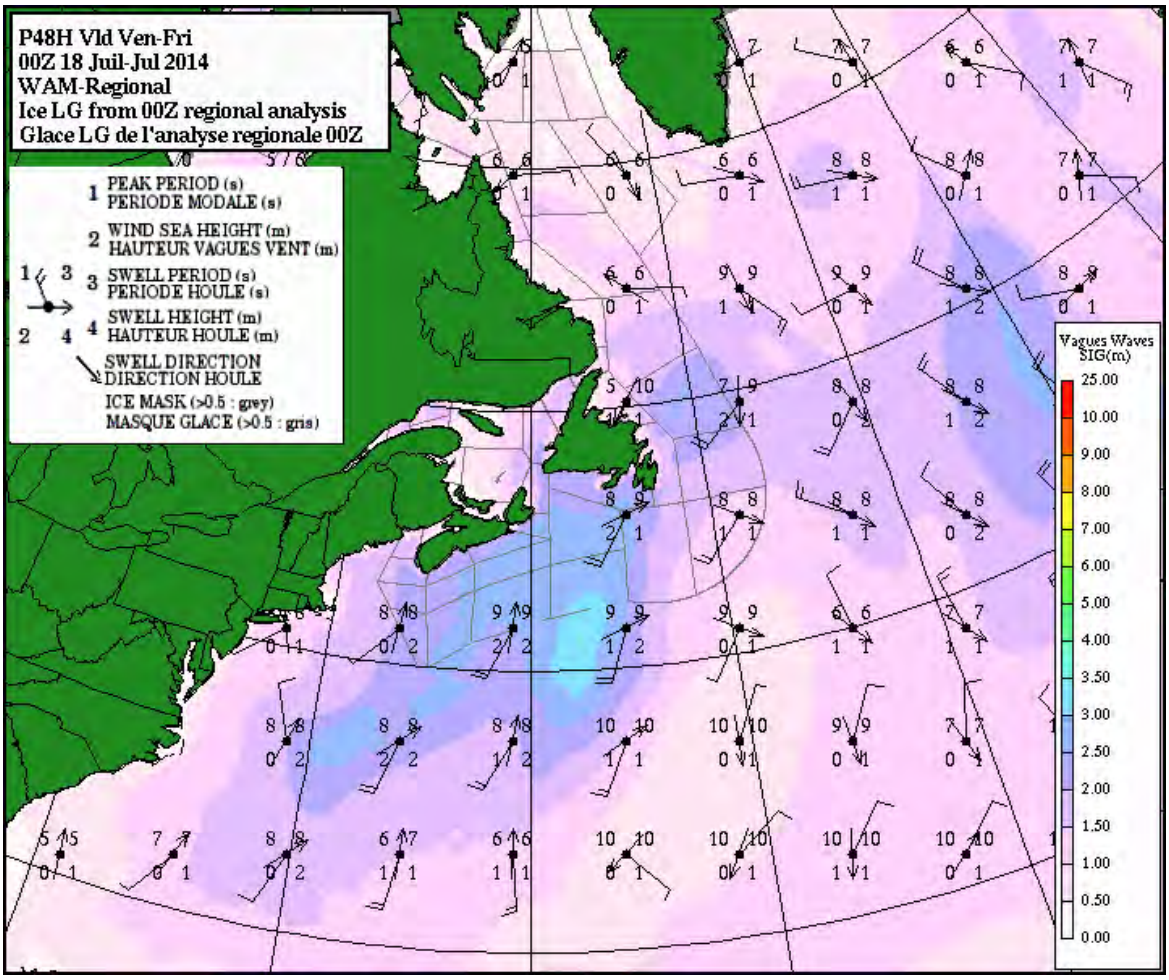

Figure 6.4. Environment Canada wave chart for the north-west Atlantic. The chart shows significant wave height as shaded contours and overlaid station diagrams at predefined model grid locations.

Source: Canadian Meteorological Centre, Environment and Climate Change, Canada (https://weather.gc.ca/model_forecast/wave_e.html)

locations (identified using letters) within the forecast area. In addition, areas of hatching are used to indicate where the waves will be directed counter to strong currents, leading to particularly steep waves forming.

Figure 6.6 shows a simple rendering of wave peak period and direction. This type of chart is a useful accompaniment to a significant wave-height chart when the onset of a long-period swell event may be of concern. In the example shown, the gradation in period values through the South Atlantic shows wave dispersion associated with propagation of swell, generated in the Southern Ocean, towards tropical West Africa.

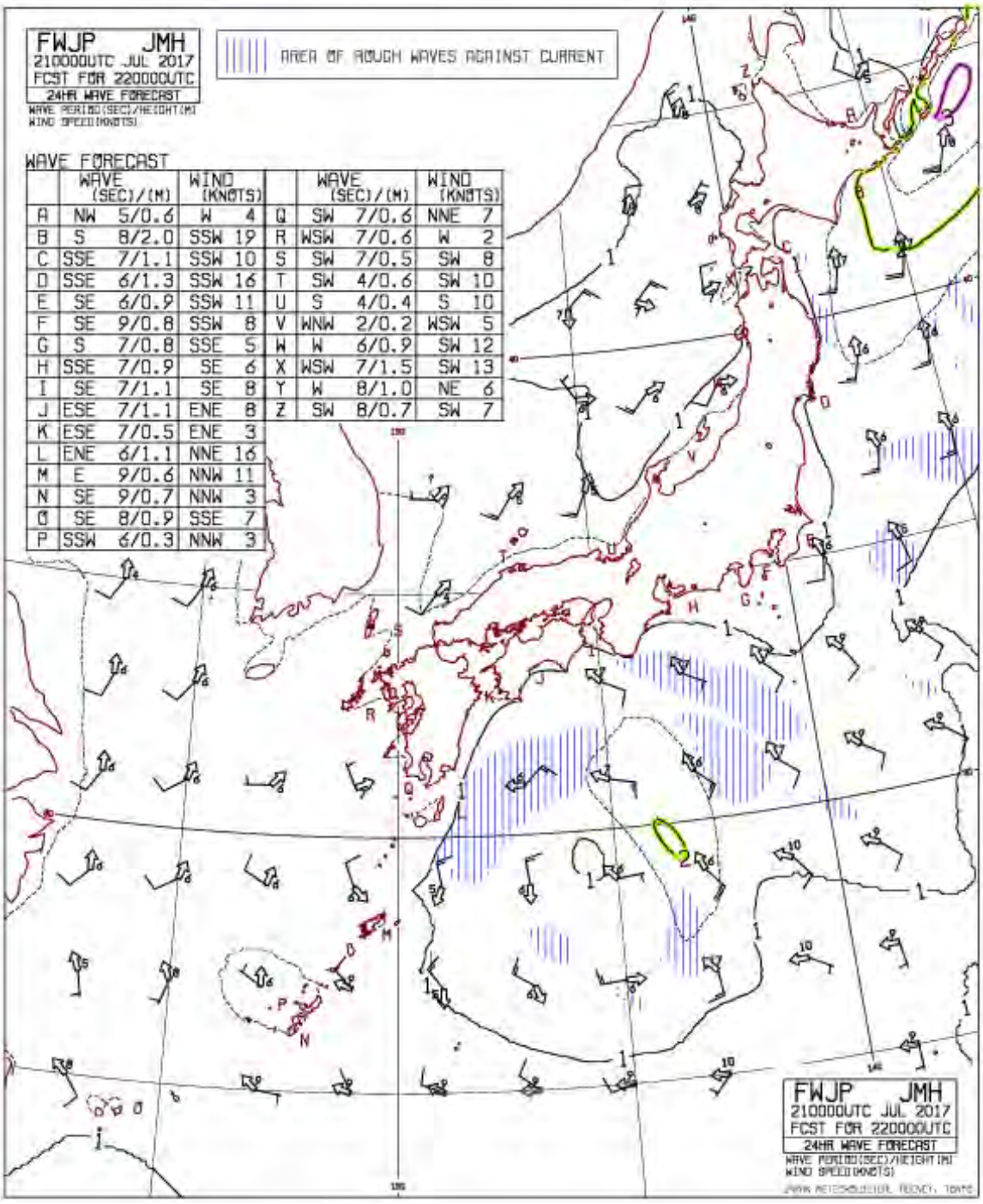

Figure 6.5. Japan Meteorological Agency (JMA) wave forecast chart for seas around Japan

Source: JMA website (https://www.data.jma.go.jp/gmd/waveinf/chart/awjp_e.html), wave forecast chart – seas around Japan

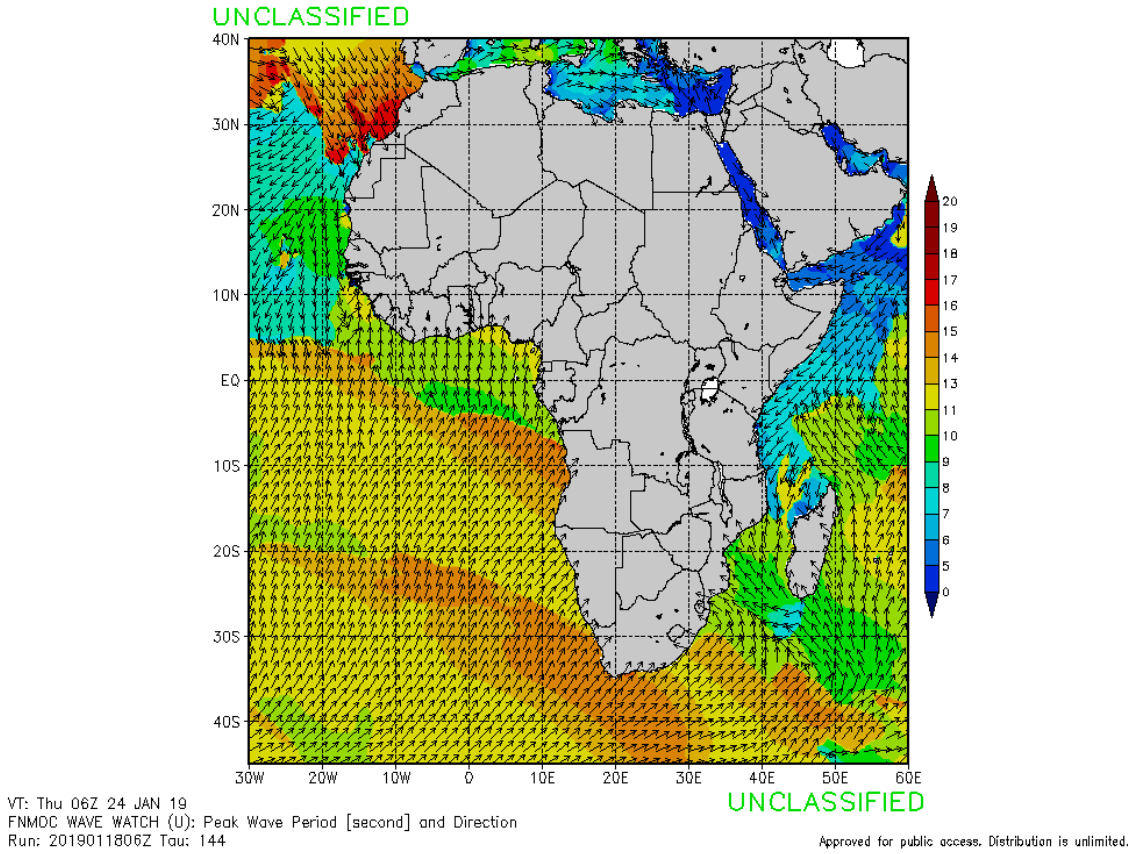

Figure 6.6. Fleet Numerical Meteorology and Oceanography Centre (FNMOC) example chart of wave peak period and direction. The gradation in period values through the South Atlantic shows wave dispersion associated with propagation of swell generated in the Southern Ocean towards tropical West Africa.

Source: FNMOC (https://www.fnmoc.navy.mil/wxmap_cgi/index.html)

6.4 CODED WAVE-MODEL PRODUCTS

The standard form for outputs from wave models is as a gridded product. The two most common formats for data exchange are GRIdded Binary (GRIB) and network Common Data Form (netCDF).

6.4.1 GRIB

GRIB is commonly used by the meteorological community to store historical and forecast weather data. Standards for GRIB are set by the WMO Commission for Basic Systems and are described in the *Manual on Codes* (WMO, 2011). Two versions of GRIB are in common operational use. The first edition (current subversion 2) is used operationally worldwide by many meteorological centres. A newer version (GRIB2) has also been introduced, and data products are moving over to this format.

GRIB files comprise two components: one part that describes the record (the header), and the actual binary data. Binary data in GRIB1 are not compressed, but GRIB2 data are compressible. The GRIB header is divided into two parts: a mandatory product definition section (PDS) and an optional grid description section (GDS). PDS describes who created the data (the research/operational centre), the numerical model/process involved (for example, numerical weather prediction or global climate model), the parameters that are stored, units of the data (for example, metres for significant wave height of combined wind waves and swell), vertical system

of the data and the time stamp. GDS provides a description of the spatial organization of the data, such as grid type, horizontal resolution and location of the origin. GRIB codes to describe wave parameters are listed under TABLES. Further details on the GRIB format can be obtained from WMOCODES. More details on file structure and PDS and GDS definitions are available under GRIB. Numerous GRIB viewers and readers are available. For example, the wgrib utility is provided by the NCEP Climate Prediction Centre under WGRIB.

6.4.2 NetCDF

NetCDF is an open standard, self-describing binary data format that is in common use in the climate science and oceanographic communities. The netCDF project home page is hosted by the Unidata programme at the University Corporation for Atmospheric Research and provides the chief source of netCDF software and standards development. NetCDF libraries presently support three different binary formats for netCDF files. The classic format was used in the first netCDF release, and is still the default format for file creation. A 64 bit offset format was introduced in version 3.6.0, and it supports larger variable and file sizes. NetCDF-4/HDF5 format was introduced in version 4.0. A growing number of extraction and data manipulation utilities are available, for example, the netCDF operators from NCO, a basic netCDF visual browser from Ncview and more complex utilities such as Panoply.

As with GRIB, netCDF files comprise a data element and a header that enables each file to be self-describing. The header describes the layout of the rest of the file, in particular, the data arrays, as well as arbitrary file metadata in the form of name/value attributes. Oceanographic data are generally supplied adhering to climate and forecast (CF) conventions for earth science data. The conventions require that metadata provide a definitive description of what the data in each variable represent and of the spatial and temporal properties of the data (including information about grids, such as grid cell bounds and cell averaging methods). This enables users of data provided from different sources to decide which data are comparable and allows the building of applications with powerful extraction, regridding and display capabilities. Further information on CF is available from CF Conventions and Metadata.

6.5 VERIFICATION OF WAVE MODELS

Appropriate verification of operational wave models against observed wind and wave data is necessary and important. The performance of a wave model must be continually assessed to determine its strengths and weaknesses so that it can be improved. Verification is also necessary to quantify the confidence that can be placed in the model products for operational forecasting purposes.

There are several levels of model testing and verification. In fundamental wave-model development (for example, where new source-term parameterizations are introduced), some idealized test cases are usually modelled. Such tests concentrate on comparisons of development of the wave spectrum, during periods of growth or dissipation, against existing numerical schemes or observations. As the basic output of spectral wave models is a two-dimensional wave spectrum, a suitable test would be to use the model to simulate the evolution of a wave spectrum with fetch or duration for stationary uniform wind fields. Data from field experiments, such as the Joint North Sea Wave Project experiment (see section 1.3.9), and an increasing number of operational networks providing spectral measurements, can be used to assess the model's performance.

The next, and most operationally useful, level of verification compares observations with analysis and forecast products generated by full two-dimensional wave models, forced using global or regional atmospheric (and ocean) fields analysed/predicted by an operational weather (ocean) forecast model. Ideally, a model would be verified by comparisons with measured wave spectra (for example Figure 6.7; Bidlot et al., 2005). The development of advanced synthetic aperture radar (ASAR) remote sensing has provided the opportunity for performance in specific frequency bands within the wave spectrum to be tested against observations with global coverage (for

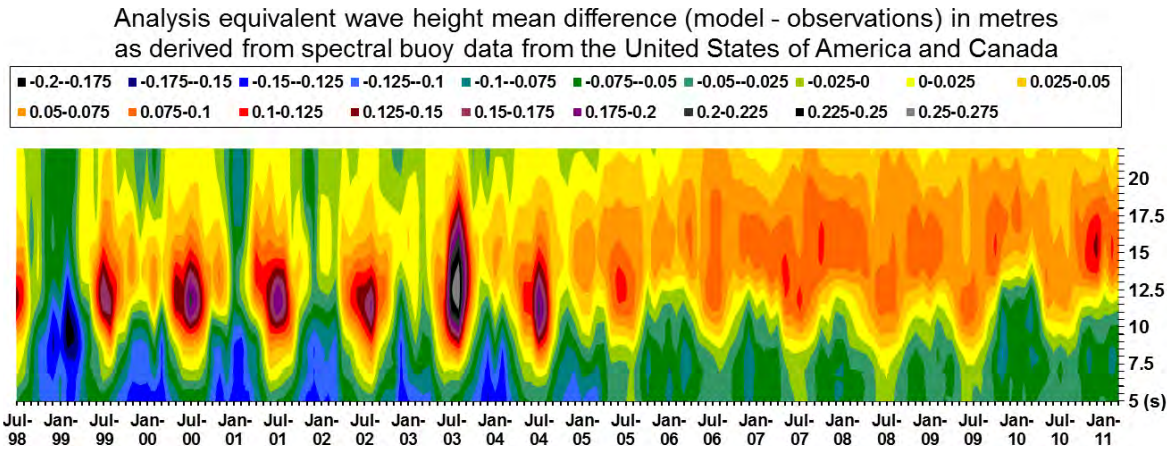

Figure 6.7. Example of (one-dimensional) spectral validation. The time stack shows the change in monthly bias (in metres) of the European Centre for Medium-Range Weather Forecasts (ECMWF) wave model against buoy observations for wave height calculated at different "subranges" of the frequency spectrum.

Source: Bidlot et al. (2006)

example, Li and Holt, 2009). However, regularly published, near-real-time measurements of the full wave spectrum remain sparse, and care needs to be taken when making direct comparisons of individual directional wave spectra. For example, when testing spectra discretized at high resolutions, the likelihood of "double penalty" effects (where a close but non-exact agreement between model and observation is penalized in a similar way to a total misrepresentation of the observed state) is high. This is particularly likely to be the case in rapidly changing conditions, where small errors in the predicted timing of a storm's evolution may lead to large differences in the comparisons. In such cases, more advanced verification techniques that relax timing constraints or make a more nuanced measure of the "distance" between modelled and observed wave spectra may need to be used. Further, it must be remembered that spectral observations are statistical estimates of the waves, and individual spectral components may have large uncertainties. Potential uncertainties include high sampling variability at which different frequencies of the wave spectrum are observed within a measurement burst, variations in the in situ buoy hull response and differences in data-processing algorithms (Swail et al., 2010).

For these reasons, operational model validation is performed using as large a data sample as possible. Key results are generally based on comparisons of parameters derived from the wave spectrum such as H_s, T_z (or T_p) and, if directional wave data are available, the mean direction (for different frequency bands). As the wind field that drives the model is intrinsically related to the model wave field, most evaluation studies also include verification of wind speed and direction to assess the forcing field errors.

Standard verification approaches use statistics derived by analysing the scatter and distribution of errors calculated from a sample of matched model and observation data, for example, by performing a regression analysis on parameters. To provide as complete a portrayal of model performance as possible, most operational verification generates several statistical parameters and analyses the magnitude and variation of these parameters to determine the overall skill of a wave model. The following are some commonly used parameters:

- Mean error or bias (values approaching zero indicate good performance);
- Root-mean-square error (RMSE; for example Figure 6.8; values approaching zero indicate good performance);
- Scatter index, defined as the ratio of RMSE to the mean observed value of the parameter (values approaching zero indicate good performance);
- Sample linear (Pearson) correlation coefficient *r* between the model and the observed value (values approaching 1.0 indicate good performance).

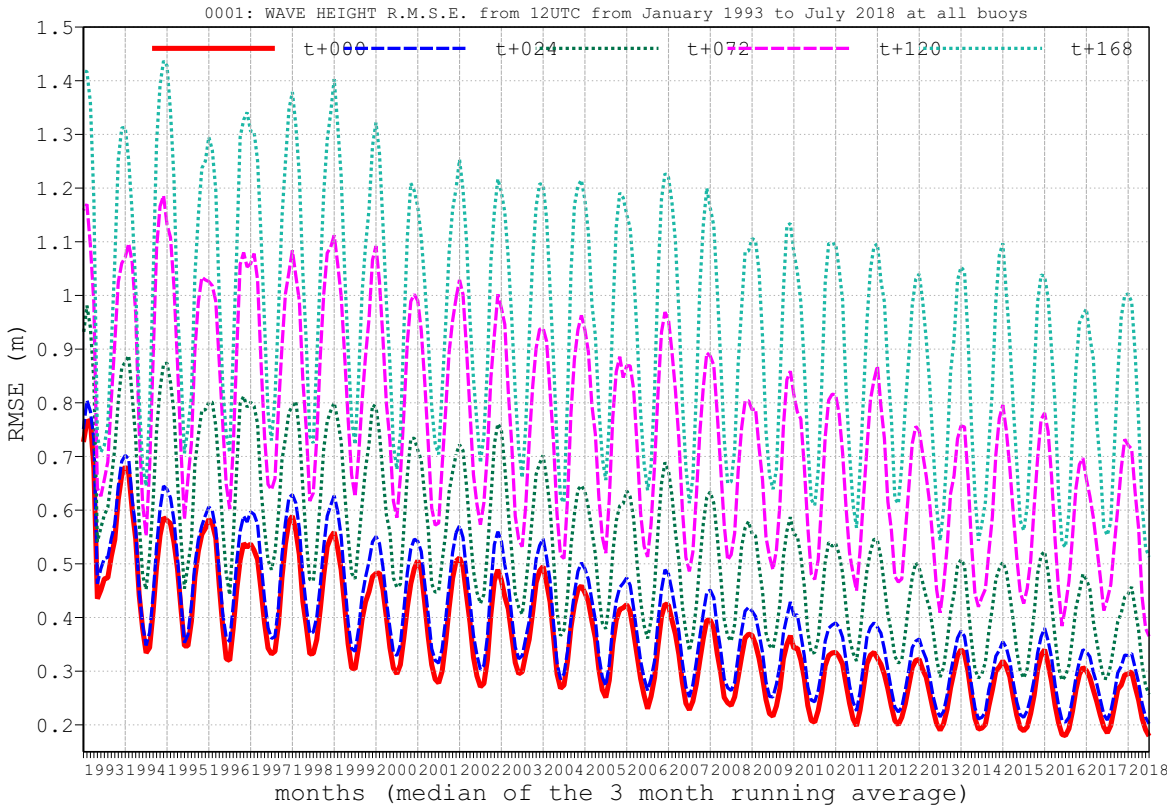

Figure 6.8. Year by year change in RMSE scores for ECMWF global wave-model forecasts of significant wave height referenced against a global network of in situ wave-measurements platforms

Source: ECMWF (https://www.ecmwf.int/en/forecasts/charts)

In addition to analysing the scatter of temporally matched data, comparison of the probability distribution functions of modelled and observed parameters over a long time sample, for example via a quantile–quantile plot, is a useful way of testing for systematic model biases while removing the influence of high-frequency temporal correlation effects (such as mismatches in the timing of predicted and observed storm peaks). Stratification of larger verification samples can be used to help identify changes in model performance under different wave regimes, such as contrasting verification for high-energy storms against calmer swell-dominated events. A simple and commonly used form of stratification is to consider the slope of the regression line between the model and observed values and the intercept of the regression line on the *y*-axis. Other tests of model performance assess the ability to predict specific events. For example, categorical statistics describe the ability to predict wave height exceeding a certain threshold. A useful summary of different verification procedures and metrics is provided by the WMO Joint Working Group on Forecast Verification Research.

Wave-model verification relies on the availability of reliable sea-state measurements and related weather data. Verification studies have traditionally used measurements of wind and waves obtained by in situ buoys and fixed platforms. Although some studies have indicated inconsistencies in the global in situ network (for example, Durrant et al., 2009*a*), these data are generally considered as "ground truth". However, the geographical extent of the in situ network is limited, particularly in the southern hemisphere. Verification of global and large regional models also makes extensive use of satellite altimeter and ASAR measurements of sea state and scatterometer measurements of wind to assess performance in open waters. To obtain statistically robust sample sizes, observed data samples of a few months to a year are typically required for regional and site-specific verification.

Verification of operational wave models at NMHSs of many countries is an ongoing activity. The verification statistics are updated periodically to monitor the model's performance. A notable

international initiative is the ongoing WMO–International Oceanographic Commission Joint Technical Commission on Oceanography and Marine Meteorology (JCOMM) Intercomparison of Operational Ocean Wave Forecasting Systems, which has operated since 1995 (Bidlot et al., 2002, 2007). The scheme has proven extremely useful in providing individual forecast centres with a long-term quality-controlled source of verification match-up data, and also a convenient check of model forecast performance against similar models run at other centres. The success of the scheme can be measured by the present participation of 17 operational centres worldwide, and a recent transition to a more operational set-up using ECMWF as the WMO Lead Centre for Wave Forecast Verification. A subset of results is regularly published on the ECMWF website verification pages.

At this stage, the scheme is limited to a comparison against commonly observed integrated wave parameters (significant wave height and period) from in situ platforms. The potential to extend the scheme to incorporate satellite observations and provide mapped products (for example, Figure 6.9) has been demonstrated by numerous centres, while work by Bidlot et al. (2005) has shown the value and feasibility of a further extension to verifying aspects of the wave spectrum (Figure 6.7).

6.6 ENSEMBLE PREDICTION SYSTEMS

By their nature, forecasts are subject to uncertainty. Some of the uncertainty is due to errors in model parameterizations of real-world processes, and some can be attributed to observation errors. However, a significant amount of uncertainty is also introduced as a result of small differentials between the analysis and the state of environmental conditions at forecast initiation. These differences can lead to much wider discrepancies between the forecast and actual state at longer lead times, depending on the stability of the background meteorological conditions. One approach to forecasting is to attempt to quantify the uncertainties and view the forecast as sampling from a probability distribution of likely conditions rather than as a single "deterministic" outcome. Continuing increases in computing resources have enabled modelling centres to adopt a probabilistic forecasting approach based on running wave EPSs.

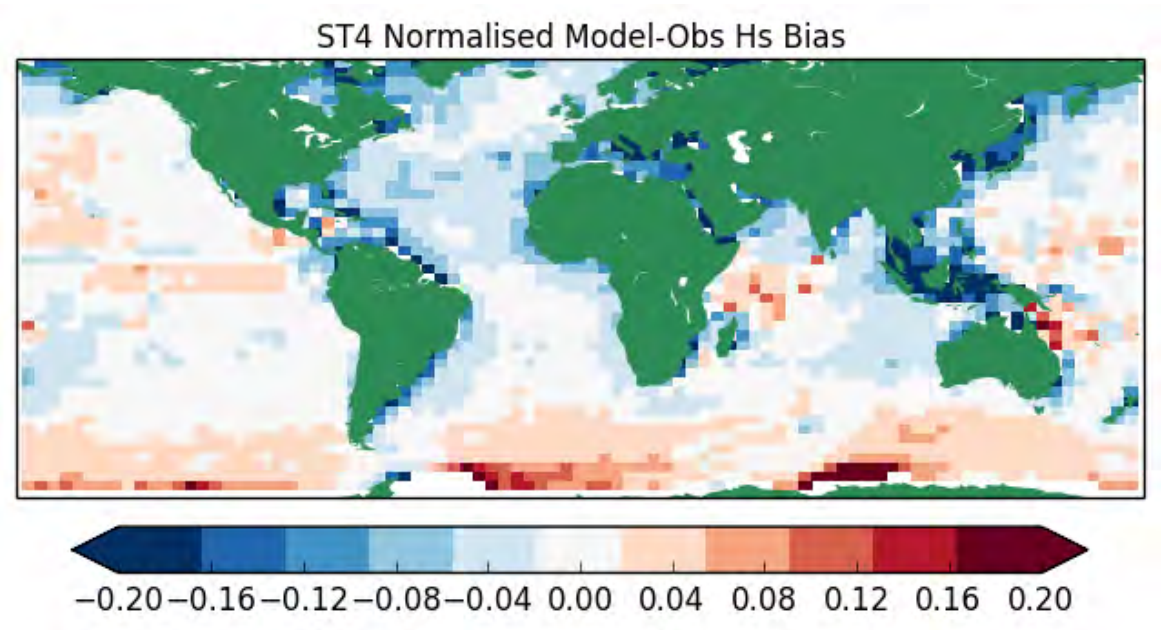

Figure 6.9 Map of significant wave-height bias (in m) for Met Office global wave forecast model against satellite altimeter missions, verified over the period September 2014 to August 2016

Source: Met Office (© British Crown copyright, Met Office)

The aim of an EPS is to provide forecasters with a measure of model and climatic uncertainty associated with a given forecast. The ensemble will indicate lower forecast uncertainty in well-specified and stable weather conditions than in unstable conditions, where the present weather state might be poorly analysed and weather system development is more dynamic. As a forced-dissipative system, wave-forecast uncertainty is mostly determined by variations in the driving atmospheric data and thus the requirement for a complex EPS based on data assimilation, using perturbed initial conditions to generate starting conditions for ensemble members as in ensemble weather prediction, is limited. Pioneering applications have been developed for global medium-range forecasts (1–4 weeks ahead) at centres such as ECMWF (Molteni et al., 1996; Saetra and Bidlot, 2004), NCEP (Chen, 2006) and FNMOC (Alves et al., 2013). Research into short-range regional ensemble systems, which have a stronger requirement for uncertainty to be well specified at forecast initialization, is ongoing at the Met Office (Bunney and Saulter, 2015), the Italian Meteorological Service (Pezzutto et al., 2016) and the Australian Bureau of Meteorology (Zieger et al., 2018).

The data provided by an ensemble (for example, Figures 6.10 and 6.11) allow more than one approach to be adopted when interpreting and issuing a forecast. For example: individual members can be identified and used to describe alternative forecast scenarios deterministically; dynamic changes in ensemble spread can be used to estimate the uncertainty associated with a deterministic product derived from the ensemble; or probability information about a given outcome (for instance, the probability of wave height exceeding a certain operating threshold) can be used directly. The choice of approach requires an understanding of the end-user requirements and the ensemble's performance. For example, as the model does not attempt to represent observation errors, the predicted probability and the probability of subsequent observation of a given event (termed "reliability" of the forecast) should not match exactly.

However, a well-specified ensemble should show a good reliability relationship. Similarly, a good ensemble will show a strong correlation between spread in the EPS forecast and error between the ensemble control/mean forecast and observations. All these behaviours are fundamentally reliant on the quality of the underlying model. In the example in Figure 6.12, reliability is shown to be significantly affected for a short-range ensemble forecast when an underlying bias is corrected. A recommended practice when assessing probability of threshold exceedance is to evaluate the probability and also the quantity by which the threshold is exceeded. For example, a forecast where 90% of ensemble members exceeded a threshold by 1 m H_s should be given a stronger level of confidence than a forecast with a similar probability of 90%, but which exceeded the threshold by only 10–20 cm.

One aspect of ensemble prediction that may have particular application is identification of low-probability, high-impact occurrences of a "dangerous" sea state within the ensemble at long range (Petroliagis and Pinson, 2012). In extreme cases, the accuracy of the underlying model may be more questionable than for everyday forecasting, but this can be mitigated using a background model climatology. Lalaurette (2003) described the ECMWF extreme forecast index (EFI) methodology for wind, temperature and precipitation parameters, in which forecast members were compared against a model climate. This EFI has also been extended to waves (Owens and Hewson, 2018). Figure 6.13 shows an example in which the figure on the left is EFI (with range –1 to 1) for significant wave height, with values nearing 1 over the Norwegian Sea. The figure on the right is the corresponding ninety-ninth percentile of the wave-height distribution for that day. Therefore, EFI indicates that the model is predicting wave heights above 4 m and that this is not usual for that time of the year.

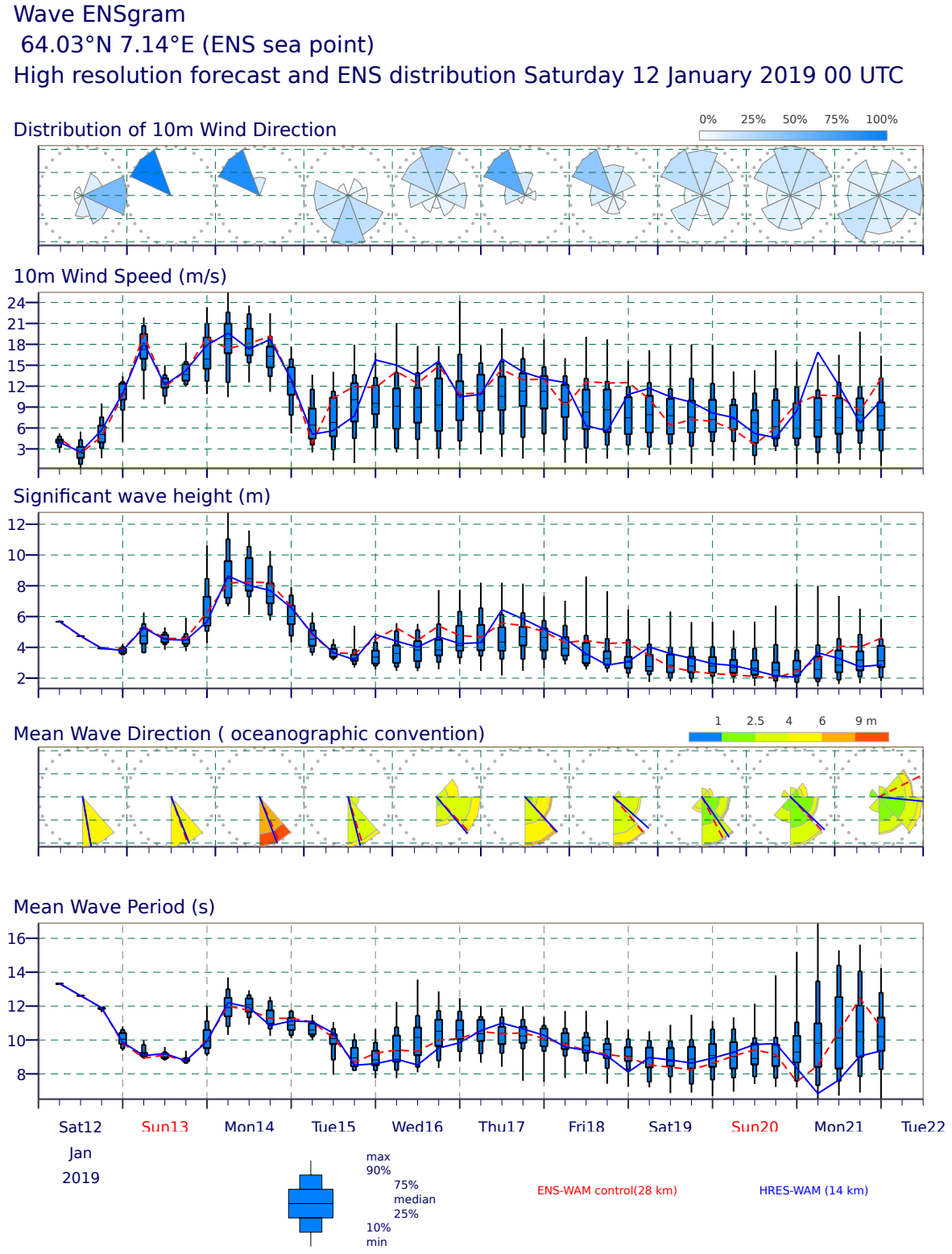

Figure 6.10. Point time-series ensemble wave forecast product from ECMWF. Top two panels show direction variability and wind speed, and total wave parameters are forecast in the lower three panels. In this instance, a high-resolution deterministic model and the ensemble control are overlaid using the blue and red lines, respectively.

Source: Interactively created at the website of the European Centre for Medium-Range Weather Forecasts, https://www.ecmwf.int/en/forecasts/charts/web/classical_meteogram (registered users only)

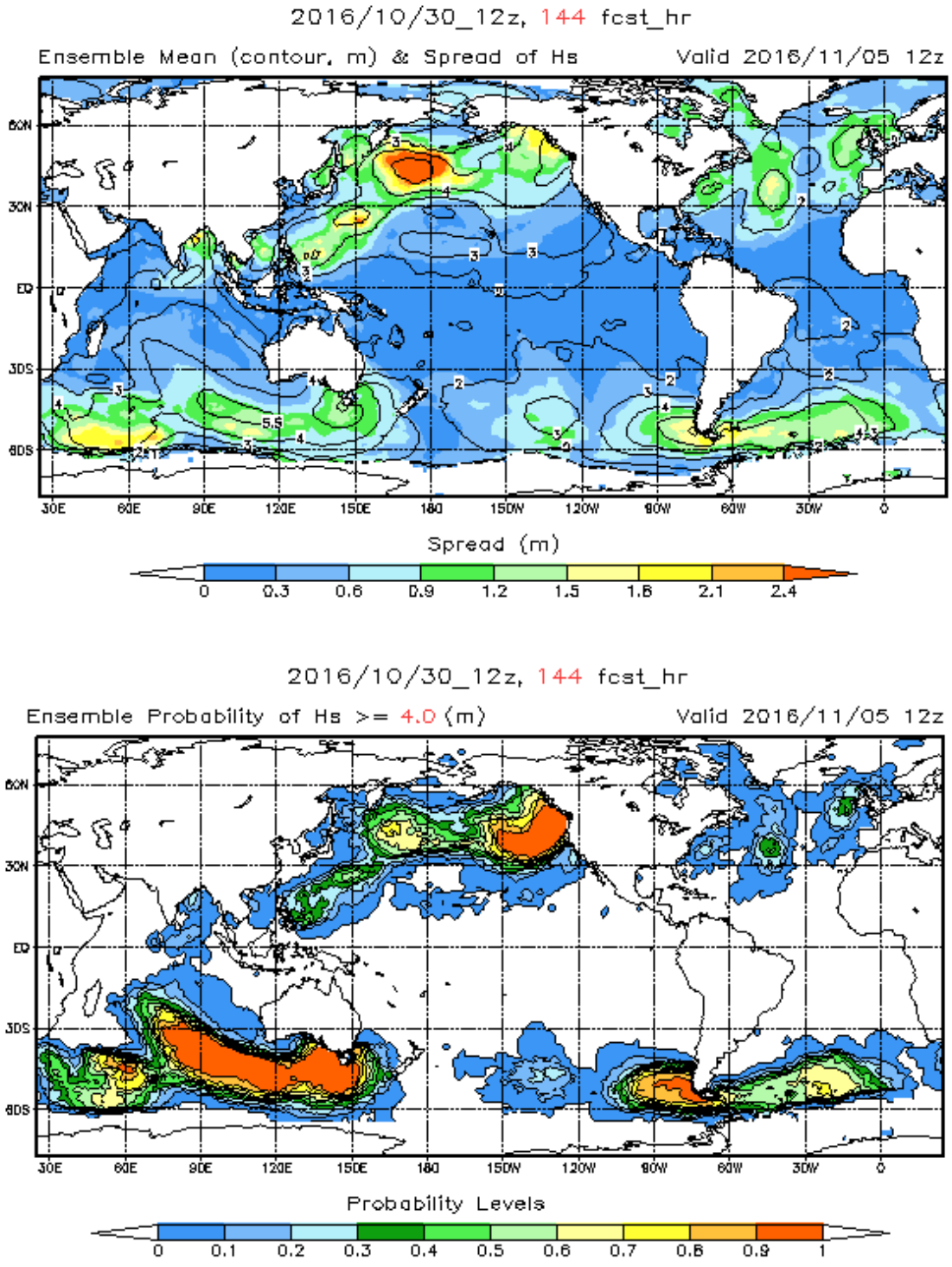

Figure 6.11. Ensemble forecast charts showing (top) ensemble mean significant wave height (contours) and spread (shading), and (bottom) probability of significant wave height exceeding 4 m

Source: NCEP (http://polar.ncep.noaa.gov/waves/nfcens/viewer.shtml)

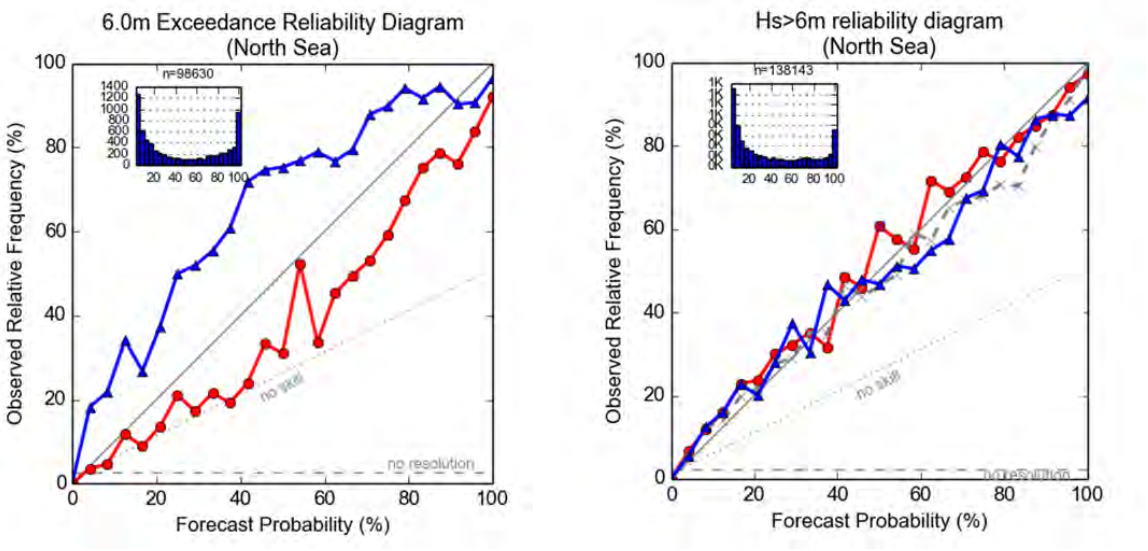

Figure 6.12. Reliability diagram for two wave EPS forecasts of significant wave height above 6 m at a forecast range of 2 d (blue, Atlantic regional model; red, regional model of the United Kingdom of Great Britain and Northern Ireland). The forecasts are considered reliable when the forecast probability and frequency of subsequent observations are similar (the data fall onto the 1:1 line). In this example, the effect of bias correcting the forecast is significant; in the right-hand panel, the lines representing forecasts after bias correction are much closer to the 1:1 line than the raw forecasts (left-hand panel).

Source: Met Office (© British Crown copyright, Met Office)

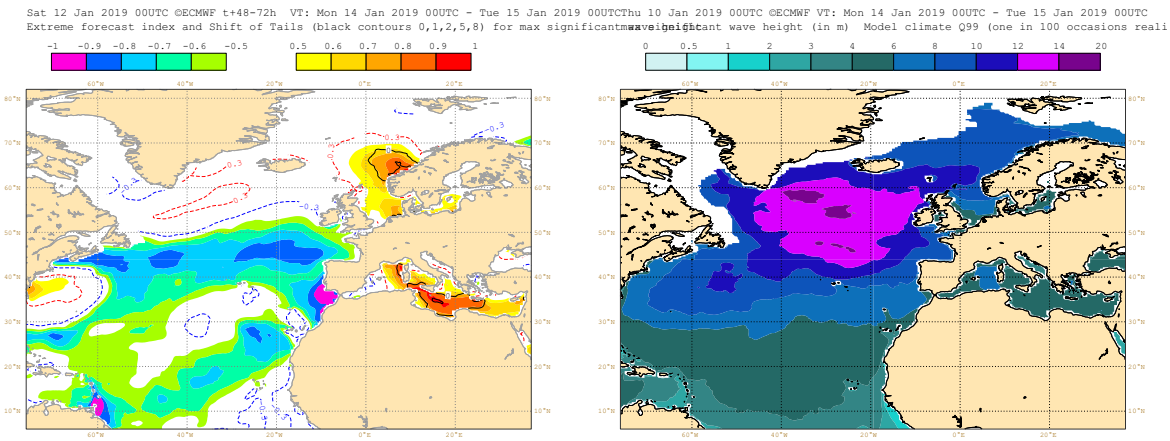

Figure 6.13. EFI (left panel) and associated ninety-ninth percentile of significant wave height derived from the model's long-term climate simulation (right panel)

Source: ECMWF (https://www.ecmwf.int/en/forecasts/charts)

A computationally cheaper version of a full ensemble system is the so-called "poor man's ensemble" (Ebert, 2001), which combines some independent model forecasts from several operational centres. The availability of such a set of forecasts can also contribute to a "consensus forecast" in which the forecasts are weighted and bias corrected according to past performance to produce an "optimal consensus forecast", which typically outperforms any of the individual model forecasts (Durrant et al., 2009*b*).

CHAPTER 7. WAVE DATA: OBSERVED, MEASURED AND MODELLED

Editors: V. Swail and F. Ocampo-Torres, with contributions from J. Ewing, D. Carter, A. Saulter, R.E. Jensen, R. Bouchard and L. Cavaleri

7.1 INTRODUCTION

Wave data are an essential component of any wave analysis and forecasting activity. Swail et al. (2010) noted that user requirements for wave data include: assimilation into operational wave prediction models; use in operational forecasting by weather prediction centres; validation of numerical wave models; calibration and validation of wave remote-sensing technologies; and validation of wave hindcast products. These are increasingly being used for climate analysis, in offshore design criteria for ships and platforms, wave-energy resource assessment and climate trend investigation. There are many other important uses for wave data, including air–sea interaction studies, upper ocean physics, coastal zone modelling and coupled ocean–atmosphere models. For the purposes of this Guide, the focus will be on the aspects of wave data, and the most frequently used sources, that directly contribute to wave analysis and forecasting.

Wave data are widely available from different sources, with varying degrees of operational readiness. These include in situ observing systems such as wave buoys and ships, and remote-sensing systems, both surface and space based. Some of these systems measure only the integral wave properties such as wave height, period and direction, while others provide a full spectral description of the wave field, either in the frequency domain alone, or a full frequency and directional spectra.

The following sections describe each of the systems in widespread use, giving the method of observation and the strengths and weaknesses of each. A full description of the details of each observing system is beyond the scope of this Guide, but it is hoped to provide enough information to make the data useful. Hauser et al. (2005), Swail et al. (2010) and Cavaleri et al. (2018) gave excellent detailed summaries of wave observation methods and processing (in situ and remotely sensed), and the issues related to them. In addition, WMO has produced companion guides on recommended approaches for visually observing or measuring waves and transmitting the information through the Global Telecommunications System (GTS), including the *Guide to Meteorological Instruments and Methods of Observation* (WMO, 2014*b*), Part II, Chapter 4, and the *Manual on Codes* (WMO, 2011). The WMO Marine Meteorology and Oceanography Programme provides a comprehensive summary of marine observing and marine data.

This chapter is organized by method of observation. Section 7.2 deals with in situ observations, both visual and measured, including wave buoys, ships and other more limited approaches. Section 7.3 discusses remotely sensed observations, including space-based observations from altimeter and synthetic aperture radar (SAR), as well as surface-based observations, including high-frequency band radar and X-band radar. Section 7.4 describes briefly another important source of data used especially for climate analysis: wave hindcast databases, including reanalyses, derived from numerical models forced by regional to global wind fields.

7.2 IN SITU WAVE DATA

7.2.1 Differences between visual and instrumental data

Although the simplest method to characterize waves is to make visual observations of height and period, this produces data that are not necessarily compatible with those from instrumental measurements.

It is somewhat paradoxical that considerable effort is made to derive appropriate significant wave heights from visual estimates of separate sea and swell to match with those obtained from measured energy spectra from instruments and modelled spectral output, while others attempt to split measured or modelled spectra into sea and swell components that are more familiar to most users of wave information – be it real-time data, forecasts or climatology – that is, a visual picture of the total sea state. The following paragraphs discuss these methods briefly.

7.2.1.1 *Estimating significant wave height from visual sea and swell*

Visual wave observations report sea and swell parameters separately. When different wave trains (for example, sea and swell or several swells) are merged, the heights do not combine linearly. Wave energy is related to the square of the wave height and it is the energy that is additive. Traditionally, when two or more wave trains are combined, the resultant height H_{combined} is determined from the square root of the sum of the squares of the heights of separate trains H_{sea} and H_{swell} (analogous to Equation 6.1):

$$H_{\text{combined}} = \sqrt{H_{\text{sea}}^2 + H_{\text{swell}}^2}. \tag{7.1}$$

More than one swell train can be combined if necessary.

However, comparisons with instrumental measurements (Wilkerson and Earle, 1990; Gulev and Hasse, 1998) show that this tends to overestimate the observed significant wave height by several tens of centimetres. Alternative estimates of significant wave height have been proposed. Wilkerson and Earle (1990) recommended using the higher of the sea and swell as the significant wave height. Barratt (1991) found that this method underestimated significant wave height in mid-latitudes, and proposed a combined approach, suggesting application of Equation 7.1 when sea and swell are within the same 45° directional sector and the maximum value in all other cases. Gulev and Hasse (1998, 1999) refined this and found that the optimal cut-off was 30°. Their formulation is now widely used, although there are likely to be regional variations depending on the nature of the wave climate.

7.2.1.2 *Partitioning spectral wave data into wind sea and swell*

Lefèvre et al. (2005) described how a two-dimensional wave-energy spectrum is commonly used to describe the distribution of the mean sea-surface elevation variance due to wind waves as a function of frequency and propagation direction. The number of frequencies multiplied by the number of directions used to describe a wave spectrum is typically more than a few hundred. Therefore, common practice when comparing sea states is to reduce the spectral information to a few parameters obtained by integration over the spectrum. The most widely used parameters are the significant wave height and the mean wave period. Portilla-Yardun et al. (2009) noted that as wind sea and swell are not measured or modelled separately, there is a need for splitting the spectrum to provide this information as part of the output products (Bidlot, 2001). This is not trivial, and many different approaches have been adopted based on some physical properties of wind and waves. Several partitioning algorithms have been proposed to identify the wave systems and their features from time series of directional wave spectra (Hanson and Phillips, 2001; Wang and Hwang, 2001; Violante-Carvalho et al., 2002; Hwang et al., 2012; Alliot et al., 2013).

7.2.2 Visual observations

Waves are generally described as either sea (wind sea) or swell. In this context, sea refers to the waves produced by the local wind at the time of observation, whereas swell refers either to waves that have arrived from elsewhere or those that were generated locally but which have subsequently ceased to be changed by the wind (as a result of a shift in wind direction, for example).

It is generally accepted that visual observations of wave height tend to approximate to the significant wave height (see definitions in section 1.3.3); comparative estimation of heights

was described in section 7.2.1. Visually observed wave periods are much less reliable than instrumentally observed ones, as the eye tends to concentrate on the nearer and steeper short-period waves, thereby ignoring the longer-period and more gently sloping waves, even though the latter may be of greater height and energy. This can be seen by examination of joint probability plots (scatter diagrams) of visually observed wave period and height. In many of these, the reported wave period is so short that the steepness (height to length ratio) is much higher than physically possible for water waves. It is almost certainly the wave period that is in error, not the height.

Useful visual observations of wave heights can be made at sea from ships (see section 7.2.2.1). Visual observations from land (section 7.2.2.3) are meaningful only at the observation site because the waves change dramatically over the last few hundred metres as they approach the shore, and the observer is too far away from the unmodified (offshore) waves to assess their characteristics. To a coastal observer, waves usually appear to approach almost normal to the shore because of refraction and may, therefore, be more likely to be oblique to the wind than is the case further offshore. Shore-based observations normally apply only to that particular location, and, although relevant to a study of local climatology or a site-specific forecast, they are rarely meaningful for any other meteorological purpose. However, they may be useful for specific user groups such as surfers.

7.2.2.1 ***Visual observations from ships***

A traditional, and historically the largest, source of wave information has been from so-called "ships of opportunity". Given the lack of surface-based measurements of waves on the open ocean, the geographical coverage offered by shipping has been utilized in the WMO Voluntary Observing Ship (VOS) Scheme. These ships are predominantly merchant ships, but the VOS programme also includes research vessels, naval and coast-guard ships, ferries, supply vessels and cruise ships. The participating ships report weather information including visual observations of waves.

By the nature of their work, mariners can be regarded as trained observers. The observation of waves is part of their daily routine, and a knowledge of changes in sea and swell is vitally important, because such changes affect the motion of the ship (pitching, rolling and heaving) and can be the cause of late arrivals and structural damage. However, Houmb et al. (1978) found that ship's mates tended to underestimate wave height in comparison to their assistants, while Gulev et al. (2003) reported that only 20%–50% of observers strictly followed the observational guidelines.

An observer on a ship can usually distinguish more than one wave train, make an estimate of the height and period of each train and give the directions of wave travel. Waves travelling in the same direction as the wind are reported as sea; all other trains are, by definition, swell (although mariners often refer to well-developed seas in long fetches, such as in the "trade winds", as swell).

The number of VOS ships has declined in recent years. The introduction of automated weather observing systems on many of the remaining VOS vessels has tended to increase the number of reports. However, these automated systems do not make wave observations (or cloud or visibility), and observers on board often do not manually enter those values in the transmitted report, so the number of wave observations has decreased.

It is not the purpose of this Guide to instruct observers on how to report waves. The guidelines for making these observations are given in the *Guide to Meteorological Instruments and Methods of Observation* (WMO, 2014*b*), Part II, Chapter 4. Guidance is also provided by many national agencies, for example the National Oceanic and Atmospheric Administration (NOAA, 2010).

Data should be distributed onto GTS using the FM 13 SHIP format. As of 2012, the Binary Universal Form for the Representation of Meteorological Data (BUFR FM-94) should have been used instead. These formats are described in the *Manual on Codes* (WMO, 2011).

The purpose of this Guide is to provide guidance on the appropriate use of the wave observations, taking into account the associated metadata and known issues with shipboard observations. Laing (1985) and Gulev et al. (2003) provided comprehensive descriptions of data processing, coding systems, changes in data formats, ad hoc corrections of biases and estimates of uncertainties in ship wave data. The following paragraphs provide a brief summary of some of the major concerns identified.

One possible source of uncertainties in visual wave estimates is poor separation between sea and swell. This problem appears when well-developed seas are reported as swell and when small swell is reported as sea, and leads to biases in sea and swell climatologies.

Visual estimates of wave height are reported in code figures, corresponding to half-metres. Hogben and Lumb (1967) reported that, in practice, observers frequently apply code 01 (0.25 m to less than 0.75 m) to wave heights less than 0.25 m, which should be coded 00. This results in a slight systematic overestimation of small waves in VOS.

Wave periods are known to be systematically underestimated in visual VOS data. One of the reasons is that it is difficult to distinguish periods if sea and swell propagate in the same direction, especially if the observational techniques are not properly applied. For example, visual wave periods will systematically be underestimated due to improper computation of the true wave period and direction from the apparent period, similar to the issue of evaluation of the true wind from the apparent wind (Gulev et al., 2003).

Historical swell period observations may also be erroneous due to the codes, which were changed in 1968. However, this change was not accepted simultaneously by all nations and owners of marine carriers, resulting in an overestimation of swell periods for 1969 and early 1970.

Visual data provide separate estimates of the wind sea and swell for the period after 1950. In the decades before 1950, officers reported the highest wave component.

The accuracy of night-time observations is generally considered to be lower than that of observations taken during daytime, when daylight provides much better conditions to estimate the sea state. At night, sailors sometimes do not follow the observational guidelines strictly, and even do not necessarily go out on the bridge to make the observations (Gulev et al., 2003). However, Gulev et al. (2003) did not find a consistent bias in night-time/daytime observations.

Waves running against a current are steeper and usually higher than when in still water. They are lower when running with the current, so observations may not be representative of the surrounding area. Similarly, refraction effects due to bottom topography in shallow water may cause a local increase or decrease in wave height.

Waves observed from a large ship seem smaller than those same waves observed from a small ship. Many observers tend to use wind information to estimate wave parameters and vice versa (Gulev et al., 2003). In other words, visual wave and wind observations are not fully independent of each other in existing observational practices.

There is general concern that VOS wave data are less reliable than satellite and model products because of their low accuracy, insufficient sampling and relatively difficult (in comparison to other parameters) procedures of preprocessing and bias corrections, but VOS wave data still have the longest period of continuous record. Moreover, these data provide separate estimates of sea and swell parameters, although the separation is done on a subjective basis by officers. In general, while visual observations from ships may have large uncertainties on an individual observation basis, they have considerable utility collectively for use in wave climatology, as long as proper quality assurance is applied (Gulev and Hasse, 1998; Gulev and Grigorieva, 2006).

7.2.2.2 ***Sources of visual wave data from ships***

Most visual wave information is derived from the observations made by the VOS Scheme, as described in the preceding sections. The observations are also logged and conveyed through

Port Meteorological Officers to central repositories nationally, and to the two Global Collection Centres, in the United Kingdom of Great Britain and Northern Ireland and Germany, as part of the WMO–International Oceanographic Commission Joint Technical Commission on Oceanography and Marine Meteorology (JCOMM) Marine Climate Data System.

The primary source for historical wave observations from ships is the International Comprehensive Ocean-Atmosphere Data Set (ICOADS; Freeman et al., 2017), through the new international partnership on ICOADS. Available global surface marine data since the late seventeenth century have been assembled, quality controlled and made widely available to the international research community. The ICOADS dataset is merged with the WMO *International List of Selected, Supplementary and Auxiliary Ships* metadata collection managed by the JCOMM in situ Observing Programmes Support Centre (JCOMMOPS), so relevant information about the observation is available with the data (WMO, 2010).

Real-time data are normally exchanged internationally via GTS of the World Weather Watch Programme. The data can be requested by contacting any Permanent Representative of a National Meteorological and Hydrological Service (NMHS) with WMO (see WMO, 2014*a*, for their details). The GTS data will gradually be integrated in the WMO Information System, which will also eventually provide a data discovery, access and retrieval service.

7.2.2.3 ***Visual observations from coastal stations***

At coastal stations, it is important to observe the height and period of waves at a spot where they are not deformed either by the wave being in very shallow water (of a depth that is a low multiple of the wave height) or by the phenomenon of reflection. This means that the spot chosen for observations should be well outside the breaker zone, not on a shoal or in an area where there is a steep bottom gradient, nor in the immediate vicinity of a jetty or steep rocks that could reflect waves back to the observation point. The observation point should be fully exposed to the sea, not sheltered by headlands or shoals.

Observations are generally more accurate if a fixed vertical staff with some form of graduated markings can be used to judge the height of passing waves. Observing an object on the surface, such as a floating buoy, may also improve estimation.

If the observations are to be of use for wave research, it is important that:

- They are always taken at the same place, so that correction for refraction and so forth can be applied later;
- The exact mean depth of water at the place and time of observation are known, so that correction for change of height with depth can be applied later.

Coastal observations of wave direction are meaningful at that particular location only. If the user does not realize that the data were obtained at a site where shallow water has a major effect (refraction), interpretation of the report could be erroneous.

There may be some visual wave observations from coastal stations in the ICOADS database. For other observations, some data may be available from the Permanent Representative of the respective NMHS.

7.2.3 **Measured wave data**

Various measurement platforms from point-source sites have measured waves for more than 60 years (for example, Tucker, 1991). These measurements typically provide the most reliable source of wave data, and are the foundation of all aspects of wind-generated surface gravity wave studies. Wave measurements have been and will continue to be used in validation of numerical wave models, calibration and validation of wave remote-sensing technologies, and validation of wave hindcast products. Wave measurements may be made in different ways, from

surface buoys, bottom-mounted systems (pressure) and acoustic profilers, to fixed systems as in the case of continuous wire gauges and step resistance, to downward-looking radar and laser. Each of these is described briefly below, with a summary of their strengths and weaknesses.

7.2.3.1 *Wave measurements from below the surface*

Systems to measure waves from below the surface have an advantage in that they are not as vulnerable to damage as systems on the surface. However, there are problems in bringing the data ashore because cables are expensive and can be damaged. An alternative technique is to transmit the information by radio from a buoy moored nearby.

Cavaleri et al. (2018) noted that pressure transducers have been used operationally for measuring waves for nearly seven decades (Bishop and Donelan, 1987; Pomaro et al., 2017). The ease of deployment, relative cost and survivability make these systems highly popular to use. Pressure transducers are most often used in shallow water (<15 m), but have also been mounted below the surface on offshore platforms in deep water. Using these, the change in pressure at the sensor is a measure of wave height. A pressure spectrum at the measurement depth can be derived from the pressure signal using spectral analysis. The measured pressures must be corrected for hydrodynamic attenuation with depth. Linear wave theory (see section 1.2) is used for this purpose (although there is evidence that the correction it gives is too small). One-dimensional wave spectra and associated parameters such as significant wave height can then be calculated. The attenuation has the effect of filtering out the shorter wavelengths; but for most practical applications, the loss of high-frequency wave information is not a disadvantage. However, if the water depth is greater than about 10–15 m, the attenuation affects too much of the frequency range and the correction factors become large, diminishing the value of the data. Sensors may be affected by biofouling, especially in coastal waters and enclosed seas. Estimates of significant wave height may also be affected by currents and non-linearities. Cavaleri et al. (2018) described various techniques to remove noise and/or compensate for currents and non-linear effects.

Upward-looking acoustic Doppler current profilers may be used in the coastal environment to estimate wave characteristics. Herbers and Lentz (2010) summarized the various systems, identifying the limitations of each system in correctly interpreting the recorded data. Under severe wave conditions, in a limited-depth coastal environment, breaking can be frequent and the presence of large air bubbles just below the surface can interfere with the acoustic measurement of the surface. Acoustic Doppler current profilers have also been suspended at a small depth below a platform or surface buoy.

Inverted echo sounders on the seabed can be used in shallow water. The travel time of the narrow beam of sound is directly related to wave elevation and gives a measurement without depth attenuation. However, in severe seas, the sound beam is scattered by bubbles from breaking waves, making the measurements unreliable.

7.2.3.2 *Wave measurements from buoys*

For open-water applications, the preferred wave-measurement platform is a buoy. Most existing buoy wave measurements are made in the coastal margins of North America and Western Europe, with data gaps in most of the rest of the global ocean, particularly in the Southern Ocean and the tropics (Figure 7.1). Figure 7.1 does not reflect all wave-measurement sites, only the ones that transmit data directly through GTS. However, these are the data that are most useful in an operational context, and most likely to be available in accessible wave archives. These data have historically been disseminated through the WMO FM-65 WAVEOB alphanumeric codes (WMO, 2011); in recent years, transmission has been increasingly in the BUFR code. In addition, in some instances (for example, NOAA/National Data Buoy Center (NDBC)), wave information has been distributed in the FM 13 SHIP message. The SHIP message is used rather than BUOY because the SHIP message provides fields for wind sea and swell parameters not found in the BUOY message. The new BUFR Moored Buoy template will allow incorporation of spectral data and wind-sea and swell parameters.

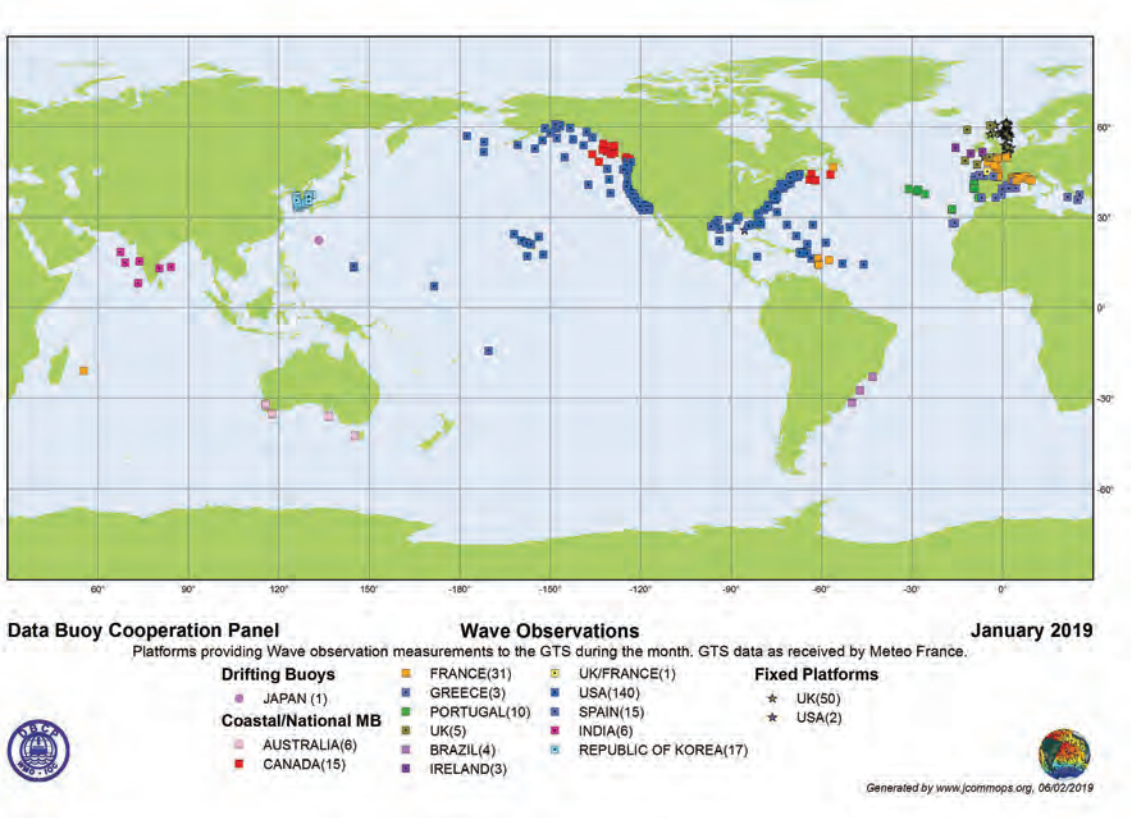

Figure 7.1. Wave observation reporting through GTS for January 2019

Source: http://www.jcommops.org/dbcp/network/maps.html

The following paragraphs describe the buoy wave-measuring systems. Additional information is provided in the *Guide to Meteorological Instruments and Methods of Observation* (WMO, 2014*b*). The technical documents by NDBC (1996, 2009) also provide complete details on wave measurements made by NOAA/NDBC, the largest operational moored buoy network.

7.2.3.2.1 Measurement systems

A buoy wave-measurement system typically has three major components: (a) the platform, comprising the hull, shape, composition, superstructure and mooring; (b) the sensor; and (c) the payload, or on-board analysis package.

Wave buoys can be spherical, discus-shaped or boat-shaped (for example, the Navy Oceanographic Meteorological Automatic Device (NOMAD); Timpe and Van de Voorde, 1995)), with sizes ranging from about 1 to 12 m for discus buoys, to less than a metre in diameter for newer spherical hulls; NOMAD buoys are 6 m in length, 3 m wide and weigh upwards of 5 200 kg. Many wave buoys are multi-purpose, and thus may have extended superstructures generally housing meteorological sensor packages. Buoys may also have solar panels for supplemental power and cages to prevent access by sea mammals. Hulls have typically been made out of aluminium, but foam construction has become more prevalent in recent years. Moorings (and bridling systems) can be open link chain, polypropylene, rope or shock cord, permitting the buoy to be free floating and actively revolving within a well-defined watch circle. The buoys must be carefully moored so that their motions are not greatly influenced by the mooring. Taut or semi-taut moorings may restrict the buoy in defining the free surface adequately.

Sensor systems have changed over the past three decades, but more so particularly in the last few years. Historically, most buoys have used accelerometers to measure buoy heave motion.

The most common type of sensor has been the strapdown accelerometer, due to its cheap cost and low maintenance requirements. In these systems, the vertical direction is along the axis of the buoy itself rather than the true vertical with respect to the Earth. This can cause serious errors as described below. Gimballed sensors have a built-in mechanical system for keeping the accelerometer vertical as the buoy and sensor tilt. They have been used operationally since the early 1970s (Steele et al., 1992, 1998) to directly determine the pitch and roll angles (or to measure the accelerations in the *x*, *y* and *z* directions). Sensor systems may sample at rates ranging from about 1 Hz to 10 Hz or more; in addition, the sampling period may range from about 17 min to more than 35 min. These variations all contribute to differences in measured waves.

The trend in recent years has been to migrate from these fixed and gimballed accelerometers to electronic motion packages housing tri-axial accelerometers combined with digital magnetometers and compass packages to cover nine degrees of freedom to measure the buoy's motion and translate it to the free surface. The cost, power consumption and size of these are significantly lower.

Non-directional wave-measurement systems report estimates of acceleration or displacement spectra. If not directly reported, displacement spectra are derived from the double time integration of the acceleration spectra.

Bender et al. (2009, 2010) demonstrated the dramatic effects of the consequences of using fixed accelerometers. They found that sustained heeling of the buoy due to currents or wind forcing on the superstructure caused large differences (26%–56%) in significant wave-height estimates; the problem of tilt was most felt in shallow water. NOAA/NDBC implemented the on-board correction proposed by Bender et al. (2010) on their buoy systems to remove this effect in extreme situations.

Directional wave-measurement systems require measurement of the buoy azimuth, pitch and roll, in addition to vertical acceleration or heave (displacement). These allow the east–west slope and north–south slope to be computed.

Directional buoy wave measurements based on buoy motion can be categorized into two types: translational (particle-following) or pitch-roll (slope-following) buoys. As directional wave information is derived from buoy motions, the measured buoy response requires a mathematical transfer function associated with the hull size, composition, superstructure, bridle-mooring and measurement systems to allow estimation of the free surface. Each buoy configuration should have its own unique transfer function that is dependent on the physical factors influencing the buoy motion. Cavaleri et al. (2018) noted that this is likely not the case in existing wave buoy networks. This dependence is particularly important at low energy levels and at short and long wave periods where the wave signal being measured is weak and the potential for added signal contamination increases.

7.2.3.2.1.1 *"First 5" wave measurements*

The objective of directional wave measurement is to obtain accurate estimates of the two-dimensional distribution of energy S in frequency f and direction θ:

$$S(f,\theta) = S(f)\left[a_1 \cos\theta + b_1 \sin\theta + a_2 \cos 2\theta + b_2 \sin 2\theta + \sum_{n=3}^{\infty} a_n \cos n\theta + b_n \sin n\theta\right]. \qquad (7.2)$$

In general, only the first four moments of the directional distribution can be resolved: mean wave direction, directional spread, skewness and kurtosis (Jensen et al., 2011). The concept of "first 5" was introduced to nominally evaluate directional estimates in wave-measurement systems (O'Reilly, 2007).

Technically, "first 5" refers to five defining variables at a particular wave frequency (or period). The first variable is the wave energy, which is related to the wave height, and the other four are the first four coefficients of the Fourier series (Equation 7.2), which defines the directional distribution of that energy. At each frequency band, the wave direction is defined and also the spread (second moment), skewness (third moment) and kurtosis (the fourth moment). The

skewness resolves how the directional distribution is concentrated and the kurtosis defines the peakedness of the distribution. Obtaining these three additional parameters for each frequency band yields an improved representation of the wave field. High-quality "first-5" observations can be used to resolve two-component wave systems at the same frequency, if they are at least 60° apart, whereas other measurement systems cannot. Although there are more than five Fourier coefficients, the "first-5" variables provide the minimum level of accuracy required for a directional wave observing system. They cover the basic information (the significant wave height H_s, peak wave period T_p and the mean wave direction at the peak wave period θ_m) along with sufficient details of the component wave systems to be used for the widest range of activities.

It is recommended that to serve the full range of users, a wave observation network should accurately resolve the details of the directional spectral wave field as well as providing the standard integrated parameters (Swail et al., 2010). It is strongly recommended that all directional wave-measuring devices should reliably estimate the first-5 standard parameters. Fields for the first-5 coefficients are expected to be included in the FM65 BUFR template for the exchange of wave spectral data on GTS.

In sensors, the payload (analysis package) acquires the raw signal and transforms it to an estimate (x,y,z) of the free surface from which ultimately directional estimators (the lowest Fourier coefficients $a_1(f)$, $b_1(f)$, $a_2(f)$ and $b_2(f)$ in Equation 7.2), frequency spectra and integral wave parameters are derived. For a particle-follower buoy, estimates of the Fourier coefficients follow directly from the measured accelerations and linear wave theory (O'Reilly et al., 1996). For a slope-following system, estimates of a_1 and b_1 incorporate various corrections for hull-mooring response. Steele et al. (1992) noted that translational buoys use α_1, α_2, r_1 and r_2, which are trigonometrically related to the four Fourier directional coefficients.

7.2.3.2.1.2 *Emerging technologies*

Recent developments have provided the possibility of using more-stable buoys equipped with a motion sensor package and an array of capacitance wave staffs to infer the water level induced by the presence of waves (Graber et al., 2000). These types of systems have proven to be reliable when measuring wind sea and swell in opposite directions, as well as providing an accurate determination of momentum fluxes between the ocean and atmosphere (Ocampo-Torres et al., 2011).

In recent years, global positioning system (GPS) technology has been introduced in wave buoys as an alternative to the traditional gimballed or strapped down accelerometers or motion sensors to measure the pitch, heave and roll of the buoy. The GPS measurement principle is based on the Doppler shift of the satellite signal frequency and provides the three velocity components of the buoy and thus of the sea surface, under the assumption that the buoy is a good water-surface follower. These GPS sensors are particularly attractive because they are small and inexpensive. Centurioni et al. (2017) gave a good description of the characteristics, advantages and possible errors associated with GPS wave measurement.

This proliferation of new wave-measurement systems capable of providing high-quality directional estimates of the free surface at greatly reduced cost is revolutionizing wave measurement. However, testing and evaluation of these new technologies must be addressed to better understand the differences in the wave measurement from one buoy system to the other. Section 7.3.2.5 describes this further.

7.2.3.2.2 **Wave measurements from drifting buoys**

Most of the global ocean suffers from a lack of measured wave data. The prospect of the development of a network of drifting buoys capable of high-quality wave measurements is transformative, as is evident from Figure 7.1. Historically, a handful of drifting buoys capable of high-quality wave measurements have been deployed, but not enough to make a significant

difference in global wave climatology or assimilation into operational wave forecast models. The emergence of new, high-quality, inexpensive sensors implemented into smaller buoy hulls has opened up the development of enhanced networks of global wave measurements.

Numerous groups have recently developed wave drifters. Activity within the Data Buoy Cooperation Panel (DBCP), to use the drifter design adopted by the Global Drifter Program, is of particular interest. Centurioni et al. (2017) described the technical characteristics of a GPS-based Directional Wave Spectra Drifter (DWSD) developed by the Lagrangian Drifter Laboratory at Scripps Institution of Oceanography. They also described the data processing methodology and evaluation results.

Briefly, DWSD consists of a sphere with a diameter of 0.39 m, a 12 kg weight and replaceable alkaline or lithium batteries. The DWSD GPS sensor measures the vertical (w), zonal (east–west, u) and meridional (south–north, v) velocity components of the buoy. Times series of $u(t)$, $v(t)$ and $w(t)$ are sampled for about 17 min at 2 Hz and are split into four overlapping segments of 256 s that are subsequently averaged. The power spectral density, co-spectra and quadrature-spectra parameters are derived with the Fourier transforms of the correlation functions of each pair of the velocity time series, giving the first-5 independent Fourier coefficients (a_0, a_1, a_2, b_1, b_2) and thus the wave spectra for each hourly (and, optionally, half-hourly) sea state.

7.2.3.2.3 Metadata

As with any source of observational data, a comprehensive metadata record is essential to properly understand the wave information originating from the different platforms, payloads and processing systems. This is necessary to understand systematic differences in the measurements from differing observing networks, or from the same observing network that has changed over time. It is also critical for climate applications to ensure temporal homogeneity of the records to eliminate spurious trends. Considerations in dealing with wave data from buoys include: hull type and construction, sensor type, processing system, sampling frequency and duration, presence of meteorological or other sensors, mooring type and water depth. Metadata from moored buoys have typically been fragmented and difficult to use in a consistent fashion. They could usually be obtained from the national agency by whom the measurements were made. As a result, JCOMM, through JCOMMOPS, has established a central repository for metadata from moored buoys.

7.2.3.2.4 Buoy data availability and sources

Unlike observations from VOS, there is no central database for observations from moored buoys, or specifically for measured waves. The ICOADS database contains most wave data from moored buoys, although it is often in ship-based format, with reduced precision of half-metres. ICOADS allows for attachments of the original buoy message, including spectral information, but this is not always the case, and is difficult to process. Most buoy wave data must be obtained directly from the responsible national agencies. In the United States of America, this is the National Centers for Environmental Information, which is the official wave archive, although many users still go directly to NDBC for data, even though the data may not have undergone the full quality control of the official archive. For other countries, users are directed to the national focal points identified in WMO (2014*a*). Efforts are under way within JCOMM to establish a Global Data Acquisition Centre specifically for wave data, as a central repository for measured wave data, but this is not yet a reality.

7.2.3.2.5 Wave-measurement evaluation

Significant differences exist in measured waves from different platforms, sensors, processing and moorings (Swail et al., 2010; Cavaleri et al., 2018). Continuous testing and evaluation of operational and pre-operational measurement systems is an essential component of a global wave observing system, equal in importance to the deployment of new assets. The overriding objective is to ensure consistent wave measurements to a level of accuracy that will serve the

requirements of the broadest range of wave information users. Interplatform tests have been pursued in the past. There have been experiments at various locations over the past 25 years, focusing on the evaluation of wave-measurement systems (for example, the Wave Direction Measurement Calibration (WADIC) project (Allender et al., 1989); Harvest Platform (O'Reilly et al., 1996); Wave Crest Sensor Intercomparison Study (van Unen et al., 1998); Flux, Etat de la mer et Télédéction en Condition de fetcH (Pettersson et al., 2003); NDBC Sensor Systems (Teng and Bouchard, 2005); and Impact of Typhoons on the Ocean in the Pacific (Collins et al., 2014)) and analysis methods to use in the evaluation process (Krogstad et al., 1999). However, as new sensor and wave-measurement systems mature, the need for more intrameasurement evaluations will emerge.

A recent study, the Field Laboratory for Ocean Sea State Investigation and Experimentation located in Monterey Canyon off the California coast, was initiated in July 2015 (Jensen et al., 2015). It was in support of the JCOMM DBCP Pilot Project on Wave Measurement Evaluation and Test (PP-WET), and continues under the guidance of the DBCP Task Team on Wave Measurement.

The above study followed a different approach as detailed by O'Reilly (2007) and Jensen et al. (2011). The four Fourier directional parameters were used to calculate the four moments of the directional distribution at each frequency band: the mean direction, spread, skewness and kurtosis. Partitioning was performed on each discrete frequency band, and a discrete energy level. A bias and root-mean-square error percentage was determined from averaging the differences between two datasets. The result was a qualitative graphic displaying a defined range of the percentage deviations. These techniques can provide useful quantitative and qualitative information, thus reducing the assessment in directional properties to a reasonable number of products.

One of the most important findings of the study was that, despite consistency in the wave height, period and direction measurements, there was a substantial variation in the frequency spectra and frequency dependent directional components (mean wave direction, spread, skewness and kurtosis), illustrating that agreement in the integral wave parameters is a necessary, but not sufficient, condition for many applications.

Cavaleri et al. (2018) provided a comprehensive description of several examples of different approaches to evaluate wave measurements from different observing systems.

7.2.3.3 ***Other wave measurements at the sea surface***

In shallow water, where a platform or structure is available, it is possible to obtain wave measurements at the sea surface using resistance or capacitance wave staffs. The wave elevation is then directly related to the change in resistance or capacity of the wave staff. However, wave staffs can be easily damaged by floating objects and are subject to fouling by marine growth.

A shipborne wave recorder (SBWR) may be used to obtain wave information from measurements of the motion of a stationary vessel or lightship. In these systems, pressure recorders mounted below the surface in the hull on both sides of the ship give measurements of the waves relative to the ship. Accelerometers in the ship measure the vertical motion of the vessel. After calibration, the sum of the signals from the pressure sensors and the accelerometers gives an estimate of the motion of the sea surface, from which the wave height and period are derived. An SBWR is a robust system that is not as vulnerable as a buoy and is also able to give wave information in extreme sea conditions. However, the measurement accuracy is generally not as good as that of a wave buoy, due to the more damped response that a ship will have to high-frequency waves. These SBWR systems are expensive, so that there are few in operation globally.

Arrays of wave recorders can provide directional detail and have been used in several oceanographic and engineering studies. The degree of directional resolution depends on the number of wave recorders and their spacing. The types of instruments that can be used include wave staffs (Donelan et al., 1985) and pressure transducers (O'Reilly et al., 1996). Wave directional information collected from such systems are usually site specific, as the recorded waves are influenced by refraction and dissipation in shallow water. The arrays can be either

mounted on an offshore platform, or bottom mounted in shallow water if the depth does not exceed 10–15 m. Pressure transducer arrays on offshore platforms should not be located deeper than 10–15 m below the surface because of depth attenuation of the surface-wave signature.

Ultrasonic or electromagnetic current meters that measure the two horizontal components of wave orbital velocity in conjunction with a pressure recorder or wave staff can provide useful directional information. These systems are usually deployed in shallow water, but can also be mounted on offshore platforms, provided that the influence of the platform is not too great. These systems are directly analogous to the pitch/roll buoy system discussed in section 7.2.3.2. Perhaps the most well-known, self-contained instrument of this type is the S4 current meter; the UCM-40 current meter is also commonly used.

New methods have allowed development of techniques based on the acoustic Doppler signal to measure fluid velocities associated with wave orbital motion. A combination of measurements of three or more time series would result in improved directional wave spectrum estimates. Typically, pressure and horizontal components of wave orbital velocities have been used to determine directional waves. Young (1994) determined an optimal configuration for arrays of sensors and, using linear wave theory, produced a table for transformation of measured information (elevation, slopes, velocities, accelerations and so forth) onto the directional wave-energy density spectrum. A promising technique has been developed to measure up to 12 time series of wave signals (orbital velocities) simultaneously to achieve a highly resolved wave directional spectrum using acoustic Doppler technology (Work, 2008).

7.2.3.4 ***Measurements from above, but near the surface***

Waves can be measured from above the surface by downward-pointing laser, infrared, radar or acoustic instruments, if a suitable platform is available. Tucker and Pitt (2001) gave a good description of these instruments. Advantages are that they are non-intrusive (do not disturb the flow), and because of their low operational costs, they are easy to maintain and service and do not require expensive ship time for deployment and recovery of wave buoys. In addition, they offer the potential to measure absolute surface elevation, when mounted on a fixed platform, providing the opportunity to investigate fundamental aspects of the wave field. However, some offshore platforms can significantly modify the wave field by refraction, diffraction and sheltering. Care must be taken in siting the instruments to minimize these effects. For "jacket"-type structures, a rough guide is that the measurement "footprint" on the sea surface should be located more than 10 leg radii away from the platform leg.

Wave measurements taken above the surface are sometimes classified as remotely sensed values, as the sensor is not in the water. However, Grønlie (2004) gave a high-level description of different radar techniques suitable for wave and surface current measurements and categorized them as direct sensors, because they involve direct measurement of surface elevation. Indirect sensors are those that involve derivation of wave information from images associated with Bragg scattering at low grazing angles such as those based on ship navigation systems, shore-based systems or satellites (described in section 7.3.1).

Commonly used instruments of the downward-looking, non-intrusive type include the EMI and Schwartz lasers and Saab and Marex (Plessey) radars. The radar instruments generally measure over a larger footprint on the ocean surface but are less able to measure high-frequency (short) waves.

Ewans et al. (2014) provided an excellent description of the use of the SAAB REX WaveRadar, which has been widely used for platform-based wave-measurement systems by the offshore oil and gas industry, with more than 500 installed worldwide. It offers in situ surface elevation wave measurements at low operational costs. There is adequate flexibility in sampling rates, allowing sampling frequencies from 1 to 10 Hz. However, with an angular microwave beam width of 10° and an implied ocean-surface footprint of the order of metres, significant limitations on the spatial and temporal resolution might be expected. There are indeed reports that the accuracy of the measurements from wave radars may not be as good as expected. The differences are

typically less than 8% and generally less than 5% (with the buoy values being higher) and therefore consistent with wave sensor intercomparisons performed in the WADIC experiment (Allender et al., 1989). Nevertheless, an explanation for these differences is desirable.

Downward-looking laser altimeters (Magnusson and Donelan, 2013; Donelan and Magnusson, 2017) have been used as the baseline for intrameasurement evaluation in the North Sea (Allender et al., 1989), as well as the more recent DBCP PP-WET. In this case, the surface elevation was measured by a square (of side 2.6 m) array of platform-mounted surface elevation sensors (laser range finders, accuracy of ±4 mm) – "LASAR". This enabled analysis of the directional properties of constituent groups that sometimes come together to produce unusually high waves or rogues. These systems have also been affixed to a moving research vessel (Donelan et al., 2005).

Much interest has been shown by the offshore industry in recent years in accurately specifying the observed asymmetry of high waves, as this affects the design of offshore structures. As an example, an array of four Optech lasers (LASAR) was mounted on a gantry between platforms at the Ekofisk offshore oil installation in the central North Sea. This configuration measured sea-surface variations at 5 Hz sampling frequency and was also used to evaluate directionality in the waves. Studies of the resulting data provided estimates of sampling variability associated with significant wave height and zero-crossing wave period, and were used to demonstrate the impact sampling variability has on short-term and long-term description of ocean waves (Bitner-Gregersen and Magnusson, 2014).

New systems based on stereo photography and videography may also be within this class of sensors to measure from above but near the surface. Such systems have already been tested and provided promising results (Benetazzo et al., 2012). Fedele et al. (2013) demonstrated that stereo-video techniques are effective for estimating the space–time wave dynamics over an area of the ocean.

7.3 REMOTE-SENSING DATA

In general, conventional wave recorders measure the displacement with respect to time of the water surface at a fixed point. Remote-sensing techniques (Shearman, 1983) are not able to measure in this way. Instead, they interrogate an area or footprint that, in the case of satellite-borne sensors, has typical dimensions of several kilometres (except for SARs, which can have a footprint of a few metres) and report some measure of the average wave conditions over the whole area. Surface-based radars can also have a range resolution of a few metres, smaller than the wavelengths of the gravity waves being measured, although the footprint is still broad in azimuth. Consequently, low-resolution sensors are rarely used for coastal or shallow-water sites, because the wave field there can vary considerably over distances much less than 1 km. The advantage of surface-based remote sensing is that equipment can usually be kept in a safe place, well away from the ravages of the sea, and be readily accessible for maintenance and testing.

Wave measurements made using remote sensing generally use active microwave sensors (radars), which send out electromagnetic waves. Deductions about wave conditions are made from the return signal. The following sections briefly describe the widely used satellite- and surface-based remote-sensing systems as applied to wave analysis and forecasting. Before considering individual sensors, some features of the interaction between electromagnetic waves and the sea surface will be discussed.

7.3.1 Active sensing of the ocean surface with electromagnetic waves

If a radar sends energy directly down towards a level, glassy, calm sea surface, the energy will be reflected from a small region directly below the radar as if from a mirror. If the surface is perturbed by waves, specular reflections (glints) will arise from facets within the radar beam and perpendicular to it – essentially from horizontal facets for a narrow beam radar (see Figure 7.2).

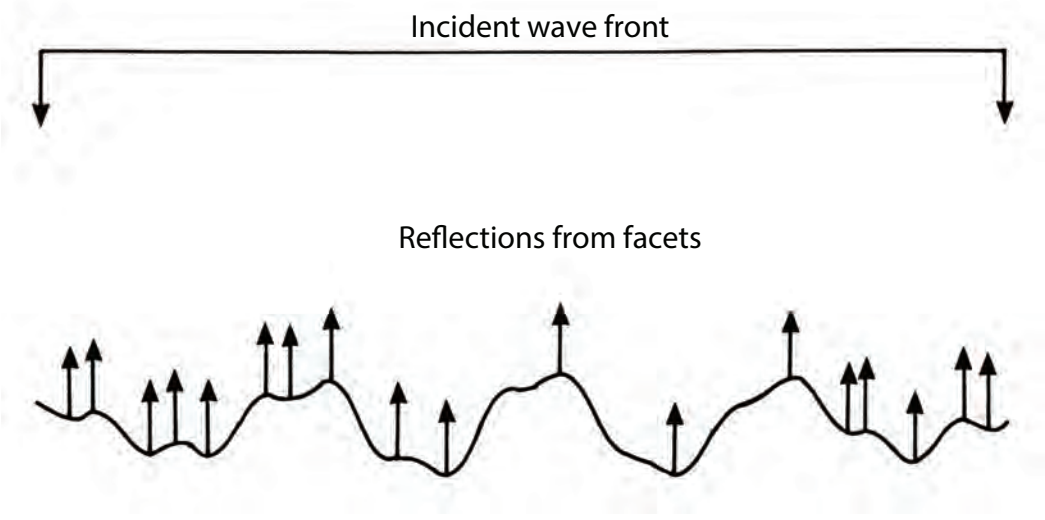

Figure 7.2. A radar altimeter normally incident on a rough sea, illustrating the different path lengths for energy reflected from facets

Source: Tucker (1991)

Consider a radio beam pointing obliquely at the sea surface at a grazing angle Δ as in Figure 7.3. If the sea wavelength λ_s is scaled to the radar wavelength λ_r, the backscattered echoes returning to the radar from successive crests will all be in phase and reinforced. The condition for this "Bragg resonant scatter" is

$$\lambda_s \cos \Delta = \frac{\lambda_r}{2}. \tag{7.3}$$

In the real sea, there will be a mix of many wavelengths and wave directions, and the Bragg resonance mechanism will select only those waves approaching or receding from the radar and of the correct wavelength. For a microwave radar, these would be ripples of a few centimetres. However, the mechanisms illustrated in Figure 7.4 ensure that the longer waves influence (modulate) the ripples by:

- "Straining" (stretching and compressing the ripples by the orbital motion of the long waves), accompanied by velocity modulation;
- Tilting the surface on which the ripples move and so modifying the Bragg resonance condition through Δ in Equation 7.3;
- Hydrodynamic interaction, which concentrates on the leading edge of long waves, or through the perturbed wind flow over the long-wave crests, both of which produce a roughness modulation.

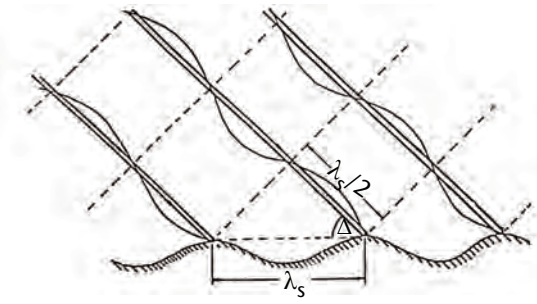

Figure 7.3. Bragg diffraction of radio waves from a sinusoidal sea wave. Conditions for constructively interfering backscatter from successive crests.

Source: Shearman (1983)

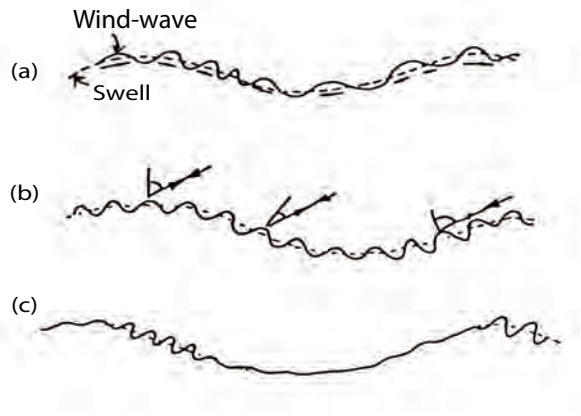

Figure 7.4. Mechanisms of spatial modulation by long gravity waves of radar scattering from capillary waves: (a) straining and velocity modulation of short wind waves by longer wind waves and swell, (b) tilt modulation and (c) roughness modulation

Source: Shearman (1983)

A radar observing backscatter from short waves by these mechanisms sees (in the spatial variation of backscatter intensity and in the Doppler spectrum) a representation of the long waves.

7.3.2 Space-based remote sensing

7.3.2.1 *Radar altimeters*

As indicated in Figure 7.2, the higher the waves then the greater the time between the arrivals of returns from the crests and from the troughs of the waves, and the higher the spread in the return pulse. From knowledge of the statistics of the sea surface, this stretching of the shape of the return pulse can be related quantitatively to the variance of the sea surface, and hence to the significant wave height H_{m_0} (using the spectral definition – see section 1.3.8). Satellite altimeters usually have a pulse rate of 1 000 Hz; estimates of H_{m_0} are derived on board, and values averaged over 1 s are transmitted. Theoretically, there should be no need to calibrate these values, but in practice, it has been found necessary to do so, comparing them with buoy measurements (Carter et al., 1992).

The strength of the return pulse is also dependent upon the statistics of the sea surface, which are affected by the wind speed over the surface. So, there is a relationship between the strength of the return pulse and the wind speed. However, this relationship is complex and not fully understood. In general, the stronger the wind, the lower the strength of the return. Various algorithms have been derived from observations that give estimates of wind speed at 10 m above the sea surface from the strength of the altimeter return, but further work needs to be done to determine which is the most accurate(for example, see the work of Witter and Chelton (1991) and the studies based on the TOPEX/Poseidon data (Freilich and Challenor, 1994; Lefèvre et al., 1994)).

Radar altimeters give near-global coverage and hence provide wave-height data for almost anywhere on the world's oceans, including areas where data were previously scarce. Some long-term satellite altimeter missions have made global measurements. These include GEOSAT, TOPEX/Poseidon, Jason-1, OSTM/Jason-2, ERS-1, ERS-2, Envisat ASAR and GFO. Current missions are Jason-2, Jason-3, CryoSat-2, HY-2, SARAL/Altika, Sentinel-1 and Sentinel 3-A. Table 7.1 lists past and present altimeter missions. Cavaleri et al. (2018) provided further information on the satellite missions and sensors. Details of the European Space Agency (ESA) missions and data are

Table 7.1. Satellite missions with reliable radar altimeter instruments

Satellite	*Launch*	*End of life*	*Altitude (km)*	*Repeat cycle (d)*
SEASAT	1978	1978	800	17
GEOSAT	1985	1990	800	17
ERS-1	1991	1996	785	35[a]
TOPEX/Poseidon	1992	2006	1 336	10
ERS-2	1995	2011 [b]	785	35[c]
GFO	1998	2008	800	17
Jason-1	2001	2013	1 336	10[c]
Envisat	2002	2012	800	35[c]
Jason-2	2008	–	1 336	10[c]
CryoSat-2	2009	–	720	369
HY-2	2011	–	963	14
SARAL/AltiKa	2013	–	800	35[c]
Jason-3	2016	–	1 336	10
Sentinel-3A	2016	–	815	27

Notes:
[a] Followed other orbits with repeat cycles of 3 d and 168 d.
[b] Limited coverage from 2003 onwards.
[c] Different orbit followed towards the end of life.

Source: Cavaleri et al. (2018)

available from Sentinel; information and data on National Aeronautics and Space Administration missions and data are available from the Physical Oceanography Distributed Active Archive Center.

Despite the resounding success using altimeter data for assimilation purposes in numerical wave prediction, evaluation of a wave-model performance and validation of wave hindcast and reanalyses, there are several concerns associated with their use. One difficulty has been the use of satellite altimetry along the coasts, due to land effects on the radar waveforms. ESA has made significant efforts on studying altimetry in the coastal zone (Coastal Altimetry Workshop Series).

A more widespread issue was identified by the ESA GlobWave Project, which noted that there were significant biases among individual altimeter datasets on different missions (see Figure 7.5). The objective of GlobWave was the provision (via a web portal) of a uniform, harmonized, quality-controlled, multisensor set of satellite wave data and ancillary information, in a common format, with consistent characterization of errors and biases. GlobWave allows easy access to a harmonized set of altimeter and SAR products. The GlobWave satellite products give a uniform set of along-track satellite wave data from all available altimeters (spanning multiple space agencies) and from ESA SAR data, allowing free access to SAR and altimeter datasets in real time and in delayed mode for:

- Altimeters: significant wave height and backscatter coefficient (Sigma0);
- SARs: swell significant wave height, dominant wavelength (per spectral partition) and mean direction (per spectral partition).

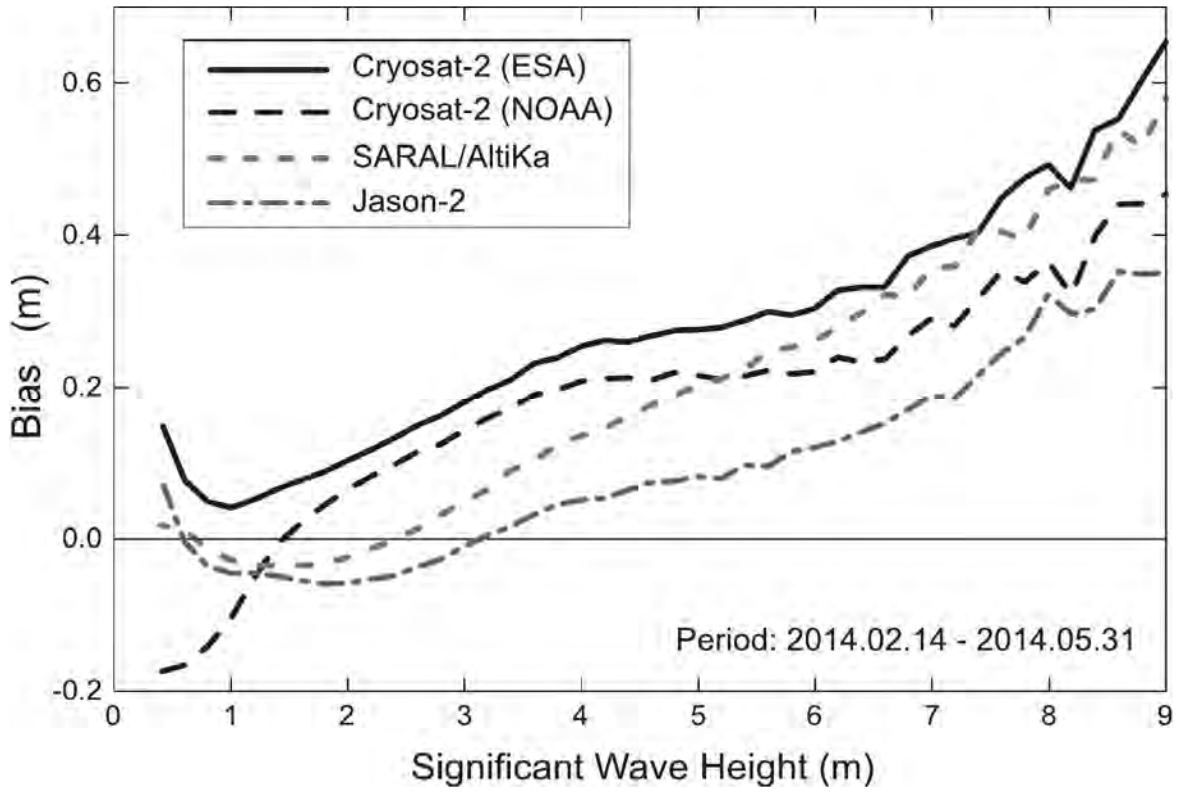

Figure 7.5. Significant wave-height difference (bias) among various altimeters and the European Centre for Medium-Range Weather Forecasts (ECMWF) operational wave model first guess as functions of significant wave height

Source: Cavaleri et al. (2018)

7.3.2.2 ***Synthetic aperture radars***

Practical aircraft and satellite-borne antennas have beam widths too large to permit wave imaging. In the synthetic aperture technique, successive radar observations are made as the aircraft or satellite travels horizontally. Subsequent optical or digital processing produces narrow focused beams and high-grade imaging of the longer waves, as evidenced by the variation of the radar-echo intensity ("radar brightness") produced by the mechanisms shown in Figure 7.4. Figure 7.6 shows an example, from Seasat, of wave imagery and Figure 7.7 shows a wave directional spectrum (with 180° ambiguity) achieved by analysis of an image. Figure 7.8 shows a high-resolution scene in north-western Spain taken from ERS-1 SAR.

A SAR has the advantage of being a broad-swath instrument, with a swath width and resolution of about 100 km and 25 m, respectively. However, the physical processes underlying its imaging of waves are complex and still not universally agreed. The main difficulty in interpreting the images of ocean waves is that the sea surface is not at rest, as assumed by the synthetic processor, and the orbital velocities of the longer waves, which transport the ripples responsible for backscattering the radar waves, are around 1 m s^{-1}. This results in a highly non-linear effect, which can lead to a complete loss of information on waves travelling in the along-track direction. Moreover, waves of length less than about 100 m travelling in any direction are not imaged by the SAR because of smearing and a decrease in the signal-to-clutter ratio.

Thus, a SAR instrument is more likely to provide useful data in the open ocean than in enclosed seas such as the North Sea, where wavelengths tend to be less than 100 m. However, even in mid-ocean, the waves can sometimes be so short that the SAR will fail to "see" them.

Given the directional wave spectrum, it is possible to obtain a good estimate of the spectrum from the SAR image. However, the problem is to go the other way: to derive the directional wave spectrum given the SAR image. Research has shown that if a global wave model is run

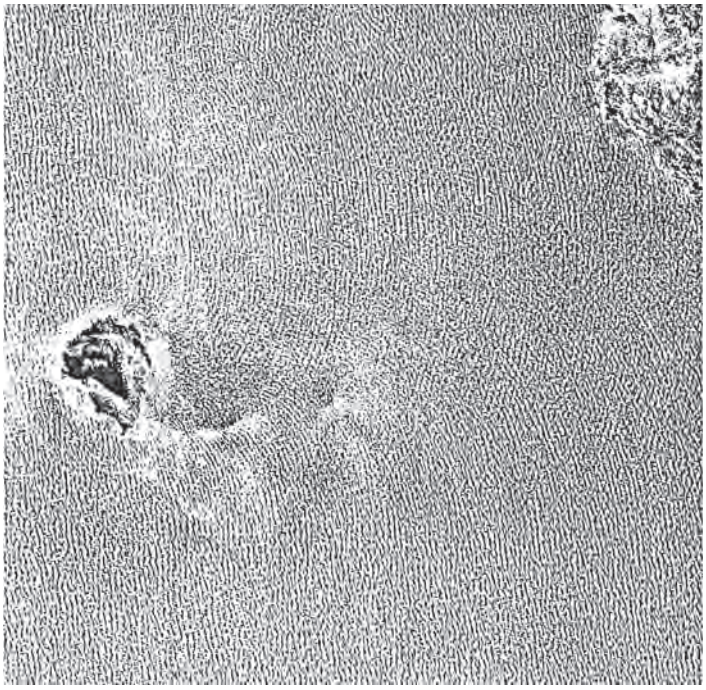

Figure 7.6. Seasat SAR image of the wave field between the Islands of Foula and Shetland

Source: ESA photograph, processed at the Royal Aircraft Establishment, United Kingdom

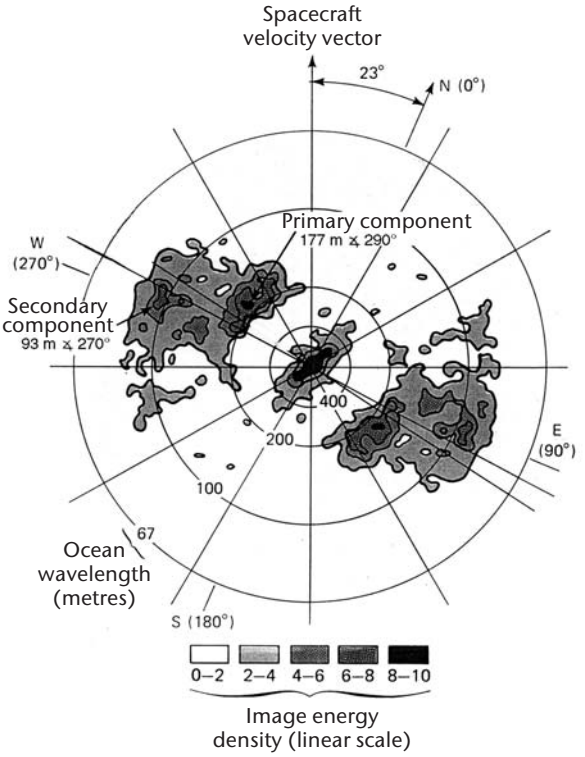

Figure 7.7. Example of directional wave-energy spectrum derived by digital processing of Seasat SAR data. The five levels of greyness indicate spectral amplitude, while the distance from the centre represents wave number ($2\pi/\lambda$). The circles are identified in wavelength. A 200 m swell system is shown coming from east-north-east and broader spread 100 m waves coming from east-north-east. The analysis has an 180° ambiguity.

Source: Beale (1981)

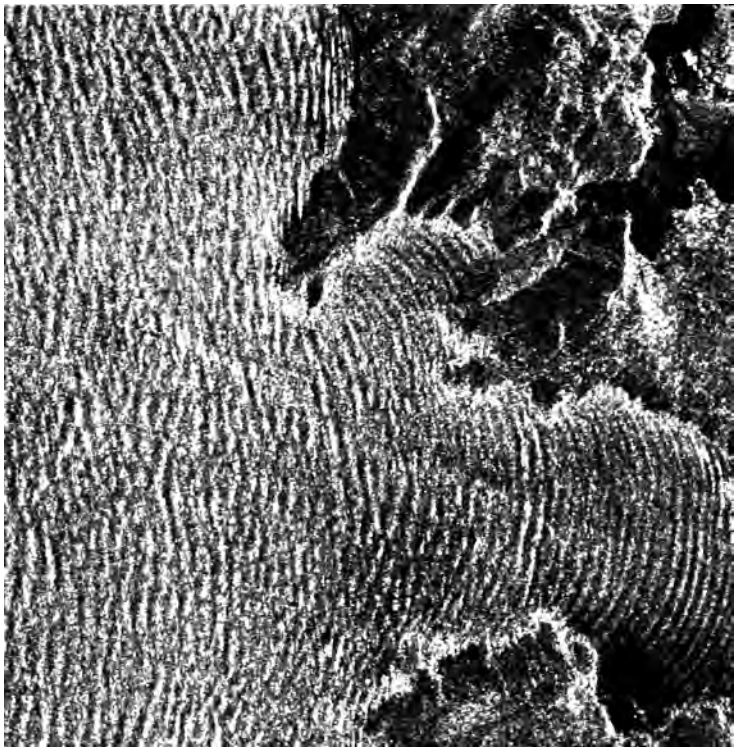

Figure 7.8. ERS-1 SAR subscene acquired on 17 January 1993 by the ESA station in Fucino, Italy. The image shows the entrance to the Ria de Betanzos (Bay of La Coruña), north-western Spain, and represents an area of 12.8 × 12.8 km^2. An east-south-east swell (travelling from west-north-west) enters the bay, and the waves are diffracted as they travel through the narrower opening of the bay. However, waves do not enter the narrow northern Ria de El Ferrol. The inner part remains wind and wave sheltered and therefore dark. As the waves get closer to the shore, their length becomes shorter, as observed near the coast to the north. The long linear feature through the middle of the image is probably linked to a strong current shear, not usually visible in such a sea state.

Source and image copyright: ESA; J. Lichtenegger, ERS Utilisation Section, ESA/European Space Research Institute, Frascati

to provide an initial estimate of the wave spectrum, then the difference between the observed SAR spectrum and that estimated from the model spectrum can be used to correct the model spectrum and hence to improve the wave-model output (Hasselmann et al., 1991).

A practical problem with SARs, which tends to inhibit their use, is the vast quantity of data produced (108 bits s^{-1}) and the consequent cost of processing and acquiring the data. Moreover, these data cannot be stored on board the satellite, so SAR data can only be obtained when the satellite is in sight of a ground-receiving station. An exception to this is ERS-1, which obtains a small SAR image, with a footprint of 5 × 5 km^2, every 200 km. These "wave vignettes" can be stored on board and transmitted later to ground. Sentinel-1 produces images in wave mode, which are 20 × 20 km^2, with a 5 × 5 m^2 spatial resolution.

New missions are providing a great amount of information suitable for retrieving directional wave spectra, especially for swell conditions. Highly developed SARs provide fine-resolution images and polarization capabilities, allowing the possibility of exploring further details of the sea-surface geometry as well as dynamic processes, including breaking waves.

Furthermore, new missions operate in wave mode, acquiring continuous imagettes over the global oceans. Some studies have been carried out to assess and validate wave information retrieved from this mode (Wang et al., 2014*a*). Global observations of ocean swell can be obtained from satellite SAR data in wave mode. These data have been used to estimate the

dissipation of swell energy for storms (Ardhuin et al., 2009). Swells can be persistent over the global ocean with energy e-folding scales exceeding 20 000 km. This scale decreases to about 2 800 km for the steepest observed swells, revealing a significant loss of swell energy.

It is possible to produce surface velocity measurements at high spatial resolutions over a large area using interferometric SARs. The data can be used to retrieve the velocity strain field and highlight ocean-surface processes such as wave breaking. The large spatial coverage of airborne or spaceborne operation further offers the opportunity to investigate the evolution of the surface-wave spectrum in high spatial (subkilometre) resolution (Hwang et al., 2013).

7.3.2.3 ***Scatterometers***

A satellite-borne scatterometer (Jones et al., 1982) is another oblique-looking radar sensor. The total echo power from its radar beam footprint is used to estimate wind speed. The relative return power from different directions gives an estimate of the wind direction, because the small-scale roughness of the sea surface, seen by the radar, is modulated by the longer wind waves. Calibration is achieved by comparison with near-surface wind measurements. The scatterometer does not give information about the waves, except for the direction of the wind waves. However, its estimates of wind velocity and hence estimates of wind stress on the sea surface are proving to be useful inputs to wave models, particularly in the Southern Ocean where few conventional measurements are made.

7.3.2.4 ***Microwave radiometers***

In addition to reflecting incident radio waves, the sea radiates thermal radio noise as a function of its temperature and emissivity. This radiation can be detected by a microwave radiometer (analogous to an astronomer's radio telescope). The emissivity varies with surface roughness, amount of foam and, to a small extent, salinity. Thus, the signal received at the antenna is mainly a combination of sea-surface temperature and wind effects, modified by atmospheric absorption and emission due to water vapour and cloud liquid water. As the sensitivity to each of these parameters is frequency dependent, a multichannel radiometer can be used to separate them.

The sea-surface temperature data complement infrared values in that they can be obtained through cloud, though with less accuracy and poorer spatial resolution. Wind speed can be derived over a broader swath than from the present satellite scatterometers, but no estimate of wind direction is obtained.

7.3.2.5 ***Emerging technologies***

Space agencies continue to expend considerable effort to improve the estimation of wave height and wave spectra from satellite remote sensing, to address the existing deficiencies and uncertainties.

Cavaleri et al. (2018) described recent developments in altimeter measurements that are important near the coast. The SARAL/AltiKa altimeter uses the K_a band, which has a wavelength of 0.8 cm compared with the 2.5 cm K_u-band wavelength used by conventional altimeters. This reduces the altimeter ground footprint by a factor of 4, which allows a higher repetition rate of 40 Hz rather than 20 Hz used by conventional K_u-band altimeters, enabling SARAL/AltiKa to measure closer to the coast.

Another development is the implementation of delay Doppler shift (also called SAR altimetry) to achieve ground footprints that are still a few kilometres wide across the track (as for conventional altimeters) but only about 300 m "long" along the track. This was first used for CryoSat and followed by Sentinel-3 SRAL (SAR and Radar Altimeter). This is expected to be the future trend. All future Sentinel-3 satellites (B, C, D and so on) and Jason-CS will carry a similar instrument.

Hauser et al. (2017) noted that as a result of SAR limitations, there are some sea-state conditions where little or no spectral wave information is available. They described a new real-aperture wave scatterometer operated at near-nadir incidence angles, dedicated to the measurement of directional spectra of ocean waves, without the limitations of SAR imaging mechanisms. This Surface Waves Investigation and Monitoring (SWIM) instrument will be on board the China France Oceanography Satellite, which was launched in 2018, and is expected to produce significant wave height and two-dimensional wave spectra at a scale of 70 km by 90 km, with wavelengths detected from 70 to 500 m.

A new instrument presently in development, the sea Surface Kinematics Multiscale Monitoring instrument, illustrates the directions satellite remote sensing will take over the next decade. This mission will use a near-nadir K_a-band Doppler radar to measure surface currents, ice drift and ocean waves at spatial scales of 40 km and more. This will reveal features on the tropical ocean and marginal ice zone dynamics that are inaccessible to other measurement systems, as well as provide global monitoring of the ocean mesoscale that surpasses the capability of today's nadir altimeters, with more accurate wave spectra than SWIM (Ardhuin et al., 2018).

7.3.3 Surface-based remote sensing

7.3.3.1 *Oblique platform-mounted sensors*

An interesting sensor for measurements at fixed sites, using the phenomena shown in Figure 7.4 to measure wave characteristics, is the Norwegian MIROS microwave wave radar (Grønlie et al., 1984). This uses an oblique 6 GHz (5 cm wavelength) beam and a radar range resolution of 7.5 m. The velocity of ripples is small compared with that of the long wavelength of interest, so that the radial velocity measured by the radar Doppler shift is dominantly due to the orbital motion of the long waves. The spectrum of the waves travelling along the radar beam is deduced by analysis of the fluctuation of the observed Doppler shift. Directional wave spectrum measurements are achieved by making measurements in six different directions (using a steerable beam) for a claimed wave-height range of 0.1–40 m and a period of 3–90 s.

Marine radars have recently been used successfully in acquiring sea-surface information to retrieve the wave spectrum in terms of their three dimensions: wave vector components and frequency. The measurements are based on the backscatter of microwaves from the ocean surface, which is visible as "sea clutter" on the radar screen (Borge et al., 1999). From this observable sea clutter, a numerical analysis is carried out; then, the unambiguous directional wave spectrum, the surface currents and sea-state parameters (such as wave periods, wavelengths and wave directions) can be derived.

7.3.3.2 *Ground-wave and sky-wave high-frequency radars*

High-frequency radar (employing the high-frequency band 3–30 MHz, wavelength 100–10 m), is of value because it is capable of measuring wave parameters from a ground station to ranges far beyond the horizon, utilizing the Doppler spectrum of the sea echo (Shearman, 1983; Gower and Barrick, 1986; Wyatt and Holden, 1994).

Ground-wave radars use vertically polarized radio waves in the high-frequency band and must be located on a sea coast, island, platform or ship. Coverage of 0–200 km in range is achievable. The potential for continuous sea-state monitoring is shown in Figure 7.9. Two stations some distance apart can triangulate on particular sea areas and can yield maps of directional spectra with a 1 h update.

Much recent effort has been devoted to improving retrieval of swell information from high-frequency radar data. Data coverage of effective Doppler spectra considered for swell frequency estimates showed the influence of islands and shallow-water effects (Wang et al., 2014*b*), in a 1 year high-frequency radar dataset collected in Brittany, France. In some other

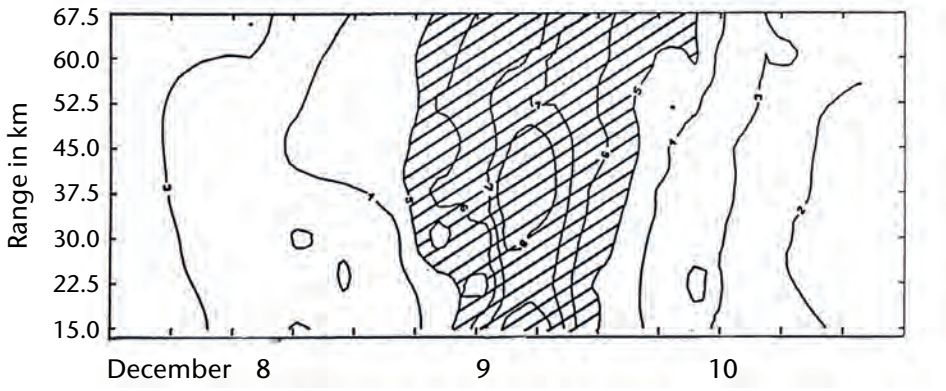

Figure 7.9. Time history of significant wave height versus range, as measured by high-frequency ground-wave radar

Source: Wyatt et al. (1985)

cases, fetch-limited wave growth has been analysed using high-frequency radar data in the Gulf of Tehuantepec, Mexico (Toro et al., 2014). These results suggested that the linear parametric model used was able to reproduce fetch-limited wave growth as reported elsewhere.

Wyatt et al. (2011) gave a review of existing work to understand high and low sea-state limitations, at high and low high-frequency radio frequencies, on wave measurement. The study extended these to measurements obtained over mid-range radio frequencies, using two different radar systems (WERA and Pisces), and different radio-frequency ranges, and demonstrated the wave-measurement capability of high-frequency radar.

Sky-wave radars are large installations, but can be located well back from the sea coast as they employ radio waves travelling through the ionosphere. Coverage extends from 900 to 3 000 km. Surface wind direction measurement is readily achieved, but ionospheric variability limits wave-height measurement (Gower and Barrick, 1986).

7.4 MODELLED DATA

A variety of modelled global and regional wave databases are now available, produced from high-quality surface marine winds fields input to increasingly sophisticated spectral wave models. The following sections briefly describe the wave hindcast process and resulting datasets, the two primary global wave reanalysis efforts (ECMWF through Copernicus, and NOAA/ National Centers for Environmental Prediction (NCEP) Climate Forecast System Reanalysis (CFSR)) and the use of archived operational wave-model products. While modelled data are not direct observations or measurements of waves or some related ocean-surface property, hindcast/ reanalysis data are useful for model testing and evaluation, and also as a cross-check on in situ wave measurements. They are particularly valuable for wave drifters and satellite wave data, including directional spectra.

7.4.1 Hindcasting

Hindcasts are playing an increasing role in marine climatology. Most recent wave climatologies, especially regional climatologies, are based on hindcast data. The same applies to design criteria produced by offshore oil and gas exploration and production companies, and the regulatory authorities in many countries around the world. The reason is simple: the costs involved in implementing a measuring programme, especially on a regional basis, and the period spent waiting for a reasonable amount of data to be collected, are unacceptable.

Therefore, given the demonstrated ability of the present generation of spectral ocean wave models, the timeliness and relatively lower cost of hindcast data become attractive. Hindcast data represent a long-term, uniform distribution in space and time of wind and wave information. The time spacing is typically 3 or 6 h, although many hindcasts produce hourly data. The database is then suitable for all manner of statistical analysis. If the period of the hindcast is sufficiently long, the database can also be used for extremal analysis to long-return periods.

There has been a proliferation of global and regional wave hindcasts covering most of the world's ocean basins in recent years (for example, Cox and Swail, 2001; Swail et al., 2007; Reistad et al., 2011; Durrant et al., 2013). Most of these have been based directly on objective numerical weather prediction wind fields. The North Atlantic wave hindcast produced for Environment Canada (Swail and Cox, 2000; Cox et al., 2011) augments that with manual kinematic analysis of surface wind fields based on ship, buoy and satellite wind data and meteorologist expertise, which improves the characterization of extreme wave conditions (Caires et al., 2004).
The International Workshop on Wave Hindcasting and Forecasting Series documents the development and evaluation of many of these hindcasts. Additional information, including future wave climate projections, is available through the JCOMM Coordinated Wave Climate Project (Hemer et al., 2012).

The *Guide to the Applications of Marine Climatology* (WMO, 1994) gives a detailed description of the hindcast process and its use in wave climatology.

7.4.2 **Reanalysis**

Global wave reanalysis databases provide valuable information for wave climate research and ocean applications. Distinction from reanalyses from hindcasts is necessary. While both are produced by running a wave model with appropriate wind forcing, the reanalyses are major integrated efforts incorporating full atmosphere/ocean/cryosphere model efforts assimilating all available historical surface and satellite data in a frozen model configuration (Kalnay et al., 1996; Uppala et al., 2005). Hindcasts typically use the wind field and ice cover, although many use the reanalysis wind fields as part of the process.

There have been few efforts to carry out a global reanalysis due to the enormous effort involved. The two most widely used are that of ECMWF and that of NOAA/NCEP. A brief description of both is given below.

7.4.2.1 ***European Centre for Medium-Range Weather Forecast ERA5 reanalysis***

Climate reanalysis ERA5 gives a numerical description of the recent climate, produced by combining models with observations. It contains estimates of atmospheric parameters such as air temperature, pressure and wind at different altitudes, and surface parameters such as rainfall, soil moisture content, sea-surface temperature and wave height.

ERA5 is the fifth generation of ECMWF atmospheric reanalyses of the global climate. ECMWF climate reanalyses started with the first Global Atmospheric Research Programme global experiment reanalyses produced in the 1980s, followed by ERA-15, ERA-40 and most recently ERA-Interim. ERA5 will eventually replace the ERA-Interim reanalysis.

ERA5 is the first reanalysis produced as an operational service and provides data at a considerably higher spatial and temporal resolution than its predecessor ERA-Interim. Hourly analysis fields are available at a horizontal resolution of 31 km, and on 137 levels from the surface up to 0.01 hPa (around 80 km). In addition, information on uncertainties is provided for each parameter at 3 h intervals and at a horizontal resolution of 62 km. A database containing all input observations, together with detailed information about how they are used, is available and accessible to users.

All ERA5 data are stored in the ECMWF main repository of meteorological data, the Meteorological Archival and Retrieval System. ERA5 is available via the Copernicus Climate Change Service (C3S) Climate Data Store, funded by the European Union.

7.4.2.2 *National Oceanic and Atmospheric Administration/National Centers for Environmental Prediction Climate Forecast System Reanalysis*

A 31 year wave hindcast (1979–2009) using the NCEP latest high-resolution CFSR wind and ice database has been generated using the third-generation wind-wave model WAVEWATCH IIIwith a mosaic of 16 two-way nested grids. The resolution of the grids ranged from 1/2° to 1/15°. Phase 1 was completed in 2012, using the operational WAVEWATCH III v3.14 and the physics package ST2, and the CFSR high-resolution winds and ice fields. Phase 2, completed in 2016, used WAVEWATCH III v5.08 and physics package ST4. Empirical fits between percentiles of altimeter derived and CFSR wind speeds along latitude bands were used to correct the CFSR winds, to remove the Southern Ocean bias in the strongest wind speeds.

In general, the database is good at representing the wave climate, although it sometimes underestimates the most extreme events (for example, Cox et al., 2011; Chawla et al., 2013). There is excellent agreement between model and data out to the 99.9th percentile at most buoys. The agreement at coastal buoys is not as good as the offshore buoys due to unresolved coastal features (topographic/bathymetric) and issues related to interpolating wind fields at the land–sea margins. There are some concerns about the wave climate in the southern hemisphere due to the overprediction of winds (early part of the database) and the lack of wave blocking due to icebergs in the model.

7.4.3 Operational modelling

One approach that is sometimes adopted to minimize the costs associated with hindcasts or reanalyses is to archive the analysis portion of operational wave analysis and forecast programmes. This is a cost-effective means of producing a continuous database, as it is a by-product of an existing operational programme. The disadvantages are that the operational time constraints mean that not all available data are included in the analysis, that time-consuming techniques such as kinematic analysis cannot be performed, that the use of backward and forward continuity in the development of weather patterns is not possible, and that it will take *N* years of operation to produce an *N* year database.

There is also a danger that such archives may introduce inhomogeneities due to changes in the characteristics of the models used. Nevertheless, this approach represents a viable way to develop a continuous database of wave information, albeit of lesser quality.

For the determination of long-return period estimates of waves, Breivik et al. (2013) explored the aggregation of large amounts of virtually uncorrelated ensemble forecasts to estimate 100 year return values of wave height, using the daily ensemble forecasts of the ECMWF Integrated Forecast System. They found that the estimates matched observed upper percentiles well in the Norwegian Sea. The results were also found to agree well with estimates based on the high-resolution hindcast NORA10 (Reistad et al., 2011).

ANNEX 1. WAVE NOMOGRAMS

The first two nomograms in this annex are designed to calculate wind-driven wave heights in deep water. The Gröen and Dorrestein (1976) nomogram was upgraded to one based on the Breugem and Holthuisjen (2007) version, which was based on a more extensive and current dataset. The rest of the nomograms were developed to estimate swell decay, mainly after the waves have moved away from their generation zone.

The second set of nomograms use a different approach, and account for the energy propagation within frequency bands. These are the Pierson–Neumann–James wave growth curves. They are more useful for swell, where the spectral distribution of the waves change, with longer period waves moving out ahead and shorter period waves lagging behind, with a resultant spread of energy over space and time. These nomograms roughly account for this.

The last two nomograms, developed by Bretschneider (1952), also account for swell decay. They are simpler than the Pierson–Neumann–James curves, and do not explicitly account for the change in spectral distribution.

1. BREUGEM AND HOLTHUISJEN (2007) WAVE GROWTH NOMOGRAM

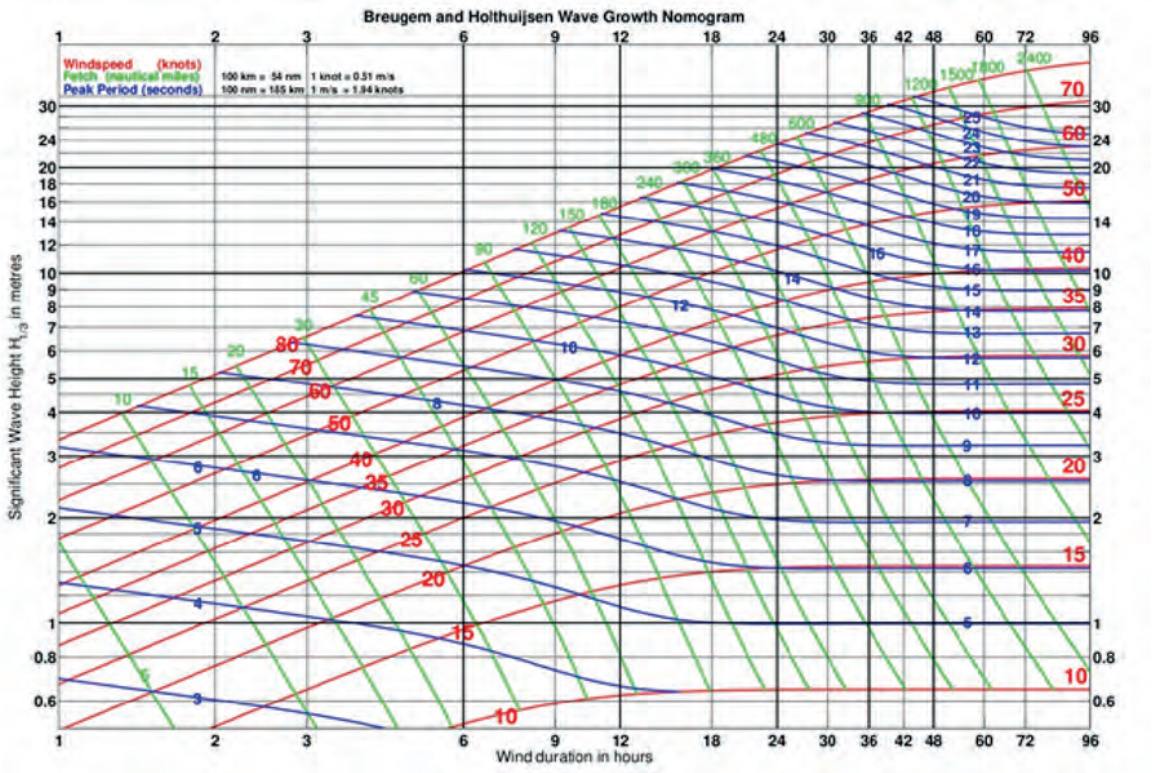

Figure 1. Manual wave growth nomogram

Source: Breugem and Holthuijsen (2007)

2. GRÖEN AND DORRESTEIN (1976) WAVE GROWTH NOMOGRAM

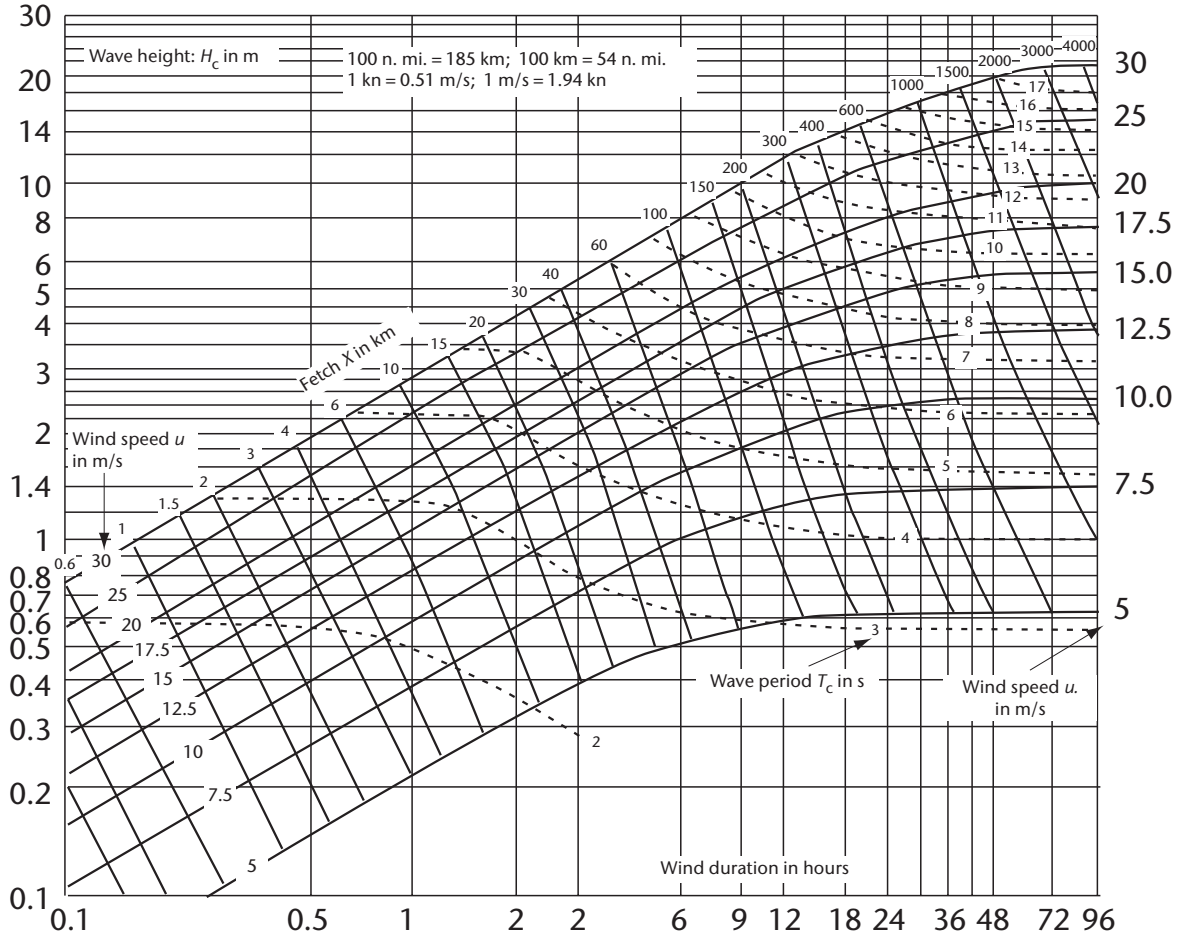

Figure 2. Manual wave forecasting diagram (kn = knots; n. mi. = nautical miles)

Source: Gröen and Dorrestein (1976)

3. PIERSON–NEUMANN–JAMES (1955) WAVE GROWTH CURVES

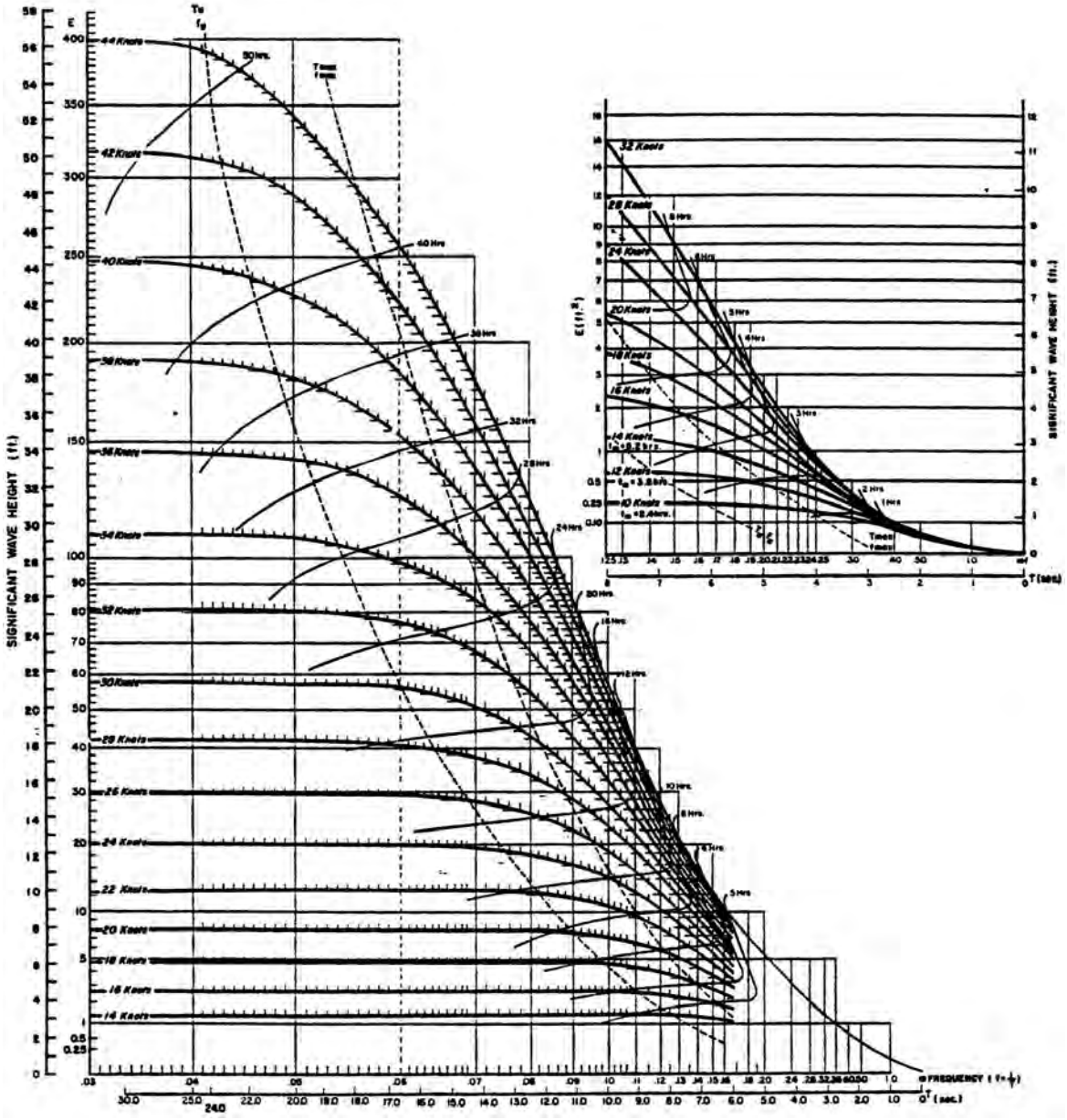

Figure 3. Duration graph: distorted co-cumulative spectra for wind speeds from 10 to 44 knots versus duration

Source: Pierson et al. (1955)

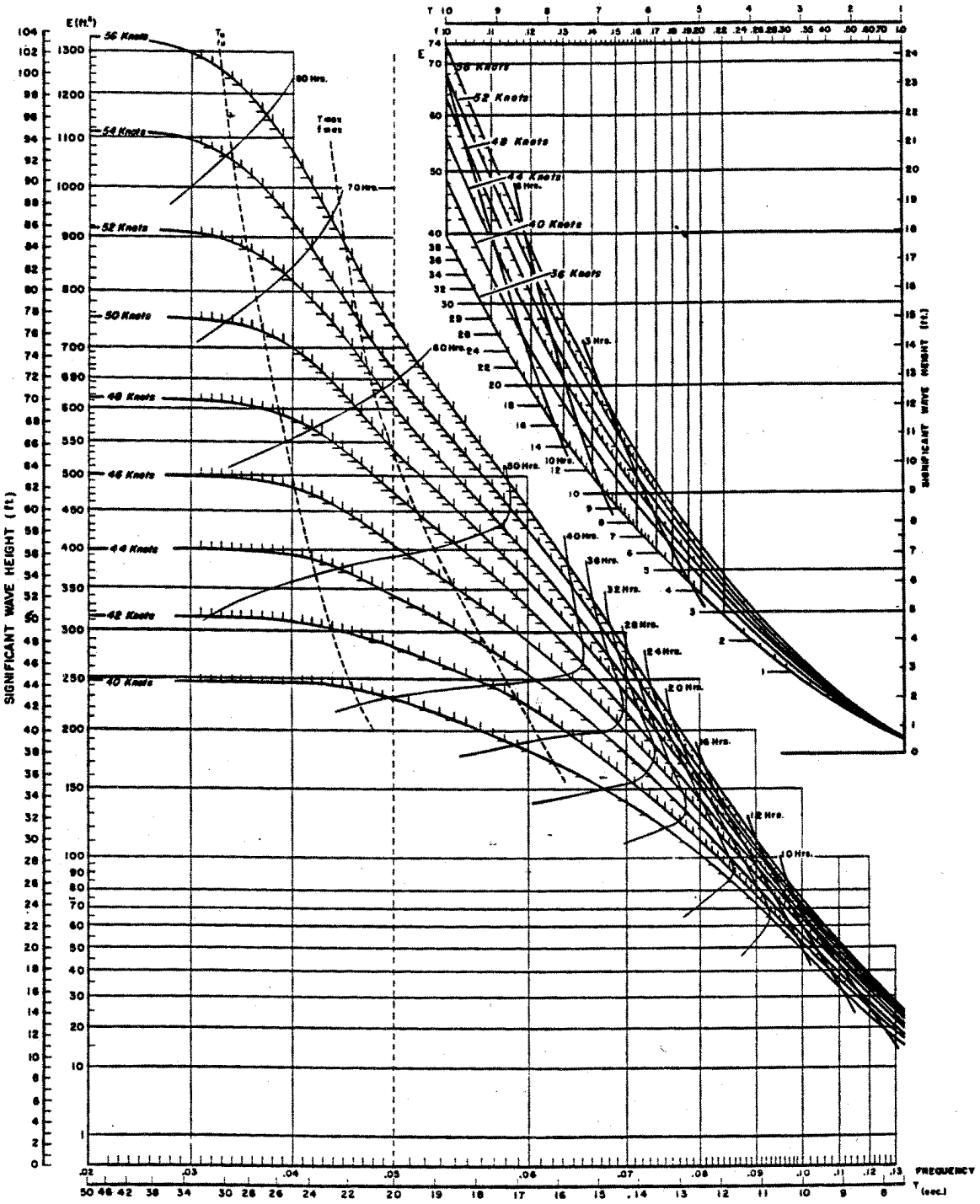

Figure 4. Duration graph: distorted co-cumulative spectra for wind speeds of 36 to 56 knots versus duration

Source: Pierson et al. (1955)

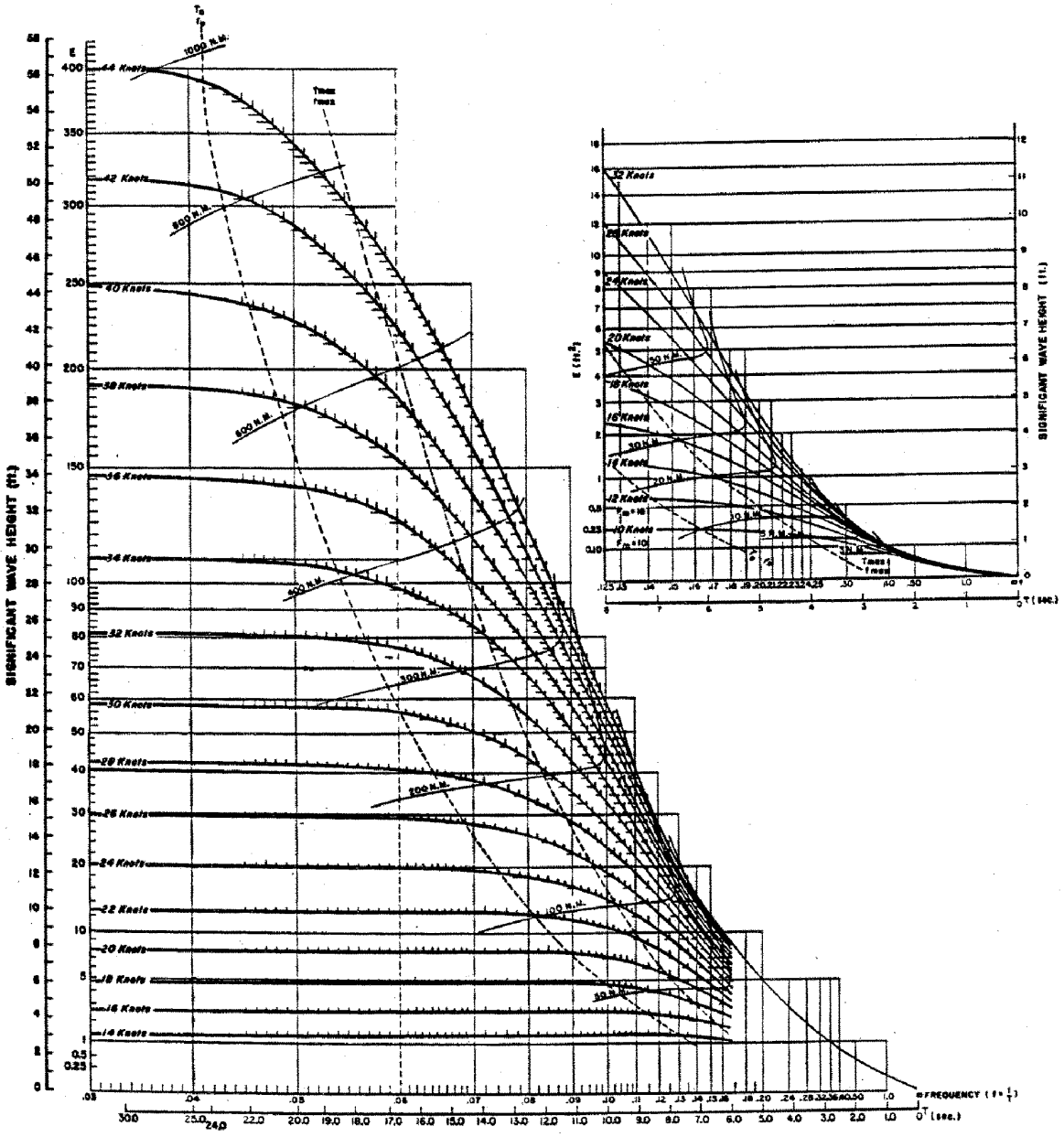

Figure 5. Fetch graph: distorted co-cumulative spectra for wind speeds of 10 to 44 knots versus fetch

Source: Pierson et al. (1955)

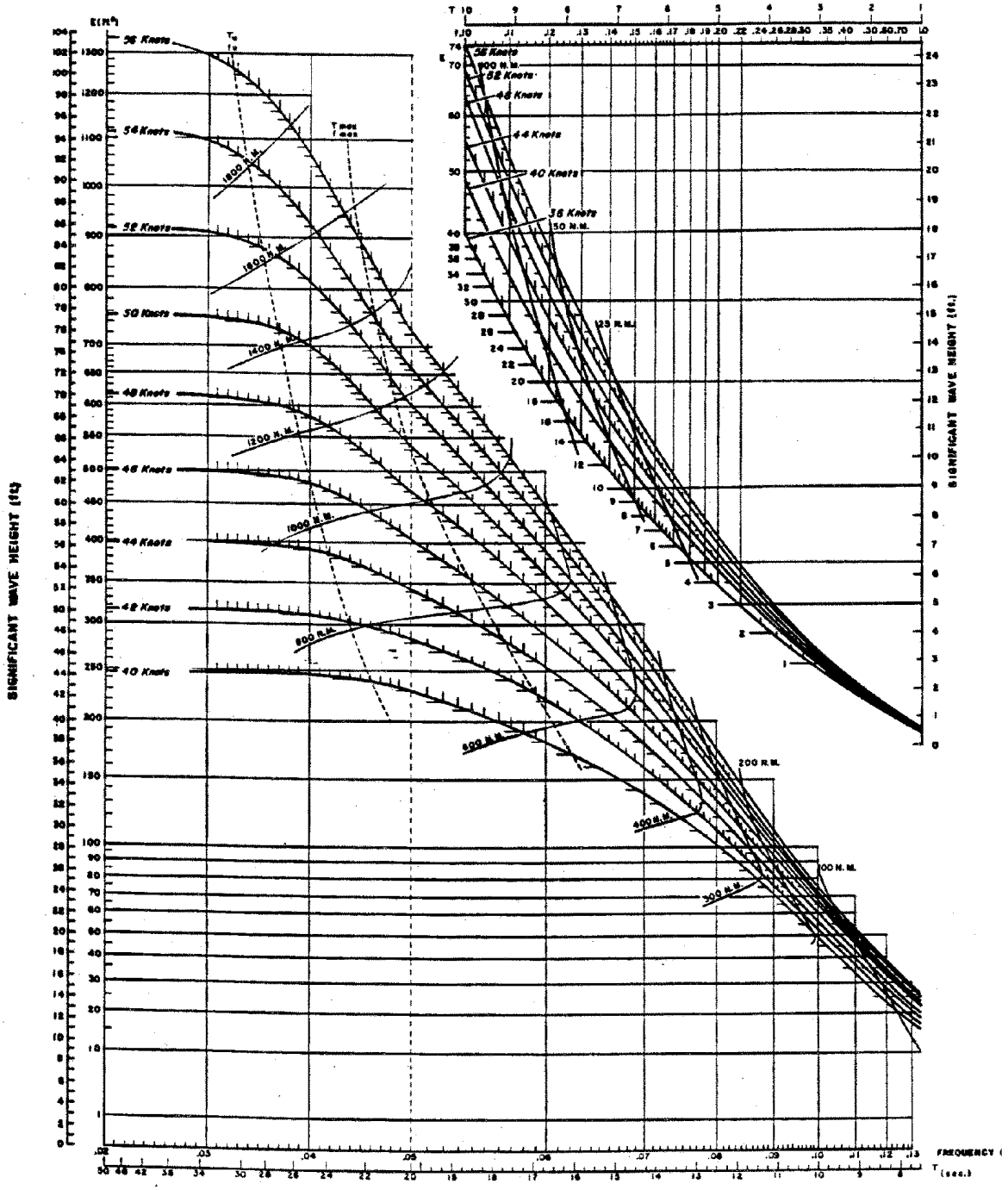

Figure 6. Fetch graph: distorted co-cumulative spectra for wind speeds of 36 to 56 knots versus fetch

Source: Pierson et al. (1955)

4. BRETSCHNEIDER (1952) SWELL DECAY NOMOGRAMS

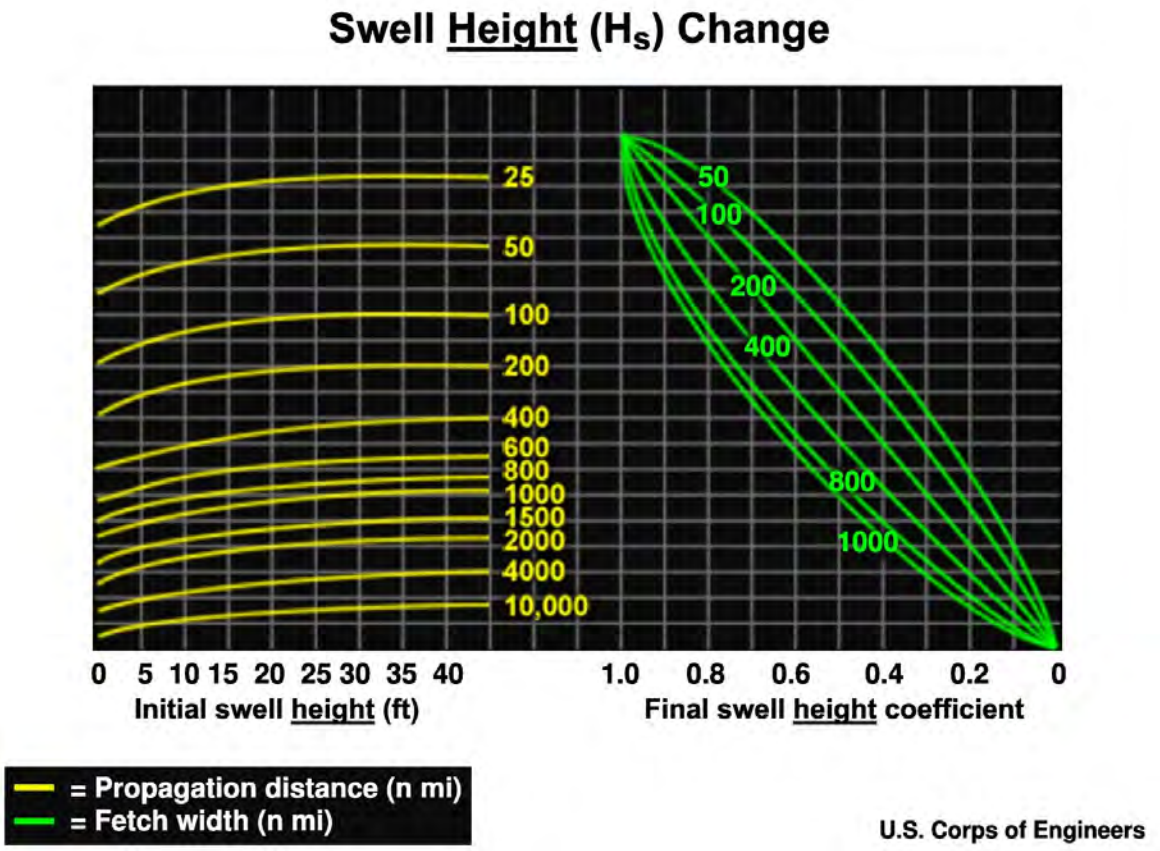

Figure 7. Bretschneider swell height decay nomogram. To calculate: choose the initial swell height (in feet) on the left horizontal axis, move vertically up to the propagation distance line in yellow (in nautical miles (n mi)), then horizontally across to the correct fetch width line in green (really defined as fetch length, in n mi), then vertically down to the swell height coefficient. Multiply the initial swell height by this coefficient.

Sources: Bretschneider (1952), CERC (1977) and COMET (2011)

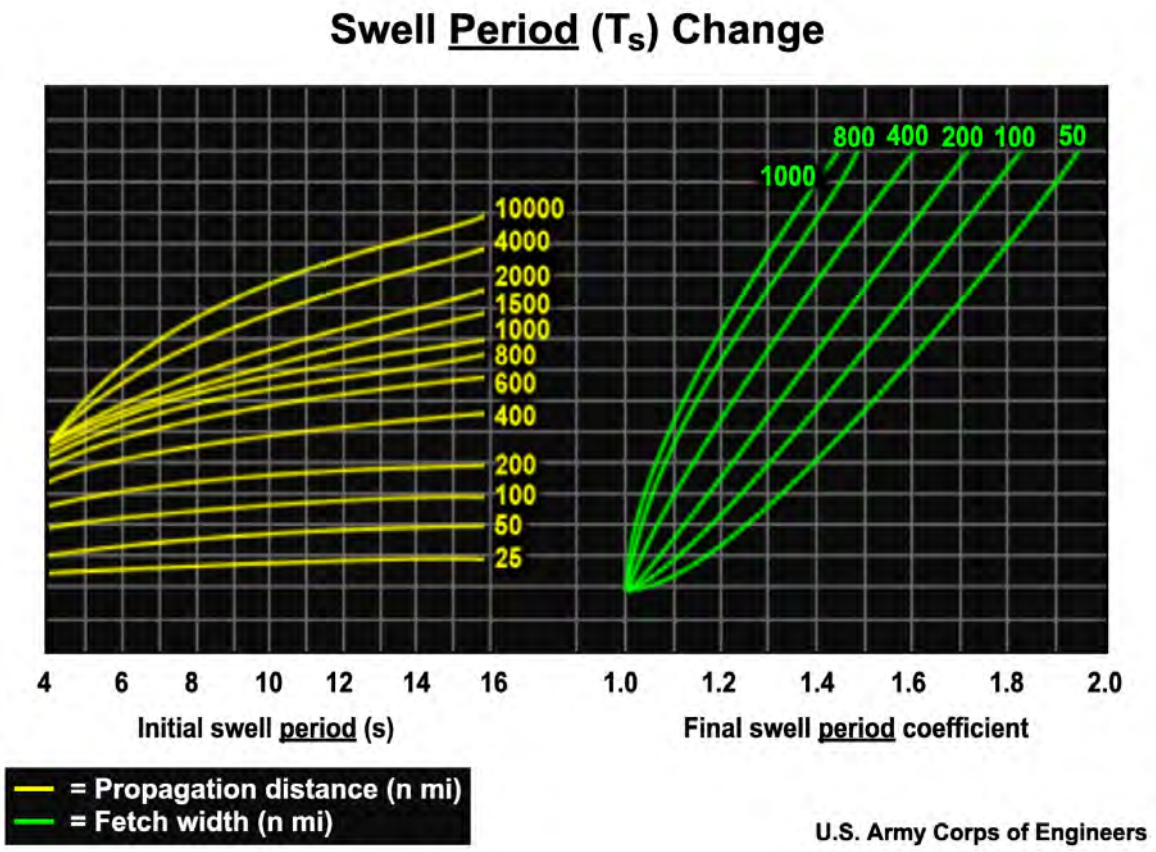

Figure 8. Bretschneider swell period decay nomogram. To calculate: choose the initial swell period (in s) on the left horizontal axis, move vertically up to the correct propagation distance line in yellow (in n mi), then horizontally across to the correct fetch width line in green (really defined as fetch length, in n mi), then vertically down to the swell period coefficient. Multiply the initial swell period by this coefficient.

Sources: Bretschneider (1952), CERC (1977) and COMET (2011)

ANNEX 2. WAVE FORECASTING: BASICS AND TIPS

This annex is designed to give the operational forecaster some basic rules for manual forecasting and a reality check for interpreting and understanding numerical model forecasts.

One of the most common sources of error for wave models is wind forcing. If a forecaster can identify systematic discrepancies between model results and observations, then using these rules and checking with nomograms can help the forecaster adjust and improve the forecast in a physically consistent way.

1. SPEED AND MOTION OF WAVE GROUPS

(a) Wave group speed (in knots) = 1.5 × peak period (in seconds).
(b) Twelve-hour movement (in degrees of latitude) = 0.3 × peak period (in seconds).
(c) Average the peak period when calculating wind-wave movement. For example, a wave grows during 12 h, going from an 8 s wave to a 10 s wave, and the group speed increases as the period increases. So, use 9 s multiplied by 0.3 to get a movement of 2.7° of latitude.
(d) Do not average the peak period for swell movement. Swell increases in peak period, and so the swell group speed increases with time. However, most swell nomograms take this into account and use the average period for time/distance calculations.

2. WAVE-HEIGHT GROWTH

(a) Wave energy is proportional to the square of the wave height, which is proportional (at least) to the square of the wind speed. So, accurate wind forecasts are essential.

(b) Fully developed seas (large fetch and duration): $H_S = (V / 12.5)^2$, where H_S is significant wave height and V is wind speed in knots.

(c) For the basic method, enter the wave growth nomogram with wind speed, fetch and duration to retrieve the significant wave height and period. For example, over 24 h with a fetch of 400 nautical miles, a 40 knot wind will generate a significant wave height of 8.2 m, and the wave height will be duration limited.

3. SWELL HEIGHT DECAY

(a) Swell height decays by:
  (i) About 25% in 12 h;
  (ii) About 40% in 24 h;
  (iii) About 50% in 36 h.
(b) Swell heights are not affected by opposing winds.
(c) On the swell nomogram, enter swell peak period and either decay distance or decay time, and retrieve the new period and also the ratio of final swell height to initial swell height. For example, in 46 h, a 5 m swell with a 10 s period moves 750 nautical miles and decays to a height of 2.2 m and a period of 11.6 s.

4. COMBINED WAVE HEIGHTS

Sum the squares of the wave components, then take the square root:

$$H_{\text{combined}} = \sqrt{H_{\text{wind}}^2 + H_{\text{swell1}}^2 + H_{\text{swell2}}^2 + H_{\text{swell}n}^2},$$

where H_{combined} is the total wave height, H_{wind} is the wave height component for wind waves and H_{swell} are swell components.

5. WIND VARIATIONS

(a) For a gradually strengthening wind: go 75% from the lowest towards the highest wind. For example, for a 20 knot wind increasing to 40 knots, use 35 knots on the nomogram.
(b) For a slackening wind: when winds drop below the speed needed to maintain the existing waves, treat the original waves as swell, and generate new wind waves with the lower wind. Then determine the combined wave height from the square root of the sum of squares.
(c) For gusty winds: average the sustained wind and the gust. So, for a 20 knot wind gusting to 30 knots, use 25 knots on the nomogram.
(d) For changing wind direction, if the direction change is:
    (i) Less than or equal to 30°, ignore it;
    (ii) Greater than 30°, treat the original wave field as swell moving off in the original direction, and develop new seas in the new direction with the new wind.

6. COLD AIR VERSUS WARM AIR WITH THE SAME WIND SPEED

Cold air builds larger seas than warm air of the same wind strength, assuming the same air pressure. Also, unstable wind profiles in the lower boundary layer generate higher waves, and stable lower boundary-layer profiles reduce the wave forcing.

7. WAVES ON CURRENTS

(a) For waves that become higher and steeper with an opposing current, and lower and flatter with a following current, the size of these effects depends on the current speed, the wave period and the wave steepness. For example, a 4 m wave with a 7 s period will diminish to 3.5 m with a following current of 3 knots, but with an opposing current of 3 knots, it will grow to a breaking wave of almost 5 m.
(b) A stable deep-water wave moving on a following current will not break.

REFERENCES

Abdalla, S. and L. Cavaleri, 2002: Effect of wind wave variability and variable air density on wave modelling. *Journal of Geophysical Research (Oceans)*, 107:17-1–17-17, doi:10.1029/2000JC000639.

Abdalla, S., J.-R. Bidlot and P. Janssen, 2006: *Global Validation and Assimilation of ENVISAT ASAR Wave Mode Spectra*. Paper presented at 2006 SEASAR Workshop, European Space Agency, Frascati, Italy.

Abdalla, S., P.A.E.M. Janssen and J.-R. Bidlot, 2010: Jason-2 OGDR wind and wave products: monitoring, validation and assimilation. *Marine Geodesy*, 33(1):239–255, doi:10.1080/01490419.2010.487798.

Ailliot, P., C. Maisondieu and V. Monbet, 2013: Dynamical partitioning of directional ocean wave spectra. *Probabilistic Engineering Mechanics*, 33:95–102, doi:10.1016/j.probengmech.2013.03.002.

Air Weather Service, 1995: *Forecasters Guide to Tropical Meteorology*. Air Weather Service Report TR 240, Illinois, updated by Colin S. Ramage.

Allender, J., T. Audunson, S.F. Barstow, S. Bjerken, H.E. Krogstad, P. Steinbakke, L. Vartdal, L. Borgman and C. Graham, 1989: The WADIC Project: a comprehensive field evaluation of directional wave instrumentation. *Ocean Engineering*, 161:505–536, doi:10.1016/0029-8018(89)90050-4.

Alves, J.H.G.M. and M.L. Banner, 2003: Performance of a saturation-based dissipation-rate source term in modelling the fetch limited evolution of wind waves. *Journal of Physical Oceanography*, 33:1274–1298, doi:10.1175/1520-0485(2003)033<1274:POASDS>2.0.CO;2.

Alves, J.-H.G.M., P. Wittmann, M. Sestak, J. Schauer, S. Stripling, N.B. Bernier, J. Mclean, Y. Chao, A. Chawla, H. Tolman, G. Nelson and S. Klotz, 2013: The NCEP–FNMOC combined wave ensemble product: expanding benefits of inter-agency probabilistic forecasts to the oceanic environment. *Bulletin of the American Meteorological Society*, December 2013:1893–1905, doi:10.1175/BAMS-D-12-00032.1.

Ardhuin, F., Y. Aksenov, A. Benetazzo, L. Bertino, P. Brandt, E. Caubet, B. Chapron, F. Collard, S. Cravatte, J.-M. Delouis, F. Dias, G. Dibarboure, L. Gaultier, J. Johannessen, A. Korosov, G. Manucharyan, D. Menemenlis, M. Menendez, G. Monnier, A. Mouche, F. Nouguier, G. Nurser, P. Rampal, A. Reniers, E. Rodriguez, J. Stopa, C. Tison, C. Ubelmann, E. van Sebille and J. Xie, 2018: Measuring currents, ice drift, and waves from space: the Sea surface KInematics Multiscale monitoring (SKIM) concept. *Ocean Science*, 14:337–354, doi:10.5194/os-14-337-2018.

Ardhuin, F., B. Chapron and F. Collard, 2009: Observation of swell dissipation across oceans. *Geophysical Research Letters*, 36:L06607, doi:10.1029/2008GL037030.

Ardhuin, F., T.H. Herbers, P.F. Jessen and W.C. O'Reilly, 2003*a*: Swell transformation across the continental shelf. Part II: Validation of a spectral energy balance equation. *Journal of Physical Oceanography*, 33:1940–1953, doi:10.1175/1520-0485(2003)033<1940:STATCS>2.0.CO;2.

Ardhuin, F., W.C. O'Reilly, T.H. Herbers and P.F. Jessen, 2003*b*: Swell transformation across the continental shelf. Part I: Attenuation and directional broadening. *Journal of Physical Oceanography*, 33:1921–1939, doi:10.1175/1520-0485(2003)033<1921:STATCS>2.0.CO;2.

Ardhuin, F., E. Rogers, A.V. Babanin, J.-F. Filipot, R. Magne, A. Roland, A.V.D. Westhuysen, P. Queffeulou, J.-M. Lefèvre, L. Aouf and F. Collard, 2010: Semiempirical dissipation source functions for ocean waves. Part 1: Definition, calibration and validation. *Journal of Physical Oceanography*, 40:1917–1941, doi:10.1175/2010JPO4324.1.

Austin, M.J., T.M. Scott, P.E. Russell and G. Masselink, 2013: Rip current prediction: development, validation, and evaluation of an operational tool. *Journal of Coastal Research*, 29(2):283–300, doi:10.2112/JCOASTRES-D-12-00093.1.

Babanin, A., 2011: *Breaking and Dissipation of Ocean Surface Waves*. Cambridge University Press.

Babanin, A.V., K.N. Tsagareli, I.R. Young and D.J. Walker, 2010: Numerical investigation of spectral evolution of wind waves, Part II: Dissipation term and evolution tests. *Journal of Physical Oceanography*, 40:667–683, doi:10.1175/2009JPO4370.1.

Banner, M.L., I.S.F. Jones and J.C. Trinder, 1989: Wavenumber spectra of short gravity waves. *Journal of Fluid Mechanics*, 198:321–344, doi:10.1017/S0022112089000157.

Barnett, T.P., 1968: On the generation, dissipation and prediction of ocean wind-waves. *Journal of Geophysical Research*, 73:513–529, doi:10.1029/JB073i002p00513.

Barratt, M.J., 1991: *Waves in the North East Atlantic*. United Kingdom of Great Britain and Northern Ireland Department of Energy Report OTI 90545. London, Her Majesty's Stationary Office.

Battjes, J.A. and J.P.F.M. Janssen, 1978: *Energy Loss and Set-up Due to Breaking in Random Waves*. Proceedings of 16th Coastal Engineering Conference, Hamburg, Germany, 569–587.

Beale, R.C., 1981: Spatial evolution of ocean wave spectra. In: *Spaceborne Synthetic Aperture Radar for Oceanography* (R. Beale, P. De Leonibus and E. Katz, eds.). Johns Hopkins Oceanographic Studies No. 7, Johns Hopkins University Press, 110–127.

Bendat, J.S. and A.G. Piersol, 1971: *Random Data: Analysis and Measurement Procedures*. New York, Wiley Interscience, doi:10.1088/0957-0233/11/12/702.

Bender, L.C., N.L. Guinasso and J.N. Walpert, 2010: A comparison of methods for determining significant wave heights—applied to a 3-m discus buoy during Hurricane Katrina. *Journal of Atmospheric and Oceanic Technology*, 27:1012–1028, doi:10.1175/2010JTECHO724.1.

Bender, L.C., N.L. Guinasso, J.N. Walpert and S.D. Howden, 2009: *A Comparison of Two Methods for Determining Wave Heights from a Discus Buoy with a Strapped-down Accelerometer*. Proceedings of 11th International Workshop on Wave Hindcasting and Forecasting, Halifax, Canada.

Benetazzo, A., F. Fedele, G. Gallego, P.C. Shih and A. Yezzi, 2012: Offshore stereo measurements of gravity waves. *Coastal Engineering*, 64:127–138, doi:10.1016/j.coastaleng.2012.01.007.

Bidlot, J.-R., 2001: *ECMWF Wave-model Products*. European Centre for Medium-Range Weather Forecasts Newsletter No. 91, Reading, United Kingdom of Great Britain and Northern Ireland, 9–15.

———, 2012: *Present Status of Wave Forecasting at ECMWF*. Proceedings of ECMWF Workshop on Ocean Waves, 25–27 June 2012.

Bidlot, J.-R., D.J. Holmes, P.A. Wittmann, R. Lalbeharry and H.S. Chen, 2002: Intercomparison of the performance of operational ocean wave forecasting systems with buoy data. *Weather Forecasting*, 17:287–310, doi:10.1175/1520-0434(2002)017<0287:IOTPOO>2.0.CO;2.

Bidlot, J.-R., P.A.E.M. Janssen and S. Abdalla, 2005: *On the Importance of Spectral Wave Observations in the Continued Development of Global Wave Models*. Proceedings of 5th International Symposium on WAVES, 2005.

———, 2006: *Extreme Waves in the ECMWF Operational Wave Forecasting System*. Proceedings of 9th International Workshop on Wave Hindcasting and Forecasting, Victoria, B.C., Canada, 24–29 September 2006.

Bidlot, J.-R., J.-G. Li, P. Wittmann, M. Faucher, H. Chen, J.-M. Lefèvre, T. Bruns, D. Greenslade, F. Ardhuin, N. Kohno, S. Park and M. Gomez, 2007: *Inter-Comparison of Operational Wave Forecasting Systems*. Proceedings of 10th International Workshop on Wave Hindcasting and Forecasting and Coastal Hazard Symposium, North Shore, Oahu, Hawaii, 11–16 November 2007.

Bishop, C.T. and M.A. Donelan, 1987: Measuring waves with pressure transducers. *Coastal Engineering*, 11:309–328, doi:10.1016/0378-3839(87)90031-7.

Bitner-Gregersen, E.M. and A.K. Magnusson, 2014: Effect of intrinsic and sampling variability on wave parameters and wave statistics. *Ocean Dynamics*, 64(11):1643–1655, doi:10.1007/s10236-014-0768-8.

Bjerknes, J. and H. Solberg, 1922: Life cycles of cyclones and the polar front theory of atmospheric circulation. *Geofysiske Publikationer*, 3(1):18, doi:10.1002/qj.49704920609.

Blackman, R.B. and J.W. Tukey, 1959: *The Measurement of Power Spectra from the Point of View of Communications Engineering*. New York, Dover.

Booij, N., R.C. Ris and L.H. Holthuijsen, 1999: A third-generation wave model for coastal regions: 1. Model description and validation. *Journal of Geophysical Research (Oceans)*, 104(C4):7649–7666, doi:10.1029/98JC02622.

Borge, J.C.N., K. Reichert and J. Dittmer, 1999: Use of nautical radar as a wave monitoring instrument. *Coastal Engineering*, 37:331–342, doi:10.1016/S0378-3839(99)00032-0.

Bourassa, M.A., D.G. Vincent and W.L. Wood, 1999: A flux parameterization including the effects of capillary waves and sea state. *Journal of the Atmospheric Sciences*, 56:1123–1139, doi:10.1175/1520-0469(1999)056<1123:AFPITE>2.0.CO;2.

Bouws, E., H. Günther, W. Rosenthal and C.L. Vincent, 1985: Similarity of the wind-wave spectrum in finite depth water: 1. Spectral form. *Journal of Geophysical Research (Oceans)*, 90(C1):975–986, doi:10.1029/JC090iC01p00975.

Breivik, L.A. and M. Reistad, 1992*: Use of ERS-1 Altimeter Wave Products at DNMI. Evaluation of Wave Heights and Wind Speeds. Assimilation in a Numerical Wave Model*. Technical Report No. 101. Norwegian Meteorological Institute.

Breivik, Ø., O.J. Aarnes, J.-R. Bidlot, A. Carrasco and Ø. Saetra, 2013: Wave extremes in the Northeast Atlantic from ensemble forecasts. *Journal of Climate*, 26:7525–7540, doi:10.1175/JCLI-D-12-00738.1.

Bretschneider, C.L., 1952: *Revised Wave Forecasting Relationships*. Proceedings of 2nd Coastal Engineering Conference, 1–5.

Breugem, W.A. and L.H. Holthuijsen, 2007: Generalized shallow water wave growth from Lake George. *Journal of Waterway Port Coastal and Ocean Engineering*, 133(3), doi:10.1061/(ASCE)0733-950X(2007)133:3(173).

Brown, R.A. and W.T. Liu, 1982: An operational large-scale marine planetary boundary layer model. *Journal of Applied Meteorology*, 21, 261–269, doi:10.1175/1520-0450(1982)021<0261:AOLSMP>2.0.CO;2.

Bunney, C. and A. Saulter, 2015: An ensemble forecast system for prediction of Atlantic–UK wind waves. *Ocean Modelling*, 96(1):103–116, doi:10.1016/j.ocemod.2015.07.005.

Businger, J.A., J.C. Wyngaard, Y. Izumi and E.F. Bradley, 1971: Flux-profile measurements in the atmospheric surface layer. *Journal of Atmospheric Sciences*, 28:181–189, doi:10.1175/1520-0469(1971)028<0181:FPRITA>2.0.CO;2.

Caires, S., A. Sterl, J.-R. Bidlot, N. Graham and V. Swail, 2004: Intercomparison of different wind wave reanalyses. *Journal of Climate*, 17(10):1893–1913, doi:10.1175/1520-0442(2004)017<1893:IODWR>2.0.CO;2.

Capon, J., 1979: Maximum-likelihood spectral estimation. In: *Nonlinear Methods in Spectral Analysis* (S. Heykin, ed.), 155–179. Berlin, Heidelberg, New York, Springer, doi:10.1007/3-540-12386-5_12.

Cardone, V.J., 1969: *Specification of the Wind Distribution in the Marine Boundary Layer for Wave Forecasting*. Geophysical Sciences Laboratory Report TR-69-1, New York University.

———, 1978: *Specification and Prediction of the Vector Wind of the United States Continental Shelf for Application to an Oil Slick Trajectory Program*. Final report, Contract T-34530, City College of the City University of New York.

Carter, D.J.T., P.G. Challenor and M.A. Srokosz, 1992: An assessment of Geosat wave height and wind speed measurements. *Journal of Geophysical Research (Oceans)*, 97:11383–11392, doi:10.1029/92JC00465.

Cavaleri, L. and L. Bertotti, 2006: The improvement of modelled wind and wave fields with increasing resolution. *Tellus*, 33:553–565, doi:10.1016/j.oceaneng.2005.07.004.

Cavaleri, L. and P.M. Rizzoli, 1981: Wind wave prediction in shallow water: theory and applications. *Journal of Geophysical Research (Oceans)*, 86:10961–10973, doi:10.1029/JC086iC11p10961.

Cavaleri, L., S. Abdalla, A. Benetazzo, l. Bertotti, J.-R. Bidlot, Ø. Breivik, S. Carniel, R.E. Jensen, J. Portills-Yandun, W.E. Rogers, A. Roland, A. Sanchez-Arcilla, J.M. Smith, J. Staneva, Y. Toledo, G.P. van Vledder and A.J. van der Westhuysen, 2018: Wave modelling in coastal and inner seas. *Progress in Oceanography*, 167:14–233, doi:10.1016/j.pocean.2018.03.010.

Centurioni, L., L. Braasch, E. Di Lauro, P. Contestabile, F. De Leo, R. Casotti, L. Franco and D. Vicinanza, 2017: *A New Strategic Wave Measurement Station off Naples Port Main Breakwater*. Proceedings of 35th Conference on Coastal Engineering, June 2017, doi:10.9753/icce.v35.waves.36.

Chalikov, D. and S. Rainchik, 2011: Coupled numerical modelling of wind and waves and theory of the wave boundary layer. *Boundary-Layer Meteorology* 138(1):1–41.

Chapron, B., H. Johnsen and R. Garello, 2001: Wave and wind retrieval from SAR images of the ocean. *Annales des Télécommunications*, 56(11–12):682–699, doi:10.1007/BF02995562.

Charney, J.G. and A. Eliassen, 1964: On the growth of the hurricane depression. *Journal of Atmospheric Sciences*, 21:68–75, doi:10.1175/1520-0469(1964)021<0068:OTGOTH>2.0.CO;2.

Charnock, H., 1955: Wind stress on a water surface. *Quarterly Journal of the Royal Meteorological Society*, 81:639, doi:10.1002/qj.49708135027.

Chawla, A. and J.T. Kirby, 2002: Monochromatic and random wave breaking at blocking points. *Journal of Geophysical Research (Oceans)*, 107(C7):4-1–4-19, doi:10.1029/2001JC001042.

Chawla, A. and H.L. Tolman, 2008: Obstruction grids for spectral wave models. *Ocean Modelling*, 22:12–25, doi:10.1016/j.ocemod.2008.01.003.

Chawla, A., D. Wilson-Diaz and H.L. Tolman, 2013: Validation of a thirty-year wave hindcast using the Climate Forecast System Reanalysis winds. *Ocean Modelling*, 70:189–206, doi:10.1016/j.ocemod.2012.07.005.

Chen, H.S., 2006: *Ensemble Prediction of Ocean Waves at NCEP*. Proceedings of 28th Ocean Engineering Conference, Taiwan.

Chen, S.S., W. Zhao, M.A. Donelan and H.L. Tolman, 2013: Directional wind–wave coupling in fully coupled atmosphere–wave–ocean models: results from CBLAST-Hurricane. *Journal of Atmospheric Sciences*, 70:3198–3215, doi:10.1175/JAS-D-12-0157.1.

Clarke, R.H. and G.D. Hess, 1974: Geostrophic departure and the functions A and B of Rossby-number similarity theory. *Boundary-Layer Meteorology*, 7:267–287, doi:10.1007/BF00240832.

Coastal Engineering Research Center (CERC), 1973: *Shore Protection Manual*. Waterways Experiment Station, United States Army Corps of Engineers.

———, 1977: *Shore Protection Manual*. Waterways Experiment Station, United States Army Corps of Engineers.

———, 1984: *Shore Protection Manual*. Waterways Experiment Station, United States Army Corps of Engineers.

Collins III, C.O., B. Lund, T. Waseda and H.C. Graber, 2014: On recording sea surface elevation with accelerometer buoys: lessons from ITOP (2010). *Ocean Dynamics*, 64(6):895–904, doi:10.1007/s10236-014-0732-7.

COMET, 2011: *Wave Life Cycle II: Propagation & Dispersion*, https://www.meted.ucar.edu/training_module.php?id=188#.XIJDK_Z2stF.

Cooley, J.W. and J.W. Tukey, 1965: An algorithm for the machine calculation of complex Fourier series. *Mathematics of Computation*, 19:297–301, doi:10.2307/2003354.

Courant, R., K. Friedrichs and H. Lewy, 1928: On the partial difference equations of mathematical physics. *IBM Journal of Research and Development*, 11(2):215–234, doi:10.1147/rd.112.0215.

Cox, A.T. and V.R. Swail, 2001: A global wave hindcast over the period 1958-1997: validation and climate assessment. *Journal of Geophysical Research (Oceans)*, 106(C2):2313–2329, doi:10.1029/2001JC000301.

Cox, A.T., V.J. Cardone and V.R. Swail, 2011: *On the Use of the Climate Forecast System Reanalysis Wind Forcing in Ocean Response Modelling*. Proceedings of 12th International Workshop on Wave Hindcasting and Forecasting and 3rd Coastal Hazards Symposium, Paper G3.

Crapper, G.D., 1984: *Introduction to Water Waves*. Ellis Harwood.

Dee, D.P., S.M. Uppala, A.J. Simmons, P. Berrisford, P. Poli, S. Kobayashi, U. Andrae, M.A. Balmaseda, G. Balsamo, P. Bauer, P. Bechtold, A.C.M. Beljaars, L. van de Berg, J.-R. Bidlot, N. Bormann, C. Delsol, R. Dragani, M. Fuentes, A.J. Geer, L. Haimberger, S.B. Healy, H. Hersbach, E.V. Hólm, L. Isaksen L, P. Kallberg, M. Köhler, M. Matricardi, A.P. McNally, B.M. Monge-Sanz, J.-J. Morcrette, B.-K. Park, C. Peubey, P. de Rosnay, C. Tavolato, J.-N. Thépaut and F. Vitart, 2011: The ERA-Interim reanalysis: configuration and performance of the data assimilation system. *Quarterly Journal of the Royal Meteorological Society*, 137:553–597, doi:10.1002/qj.828.

Delpey, M.T., F. Ardhuin, F. Collard and B. Chapron, 2010: Space-time structure of long ocean swells fields. *Journal of Geophysical Research (Oceans)*, 115 (C12037), doi:10.1029/2009JC005885.

Dobson, F.W., 1981: *Review of Reference Height for and Averaging Time of Surface Wind Measurements at Sea*. Marine Meteorology and Related Oceanographic Activities Report No. 3. Geneva, World Meteorological Organization.

Donelan, M., 1982: *The Dependence of the Aerodynamic Drag Coefficients on Wave Parameters*. Proceedings of the 1st International Conference on Meteorology and Air-sea Interaction of the Coastal Zone, The Hague, Netherlands, American Meteorological Society, 381–387.

———, 1990: Air-sea interaction from the sea. In: *Ocean Engineering Science*, Volume 9. John Wiley & Sons.

Donelan, M.A. and A.K. Magnusson, 2017: The making of the Andrea wave and other rogues. *Scientific Reports*, 7:44124, doi:10.1038/srep44124.

Donelan, M.A., A.V. Babanin, I.R. Young and M.L. Banner, 2006: Wave-follower field measurements of the wind-input spectral function. Part II: Parameterization of the wind input. *Journal of Physical Oceanography*, 36:1672–1689, doi:10.1175/JPO2933.1.

Donelan, M.A., A.V. Babanin, I.R. Young, M.L. Banner and C. McCormick, 2005: Wave-follower field measurements of the wind-input spectral function. Part I: Measurements and calibrations. *Journal of Atmospheric and Oceanic Technology*, 22:799–813, doi:10.1175/JTECH1725.1.

Donelan, M.A., W. Drennan and A.K. Magnusson, 1996: Nonstationary analysis of the directional properties of propagating waves. *Journal of Physical Oceanography*, 26(9):1901–1914, doi:10.1175/1520-0485(1996)026<1901:NAOTDP>2.0.CO;2.

Donelan, M.A., J. Hamilton and W.H. Hui, 1985: Directional spectra of wind generated waves. *Philosophical Transactions of the Royal Society of London. Series A, Mathematical and Physical Sciences*, 315:509–562, doi:10.1098/rsta.1985.0054.

Dorrestein, R., 1960: Simplified method of determining refraction coefficients for sea waves. *Journal of Geophysical Research*, 65:637–642, doi:10.1029/JZ065i002p00637.

Draper, L., 1963: Derivation of a 'design wave' from instrumental records of sea waves. *Proceedings of the Institute of Civil Engineers*, 26:291–304, doi:10.1680/iicep.1963.10442.

———, 1966: *The Analysis and Presentation of Wave Data – a Plea for Uniformity*. Proceedings of the 10th International Conference on Coastal Engineering, Tokyo.

Drennan, W.M., M.A. Donelan, E.A. Terray and K.B. Katsaros, 1996: Oceanic turbulence dissipation measurements in SWADE. *Journal of Physical Oceanography*, 26:808–815, doi:10.1175/1520-0485(1996)026<0808:OTDMIS>2.0.CO;2.

Drennan, W.M., G.C. Graber, D. Hauser and C. Quentin, 2003: On the wave age dependence of wind stress over pure wind seas. *Journal of Geophysical Research (Oceans)*, 108:8062, doi:10.1029/2000JC000715.

Durrant, T., D.J.M. Greenslade, M. Hemer and C. Trenham, 2013: *A 30-year Global Wave Hindcast Focused on the South Pacific*. Proceedings of the 13th International Workshop on Wave Hindcasting and Forecasting and 4th Coastal Hazards Symposium, Paper N1.

Durrant, T.H., D.J.M. Greenslade and I. Simmonds, 2009*a*: Validation of Jason-1 and Envisat remotely sensed wave heights. *Journal of Atmospheric and Oceanic Technology*, 26:123–134, doi:10.1175/2008JTECHO598.1.

Durrant, T.H., F. Woodcock and D.J.M. Greenslade, 2009*b*: Consensus forecasts of modeled wave parameters. *Weather and Forecasting*, 24:492–503, doi:10.1175/2008WAF2222143.1.

Dvorak, V.F., 1975: Tropical cyclone intensity analysis and forecasting from satellite imagery. *Monthly Weather Review*, 103:420–430, doi:10.1175/1520-0493(1975)103<0420:TCIAAF>2.0.CO;2.

———, 1984: *Tropical Cyclone Intensity Analysis using Satellite Data*. National Oceanic and Atmospheric Administration Technical Report NESDIS 11.

Ebert, E., 2001: Ability of a poor man's ensemble to predict the probability and distribution of precipitation. *Monthly Weather Review*, 129:2461–2480, doi:10.1175/1520-0493(2001)129<2461:AOAPMS>2.0.CO;2.

Edson, J.B., V. Jampana, R.A. Weller, S.P. Bigorre, A.J. Plueddemann, C.W. Fairall, S.D. Miller, L. Mahrt, D. Vickers and H. Hersbach, 2013: On the exchange of momentum over the open ocean. *Journal of Physical Oceanography*, 43:1589–1610, doi:10.1175/JPO-D-12-0173.1.

Ekman, V.W., 1905: On the influence of the earth's rotation on ocean currents. *Arkiv för Matematik, Astronomi och Fysik*, 2(11), http://jhir.library.jhu.edu/handle/1774.2/33989.

Eldeberky, Y., 1996: Nonlinear transformation of wave spectra in the nearshore zone. PhD Thesis, Department of Civil Engineering, Delft University of Technology, The Netherlands.

Eldeberky, Y. and J.A. Battjes, 1995: *Parametrization of Triad Interactions in Wave Energy Models*. Proceedings of the Coastal Dynamics Conference, Gdansk, Poland, 140–148.

Elgar, S. and R.T. Guza, 1985: Observation of bispectra of shoaling surface gravity waves. *Journal of Fluid Mechanics*, 161:425–448, doi:10.1017/S0022112085003007.

Engle, J., J. MacMahan, R.J. Thieke, D.M. Hanes and R.G. Dean, 2002: *Formulation of a Rip Current Predictive Index Using Rescue Data*. Proceedings of National Conference on Beach Preservation Technology, Florida Shore and Beach Preservation Association, Biloxi, Mississippi.

Ewans, K., G. Feld and P. Jonathan, 2014: On wave radar measurement. *Ocean Dynamics*, 64:1281–1303, doi:10.1007/s10236-014-0742-5.

Ewing, J.A., 1971: A numerical wave prediction model for the North Atlantic Ocean. *Deutsche Hydrogrgraphische Zeitschrift*, 24:241–261, doi:10.1007/BF02225707.

Fedele, F., A. Benetazzo, G. Gallego, P.C. Shih, A. Yezzi, F. Barbariol and F. Ardhuin, 2013: Space–time measurements of oceanic sea states. *Ocean Modelling*, 70:103–115, doi:10.1016/j.ocemod.2013.01.001.

Filipot, J.-F. and F. Ardhuin, 2012: A unified spectral parameterization for wave breaking: from the deep ocean to the surf zone. *Journal of Geophysical Research (Oceans)*, 117, doi:10.1029/2011JC007784.

Filipot, J.-F., F. Ardhuin and A.V. Babanin, 2010: A unified deep-to-shallow water wave-breaking probability parameterization. *Journal of Geophysical Research*, 115(C4), doi:10.1029/2009JC005448.

Forristall, G.Z., 1978: On the statistical distribution of wave heights in a storm. *Journal of Geophysical Research (Oceans)*, 83:2353–2358, doi:10.1029/JC083iC05p02353.

———, 2000: Wave crest distributions: observations and second order theory. *Journal of Physical Oceanography*, 30:1931–1943, doi:10.1175/1520-0485(2000)030<1931:WCDOAS>2.0.CO;2.

Freeman, E., S.D. Woodruff, S.J. Worley, S.J. Lubker, E.C. Kent, W.E. Angel, D.I. Berry, P. Brohan, R. Eastman, L. Gates, W. Gloeden, Z. Ji, J. Lawrimore, N.A. Rayner, G. Rosenhagen and S.R. Smith, 2017: ICOADS Release 3.0: a major update to the historical marine climate record. *International Journal of Climatology*, 37:2211–2237, doi:10.1002/joc.4775.

Freilich, M.H. and P.G. Challenor, 1994: A new approach for determining fully empirical altimeter wind speed model function. *Journal of Geophysical Research (Oceans)*, 99:25051–25062, doi:10.1029/94JC01996.

French, J.R., W.M. Drennan and J.A. Zhang, 2007: Turbulent fluxes in the hurricane boundary layer, Part I: Momentum flux. *Journal of Atmospheric Sciences*, 64:1089–1102, doi:10.1175/JAS3887.1.

Fujita, T., 1952: Pressure distribution within typhoon. *Geophysical Magazine*, 23(4):437–451.

Gagnaire-Renou, E., M. Benoit and P. Forget, 2010: Ocean wave spectrum properties as derived from quasi-exact computations of nonlinear wave-wave interactions. *Journal of Geophysical Research (Oceans)*, 115:C12058, doi:10.1029/2009JC005665.

Gallop, S.L., K.R. Bryan, G. Coco and S.A. Stephens, 2011: Storm-driven changes in rip channel patterns on an embayed beach. *Geomorphology*, 127:179–188, doi:10.1016/j.geomorph.2010.12.014.

Garratt, J.R., 1994: The atmospheric boundary layer. *Earth-Science Reviews*, 37:89–134, doi:10.1002/joc.3370140113.

Geernaert, G.L. and K.B. Katsaros, 1986: Incorporation of stratification effects on the oceanic roughness length in the derivation of the neutral drag coefficient. *Journal of Physical Oceanography*, 16:1580–1584, doi:10.1175/1520-0485(1986)016<1580:IOSEOT>2.0.CO;2.

Goda, Y., 1970: *Numerical Experiments on Wave Statistics with Spectral Simulation*. Report of the Port and Harbour Research Institute, Volume 9, No. 3, 1–57.

———, 1978: *The Observed Joint Distribution of Periods and Heights of Sea Waves*. Proceedings of the 16th Coastal Engineering Conference, Hamburg, Germany, 227–246, doi:10.1061/9780872621909.013.

Gower, J.F. and D.E. Barrick (eds.), 1986: Special issue on high-frequency radar for ocean and ice mapping and ship location. *IEEE Journal of Oceanic Engineering*, 11(2).

Graber, H.C., E.A. Terray, M.A. Donelan, W.M. Drennan, J.C.V. Leer and D.B. Peters, 2000: ASIS—a new air–sea interaction spar buoy: design and performance at sea. *Journal of Atmospheric and Oceanic Technology*, 17:708–720, doi:10.1175/1520-0426(2000)017<0708:AANASI>2.0.CO;2.

Greenslade, D.J.M. and I.R. Young, 2004: Background errors in a global wave model determined from altimeter data. *Journal of Geophysical Research (Oceans)*, 109(C9), doi:10.1029/2004JC002324.

———, 2005*a*: Forecast divergences of a global wave model. *Monthly Weather Review*, 133(8):2148–2162, doi:10.1175/MWR2974.1.

———, 2005*b*: The impact of altimeter sampling patterns on estimates of background errors in a global wave model. *Journal of Atmospheric and Oceanic Technology*, 22:1895–1917, doi:10.1175/JTECH1811.1.

Gröen, P. and R. Dorrestein, 1976: *Zeegolven*. Opstellen op Oceanografisch en Maritiem Meteorologisch Gebied (*Sea Waves*. Lecture Notes on Oceanographic and Maritime Meteorology), Volume 11.

Grønlie, Ø., 2004: Wave radars – a comparison of different concepts and techniques. *Hydro International*, 8(5).

Grønlie, Ø., D.C. Brodtkorb and J. Wøien, 1984: MIROS: A microwave remote sensor for the ocean surface. *Norwegian Maritime Research Quarterly Review*, 12(3):24–28, doi:10.1007/978-94-015-7717-5_48.

Gulev, S.K. and V. Grigorieva, 2006: Variability of the winter wind waves and swell in the North Atlantic and North Pacific as revealed by the Voluntary Observing Ship data. *Journal of Climate*, 19:5667–5685, doi:10.1175/JCLI3936.1.

Gulev, S.K. and L. Hasse, 1998: North Atlantic wind waves and wind stress fields from voluntary observing data. *Journal of Physical Oceanography*, 28:1107–1130, doi:10.1175/1520-0485(1998)028<1107:NAWWAW>2.0.CO;2.

———, 1999: Changes of wind waves in the North Atlantic over the last 30 years. *International Journal of Climatology*, 19:1091–1117, doi:10.1002/(SICI)1097-0088(199908)19:10<1091::AID-JOC403>3.0.CO;2-U.

Gulev, S.K., V. Grigorieva, A. Sterl and D. Woolf, 2003: Assessment of the reliability of wave observations from voluntary observing ships: insights from the validation of a global wind wave climatology based on voluntary observing ship data. *Journal of Geophysical Research (Oceans)*, 108(C7):3236, doi:10.1029/2002JC001437.

Haltiner, G.J. and F.L. Martin, 1957: *Dynamic and Physical Meteorology*. McGraw-Hill Book Company.

Haltiner, G.J. and R.T. Williams, 1980: *Numerical Prediction and Dynamic Meteorology*. John Wiley & Sons.

Hanson, J.L. and O.M. Phillips, 2001: Automated analysis of ocean surface directional wave spectra. *Journal of Atmospheric and Oceanic Technology*, 18:277–293, doi:10.1175/1520-0426(2001)018<0277:AAOOSD>2.0.CO;2.

Hasselmann, K., 1962: On the non-linear energy transfer in a gravity wave spectrum. Part 1: General theory. *Journal of Fluid Mechanics*, 12:481–500, doi:10.1017/S0022112062000373.

———, 1974: On the spectral dissipation of ocean waves due to whitecapping. *Boundary-Layer Meteorology*, 6:107–127, doi:10.1007/BF00232479.

Hasselmann, S. and K. Hasselmann, 1981: *A Symmetrical Method of Computing the Non-linear Transfer in a Gravity-wave Spectrum*. Hamburger Geophysikalische Einzelschriften.

———, 1985: Computations and parameterizations of the non-linear energy transfer in a gravity wave spectrum. Part I. A new method for efficient calculations of the exact non-linear transfer integral. *Journal of Physical Oceanography*, 15:1369–1377, doi:10.1175/1520-0485(1985)015<1369:CAPOTN>2.0.CO;2.

Hasselmann, K., T.P. Barnett, E. Bouws, H. Carlson, D.E. Cartwright, K. Enke, J.A. Ewing, H. Gienapp, D.E. Hasselmann, P. Kruseman, A. Meerburg, P. Muller, D.J. Olbers, K. Richter, W. Sell and H. Walden, 1973: Measurements of wind-wave growth and swell decay during the Joint North Sea Wave Project (JONSWAP). *Ergänzungsheft zur Deutschen Hydrographischen Zeitschrift*, A8(12).

Hasselmann, D.E., M. Dunckel and J.A. Ewing, 1980: Directional wave spectra observed during JONSWAP (1973). *Journal of Physical Oceanography*, 10:1264–1280, doi:10.1175/1520-0485(1980)010<1264:DWSODJ>2.0.CO;2.

Hasselmann, S., K. Hasselmann, J.H. Allender and T.P. Barnett, 1985: Computations and parameterizations of the non-linear energy transfer in a gravity wave spectrum. Part II: Parameterizations of the non-linear energy transfer for application in wave models. *Journal of Physical Oceanography*, 15(11):1378–1391, doi:10.1175/1520-0485(1985)015<1378:CAPOTN>2.0.CO;2.

Hasselmann, K., S. Hasselmann, C. Brüning and A. Speidal, 1991: Interpretation and application of SAR wave image spectra in wave models. In: *Directional Ocean Wave Spectra* (R.C. Beal, ed.), 117–124. Baltimore, Johns Hopkins University Press.

Hasselmann, K., D.B. Ross, P. Müller and W. Sell, 1976: A parametric wave prediction model. *Journal of Physical Oceanography*, 6(2):200–228, doi:10.1175/1520-0485(1976)006<0200:APWPM>2.0.CO;2.

Hauser, D., K.K. Kahma, H.E. Krogstad, S. Lehner, J. Monbaliu and L.R. Wyatt (eds.), 2005: *Measuring and Analysing the Directional Spectrum of Ocean Waves*. COST Action 714, EUR 21367. Luxembourg, Office for Official Publications of the European Communities.

Hauser, D., C. Tison, T. Amiot, L. Delaye, N. Corcoral and P. Castillan, 2017: SWIM: the first spaceborne wave scatterometer. *IEEE Transactions in Geoscience and Remote Sensing*, 55(5):3000–3014, doi:10.1109/TGRS.2017.2658672.

Hemer, M.A., X.L. Wang, R. Weisse and V.R. Swail, 2012: Advancing wind-waves climate science: the COWCLIP project. *Bulletin of the American Meteorological Society*, 93(June 2012):791–796, doi:10.1175/BAMS-D-11-00184.1.

Herbers, T.H.C. and S.J. Lentz, 2010: Observing directional properties of ocean swell with an acoustic doppler current profiler (ADCP). *Journal of Atmospheric and Oceanic Technology*, 27:210–225, doi:10.1175/2009JTECHO681.1.

Hersbach, H., 2011: Sea surface roughness and drag coefficient as functions of neutral wind speed. *Journal of Physical Oceanography*, 41:247–251, doi:10.1175/2010JPO4567.1.

Hogben, N. and F.E. Lumb, 1967: *Ocean Wave Statistics*. London, Ministry of Technology, Her Majesty's Stationary Office.

Högström, U., A.-S. Smedman, E. Sahlée, W.M. Drennan, K.K. Kahma, C. Johansson, H. Pettersson and F. Zhang, 2009: The atmospheric boundary layer during swell: a field study and interpretation of the turbulent kinetic energy budget for high wave ages. *Journal of Atmospheric Sciences*, 66:2764–2779, doi:10.1175/2009JAS2973.1.

Holland, G., 1980: An analytic model of the wind and pressure profiles in hurricanes. *Monthly Weather Review*, 108:1212–1218, doi:10.1175/1520-0493(1980)108<1212:AAMOTW>2.0.CO;2.

Holt, T. and S. Raman, 1988: A review and comparative evaluation of multilevel boundary layer parameterisations for first-order and turbulent kinetic energy closure scheme. *Reviews of Geophysics*, 26(4):761–780, doi:10.1029/RG026i004p00761.

Holthuijsen, L.H., 2007: *Waves in Oceanic and Coastal Waters*. New York, Cambridge University Press.

Houmb, O.G., K. Mo and T. Overvik, 1978: *Reliability Tests of Visual Wave Data and Estimation of Extreme Sea States*. Report 5, Division of Port and Ocean Engineering, University of Trondheim, Norwegian Institute of Technology, Trondheim.

Hu, X.-M., J.W. Nielsen-Gammon and F. Zhang, 2010: Evaluation of three planetary boundary layer schemes in the WRF model. *Journal of Applied Meteorology and Climatology*, 49:1831–1844, doi:10.1175/2010JAMC2432.1.

Hurley, P.J., 1997: An evaluation of several turbulence schemes for the prediction of mean and turbulent fields in complex terrain. *Boundary-Layer Meteorology*, 83:43–73, doi:10.1023/A:1000217722421.

Hwang, P.A., F.J. Ocampo-Torres and H. García-Nava, 2012: Wind sea and swell separation of 1D wave spectrum by a spectrum integration method. *Journal of Atmospheric and Oceanic Technology*, 29(1):116–128, doi:10.1175/JTECH-D-11-00075.1.

Hwang, P.A., J. Toporkov, M. Sletten and S. Menk, 2013: Mapping surface currents and waves with interferometric synthetic aperture radar in coastal waters: observations of wave breaking in swell-dominant conditions. *Journal of Physical Oceanography*, 43:563–582, doi:10.1175/JPO-D-12-0128.1.

Jansen, P.C.M., 1986: Laboratory observations of the kinematics in the aerated region of breaking waves. *Coastal Engineering*, 9:453–477, doi:10.1016/0378-3839(86)90008-6.

Janssen, P.A.E.M., 1991: Quasi-linear theory of wind-wave generation applied to wave forecasting. *Journal of Physical Oceanography*, 21:1631–1642, doi:10.1175/1520-0485(1991)021<1631:QLTOWW>2.0.CO;2.

———, 2004: *The Interaction of Ocean Waves and Wind*. Cambridge, Cambridge University Press, doi:10.1017/CBO9780511525018.

———, 2008: Progress in ocean wave forecasting. *Journal of Computational Physics*, 227(7):3572–3594, doi:10.1016/j.jcp.2007.04.029.

Janssen, P.A.E.M. and J.-R. Bidlot, 2009: *On the Extension of the Freak Wave Warning System and its Verification*. European Centre for Medium-Range Weather Forecasts Technical Memorandum 588.

Janssen, P.A.E.M. and P. Viterbo, 1996: Ocean waves and the atmospheric climate. *Journal of Climate*, 9:1269–1287, doi:10.1175/1520-0442(1996)009<1269:OWATAC>2.0.CO;2.

Janssen, P.A.E.M., S. Abdalla, L. Aouf, J.-R. Bidlot, P. Challenor, D. Hauser, H. Hersbach, J.-M. Lefèvre, D. Vandemark, P. Queffeulou and Y. Quilfen, 2008: *15 Years Using Altimeter Sea State Products*. European Centre for Medium-Range Weather Forecasts Technical Memorandum 552.

Janssen, P.A.E.M., S. Abdalla, H. Hersbach and J.R. Bidlot, 2007: Error estimation of buoy, satellite, and model wave height data. *Journal of Atmospheric and Oceanic Technology*, 24:1665–1677, doi:10.1175/JTECH2069.1.

Janssen, P.A.E.M., Ø. Breivik, K. Mogensen, F. Vitart, M. Balmaseda, J.-R. Bidlot, S. Keeley, M. Leutbecher, L. Magnusson and F. Molteni, 2013: *Air-sea Interaction and Surface Waves*. European Centre for Medium-Range Weather Forecasts Technical Memorandum 712.

Jenkins, A.D., 1992: A quasi-linear eddy-viscosity model for the flux of energy and momentum to wind waves using conservation-law equations in a curvilinear coordinate system. *Journal of Physical Oceanography*, 22:844–858, doi:10.1175/1520-0485(1992)022<0843:AQLEVM>2.0.CO;2.

Jenkins, G.M. and D.G. Watts, 1968: *Spectral Analysis and its Applications*. Holden-Day.

Jensen, R.E., V.R. Swail, R.H. Bouchard, R.E. Riley, T.J. Hesser, M. Blaseckie and C. MacIsaac, 2015: *Field Laboratory for Ocean Sea State Investigation: FLOSSIE Intra-measurement Evaluation of 6N Wave Buoy Systems*. Proceedings of 14th International Workshop on Wave Hindcasting and Forecasting, Key West, Florida, 8–13 November 2015.

Jensen, R.E., V.R. Swail, B. Lee and W.A. O'Reilly, 2011: *Wave Measurement Evaluation and Testing*. Proceedings of 12th International Workshop on Wave Hindcasting and Forecasting, Kohala Coast, Hawaii.

Jiang, H., J.E. Stopa, H. Wang, R. Husson, A. Mouche, B. Chapron and G. Chen, 2016: Tracking the attenuation and nonbreaking dissipation of swells using altimeters. *Journal of Geophysical Research (Oceans)*, 121:1446–1458, doi:10.1002/2015JC011536.

Jones, I.S.F. and Y. Toba (eds.), 2001: *Wind Stress Over the Ocean*. Cambridge University Press, doi:10.1017/CBO9780511552076.

Jones, W.L., L.C. Schroeder, D.H. Boggs, E.M. Bracalente, R.A. Brown, G.J. Dame, W.J. Pierson and F.J. Wentz, 1982: The SEASAT-A scatterometer: the geophysical evaluation of remotely sensed wind vectors over the ocean. *Journal of Geophysical Research*, 87(C5):3297–3317, doi:10.1029/JC087iC05p03297.

Kahma, K. and C. Calkoen, 1992: Reconciling discrepancies in the observed growth of wind – generated waves. *Journal of Physical Oceanography*, 22:1389–1405, doi:10.1175/1520-0485(1992)022<1389:RDITOG>2.0.CO;2.

Kahma, K.K., M.A. Donelan, W.M. Drennan and E.A. Terray, 2016: Evidence of energy and momentum flux from swell to wind. *Journal of Physical Oceanography*, 46:2143–2156, doi:10.1175/JPO-D-15-0213.1.

Kalnay, E., M. Kanamitsu, R. Kistler, W. Collins, D. Deaven, L. Gandin, M. Iredell, S. Saha, G. White, J. Woollen, Y. Zhu, M. Chelliah, W. Ebisuzaki, W. Higgins, J. Janowiak, K.C. Mo, C. Ropelewski, J. Wang, A. Leetmaa, R. Reynolds, R. Jenne and D. Joseph, 1996: The NCEP/NCAR 40-Year Reanalysis Project. *Bulletin of the American Meteorological Society*, 77:437–471, doi:10.1175/1520-0477(1996)077<0437:TNYRP>2.0.CO;2.

Kara, A.B., A.J. Wallcraft and M.A. Bourassa, 2008: Air-sea stability effects on the 10 m winds over the global ocean: evaluations of air-sea flux algorithms. *Journal of Geophysical Research (Oceans)*, 113(C4), doi:10.1029/2007JC004324.

Kent, E. and P.K. Taylor, 1997: Choice of a Beaufort equivalent scale. *Journal of Atmospheric and Oceanic Technology*, 14, 228–242, doi:10.1175/1520-0426(1997)014<0228:COABES>2.0.CO;2.

Kinsman, B., 1965: *Wind Waves: Their Generation and Propagation on the Ocean Surface*. Englewood Cliffs, New Jersey, Prentice Hall Inc., doi:10.1126/science.150.3697.737-a. Reprinted by Dover Publications, 1984.

Kishimoto, K., M. Sasaki and M. Kunitsugu, 2013: *Cloud Grid Information Objective Dvorak Analysis (CLOUD) at the RSMC Tokyo - Typhoon Center*. Technical Review No. 15, Regional Specialized Meteorological Center Tokyo - Typhoon Center.

Koba, H., T. Hagiwara, S. Asano and S. Akashi, 1990: Relationships between CI number from Dvorak's technique and minimum sea level pressure or maximum wind speed of tropical cyclone (in Japanese). *Journal of Meteorological Research*, 42:59–67, doi:10.4172/2332-2594.1000180.

Kobayashi, S., Y. Ota, Y. Harada, A. Ebita, M. Moriya, H. Onoda, K. Onogi, H. Kamahori, C. Kobayashi, H. Endo, K. Miyaoka and K. Takahashi, 2015: The JRA-55 reanalysis: general specifications and basic characteristics. *Journal of Meteorological Society Japan, Series II*, 93(1):5–48, doi:10.2151/jmsj.2015-001.

Kohno, N., 2013: *An Approach for Tough Navigation Sea Information*. Proceedings of 13th International Workshop on Wave Hindcasting and Forecasting, Banff, Alberta, Canada.

Komen, G.J., L. Cavaleri, M. Donelan, K. Hasselmann, S. Hasselmann and P.A.E.M. Janssen, 1994: *Dynamics and Modelling of Ocean Waves*. Cambridge University Press, doi:10.1017/S0022112096220166.

Komen, G.J., S. Hasselmann and K. Hasselmann, 1984: On the existence of a fully developed wind-sea spectrum. *Journal of Physical Oceanography*, 14:1271–1285, doi:10.1175/1520-0485(1984)014<1271:OTEOAF>2.0.CO;2.

Konishi, T., 1995: An experimental storm surge prediction for the western part of the Inland Sea with application to Typhoon 9119. *Papers in Meteorology and Geophysics*, 46:9–17, doi:10.2467/mripapers.46.9.

Krishna, K., 1981: A two-layer first order closure model for the study of the baroclinic atmospheric boundary layer. *Journal of Atmospheric Sciences*, 38:1401–1417, doi:10.1175/1520-0469(1981)038<1401:ATLFOC>2.0.CO;2.

Krogstad, H.E., J. Wolf, S.P. Thompson and L.R. Wyatt, 1999: Methods for intercomparison of wave measurements. *Coastal Engineering*, 37:235–257, doi:10.1016/S0378-3839(99)00028-9.

Lai, P., M. Hannam, V. McCarthy and S. Sovilla, 2006: *Motion Forecasting and Monitoring for Offshore Installation and Decommissioning Operation*. Proceedings of International Marine Contractors 2006 Annual Seminar.

Laing, A.K., 1985: An assessment of wave observations from ships in Southern Ocean. *Journal of Climate Applied Meteorology and Climatology*, 24:481–494, doi:10.1175/1520-0450(1985)024<0481:AAOWOF>2.0.CO;2.

Lalaurette, F., 2003: Early detection of abnormal weather conditions using a probabilistic extreme forecast index. *Quarterly Journal of the Royal Meteorological Society*, 129:3037–3057, doi:10.1256/qj.02.152.

Large, W.G. and S. Pond, 1981: Open ocean momentum flux measurements in moderate to strong winds. *Journal of Physical Oceanography*, 11(3):324–336, doi:10.1175/1520-0485(1981)011<0324:OOMFMI>2.0.CO;2.

Lascody, R.L., 1998: East Central Florida rip current program. *National Weather Digest*, 22(2):25–30, https://www.weather.gov/media/mlb/marine/ripinit.pdf.

Lazanoff, S.M. and N. Stevenson, 1975: *An Evaluation of a Hemispherical Operational Wave Spectra Model*. Technical Note 75-3. Fleet Numerical Weather Central, Monterey, California, http://www.dtic.mil/dtic/tr/fulltext/u2/a099334.pdf.

LeBlond, P.H. and L.A. Mysak, 1978: *Waves in the Ocean*. Amsterdam, Elsevier.

Lefèvre, J.-M. and L. Aouf, 2012: *Latest Developments in Wave Data Assimilation*. Proceedings of European Centre for Medium-Range Weather Forecasts Workshop on Ocean Waves, 175–188.

Lefèvre, J.M., J. Barckicke and Y. Menard, 1994: A significant wave height dependent function for Topex/Poseidon wind speed retrieval. *Journal of Geophysical Research*, 99:25035–25049, doi:10.1029/94JC01958.

Lefèvre, J.-M., C. Quentin, D. Hauser and J.-R. Bidlot, 2005: Partitioning of wave spectra. In: *Measuring and Analyzing the Directional Spectrum of Ocean Waves*, Chapter 10, 441–455. COST Action 714, EUR 21367. Luxembourg, Office for Official Publications of the European Communities.

Lehner, S. and F.J. Ocampo-Torres, 2004: *The SAR Measurement of Ocean Waves: Wave Session Whitepaper*. Proceedings of 2nd Workshop on Coastal and Marine Applications of SAR, Svalbard, Norway, 8–12 September 2003, ESA SP-565, June 2004 (H. Lacoste, ed.).

Lehner, S., A. Pleskachevsky and M. Bruck, 2012: High resolution satellite measurements of coastal wind field and sea state. *International Journal of Remote Sensing*, 33:7337–7360, doi:10.1080/01431161.2012.685975.

Lehner, S., J. Schulz-Stellenfleth, J.B. Schättler, H. Breit and J. Horstmann, 2000: Wind and wave measurements using complex ERS-2 wave mode data. *IEEE Transactions on Geoscience and Remote Sensing*, 38:2246–2257, doi:10.1109/36.868882.

Li, J.G., 2012: Propagation of ocean surface waves on a spherical multiple-cell grid. *Journal of Computational Physics*, 231:8262–8277, doi:10.1016/j.jcp.2012.08.007.

Li, J.G. and M. Holt, 2009: Comparison of ENVISAT ASAR ocean wave spectra with buoys and altimeter data via a wave model. *Journal of Atmospheric and Oceanic Technology*, 26:593–614, doi:10.1175/2008JTECHO529.1.

Lionello, P., H. Günther and P.A.E.M. Janssen, 1992: *Assimilation of Altimeter Data in a Global Third Generation Wave Model*. Technical Report No. 67, European Centre for Medium-Range Weather Forecasts.

Liu, B., H. Liu, L. Xie, C. Guan and D. Zhao, 2011: A coupled atmosphere–wave–ocean modeling system: simulation of the intensity of an idealized tropical cyclone. *Monthly Weather Review*, 139:132–152, doi:10.1175/2010MWR3396.1.

Liu, P.C., C.H. Wu, A.J. Bechle, K.R. MacHutchon and H.S. Chen, 2010: What do we know about freaque waves in the ocean and lakes and how do we know it? *Natural Hazards and Earth System Sciences*, 10:1–6, doi:10.5194/nhess-10-2191-2010.

Liu, W.T. and W. Tang, 1996: *Equivalent Neutral Wind*. Jet Propulsion Laboratory Publication 96-17, https://ntrs.nasa.gov/archive/nasa/casi.ntrs.nasa.gov/19970010322.pdf.

Liu, W.T., K.B. Katsaros and J.A. Businger, 1979: Bulk parameterization of air-sea exchanges of heat and water vapour including the molecular constraints at the interface. *Journal of Atmospheric Sciences*, 36:1722–1735, doi:10.1175/1520-0469(1979)036<1722:BPOASE>2.0.CO;2.

Longuet-Higgins, M.S., 1952: On the statistical distribution of the heights of sea waves. *Journal of Marine Research*, 11:245–266.

Longuet-Higgins, M.S., D.E. Cartwright and N.D. Smith, 1963: Observations of the directional spectrum of sea waves using the motions of a floating buoy. In: *Ocean Wave Spectra*. Prentice Hall, 111–136.

Lonnberg, P. and A. Hollingsworth, 1986: The statistical structure of short-range forecast errors as determined from radiosonde data. Part II: The covariance of height and wind errors. *Tellus*, 38A:137–161, doi:10.3402/tellusa.v38i2.11708.

Lorenc, A., 2003: Modelling of error covariances by 4D-Var data assimilation. *Quarterly Journal of Royal Meteorological Society*, 129:3167–3182, doi:10.1256/qj.02.131.

Lorenz, E.N., 1963: Deterministic non-periodic flow. *Journal of Atmospheric Sciences*, 20(2):130–141, doi:10.1175/1520-0469(1963)020<0130:DNF>2.0.CO;2.

Louis, J.F., 1979: A parametric model of vertical eddy fluxes in the atmosphere. *Boundary-Layer Meteorology*, 17:187202, doi:10.1007/BF00117978.

Lygre, A. and H.E. Krogstad, 1986: Maximum entropy estimation of the directional distribution in ocean wave spectra. *Journal of Physical Oceanography*, 16:2052–2060, doi:10.1175/1520-0485(1986)016<2052:MEEOTD>2.0.CO;2.

Maat, N., C. Kraan and W.A. Oost, 1991: The roughness of wind waves. *Boundary-Layer Meteorology*, 54:89–103, doi:10.1007/BF00119414.

Magnusson, A.K. and M.A. Donelan, 2013: The Andrea wave characteristics of a measured North Sea rogue wave. *Journal of Offshore Mechanics and Arctic Engineering*, 135(3):031108-1, doi:10.1115/1.4023800.

Margules, M., 1906: Zur Sturmtheorie. *Meteorologische Zeitschrift*, 23(11):481–497, arXiv:1704.06128.

Massel, S.R., 2013: *Ocean Surface Waves: Their Physics and Prediction*. Second edition. Advanced Series in Ocean Engineering, Volume 36. World Scientific.

Masuda, A., 1980: Nonlinear energy transfer between wind waves. *Journal of Physical Oceanography*, 10:2082–2093, doi:10.1175/1520-0485(1980)010<2082:NETBWW>2.0.CO;2.

Meindl, A., 1996: *Guide to Moored Buoys and Other Ocean Data Acquisition Systems*. Technical Document 08, Data Buoy Cooperation Panel, https://www.oceanbestpractices.net/handle/11329/81.

Mellor, G.L. and T. Yamada, 1974: A hierarchy of turbulence closure models for planetary boundary layers. *Journal of Atmospheric Sciences*, 31:1791–1806, doi:10.1175/1520-0469(1974)031<1791:AHOTCM>2.0.CO;2.

Mendenhall, B.R., 1967: *A Statistical Study of Frictional Wind Veering in the Planetary Boundary Layer*. Atmospheric Science Paper 116, Department of Atmospheric Sciences, Colorado State University.

Mercer, D., 2008: *Breugem and Holthuijsen Nomogram for Deep Water Waves*. Science Report Series 2008-05, Meteorological Service of Canada, Atlantic Region.

Miles, J.W., 1957: On the generation of surface waves by shear flows. *Journal of Fluid Mechanics*, 3:185–204, doi:10.1017/S0022112057000567.

———, 1960: On the generation of surface waves by turbulent shear flows. *Journal of Fluid Mechanics*, 7:469–478, doi:10.1017/S0022112060000220.

Mitsuyasu, H., F. Tasai, T. Suhara, S. Mizuno, M. Okhuso, T. Honda and K. Rikiishi, 1975: Observations of the directional spectrum of ocean waves using a cloverleaf buoy. *Journal of Physical Oceanography*, 5:750–760, doi:10.1175/1520-0485(1975)005<0750:OOTDSO>2.0.CO;2.

Molteni, F., R. Buizza, T.N. Palmer and T. Petroliagis, 1996: The ECMWF ensemble prediction system: methodology and validation. *Quarterly Journal of the Royal Meteorological Society*, 122(529):73–119, doi:10.1002/qj.49712252905.

Monin, A.S. and A.M. Obukhov, 1954: Basic laws of turbulent mixing in the ground layer of the atmosphere. *Akademii Nauk SSSR Geofiz Instituta Trudy*, 151:163–181.

Moon, I., I. Ginis and T. Hara, 2004: Effect of surface waves on Charnock coefficient under tropical cyclones. *Geophysics Research Letters*, 31:L20302, doi:10.1029/2004GL020988.

Munk, W.H., 1951: *Origin and Generation of Waves*. Proceedings of the 1st Coastal Engineering Conference, Long Beach, California, 1–4, doi:10.9753/icce.v1.1.

National Data Buoy Center, 1996: *Nondirectional and Directional Wave Data Analysis Procedures*. Technical Document 96-01, National Data Buoy Center, http://www.ndbc.noaa.gov/wavemeas.pdf.

———, 2009: *Handbook of Automated Data Quality Control Checks and Procedures*. Technical Document 09-02, National Data Buoy Center, http://www.ndbc.noaa.gov/NDBCHandbookofAutomatedDataQualityControl2009.pdf.

National Oceanic and Atmospheric Administration, 2010: *National Weather Service Observing Handbook No. 1 – Marine Surface Weather Observations*. Stennis Space Center, Mississippi.

Neumann, G. and W.J. Pierson, 1966: *Principles of Physical Oceanography*. London, Prentice Hall.

Ocampo-Torres, F.J., H. García-Nava, R. Durazo, P. Osuna, G.M. Díaz Méndez and H.C. Graber, 2011: The IntOA experiment: a study of ocean–atmosphere interactions under moderate to strong offshore winds and opposing swell conditions in the Gulf of Tehuantepec, Mexico. *Boundary-Layer Meteorology*, 138:433–451, doi:10.1007/s10546-010-9561-5.

Oertel, H. (ed.), 2004: *Prandtl's Essentials of Fluid Dynamics*. New York, Springer, doi:10.1007/978-1-4419-1564-1.

O'Reilly, W.C., 2007: *An Introduction to Directional Wave Observations*. Wave Sensor Workshop, Alliance for Coastal Technologies, St Petersburg, Florida, 7–9 March 2007.

O'Reilly, W.C., T.H. Herbers, R.J. Seymour and R.T. Guza, 1996: A comparison of directional buoy and fixed platform measurements of Pacific swell. *Journal of Atmospheric and Oceanic Technology*, 13:231–238, doi:10.1175/1520-0426(1996)013<0231:ACODBA>2.0.CO;2.

Oyama, R., K. Nagat, H. Kawada and N. Koide, 2016: *Development of a Product based on Consensus between Dvorak and AMSU Tropical Cyclone Central Pressure Estimates at JMA*. Technical Review No. 18, Regional Specialized Meteorological Center Tokyo - Typhoon Center.

Perrie, W., B. Toulany, D.T. Resio, A. Roland, J.-P. Auclair, 2013: A two-scale approximation for wave–wave interactions in an operational wave model. *Ocean Modelling*, 70:38–51, doi:10.1016/j.ocemod.2013.06.008.

Owens, R.G. and T. Hewson, 2018: *User Guide to ECMWF Products*. European Centre for Medium-Range Weather Forecasts, doi:10.21957/m1cs7h.

Petroliagis, T.I. and P. Pinson, 2012: Early warnings of extreme winds using the ECMWF Extreme Forecast Index. *Meteorological Applications*, 21(2):171–185, doi:10.1002/met.1339.

Pettersson, H., H.C. Graber, D. Hauser, C. Quentin, K.K. Kahma, W.M. Drennan and M.A. Donelan, 2003: Directional wave measurements from three wave sensors during the FETCH experiment. *Journal of Geophysical Research (Oceans)*, 108(C3):8061, doi:10.1029/2001JC001164.

Pezzutto, P., A. Saulter, L. Cavaleri, C. Bunney, F. Marcucci, L. Torrisi and S. Sebastianelli, 2016: Performance comparison of meso-scale ensemble wave forecasting systems for Mediterranean sea states. *Ocean Modelling*, 104:171–186, doi:10.1016/j.ocemod.2016.06.002.

Phillips, D.W., 1957: On the generation of waves by a turbulent wind. *Journal of Fluid Mechanics*, 2:417–445, doi:10.1017/S0022112057000233.

———, 1958: The equilibrium range in the spectrum of wind-generated waves. *Journal of Fluid Mechanics*, 4:426–434, doi:10.1017/S0022112058000550.

———, 1972: Modification of surface air over Lake Ontario in winter. *Monthly Weather Review*, 100:662–670, doi:10.1175/1520-0493(1972)100<0662:MOSAOL>2.3.CO;2.

Phillips, D.W. and J.G. Irbe, 1978: *Lake to Land Comparison of Wind, Temperature, and Humidity of Lake Ontario during the International Field Layer for the Great Lakes*. CLI 2-77, Atmospheric Environment Service, Environment Canada.

Pierson, W.J., 1979: *TWINDX: A Planetary Boundary Layer Model for the Winds in Extratropical and Tropical Ocean Areas*. Contract No. N00014-77-C-0206. Naval Environmental Prediction Research Center, Monterey, California.

———, 1990: Examples of, reasons for, and consequences of the poor quality of wind data from ships for the marine boundary layer: implications for remote sensing. *Journal of Geophysical Research (Oceans)*, 95:13313–13340, doi:10.1029/JC095iC08p13313.

Pierson, W.J. and L. Moskowitz, 1964: A proposed spectral form for fully developed wind-seas based on the similarity theory of S.A. Kitaigorodskii. *Journal of Geophysical Research*, 69(24):5181–5190, doi:10.1029/JZ069i024p05181.

Pierson, W.J., G. Neumann and R.W. James, 1955: *Practical Methods for Observing and Forecasting Ocean Waves by Means of Wave Spectra and Statistics*. Publication 603, US Naval Oceanographic Office.

Pierson, W.J., L.J. Tick and L. Baer, 1966: *Computer-based Procedure for Preparing Global Wave Forecasts and Wind Field Analysis Capable of using Wave Data obtained by a Spacecraft*. Proceedings of 6th Naval Hydrodynamics Symposium, Washington, 499–533.

Polavarpu, S., S. Ren, Y. Rochon, D. Sankey, N. Ek, J. Koshyk and D. Tarasick, 2005: Data assimilation with the Canadian middle atmospheric model. *Atmosphere-Ocean*, 43(1):77–100, doi:10.3137/ao.430105.

Pomaro, A., L. Cavaleri and P. Lionello, 2017: Climatology and trends of the Adriatic Sea wind waves: analysis of a 37-year long instrument dataset. *International Journal of Climatology*, 37(12):4237–4250, doi:10.1002/joc.5066.

Popinet, S., R.M. Gorman, G.J. Rickard and H.L. Tolman, 2010: A quadtree-adaptive spectral wave model. *Ocean Modelling*, 34:36–49, doi:10.1016/j.ocemod.2010.04.003.

Portilla-Yardun, J., F.J. Ocampo-Torres and J. Monbaliu, 2009: Spectral partitioning and identification of wind sea and swell. *Journal of Atmospheric and Oceanic Technology*, 26:107–122, doi:10.1175/2008JTECHO609.1.

Powell, M.D., P.J. Vickery and T.A. Reinhold, 2003: Reduced drag coefficient for high wind speeds in tropical cyclones. *Nature*, 422:279–283, doi:10.1038/nature01481.

Reistad, M., Ø. Breivik, H. Haakenstad, O.J. Aarnes, B.R. Furevik and J.-R. Bidlot, 2011: A high-resolution hindcast of wind and waves for the North Sea, the Norwegian Sea, and the Barents Sea. *Journal of Geophysical Research (Oceans)*, 116:C05019, doi:10.1029/2010JC006402.

Resio, D.T., W. Perrie, S. Thurston and J. Hubbertz, 1992: *A Generic Third-generation Wave Model: AL*. Proceedings of 3rd International Workshop on Wave Hindcasting and Forecasting, Montreal, Quebec, 102–114.

Richardson, L.F., 1922: *Weather Prediction by Numerical Process*. Cambridge University Press, doi:10.1017/CBO9780511618291. Reprinted by Dover in 1965. .

Roland, A., 2008: Development of WWM II: spectral wave modelling on unstructured meshes. PhD Thesis, Technische Universität Darmstadt, Institute of Hydraulic and Water Resources Engineering.

Roland, A., A. Cucco, C. Ferrarin, T.W. Hsu and J.M. Lia, 2009: On the development and verification of a 2-D coupled wave-current model on unstructured meshes. *Journal of Marine Systems*, Supplement, S244–S254, doi:10.1016/j.jmarsys.2009.01.026.

Roll, H.U., 1965: *Physics of the Marine Atmosphere*. Academic Press, doi:10.1002/qj.49709239233.

Rye, H., 1977: The stability of some currently used wave parameters. *Coastal Engineering*, 1:17–30, doi:10.1016/0378-3839(77)90004-7.

Saetra, O. and J.-R. Bidlot, 2004: On the potential benefit of using probabilistic forecast for waves and marine winds based on the ECMWF ensemble prediction system. *Weather and. Forecasting*, 19:673–689, doi:10.1175/1520-0434(2004)019<0673:PBOUPF>2.0.CO;2.

Savina, H. and J.M. Lefèvre, 2004: *Sea State in Marine Safety Information: Present State, Future Prospects*. Presented at Rogue Waves 2004, Brest, France, 20–22 October 2004.

Schloemer, R.W., 1954: *Analysis and Synthesis of Hurricane Wind Patterns over Lake Okeechobee, Florida*. Hydrometeorological Report No. 31, Washington, D.C., United States Department of Commerce.

Schwab, D.J., 1978: Simulation and forecasting of Lake Erie storm surges. *Monthly Weather Review*, 106:1476–1487, doi:10.1175/1520-0493(1978)106<1476:SAFOLE>2.0.CO;2.

Shearman, E.D.R., 1983: Radio science and oceanography. *Radio Science*, 18(3):299–320, doi:10.1029/RS018i003p00299.

Shearman, R.J. and A.A. Zelenko, 1989: *Wind Measurements Reduction to a Standard Level*. Marine Meteorology and Related Oceanographic Activities Report 22 (WMO/TD-No. 311). Geneva, World Meteorological Organization.

Shemdin, O.H., K. Hasselmann, S.V. Hsiao and K. Herterich, 1978: Non-linear and linear bottom interaction effects in shallow water. In: *Turbulent Fluxes through the Sea Surface; Wave Dynamics and Prediction*. Plenum Press, 347–372, doi:10.1007/978-1-4612-9806-9_23.

Shin, H.H. and S.Y. Hong, 2011: Intercomparison of planetary boundary-layer parametrizations in the WRF model for a single day from CASES-99. *Boundary-Layer Meteorology*, 139:261–281, doi:10.1007/s10546-010-9583-z.

Smedman, A.-S., U. Högström, U.E. Sahleé, W.M. Drennan, K.K. Kahma, H. Pettersson and F. Zhang, 2009: Observational study of marine atmospheric boundary layer characteristics during swell. *Journal of Atmospheric Sciences*, 66:2747–2763, doi:10.1175/2009JAS2952.1.

Smith, R.K., 1997: On the theory of CISK. *Quarterly Journal of the Royal Meteorological Society*, 123:407–418, doi:10.1002/qj.49712353808.

Snodgrass, F.E., G.W. Groves, K.F. Hasselmann, G.R. Miller, W.H. Munk and W.H. Powers, 1966: Propagation of ocean swell across the Pacific. *Philosophical Transactions of the Royal Society of London. Series A, Mathematical and Physical Sciences*, 259:431–497, doi:10.1098/rsta.1966.0022.

Snyder, R.L. and C.S. Cox, 1966: A field study of the wind generation of ocean waves. *Journal of Marine Research*, 24(2):141–178.

Snyder, R.L., F.W. Dobson, J.A. Elliott and R.B. Long, 1981: Array measurements of atmospheric pressure fluctuations above surface gravity waves. *Journal of Fluid Mechanics*, 102:1–59, doi:10.1017/S0022112081002528.

Sorensen, O.R., H. Kofoed-Hansen, M. Rugbjerg and L.S. Sorensen, 2004: *A Third Generation Spectral Wave Model using an Unstructured Finite Volume Technique*. Proceedings of 29th International Conference on Coastal Engineering, 2004.

Steele, K.E., C.-C. Teng and D.W. Wang, 1992: Wave direction wave measurements using pitch-roll buoys. *IEEE Journal of Oceanic Engineering*, 19(4):349–372, doi:10.1016/0029-8018(92)90035-3.

Steele, K.E., D.W. Wang, M.D. Earle, E.D. Michelena and R.J. Dagnall, 1998: Buoy pitch and roll computed using three angular rate sensors. *Coastal Engineering*, 35:123–139, doi:10.1016/S0378-3839(98)00025-8.

Stokes, G.G., 1847: On the theory of oscillatory waves. *Transactions of the Cambridge Philosophical Society*, 8:441–455.

———, 1880: Considerations relative to the greatest height of oscillatory irrotational waves which can be propagated without change of form. In: *Mathematical and Physical Papers*, Volume 1, 225–228. Cambridge University Press.

Stopa, J.E., F Ardhuin, A. Babanin and S. Zieger, 2016: Comparison and validation of physical wave parameterizations in spectral wave models. *Ocean Modelling*, 103:2–17.

Stull, R.B., 1988: *An Introduction to Boundary Layer Meteorology*. Dordrecht, Boston, London, Kluwer Academic Publishers, doi:10.1017/S0022112091211921.

Sverdrup, H.U. and W.H. Munk, 1947: *Wind, Sea and Swell: Theory of Relations for Forecasting*. H.O. Pub. 601, Washington, D.C., US Navy Hydrographic Office, doi:10.5962/bhl.title.38751.

Swail, V.R. and A.T. Cox, 2000: On the use of NCEP/NCAR reanalysis surface marine wind fields for a long term North Atlantic wave hindcast. *Journal of Atmospheric and Oceanic Technology*, 17(4):532–545, doi:10.1175/1520-0426(2000)017<0532:OTUONN>2.0.CO;2.

Swail, V.R., V.J. Cardone, M. Ferguson, D.J. Gummer and A.T. Cox, 2007: *The MSC Beaufort Sea Wind and Wave Reanalysis*. Proceedings of 10th International Workshop on Wave Hindcasting and Forecasting and Coastal Hazards Symposium, Oahu, Hawaii, 11–16 November 2007, Paper E1.

Swail, V.R., V.J. Cardone, M. Ferguson, D.J. Gummer, E.L. Harris, E.A. Orelup and A.T. Cox, 2006: *The MSC50 Wind and Wave Reanalysis*. Proceedings of 9th International Workshop on Wave Hindcasting & Forecasting, 24–29 September 2006, Victoria, British Columbia.

Swail, V.R., E.A. Ceccacci and A.T. Cox, 2000: *The AES40 North Atlantic Wave Reanalysis: Validation and Climate Assessment*. Proceedings of 6th International Workshop on Wave Hindcasting and Forecasting, 6–10 November 2000, Monterey, California.

Swail, V., R. Jensen, B. Lee, J. Turton, J. Thomas, S. Gulev, M. Yelland, P. Etala, D. Meldrum, W. Birkemeier, W. Burnett and G. Warren, 2010: *Wave Measurements, Needs and Developments for the Next Decade*. Proceedings of OceanObs'09: Sustained Ocean Observations and Information for Society Conference (Volume 2), Venice, Italy, 21–25 September 2009 (J. Hall, D.E. Harrison and D. Stammer, eds.). ESA Publication WPP-306.

SWAMP Group, 1985: *Ocean Wave Modelling*. Plenum Press, doi:10.1007/978-1-4757-6055-2.

Tang, D.L. and G. Sui (eds.), 2014: *Typhoon Impact and Crisis Management*. Advances in Natural and Technological Hazards Research, Volume 40, doi:10.1007/978-3-642-40695-9.

Tayfun, M.A., 1981: Distribution of crest-to-trough wave height. *Journal of Waterway, Port, Coastal and Ocean Engineering*, 107:149–158, doi:10.1016/0029-8018(85)90014-9.

———, 1983: Frequency analysis of wave heights based on wave envelope. *Journal of Geophysical Research (Oceans)*, 88(C12):7573–7587, doi:10.1029/JC088iC12p07573.

Taylor, P.K., E. Kent, M. Yelland and B. Moat, 1994: *The Accuracy of Wind Observations from Ships*. Proceedings of International COADS Wind Workshop, Kiel, Germany, May 1994, 132–151.

———, 1999: *The Accuracy of Marine Surface Winds from Ships and Buoys*. Presented at CLIMAR 99, WMO Workshop on Advances in Marine Climatology, Vancouver, British Columbia. World Meteorological Organization, 59–68.

Teng, C.-C. and R.H. Bouchard, 2005: *Directional Wave Measured from Data Buoys using Angular Rate Sensors and Magnetometers*. Proceedings of 5th Ocean Wave Measurement and Analysis, Madrid, Spain.

Timpe, G.L. and N. Van de Voorde, 1995: *NOMAD Buoys: An Overview of Forty Years of Use*. OCEANS'95, MTS/IEEE, Challenges of Our Changing Global Environment, Volume 1, 309–315, 9–12 October 1995, San Diego, California, doi:10.1109/OCEANS.1995.526788.

Tolman, H.L., 1990: Wind wave propagation in tidal seas. Doctoral Thesis, Delft University of Technology.

———, 1994: Wind-waves and moveable-bed bottom-friction. *Journal of Physical Oceanography*, 24(5):994, doi:10.1175/1520-0485(1994)024<0994:WWAMBB>2.0.CO;2.

———, 2002: *Validation of WAVEWATCH III, V 1.15 for a Global Domain*. Technical Note 213, Marine Modelling & Analysis Branch, National Center for Environmental Prediction, Camp Springs, Maryland.

———, 2008: A mosaic approach to wind wave modelling. *Ocean Modelling*, 25:35–47, doi:10.1016/j.ocemod.2008.06.005.

———, 2013: A generalized multiple discrete interaction approximation for resonant four-wave interactions in wind wave models. *Ocean Modelling*, 70:11–24, doi:10.1016/j.ocemod.2013.02.005.

Tolman, H.L. and D. Chalikov, 1996: Source terms in a third-generation wind wave model. *Journal of Physical Oceanography*, 26:2497–2518, doi:10.1175/1520-0485(1996)026<2497:STIATG>2.0.CO;2.

Tolman, H.L., M.L. Banner and J.M. Kaihatu, 2012: The NOPP operational wave model improvement project. *Ocean Modelling*, 70:2–10, doi:10.1016/j.ocemod.2012.11.011.

Toro, V.G., F.J. Ocampo-Torres, P. Osuna, H. Garcia-Nava, X. Flores-Vidal and R. Durazo, 2014: Analysis of fetch-limited wave growth using high-frequency radars in the Gulf of Tehuantepec. *Ciencias Marinas*, 40:113–132, doi:10.7773/cm.v40i2.2403.

Tucker, M.J., 1956: A shipborne wave recorder. *Transactions of Institute of Naval Architects, London*, 98(1):236–250, https://eprints.soton.ac.uk/id/eprint/392248.

———, 1991: *Waves in Ocean Engineering: Measurement Analysis, Interpretation*. Ellis Horwood Limited.

Tucker, M.J. and E.G. Pitt, 2001: *Waves in Ocean Engineering*. Elsevier Ocean Engineering Book Series, Volume 5.

Turner, J. and S. Pendlebury (eds.), 2004: *The International Antarctic Weather Forecasting Handbook*. British Antarctic Survey.

Uppala, S.M., P.W. Kållberg, A.J. Simmons, U. Andrae, V. Da Costa Bechtold, M. Fiorino, J.K. Gibson, J. Haseler, A. Hernandez, G.A. Kelly, X. Li, K. Onogi, S. Saarinen, N. Sokka, R.P. Allan, E. Andersson, K. Arpe, M.A. Balmaseda, A.C.M. Beljaars, L. Van De Berg, J.-R. Bidlot, N. Bormann, S. Caires, F. Chevallier, A. Dethof, M. Dragosavac, M. Fisher, M. Fuentes, S. Hagemann, E. Hólm, B.J. Hoskins, L. Isaksen, P.A.E.M. Janssen, R. Jenne, A.P. Mcnally, J.-F. Mahfouf, J.-J. Morcrette, N.A. Rayner, R.W. Saunders, P. Simon, A. Sterl, K.E. Trenberth, A. Untch, D. Vasiljevic, P. Viterbo and J. Woollen, 2005: The ERA-40 Re-analysis. *Quarterly Journal of the Royal Meteorological Society*, 131:2961–3012, doi:10.1256/qj.04.176.

Van der Westhuysen, A.J. and H.L. Tolman, 2011: *Quasi-stationary WAVEWATCH III for the Nearshore*. Proceedings of 12th International Workshop on Wave Hindcasting and Forecasting, Hawaii.

Van Dongeren, A., M. van Ormondt, L. Sembiring, R. Sasso, M. Austin, C. Briere, C. Swinkels, D. Roelvink and J. van Thiel de Vries, 2013: Rip current predictions through model-data assimilation on two distinct beaches. Proceedings of 7th International Conference on Coastal Dynamics, Arcachon, France, 24–28 June 2013, 1775–1786.

van Unen, R.F., A.A. van Beuzekom, G.Z. Forristall, J.-P. Mathisen and J. Starke, 1998: *WACSIS-Wave Crest Sensor Intercomparison Study at the Meetpost Noordwijk Measurement Platform*. Proceedings of Oceans '98 Conference, Nice, France, 28 September–1 October 1998. IEEE, 192–197, doi:10.1109/OCEANS.1998.726389.

van Vledder, G.Ph., 2006: The WRT method for the computation of non-linear four-wave interactions in discrete spectral wave models. *Coastal Engineering*, 53:223–242, doi:10.1016/j.coastaleng.2005.10.011.

———, 2012: *Efficient Algorithms for Non-linear Four-wave Interactions*. Proceedings of ECMWF Workshop on Ocean Waves, 25–27 June 2012.

van Vledder, G.P. and D.P. Hurdle, 2002: *Performance of Formulations for Whitecapping in Wave Prediction Models*. Proceedings of 21st International Conference on Offshore Mechanics and Arctic Engineering, Oslo, Norway. Ocean, Offshore and Arctic Engineering Division, American Society of Mechanical Engineers (ASME International), Paper No. OMAE2002-28146, 155–163, doi:10.1115/OMAE2002-28146.

Velden, Ch., B. Harper, F. Wells, J.L. Beven, R. Zehr, T. Olander, M. Mayfield, Ch. Guard, M. Lander, R. Edson, L. Avila, A. Burton, M. Turk, A. Kikuchi, A. Christian, P. Caroff and P. McCrone, 2006: The Dvorak tropical cyclone intensity estimation technique: a satellite-based method that has endured for over 30 years. *Bulletin of American Meteorological Society*, 1195–1210, doi:10.1175/BAMS-87-9-1195.

Verploegh, G., 1967: Observation and analysis of the surface wind over the ocean. *KNMI, Mededelingen en Verhandelingen*, 89.

Verschell, M.A., M.A. Bourassa, D.E. Weissman and J.J. O'Brien, 1999: Ocean model validation of the NASA scatterometer winds. *Journal of Geophysical Research*, 104(11):359–11, 374 doi:10.1029/1998JC900105.

Viggosson, G. and J. Bernodusson, 2009: *The Icelandic Information System on Weather and Sea State Related to Fishing Vessels' Crews and Stability*. Seminar on Fishing Vessels' Crews and Stability, World Fishing Exhibition 2009, Vigo, Spain.

Violante-Carvalho, N. and A.V.C. Ramos, 2006: A review of the techniques for the assimilation of the two-dimensional directional spectrum into wave models. *Revista Ciências Exatas e Naturais*, 8(1).

Violante-Carvalho, N., C.E. Parente, I.S. Robinson and L.M.P. Nunes, 2002: On the growth of wind generated waves in a swell dominated region in the South Atlantic. *Journal of Offshore Mechanics and Arctic Engineering*, 124:14–21, doi:10.1115/1.1423636.

WAMDI Group (S. Hasselmann, K. Hasselmann, E. Bauer, P.A.E.M. Janssen, G. Komen, L. Bertotti, P. Lionello, A. Guillaume, V.C. Cardone, J.A. Greenwood, M. Reistad, L. Zambresky and J.A. Ewing), 1988: The WAM model—a third generation wave prediction model. *Journal of Physical Oceanography*, 18:1775–1810, doi:10.1175/1520-0485(1988)018<1775:TWMTGO>2.0.CO;2.

Wang, D.W. and P.A. Hwang, 2001: An operational method for separating wind sea and swell from ocean wave spectra. *Journal of Atmospheric and Oceanic Technology*, 18:2052–2062, doi:10.1175/1520-0426(2001)018<2052:AOMFSW>2.0.CO;2.

Wang, H., J. Zhu and J. Yang, 2014*a*: Error analysis on ESA's Envisat ASAR wave mode significant wave height retrieval using triple collocation model. *Remote Sensing*, 6:12217–12233, doi:10.3390/rs61212217.

Wang, W., P. Forget and C. Guan, 2014*b*: Inversion of swell frequency from a 1-year HF radar dataset collected in Brittany (France). *Ocean Dynamics*, 64(10):1447–1456, doi:10.1007/s10236-014-0759-9.

WAVEWATCH III Development Group, 2016: *User Manual and System Documentation of WAVEWATCH III Version 5.16*. Technical Note 329. National Oceanic and Atmospheric Administration/National Weather Service/National Centers for Environmental Prediction.

Wilkerson, J.C. and M.D. Earle, 1990: A study of differences between environmental reports by ships in the voluntary observing program and measured from NOAA buoys. *Journal of Geophysical Research (Oceans)*, 95:3373–3385, doi:10.1029/JC095iC03p03373.

WISE Group, L. Cavaleri, J.-H.G.M. Alves, F. Ardhuin, A. Babanin, M. Banner, K. Belibassakis, M. Benoit, M. Donelan, J. Groeneweg, T.H.C. Herbers, P. Hwang, P.A.E.M. Janssen, T. Janssen, I.V. Lavrenov, R. Magne, J. Monbaliu, M. Onorato, V. Polnikov, D. Resio, W.E. Rogers, A. Sheremet, J. McKee Smith, H.L. Tolman, G. van Vledder, J. Wolf and I. Young, 2007: Wave modelling - the state of the art. *Progress in Oceanography*, 75(4):603–674, doi:10.1016/j.pocean.2007.05.005.

Witter, D.L. and D.B. Chelton, 1991: A Geosat altimeter wind speed algorithm and a method for altimeter wind speed algorithm development. *Journal of Geophysical Research (Oceans)*, 96:8853–8860, doi:10.1029/91JC00414.

Work, P., 2008: Nearshore directional wave measurements by surface-following buoy and acoustic Doppler current profiler. *Ocean Engineering*, 35:727–737, doi:10.1016/j.oceaneng.2008.02.005.

World Meteorological Organization, 1970: *The Beaufort Scale of Wind Force*. Marine Science Affairs 3. Geneva.

———, 1976: *Handbook on Wave Analysis and Forecasting* (WMO-No. 446). Geneva.

———, 1994: *Guide to the Applications of Marine Climatology* (WMO-No. 781). Geneva.

———, 1988: *Guide to Wave Analysis and Forecasting*. First edition (WMO-No. 702). Geneva.

———, 1998: *Guide to Wave Analysis and Forecasting*. Second edition (WMO-No. 702). Geneva.

———, 2010: *International List of Selected, Supplementary and Auxiliary Ships* (WMO-No. 47). Geneva.

———, 2011: *Manual on Codes – International Codes, Volume I.1, Annex II to the WMO Technical Regulations: Part A – Alphanumeric Codes* (WMO-No. 306). Geneva.

———, 2012: *Manual on Marine Meteorological Services, Volume I – Global Aspects. Annex VI to the WMO Technical Regulations* (WMO-No. 558). Geneva.

———, 2014*a*: *Composition of the WMO* (WMO-No. 5). Geneva.

———, 2014*b*: *Guide to Meteorological Instruments and Methods of Observation* (WMO-No. 8). Geneva.

———, 2015: *Manual on the Global Observing System, Volume 1 – Global Aspects: Annex V to the WMO Technical Regulations* (WMO No. 544). Geneva.
———, 2018: *Guide to Marine Meteorological Services* (WMO-No. 471). Geneva.
Woodruff, S.D., S.J. Worley, S.J. Lubker, Z. Ji, E.J. Freeman, D.I. Berry, P. Brohan, E.C. Kent, R.W. Reynolds, S.R. Smith and C. Wilkinson, 2011: ICOADS release 2.5: extensions and enhancements to the surface marine meteorological archive. *International Journal of Climatology*, 31:951–967, doi:10.1002/joc.2103.
Worley, S.J., S.D. Woodruff, R.W. Reynolds, S.J. Lubker and N. Lott, 2005: ICOADS release 2.1 data and products. *International Journal of Climatology*, 25:823–842, doi:10.1002/joc.1166.
Wu, J., 1980: Wind-stress coefficients over sea surface near neutral conditions—a revisit. *Journal of Physical Oceanography*, 10:727–740, doi:10.1175/1520-0485(1980)010<0727:WSCOSS>2.0.CO;2.
———, 1982: Wind-stress coefficients over sea surface from breeze to hurricane. *Journal of Geophysical Research (Oceans)*, 87:9704–9706, doi:10.1029/JC087iC12p09704.
Wyatt, L.R. and G. Holden, 1994: Limits in direction and frequency resolution for HF radar ocean wave directional spectra measurements. *Global Atmosphere-Ocean System*, 2:265–290, doi:10.1175/1520-0426(2000)017<1651:LTTIOH>2.0.CO;2.
Wyatt, L.R., J.J. Green and A. Middleditch, 2011: HF radar data quality requirements for wave measurement. *Coastal Engineering*, 58:327–336, doi:10.1016/j.coastaleng.2010.11.005.
Wyatt, L.R., J. Venn, M.D. Moorhead, G.B. Burrows, A.M. Ponsford and J. van Heteren, 1985: HF radar measurements of significant wave height and mean period during NURWEC. In: *Evaluation, Comparison and Calibration of Oceanographic Instruments. Advances in Underwater Technology and Offshore Engineering*. London, Graham and Trotman, 209–222.
Yoshizumi, S., 1968: On the asymmetry of wind distribution in the lower layer in typhoon. *Journal of Meteorological Society of Japan*, 46:153–159, doi:10.2151/jmsj1965.46.3_153.
Young, I.R., 1994: On the measurement of directional wave spectra. *Applied Ocean Research*, 16:283–294, doi:10.1016/0141-1187(94)90017-5.
Young, I.R. and A.V. Babanin, 2006: Spectral distribution of energy dissipation of wind generated waves due to dominant wave breaking. *Journal of Physical Oceanography*, 36:376–394, doi:10.1175/JPO2859.1.
Zieger, S., A.V. Babanin, W.E. Rogers and I.R. Young, 2015: Observation-based source terms in the third-generation wave model WAVEWATCH. *Ocean Modelling*, 96:2–25, doi:10.1016/j.ocemod.2015.07.014.
Zieger, S., D.J.M. Greenslade and J.D. Kepert, 2018: Wave ensemble forecast system for tropical cyclones in the Australian region. *Ocean Dynamics*, 68(4–5):603–625, doi:10.1007/s10236-018-1145-9.
Zijlema, M., 2009: *Parallel, Unstructured Mesh Implementation for SWAN*. Proceedings of 31st International Conference on Coastal Engineering, Hamburg, Germany, 2009, 470–482, doi:10.1142/9789814277426_0040.
———, 2010: Computation of wind-wave spectra in coastal waters with SWAN on unstructured grids. *Coastal Engineering*, 57:267–277, doi:10.1016/j.coastaleng.2009.10.011.

FURTHER READING

Khandekar, M.L., 1989: *Operational Analysis and Prediction of Ocean Wind Waves*. Coastal and Estuarine Studies No. 33. New York, Springer-Verlag, doi:10.1007/978-1-4613-8952-1.
Kitaigorodskii, S.A., 1970: *The Physics of Air Sea Interaction*. Gidrometeorologicheskoe Izdatel'stvo, Leningrad (translated from Russian). Israel Programme for Scientific Translations, Jerusalem.
Lighthill, J., 1978: *Waves in Fluids*. Cambridge University Press.
Stoker, J.J., 1957: *Water Waves*. New York, Interscience.
Young, I.R. and G.J. Holland, 1996: *Atlas of the Oceans: Wind and Wave Climate*. Pergamon, doi:10.1002/(SICI)1097-0088(199804)18:5<579::AID-JOC273>3.0.CO;2-O.

For more information, please contact:

World Meteorological Organization

7 bis, avenue de la Paix – P.O. Box 2300 – CH 1211 Geneva 2 – Switzerland

Communication and Public Affairs Office

Tel.: +41 (0) 22 730 83 14/15 – Fax: +41 (0) 22 730 80 27

Email: cpa@wmo.int

public.wmo.int

JN 181407